9-24-2012 12:00 AM

Nano TiO2/Graphene Composites for Photovoltaic and Photocatalytic Materials

Nasrin Farhangi
The University of Western Ontario

Supervisor
Paul A. Charpentier
The University of Western Ontario

Graduate Program in Chemical and Biochemical Engineering
A thesis submitted in partial fulfillment of the requirements for the degree in Doctor of Philosophy

"NANO TiO_2/GRAPHENE COMPOSITES FOR PHOTOVOLTAIC AND PHOTOCATALYTIC MATERIALS"

(Spine Title: TiO_2-based Nanomaterials on Graphene sheets)

(Thesis format: Integrated Article)

by

Nasrin Farhangi

Graduate Program in Chemical and Biochemical Engineering

A thesis submitted in partial fulfillment
of the requirements for the degree of
Doctor of Philosophy

School of Graduate and Postdoctoral Studies
The University of Western Ontario
London, Ontario, Canada

THE UNIVERSITY OF WESTERN ONTARIO
School of Graduate and Postdoctoral Studies

CERTIFICATE OF EXAMINATION

Supervisor	Examiners
Prof. Paul A Charpentier	Prof. Sohrab Rohani
Supervisory Committee	Prof. Chunbao Charles Xu
Prof. Madhumita (Mita) Ray	Prof. Jun Yang
Prof. Lars Rehmann	Prof. Aiping Yu

The thesis by

Nasrin Farhangi

Entitled:

Nano TiO_2/Graphene Composites for Photovoltaic and Photocatalytic Materials

is accepted in partial fulfillment of the
requirements for the degree of
Doctor of Philosophy

_____ Date

_____ Chair of the Thesis Examination Board

ABSTRACT

Graphene has been recognized as one of the most exciting carbon based materials of the present decade due to its unique electronic, mechanical and thermal properties. High surface area exfoliated graphene sheets with controllable surface functionality is an attractive two-dimensional surface for attaching different metals and semiconductors for improving the performance of catalysts, sensors, photoelectronic and energy conversion devices. Graphene is an ideal material which can be used for improving various metal oxide properties such as those of titania (TiO_2). TiO_2/graphene composites have shown excellent properties compared to bare TiO_2 in various applications. In high quality graphene sheets, electrons can travel without scattering at room temperature making them potentially ideal electron transfer bridges, that can also act as an extended charge carrier network resulting in the potential for reduced electron-hole recombination rates when in direct contact with TiO_2. The absorbance capability of TiO_2 has also been improved when anchored onto highly porous graphene. By chemical modification of these networks, the surface properties can be adjusted for using the composites for tailored applications.

This research has focused on the synthesis and modification of TiO_2 nanomaterials on the surface of graphene sheets via an acid modified sol-gel process in supercritical carbon dioxide ($scCO_2$). Acetic acid was used as the polycondensation agent while titanium isopropoxide was used as the Ti alkoxide. The resultant materials were characterized by electron microscopy (SEM and TEM), N_2 physisorption, FTIR, XRD, XPS, thermal analysis, Raman spectroscopy, UV-Vis and PL analysis. The results showed that functionalized graphene sheets containing carboxylate groups acted as templates for anchoring modified TiO_2 nanoparticles and nanowires on the surface. First, sonication following by $scCO_2$ washing was used to anchor commercial anatase TiO_2 on the graphene. TiO_2 nanowires were then synthesized by using a sol-gel method in the green solvent $scCO_2$ using titanium alkoxides. Uniform TiO_2 nanowires with diameters less than 40 nm were decorated on the surface of the graphene sheets. One-dimensional, precisely oriented TiO_2 nanostructures are more effective than TiO_2 nanoparticles as their percolation pathways are excellent for charge transfer. Fe doped TiO_2 morphologies on the graphene sheets were also prepared in both organic solvents and $scCO_2$ to extend these devices band gap into the visible region. TiO_2 nanoparticles less than 5 nm were

uniformly formed on the graphene sheets when ethanol was used as the solvent. Doped TiO_2 nanoparticles and nanowires showed smaller crystal size, higher visible absorption, higher surface area and higher thermal stability compared to similar materials without graphene. However, Fe doped nanowires prepared in $scCO_2$ showed higher surface area and photocatalytic activity than those prepared in organic solvents. ZrO_2-TiO_2 bimetallic nanomaterials were also synthesized on the graphene sheets in $scCO_2$ with different morphologies including nanofibers and nanotubes depending on the initial concentrations of precursors. The synthesized materials were examined for both photocatalytic and photovoltaic performance, with both materials providing higher activity than bare TiO_2 and corresponding materials without graphene.

Possible interactions between TiO_2 and Fe doped TiO_2 with graphene sheets and functionalized graphene sheets were studied by calculating adsorption energy values using the Vienna ab-initio Simulation Package (VASP) based on density functional theory (DFT). The results showed that both physical and chemical interactions are present and responsible for stable interaction between TiO_2 and graphene sheets. The resulting modified TiO_2 nanostructured materials on graphene sheets exhibited a higher visible adsorption, higher surface area, smaller crystallite size, and greater thermal stability, which are all desirable features for catalysts, support materials, semiconductors, and electrodes in dye-sensitized solar cells (DSSC). Nanomaterials prepared by these simple, scalable, environmentally friendly synthesis procedures are potentially attractive for commercial employment.

Keywords: Graphene, TiO_2, nanowires, nanoparticles, nanotubes, Photocatalysis, Photovoltaic, Fe doped TiO_2, TiO_2-ZrO_2 nanomaterials, DFT, VASP.

CO-AUTHORSHIP

Title: TiO_2 and Graphene Sheets Interactions; Experimental and Theoretical Studies.

Authors: Nasrin Farhangi, Serge Ayissi, Yaocihuatl Medina-Gonzalez, and Paul A. Charpentier.

The experimental works were conducted by Nasrin Farhangi under the guidance of advisor Dr. Paul A. Charpentier. Photocurrent testing was carried by Yaocihuatl Medina-Gonzalez. Theoretical calculations of this manuscript were done by Serge Ayissi. Writing and data analysis of this chapter was conducted by Nasrin Farhangi under supervision of Dr. Charpentier. This manuscript is under preparation for publication.

Title: Growing TiO_2 Nanowires on the Surface of Graphene Sheets in Supercritical CO_2: Characterization and Photoefficiency.

Authors: Nasrin Farhangi, Yaocihuatl Medina-Gonzalez, Rajib Roy Chowdhury, and Paul A. Charpentier.

The experimental works were conducted by Nasrin Farhangi under the guidance of advisor Dr. Paul A. Charpentier. Yaocihuatl Medina-Gonzalez and Rajib Roy Chowdhury had great help in discussion and photoefficency testing. The draft of this manuscript was written by Nasrin Farhangi. Modifications were carried out under close supervision of Paul A. Charpentier. The final version of this article was published by the Nanotechnology. 2012 23 294005 doi:10.1088/0957-4484/23/29/294005.

Title: Visible light active Fe doped TiO_2 nanowires grown on graphene using supercritical CO_2.

Authors: Nasrin Farhangi, Rajib Roy Chowdhury, Yaocihuatl Medina-Gonzalez, Madhumita B. Ray, Paul A. Charpentier.

The catalysts development, experimental works were conducted by Nasrin Farhangi under the guidance of advisor Dr. Paul A. Charpentier. Rajib Roy Chowdhury examined synthesized materials in degradation of Estrone. The draft of this manuscript was written by Nasrin Farhangi. Modifications were carried out under the close supervision of Paul A. Charpentier. The final version of this article was published by the Applied Catalysis B: Environmental. 2011, 100, 25-32.

Title: Fe doped TiO_2–Graphene Nanostructures as Advanced Photocatalytic Materials.

Authors: Nasrin Farhangi, Serge Ayissi, Rajib Roy Chowdhury and Paul A. Charpentier.

The synthesis and characterication of synthesized nanomaterilas was conducted by Nasrin Farhangi under guidance of Dr. Paul Charpentier. Photocatalysis testing was carried out by Rajib Roy Chowdhury. Theoretical calculations of this manuscript were done by Serge Ayissi. The draft of this chapter was written by Nasrin Farhangi and corrected by Dr. Paul Charpentier. This manuscript is under preparation for publication.

Title: Synthesis and photocatalytic activity of ZrO_2/TiO_2 nanomaterials on the surface of graphene sheets prepared in Supercritical CO_2.

Authors: Nasrin Farhangi, Rajib Roy Chowdhury and Paul A. Charpentier.

The synthesis and characterisation of synthesized nanomaterilas was conducted by Nasrin Farhangi under guidance of Dr. Paul Charpentier. Photocatalytic test was carried by Rajib Roy Chowdhury. The draft of this chapter was written by Nasrin Farhangi and corrected by Dr. Paul Charpentier. This manuscript is under preparation for publication.

DEDICATION

To the people whose love and support make my life meaningful

my parents

my husband Omid

and

my son Ali

ACKNOWLEDGMENTS

First and foremost I offer my sincerest gratitude to my supervisor, Dr. Paul A. Charpentier, who has supported me throughout my thesis with his patience and knowledge whilst allowing me the room to work in my own way. I attribute the level of my PhD degree to his encouragement and effort.

I gratefully thank Dr. Yaocihuatl Medina-Gonzalez and Dr. Serge Ayissi for their valuable help, advice and constructive comments on this thesis. Thanks to Dr. Jeff Wood using his precious times to read this thesis and gave his comments about it.

I gratefully thank Dr. Ajay Ray for his great support, Dr. Mita Ray and Rajib Roy Chowdhury for their impressive help in photocatalysis studies.

I would also like to extend acknowledgement to my fellow group members, who provided their ongoing support, questions and suggestions.

Finally, I would like to express my love and gratitude to my beloved families; my parents, my husband Omid and my son Ali for their support & endless love.

TABLE OF CONTENT

LIST OF TABLES

LIST OF FIGURES

LIST OF SCHEMES

LIST OF APPENDICES

NOMENCLATURE

Abbreviations:

Abs	absorbance
AC	activated carbon
AOP	advanced oxidation porocess
BET	brunauer-emmett-teller
CB	conduction band
CNTs	carbon nanotubes
DSSC	dye sensitized solar cell
D	disordered band
1D	one dimensional
2D	two dimensional
DFT	density functional theory
Eads	adsorption energy
EG	exfoliated graphite
FF	fill factor
FGSs	functionalized graphene sheets
FTIR	fourier transform infrared spectroscopy
G	graphitic band
GO	graphite oxide
HAc	acetic acid
MWNTs	multi walled carbon nanotubes
PCA	photocatalytic activity
PL	photoluminescence
PV	photovoltaic
QD	quantum dot
SCF	supercritical fluid
$scCO_2$	supercritical CO_2
SEM	scanning electron microscopy
SWNTs	multi walled carbon nanotubes
TiO_2	titania

TEM	transmission electron microscopy
TGA	thermogravimetric analysis
TIP	titanium(IV) *iso*-propoxide
UV	ultraviolet
VASP	Vienna ab-initio Simulation Package
VB	valence band
VOCs	volatile organic compounds
XPS	x-ray photon spectroscopy
XRD	x-ray diffraction
ZPO	zirconium(IV) propoxide

Symbols:

E_x	electron affinity
I_{SC}	maximum current delivered by the solar cell
I_R	integrated intensity of rutile
I_A	integrated intensity of anatase
C	concentration
k	reaction rate constant
P_c	critical pressure
Pin	the intensity of the incident light
Pmax,	maximum power delivered by the solar cell
R	universal gas constant
R	acid to metal alkoxide ratio
T_c	critical temperature
T	reaction temperature
t	time
V	molar volume
V_{OC}	potential that develops between electrodes of the solar cell
V_{pore}	pore volume per gram
W	weight
X_{Rutile}	weight fraction of rutile

θ	half the angle of diffraction
η	solar cell efficiency
Φ	work function
λ	wavelength (nm)

Chapter 1

General Introduction

1.1. Graphene.

Graphene is the term given to a monolayer of graphite, whose carbon atoms are tightly packed into a honeycomb lattice (Figure 1.1). For several years, graphene was only a theoretical concept as scientists assumed that the material was unstable, favoring other curved structures of carbon such as carbon nanotubes (CNTs) or fullerenes, e.g. buckyballs [1]. In 2004, a group led by Andre Konstantin Geim at the University of Manchester created small fragments of graphene monolayers by using a micro-mechanical method termed the "scotch tape method". This simple method used adhesive tape (Scotch Tape), which allowed graphite crystals to be repeatedly split into increasingly thinner pieces. The tape was dissolved in acetone, and, after a few further steps, the flakes including monolayers of graphene were deposited on a silicon wafer. By this method, small amounts of high quality graphene were obtained [2].

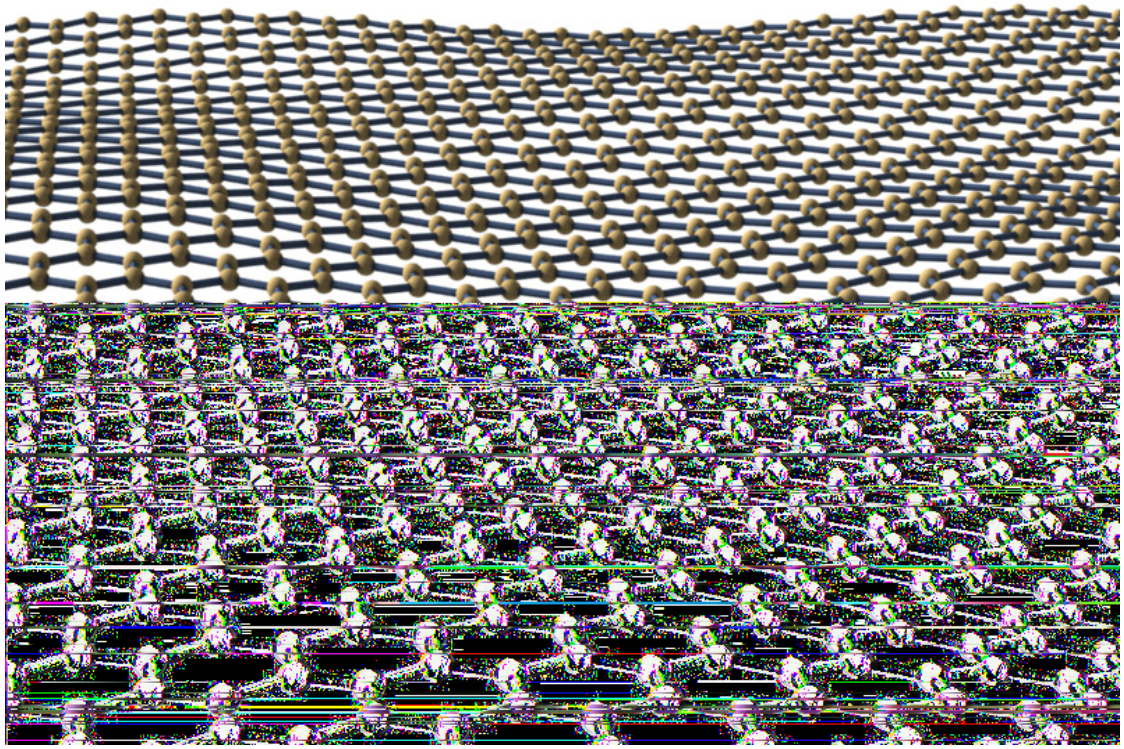

Figure 1.1. Schematic of Graphene Sheet [3].

Graphene sheets show high electrical conductivity and high current carrying capacity in two dimensions. Each carbon atom has one free electron available, with this giant aromatic structure having the ability for electronic conduction. Graphene can also conduct heat in two dimensions, providing the potential for new high thermally conductive plastics [3]. Graphene's theoretical surface area is 2600 m^2/g, compared to approximately 1000 m^2/g for CNTs [4]. Graphenes mechanical properties are also much higher than CNTs as when microcracks in a composite structure encounter a two-dimensional graphene sheet, they are deflected or forced to tilt and twist around the sheet. This process helps to absorb the energy responsible for crack propagation. In addition, crack deflection processes are far more effective for two-dimensional sheets with a high aspect ratio compared to one-dimensional CNTs [5]. For all these reasons, graphene is an attractive material which has potential applications in nanoelectronic devices [6], dye-sensitized solar cell*s* (DSSCs) [7], sensors [8] and photocatalysts [9].

Currently, there is a major challenge towards scaling up graphene production [10]. Production of graphene from inexpensive, earth abundant graphite using an easily scalable and inexpensive process would be very attractive to compete against the relatively expensive processes used for carbon nanotubes [11]. To date, several synthesis methods have been reported for graphene preparation including: epitaxial growth, organic synthesis [12] and chemical exfoliation of graphite [13]. Exfoliation of graphite oxide is viewed as one of the most convenient and low cost methods for graphene production. In graphite oxide, individual layers have larger distances between them compared to native graphite and can readily exfoliate into individual graphite oxide sheets. A chemical or thermal reduction process can reduce these sheets to graphene (Figure 1.2)[4].

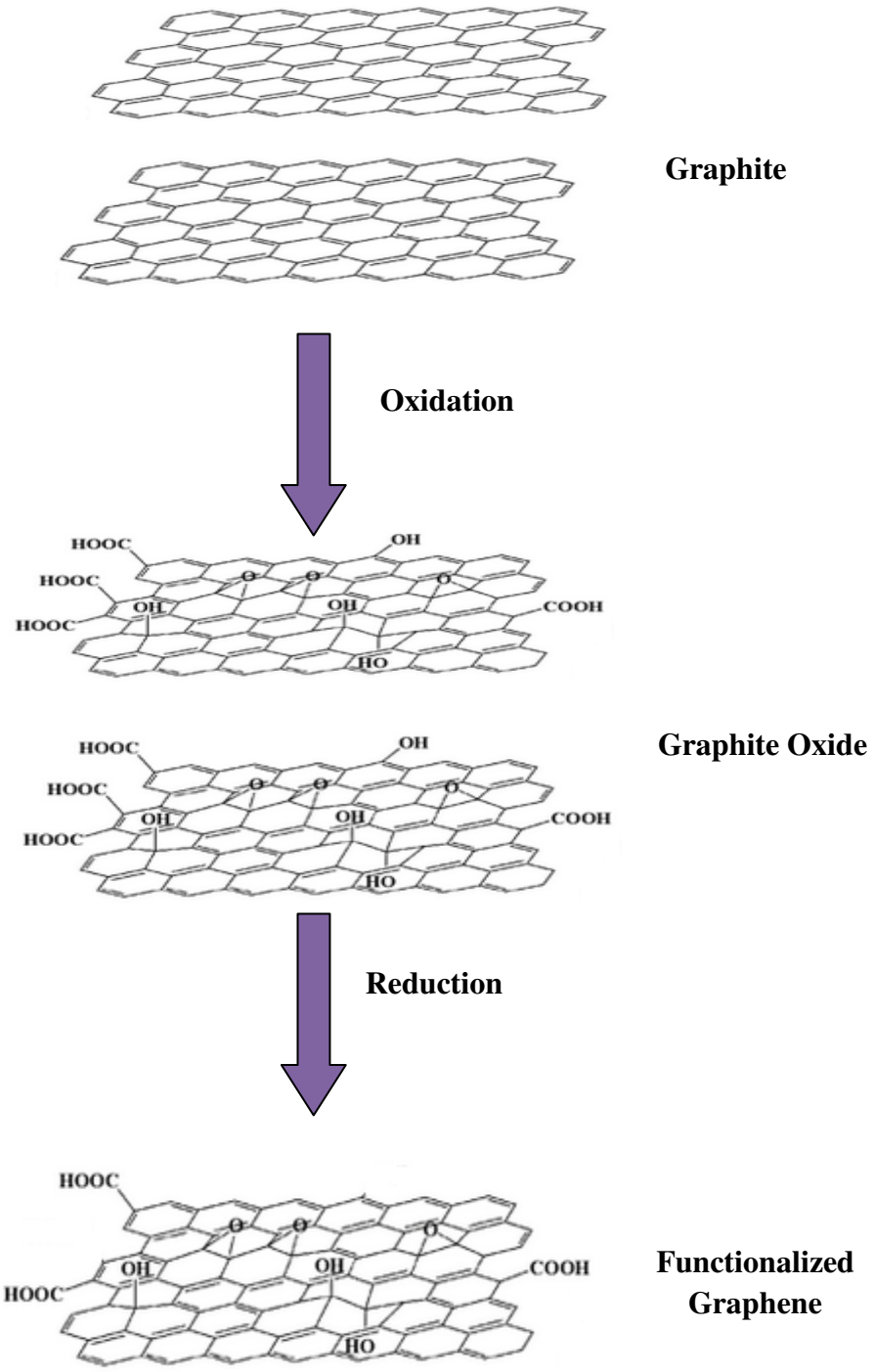

Figure 1.2. Synthesis of graphene sheets from graphite.

1.1.1. Functionalized Graphene Sheets (FGSs).

Most attempts at graphite oxide synthesis have used an acid treatment to produce graphite oxide from graphite. Graphite oxide then converts to nanoplates through thermal or chemical reduction in which one to several graphene sheets stack together. Although nanoplatelets of a few sheets in thickness have been generated by a solution approach [14], a thermal expansion approach was found to be a poor method to produce single graphene sheets. Expanded graphite (EG) (produced by heating sulphuric acid-intercalated graphite) has also been explored as a nanofiller in polymers. EG is composed of many graphene sheets held together by van der Waals forces in rigid nanoplatelets, hundreds of nanometers thick. These characteristics typically limit the performance of EG as most of the graphene sheets in the stacks are not available to effectively interact with the host matrix. It is believed that usually either insufficient oxidation of graphite during the acid treatment or inadequate pressure buildup during the thermal heat treatment stage(s) prevents the production of single graphene sheets.

In 2006, Hannes et al. reported an optimal combination of graphite oxidation and thermal treatment to produce bulk quantities of functionalized single graphene sheets [4, 15]. They observed that during the oxidation process, functional groups on the surface of graphite oxide decomposed to CO_2, causing expansion of the interstices between the graphene sheets during rapid heating. While this decomposition/expansion step is exothermic, vaporization of water is an endothermic process delaying the heating process. For successful production of graphene sheets, it is essential to completely oxidize graphite by using a strong oxidizing reagent while minimizing the role of water vaporization to maximize heating. A solution of sulphuric acid, nitric acid, and potassium chlorate was used to oxidize natural graphite (for >96 h), similar to a process first described in 1898 [16]. For thermal exfoliation, the dried graphite oxide is charged into a quartz tube and then purged with argon. Rapid heating (>2000 °C/min) to 1050 °C splits the graphite oxide into individual sheets. By this method, functionalized single graphene sheets were successfully produced (Figure 1.3) with the volume expanding 500-1000 times, the surface area increasing to 700-1500 m^2/g (determined by BET), and the disappearance of all XRD diffraction peaks (Figure 1.4). Despite the defective structure of the graphene sheets after the reduction step (which introduces functional groups onto

the surface), DC conductivities at a bulk density of ~0.3 g/cm^3 were found to range from 1-2.3 x10^3 S/m [15]. In an NMR study, graphite oxide used for thermal reduction was found to contain aromatic sheets which were randomly functionalized with oxidized aliphatic six-membered rings. The oxidized rings contain C-O-C (epoxide) and C-OH groups, while the sheets were terminated with C-OH and -COOH groups. Some of these functional groups are still retained after thermal treatment which can potentially provide better interaction between functionalized graphene sheets and host materials such as semiconductors, metals and polymer matrix [17]. In Table 1.1 the elemental components and surface areas of SWNTs, expanded graphite and functionalized graphene sheets are compared.

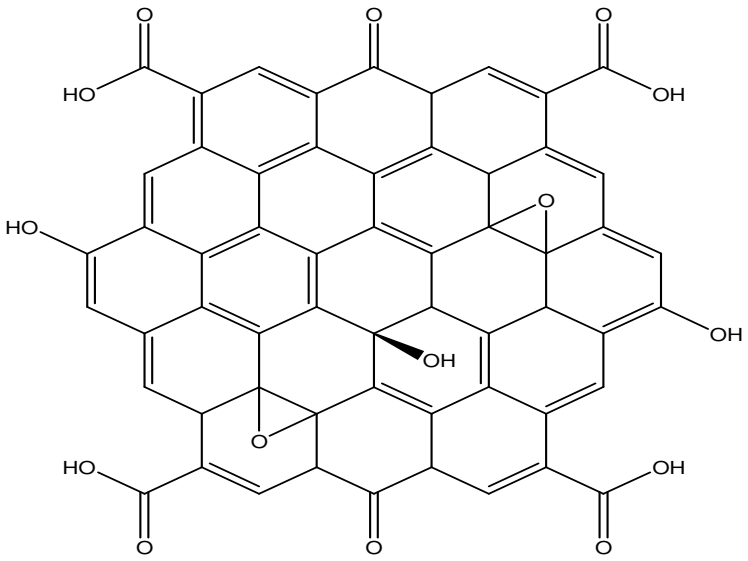

Figure 1.3. Functionalized Graphene Sheets (FGSs).

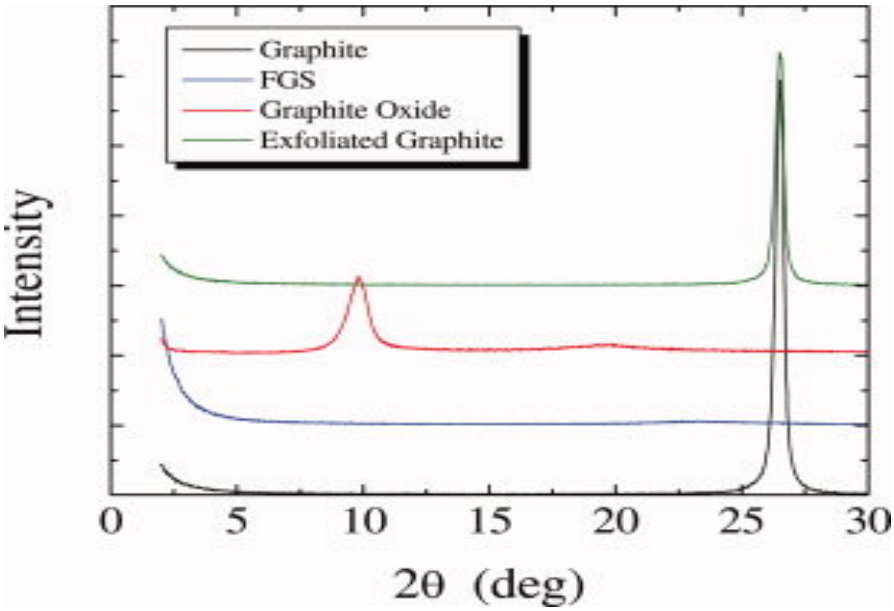

Figure 1.4. XRD Pattern of Graphite, FGSs, GO, and EG [18].

Table 1.1. Elemental analysis and surface area data for SWCNT, EG, and FGSs [18].

Sample	C (at%)	O (at%)	H (at%)	N (at%)	BET (m^2/g)
SWCNT	95.21	0.84	-	-	827
EG	93.68	1.59	-	0.11	20
FGSs	83.37	6.58	9.75	0.1	1500

SWCNT: Single wall carbon nanotube; EG: Expanded Graphite, FGSs: Functionalized graphene sheets.

1.1.2. Using Graphene as a Catalyst Mat.

Recently, graphene based systems have been widely examined for different applications such as polymer composites [11], drug delivery [19], sensing [20], catalysis [21], photovoltaics [22] and nanoelectronics [23]. Two-dimensional graphene sheets can be utilized as a catalyst mat for harnessing catalyst particles onto individual sheets, potentially providing greater adaptability in carrying out selective catalytic or sensing processes [24].

Metal oxides such as TiO_2 and ZnO, which are photocatalytically active under UV irradiation, can be bonded physically to the graphene sheets or chemically attached through carboxylic acid functional groups on the edges of the graphene sheets (Figure

1.5). These nanoparticles can be maintained suspended in solution, hence minimizing the aggregation effect [25]. As described below, these graphene/metal oxide nanocomposite materials have tremendous potential in next-generation photovoltaic and photocatalytic materials.

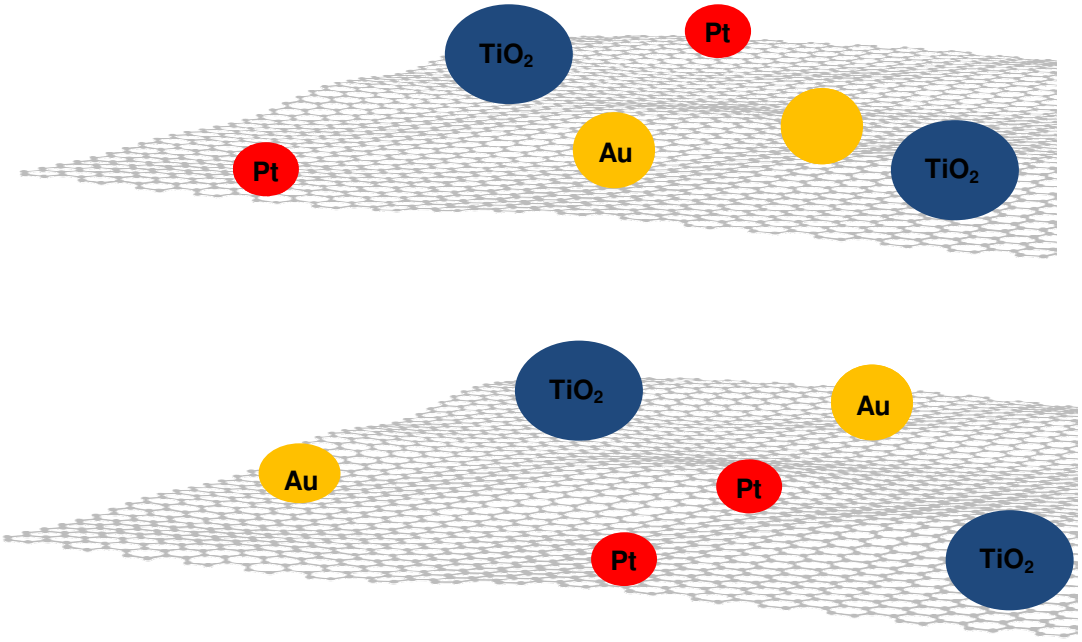

Figure 1.5. Using graphene as a catalyst mat [26].

1.2. TiO_2 and its applications.

1.2.1. Photocatalysis on TiO_2 surface.

Purifying wastewater has become a current topic of critical environmental importance, and is an area in which photocatalysis using graphene/metal oxides may provide a solution [26]. Large amounts of organic pollutants are produced by various commercial, household and agricultural activities, which are often released into the eco-system. These contaminants are usually toxic and carcinogenic and can cause serious health and environmental problems [27]. These organic pollutants are also UV stable and resistant to biodegradation. In the past century, researchers have tried various physical methods for

removing these contaminants from wastewater including ultrafiltration, adsorption, biological treatment, coagulation, and ion exchange [28]. Although these methods have some advantages, they are not very efficient for a number of applications.

In 1972, photocatalytic splitting of water on a TiO_2 electrode was discovered by Fujishima and Honda [29]. Since then, researchers have focused on heterogeneous photocatalysis and attempted to understand this fundamental process, as well as enhancing the photocatalytic activity of TiO_2 for various applications [30, 31]. One of the most interesting uses of TiO_2-based heterogenous photocatalysts is decomposition of organic pollutants in both air and water at relatively low costs [32, 33]. For the metal oxide component of the photocatalyst, many semiconductor materials have been examined including CdS, SnO_2, WO_3, TiO_2, and ZnO. Of these, titania (TiO_2) photocatalysts have demonstrated many advantages over competing technologies and considerable effort has been directed towards developing TiO_2 semiconductor photocatalysts for solving emerging environmental problems [34].

For removing organic pollutants by photocatalysis, three components are required, a catalytic surface (usually a semiconductor material), a strong oxidizing agent (in most cases oxygen) and a photon with equal or higher energy than the band gap energy of the photocatalyst [35]. TiO_2 is often used as an excellent photocatalyst as it is relatively cheap, abundant, non-toxic, chemically inert and photoreactive [36]. In a photocatalytic process, it is preferable to completely degrade the organic molecules to CO_2 and H_2O, which happens on TiO_2's surface under mild temperature and pressure conditions [37].

In photogenerated catalysis, the photocatalytic activity (PCA) depends on the ability of the catalyst to create electron–hole pairs, which generate free radicals able to undergo secondary reactions. Commercial application of the process is known as Advanced Oxidation Process (AOP). Generally, the defining factor is the production and use of the hydroxide anion [38].

Two different crystal structures of TiO_2 are commonly used in photocatalytic reactions. The rutile phase of TiO_2 is the more thermodynamically stable phase, while the anatase crystalline phase of TiO_2 has higher charge-carrier mobility and greater photocatalytic activity compared to the rutile phase. However, anatase TiO_2 has a large band gap (3.2 eV), and can absorb only 4% of solar irradiation, being a major problem of using TiO_2

[39]. In a typical photocatalytic process illustrated using TiO_2 (Figure 1.6), a photon (hν) with equal or higher energy than the band gap reaches the surface of the photocatalyst (TiO_2):

$$TiO_2 + h\nu \rightarrow TiO_2^* (e^- + h^+) \quad (1.1)$$

Several steps are involved in this process including: electron transfer from the adsorbed water to the electron-hole ($e^- + h^+$):

$$h^+ + H_2O \rightarrow HO^\bullet + H^+ \quad (1.2)$$

water dissociation into ions:

$$H_2O \rightarrow H^+ + OH^- \quad (1.3)$$

molecular oxygen acts as an acceptor species in the electron-transfer reaction:

$$e^- + O_2 \rightarrow O_2^- \quad (1.4)$$

super-oxide onions can subsequently be involved in the following reactions:

$$O_2^- + H^+ \rightarrow HO_2^\bullet \quad (1.5)$$

$$H^+ + O_2^- + HO_2^\bullet \rightarrow H_2O_2 + O_2 \quad (1.6)$$

and photoconversion of hydrogen peroxide gives more $HO^\bullet$ free radical groups:

$$H_2O_2 + h\nu \rightarrow 2\ HO^\bullet \quad (1.7)$$

Finally, both superoxide anions (O_2^-) and hydroxyl radicals ($HO^\bullet$) can oxidize organic adsorbed pollutants onto the surface of TiO_2 and convert them to CO_2 and H_2O [38]. Other exciting applications of TiO_2 nanoparticles is passive decontamination on self-cleaning surfaces [40, 41]. However, this coating requires the use of UV lamps for photocatalytic degradation of biological pollutants. Hydrogen gas also can be produced from water splitting on the surface of TiO_2 [42, 43].

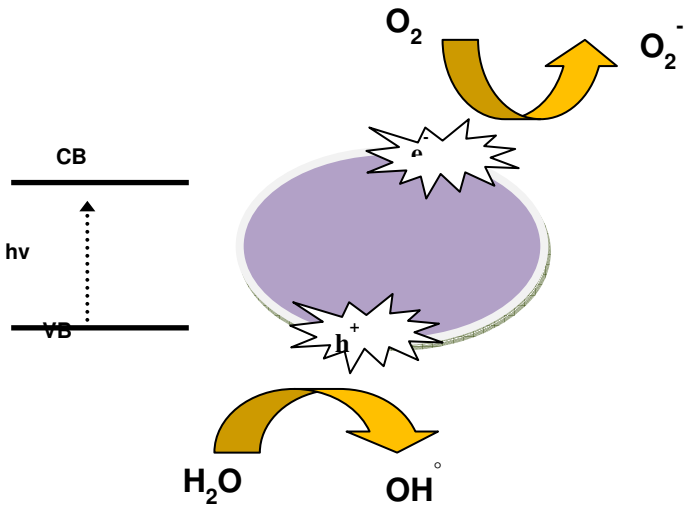

Figure 1.6. The principle of TiO_2 photocatalysis.

1.2.2. Photovoltaic Applications.

Global warming and exhaustion of fossil fuels are very serious problems that need to be solved [44]. In this regard, many researchers are focusing on gaining energy from the sun which is cheap, clean and renewable. In the 21st century, solar energy is expected to make increasing contributions to the world's energy supply, as the worldwide demand for energy is projected to more than double by 2050, and more than triple by the end of this century [45]. The reserves of fossil fuels in current use are not expected to be sufficient to meet this demand over the long term and their continued use produces harmful side effects such as pollution that threatens human health and greenhouse gases that accelerate climate change [46]. Solar cells are being viewed as the best devices for converting the suns energy into useful heat and electricity for next generation energy needs [47]. Currently, the cost of producing heat and electricity using solar cells is still higher compared to commercial fossil fuels or using nuclear energy[48]. Therefore, designing higher efficiency and cheaper solar cells is critical to meet next generation energy demand [49]. Different kinds of solar cells are available; many of which work on the photovoltaic (PV) principle on the basis of p-n junctions of semiconductors. However, the efficiency of current solar cells is still relatively low, inhibiting their widespread adoption and the cost/Watt is relatively high, stimulating scientists and engineers to develop new materials by modifying semiconductors to absorb more energy from the sun

while producing electricity more efficiently [50, 51]. Here, earth abundant and earth friendly materials are of tremendous interest for higher efficiency solar cells. Graphene/metal oxide nanocomposites can be considered as earth abundant and earth friendly, with favourable electrical properties of tremendous interest providing potential for examination in these emerging solar devices.

Of the photovoltaic devices, current interest is towards using dye-sensitized solar cells (DSSCs) which are based on a semiconductor formed between a photo-sensitized anode and an electrolyte. These are also known as Grätzel cells, which were invented by Michael Grätzel at Ecole Polytechnique de Lausanne [47]. These cells are made of low-cost materials, are technically attractive and easy to fabricate, but still their efficiency is not high enough to allow them to compete with fossil fuels for electrical generation [52]. A schematic of a DSSC is presented in Figure 1.7. A layer of nanocrystalline porous TiO_2 nanoparticles covered with a molecular dye is the main component of the solar cell. The TiO_2 is immersed under an electrolyte solution; an anode and cathode (conductive glass) are placed on both sides of the cell. One of the electrodes is covered by gold or platinum. The dye layer absorbs the sunlight and its electrons excite and flow into the TiO_2, then flow toward the transparent electrode. After flowing through the external circuit, the electrons are re-introduced into the cell on a metal electrode on the back of the cell, flowing into the electrolyte. The dye molecules take in the lost electron from the electrolyte [50].

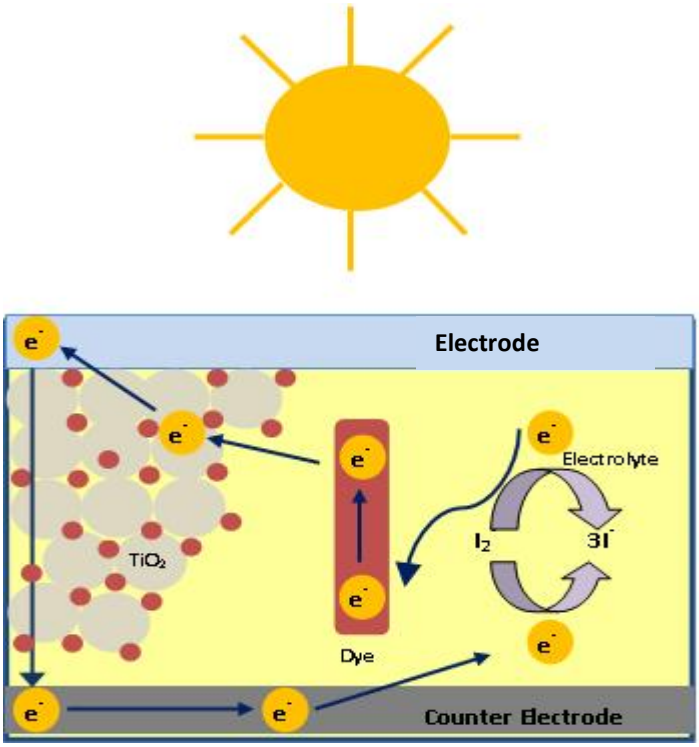

Figure 1.7. Schematic of the dye-sensitized nanocrystalline TiO_2 solar cell.

Typical voltage-current characteristics (IV curve) of a cell without illumination are shown in Figure 1.8. Without illumination, no current flows through the diode. With incident sunlight, the IV curve shifts up and indicates external current flow between electrodes.

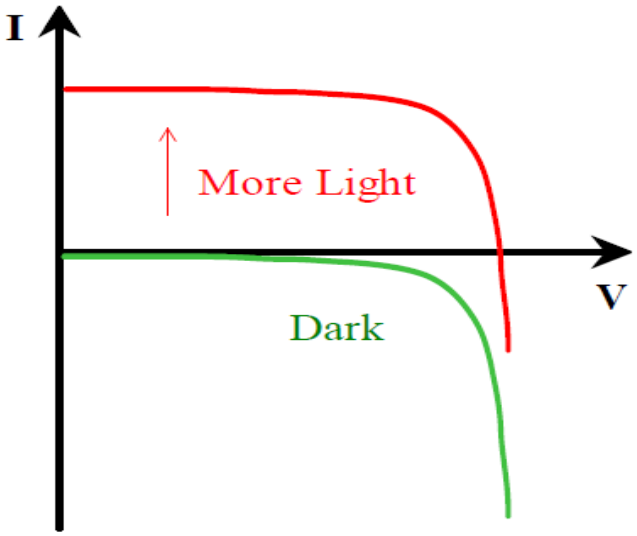

Figure 1.8. The solar cell IV curve as the incident light increases.

The short circuit current, I_{SC}, flows with zero external resistance (V=0) and is the maximum current delivered by the solar cell at each illumination level. Open circuit voltage, V_{OC}, is the potential that develops between electrodes of the solar cell when the external load resistance is very large. The maximum power delivered by the solar cell is known as *Pmax,* which is the area of the largest rectangle under the IV curve. (Figure 1.9)

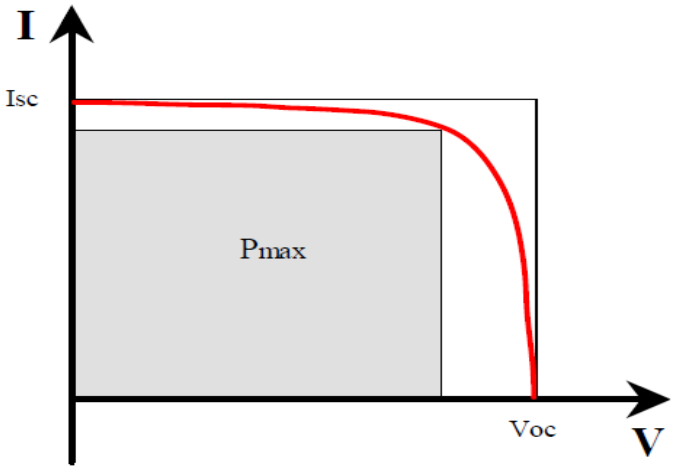

Figure 1.9. Pmax, maximum power delivered by the solar cell.

The fill factor (*FF*) is a commonly used number characterizing the solar cell, which is defined as the ratio of *Pmax* to the area of the rectangle formed by V_{OC} and I_{SC}:

$$\boldsymbol{FF} = \frac{\boldsymbol{Pmax}}{\boldsymbol{I_{SC}V_{OC}}} \tag{1.8}$$

The efficiency is commonly used for comparing the performance of one solar cell to another. Efficiency is generally defined as the ratio of energy output from the solar cell to input energy from the sun. The overall efficiency (η) of the photovoltaic cell is calculated from the circuit current density (I_{SC}), the open-circuit photovoltage (V_{OC}), the fill factor of the cell (*FF)* and the intensity of the incident light (*Pin*= 1000 W/m^2).

$$\boldsymbol{\eta}\ (\%) = \frac{\boldsymbol{P_{max}}}{\boldsymbol{P_{in}}} = \frac{\boldsymbol{Isc \times Voc \times FF}}{\boldsymbol{P_{in}}} \tag{1.9}$$

1.3. Modifications of TiO_2 Nanomaterials for different applications.

There are many methods that can be employed to improve the photocatalytic reactivity of TiO_2 in both the UV and visible regions. A variety of studies have reported that doping different materials into TiO_2 helps extend its band gap into the visible region [53-57]. Another approach is to dope TiO_2 with metals [58] or mixing TiO_2 with a conductive phase, as mixed phase TiO_2 composites show higher photocatalytic activity compared to their pure phases due to the formation of solid-solid interfaces [59]. These interfaces help facilitate charge transfer and reduce electron-hole recombination. Moreover, some researchers believe that during photocatalysis reactions with pollutant molecules, the TiO_2 surface may undergo agglomeration that can reduce the light intensity on the active site, with a resultant minimization in photocatalytic efficiency [60]. This has led to researchers studying mesoporous supports such as alumina, silica and zeolites for better dispersion of the TiO_2 [61, 62]. Carbonaceous materials are also good candidates for modifying properties of TiO_2 as most of them are mesoporous [63]. They can also enhance activity by absorbing visible light and extend TiO_2's band gap to higher wavelengths. In addition, the conductivity of carbon nanotubes (and potentially graphene) is very high, so that when they are in contact with TiO_2, a Schottky Barrier is formed. A Shottky barrier is formed when a semiconductor is in contact with another phase such as metals, in which its electric charges are redistributed forming an electrical double layer. The n-type semiconductor (TiO_2) and metal, both of which are electrically neutral and isolated from one another, have different Fermi level positions. Typically, metals have a higher work function (Φ_m) than semiconductors (Φ_s). When the two materials are in contact electrically, electrons migrate from the semiconductor to the metal to align their Fermi levels as shown in Figure 1.10 [64]. This formation of a Schottky barrier results in the metal having an excess negative charge and the semiconductor having an excess positive charge. Φ_b is the height of the barrier and can be calculated by:

$$\Phi_b = \Phi_m - E_x \qquad (1.10)$$

E_x is the electron affinity, i.e. the distance between the conduction band and vacuum level of the semiconductor. An ideal metal-semiconductor contact is illustrated in Figure 1.10. The produced Schottky barrier at the metal-semiconductor interface can act as an electron

trap, preventing electron-hole recombination which is of importance for both the photocatalytic and photovoltaic devices examined in this thesis.

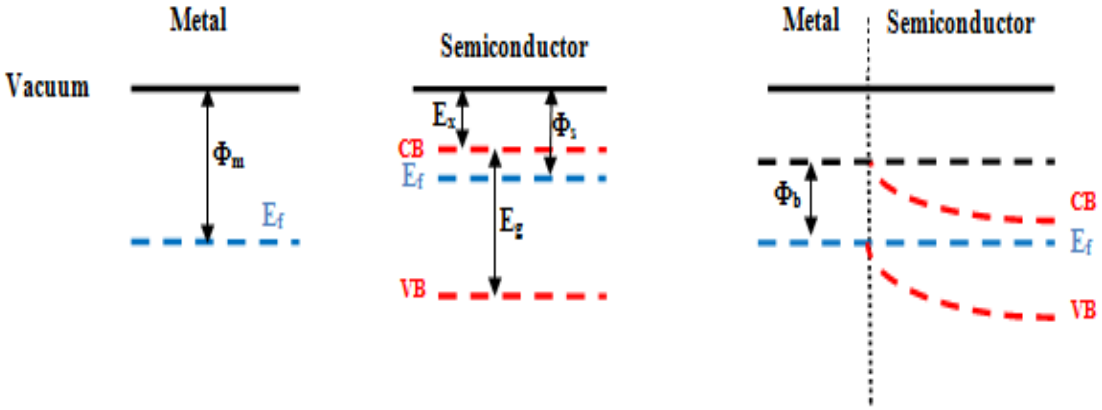

Figure 1.10. Schottky barrier at the contact between the metal and the semiconductor with the different electron affinities.

TiO_2's excited electrons can transfer to the carbon-based materials, followed by a reduction in the electron-hole recombination. New forms of carbon-based materials such as carbon nanotubes and graphene show high conductivity and high surface areas which are favoured for charge recombination of TiO_2 [59]. Recently, many theoretical studies have also been conducted to investigate interactions of TiO_2 and graphene including their band gap, physical interactions and charge transfer [65, 66], which is also a component of this thesis.

1.4. Theoretical approach.

Theoretical approaches are highly desirable in the field of nano- and materials science, particularly for understanding both the growth of nanomaterials and their subsequent physical properties. These methods, which provide access to the atomic and electronic structure, are called ab initio (or first-principle) methods. These are based on a determination of chemical bonding starting from the basic theorems of quantum mechanics. First-principle methods such as ab-initio do not require experimental data,

other than an understanding of the chemical structure of the system. Although highly predictive, these methods are computationally intensive. In order to solve the Schrodinger equations for a multiple-atomic/electronic system such as those of interest in this work, approximations are required in order to make the calculations feasible. Among the ab initio methods, the density functional theory (DFT) approach has become the most popular one. DFT has become a standard approach to study the properties of materials, interpret the experimental results, check the accuracy of simpler simulation schemes through its practical implementation using commercially available code[67].

The Vienna Ab-initio Simulation Package, better known as VASP, is one of the computer programs which is available for atomic scale material modelling, e.g. providing electronic structure calculations and quantum-mechanical molecular dynamics from first principles. VASP computes an approximate solution to the Schrödinger equation, including density functional theory (DFT) [68].

Crystalline solids and surfaces such as metal oxides and graphene are characterized by a practically infinite number of atoms, and their positions are related by certain symmetries inherent to the crystal structure. The problem faced by DFT and, in general, first-principle calculations, is how to handle the infinite number of interacting electrons moving in the static fields of an infinite numbers of ions. To start a DFT calculation, first, we need to define a collection of atoms to present a simple cubic material. Precisely, we need to specify a set of atoms and repeating this set in every direction to create the full three dimensional crystal structures. It is useful to do this task in two steps; first, a defined volume needs to be defined that fills space when repeated in all directions. For a simple cubic metal oxide, we can choose this volume as a cube of side length 'a' with a corner at (0, 0, 0) and edges pointing along the x,y and z coordinates in three dimensional space. Second, we define the positions of the atoms that are available in this volume[69]. The vectors that define the cell volume and atom positions within the cell are called supercells, which are the most basic input into a DFT calculation (Figure 1.11).

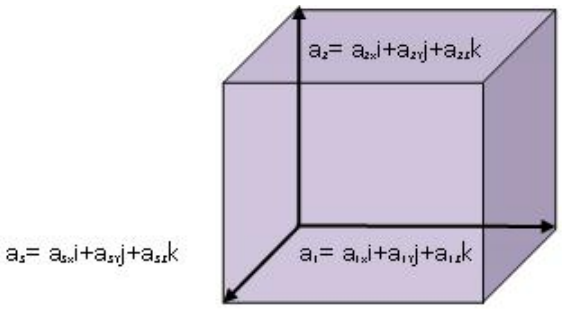

Figure 1.11. Initial geometry specified by the periodically repeating unit "Supercell", specified by 3 vectors {a1, a2, a3}.

Periodic boundary conditions, is another approximation in first principal studies. The central cubical simulation box forms a convenient system for measuring locations of the N molecules[69]. A 2-dimensional version of such a periodic system is shown in Figure 1.12. As a particle moves through a boundary, all of its corresponding images move across their corresponding boundaries. The number of particles in the central box is conserved. It is not necessary to store the coordinates of all images in a simulation (this would be an infinite number), just those of the molecules in the central box considered in a certain period of time. When a molecule leaves the box by crossing a boundary, attention may be switched to the identical molecule entering from the opposite side.

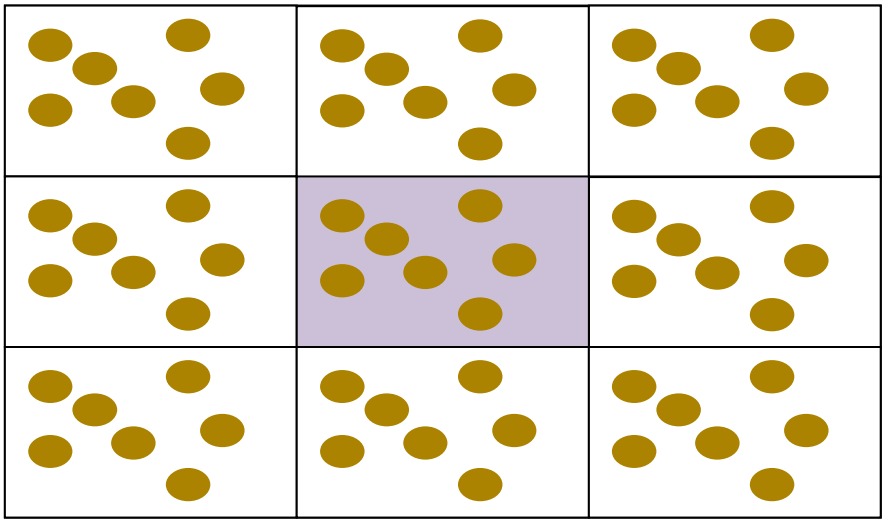

Figure 1.12. Representation of Periodic boundary conditions. The central box is outlined by a light purple background.

Although there are a few recent theoretical studies available on graphene-TiO_2 systems [65, 70], there are still many different parameters which need be calculated and modified to have the most stable composites for different applications. In this thesis, the structure of TiO_2 on the surface of graphene was investigated, while also calculating the corresponding adsorption energies to find the most stable configuration. Most of the theoretical studies on graphene and TiO_2 to date have only investigated ideal graphene sheets without functional groups or defective sites on its surface. In this work, chemical groups validated by experimentation, were introduced onto the edges of graphene sheets to compare the results of ideal graphene and Functionalized graphene sheets when interacting with different structures of TiO_2.

1.5. Scope of the Research.

The main objective of this project was to investigate our hypothesis both experimentally and computationally that graphene could be used as a template to grow unique metal oxide nanostructures using sol-gel chemistry, forming functional nanodevices. Towards this goal, the use of supercritical carbon dioxide ($scCO_2$) was investigated as a green enabling solvent, allowing superior quality catalysts and functional titania/graphene devices to be formed.

The following were identified as specific objectives of this project:

I. Synthesis of the following different types of modified TiO_2 nanomaterials using a sol-gel technique in $scCO_2$:
    a. TiO_2 nanowires on the surface of graphene sheets using a sol-gel method in $scCO_2$ (Chapter 3).
    b. Fe doped TiO_2 nanowires on the surface of graphene sheets using a sol-gel method in $scCO_2$ (Chapter 4).
    c. ZrO_2/TiO_2 nanomaterials on the surface of graphene sheets using sol-gel method in $scCO_2$ (Chapter 5).
    d. Fe doped TiO_2 nanoparticles on the surface of graphene sheets using sol-gel method in ethanol (Chapter 7).

II. Characterization of the synthesized nanomaterials using different physical and chemical techniques in order to,
    a. Study the surface characteristics, morphology, composition and electronic properties.
    b. Investigate the effects of different operating variables and doping agents (ions) on the properties.
III. Evaluation of the performance of selective nanomaterials as photocatalysts for the degradation of E2 (a model compound).
IV. Apply prepared materials as an active layer in DSSCs and compare their efficiency with commercial TiO_2 (anatase).
V. Using the Vienna ab-initio Simulation Package (VASP) based on the density functional theory (DFT) to investigate possible interactions between TiO_2, Fe doped TiO_2 and graphene sheets.(Chapters 6 and 7)

1.6. References.

[1] N.K. Geim AK, Nature Nanotechnology 6 (2007).
[2] K.S.G. Novoselov, A. K., Science 306 (2004).
[3] A.A. Balandin, S. Ghosh, W. Bao, I. Calizo, D. Teweldebrhan, F. Miao, C.N. Lau, Nano Letters 8 (2008) 902-907.
[4] H.C. Schniepp, J.L. Li, M.J. McAllister, H. Sai, M. Herrera-Alonso, D.H. Adamson, R.K. Prud'homme, R. Car, D.A. Saville, I.A. Aksay, The Journal of Physical Chemistry B 110 (2006) 8535-8539.
[5] M.A. Rafiee, J. Rafiee, Z. Wang, H. Song, Z.-Z. Yu, N. Koratkar, ACS Nano 3 (2009) 3884-3890.
[6] G. Eda, G. Fanchini, M. Chhowalla, Nat Nano 3 (2008) 270-274.
[7] N. Yang, J. Zhai, D. Wang, Y. Chen, L. Jiang, ACS Nano 4 (2010) 887-894.
[8] P.K. Ang, W. Chen, A.T.S. Wee, K.P. Loh, Journal of the American Chemical Society 130 (2008) 14392-14393.
[9] P.W. Sutter, J.-I. Flege, E.A. Sutter, Nat Mater 7 (2008) 406-411.
[10] F.D. Xu MS, Sagisaka K, et al., ACS Nano 5 (2011) 1522-1528.
[11] S. Stankovich, D.A. Dikin, G.H.B. Dommett, K.M. Kohlhaas, E.J. Zimney, E.A. Stach, R.D. Piner, S.T. Nguyen, R.S. Ruoff, Nature 442 (2006) 282-286.
[12] W.X. Jiao LY, Diankov G, et al., Nature Nanotechnology 5 (2010) 321-325.
[13] W.S. Ang PK, Bao QL, et al., ACS Nano 3 (2009) 3587-3594.
[14] L.-B. Luo, S.-H. Yu, H.-S. Qian, T. Zhou, Journal of the American Chemical Society 127 (2005) 2822-2823.

[15] M.J. McAllister, J.L. Li, D.H. Adamson, H.C. Schniepp, A.A. Abdala, J. Liu, M. Herrera-Alonso, D.L. Milius, R. Car, R.K. Prud'homme, I.A. Aksay, Chemistry of Materials 19 (2007) 4396-4404.
[16] L. Staudenmaier, Ber. Dtsch. Chem. Ges. 31 (1898) 1481.
[17] S. Ansari, E.P. Giannelis, Journal of Polymer Science, Part B: Polymer Physics 47 (2009) 888-897.
[18] S.G. Ansari, E. P., Journal of Polymer Science: Part B: Polymer Physics 47 (2009) 888-897.
[19] Z. Liu, J.T. Robinson, S.M. Tabakman, K. Yang, H. Dai, Materials Today 14 316-323.
[20] Z. Cheng, Q. Li, Z. Li, Q. Zhou, Y. Fang, Nano Letters 10 (2010) 1864-1868.
[21] I.V. Lightcap, T.H. Kosel, P.V. Kamat, Nano Letters 10 (2010) 577-583.
[22] L. Gomez De Arco, Y. Zhang, C.W. Schlenker, K. Ryu, M.E. Thompson, C. Zhou, ACS Nano 4 (2010) 2865-2873.
[23] Z. Wei, D. Wang, S. Kim, S.-Y. Kim, Y. Hu, M.K. Yakes, A.R. Laracuente, Z. Dai, S.R. Marder, C. Berger, W.P. King, W.A. de Heer, P.E. Sheehan, E. Riedo, Science 328 (2010) 1373-1376.
[24] K.T. Lightcap IV, Kamat PV, Nano Letters 10 (2010) 577-583.
[25] V.K. Prashant, |J. Phys. Chem. Lett. 1 (2010) 520-527.
[26] S. Malato, J. Blanco, J. Cáceres, A.R. Fernández-Alba, A. Agüera, A. Rodríguez, Catalysis Today 76 (2002) 209-220.
[27] D.W. Kolpin, E.T. Furlong, M.T. Meyer, E.M. Thurman, S.D. Zaugg, L.B. Barber, H.T. Buxton, Environmental Science & Technology 36 (2002) 1202-1211.
[28] N.M. Mahmoodi, M. Arami, Journal of Photochemistry and Photobiology B: Biology 94 (2009) 20-24.
[29] A. Fujishima, K. Honda, Nature 238 (1972) 37-38.
[30] M.A. Fox, M.T. Dulay, Chemical Reviews 93 (1993) 341-357.
[31] A. Fujishima, T.N. Rao, D.A. Tryk, Journal of Photochemistry and Photobiology C: Photochemistry Reviews 1 (2000) 1-21.
[32] M.R. Hoffmann, S.T. Martin, W. Choi, D.W. Bahnemann, Chemical Reviews 95 (1995) 69-96.
[33] A.L. Linsebigler, G. Lu, J.T. Yates, Chemical Reviews 95 (1995) 735-758.
[34] J.-M. Herrmann, Catalysis Today 53 (1999) 115-129.
[35] M.R. Prairie, L.R. Evans, B.M. Stange, S.L. Martinez, Environmental Science & Technology 27 (1993) 1776-1782.
[36] S.U.M. Khan, M. Al-Shahry, W.B. Ingler, Science 297 (2002) 2243-2245.
[37] W. Choi, A. Termin, M.R. Hoffmann, The Journal of Physical Chemistry 98 (1994) 13669-13679.
[38] J.C. Yu, W. Ho, J. Lin, H. Yip, P.K. Wong, Environmental Science & Technology 37 (2003) 2296-2301.
[39] T. Ohno, K. Sarukawa, K. Tokieda, M. Matsumura, Journal of Catalysis 203 (2001) 82-86.
[40] R. Wang, N. Sakai, A. Fujishima, T. Watanabe, K. Hashimoto, The Journal of Physical Chemistry B 103 (1999) 2188-2194.
[41] H. Zhang, G. Chen, Environmental Science & Technology 43 (2009) 2905-2910.
[42] S.K. Mohapatra, M. Misra, V.K. Mahajan, K.S. Raja, The Journal of Physical Chemistry C 111 (2007) 8677-8685.

[43] A. Galińska, J. Walendziewski, Energy & Fuels 19 (2005) 1143-1147.
[44] P.M. Vitousek, Ecology 75 (1994) 1861-1876.
[45] M. GrÄtzel, Accounts of Chemical Research 42 (2009) 1788-1798.
[46] E. Alsema, Renewable and Sustainable Energy Reviews 2 (1998) 387-415.
[47] U. Bach, D. Lupo, P. Comte, J.E. Moser, F. Weissortel, J. Salbeck, H. Spreitzer, M. Gratzel, Nature 395 (1998) 583-585.
[48] J.A. Turner, Science 285 (1999) 687-689.
[49] T. Horiuchi, H. Miura, K. Sumioka, S. Uchida, Journal of the American Chemical Society 126 (2004) 12218-12219.
[50] B. O'Regan, M. Gratzel, Nature 353 (1991) 737-740.
[51] B. O'Regan, F. Lenzmann, R. Muis, J. Wienke, Chemistry of Materials 14 (2002) 5023-5029.
[52] M. Grätzel, Progress in Photovoltaics: Research and Applications 8 (2000) 171-185.
[53] J.C. Yu, Yu, Ho, Jiang, Zhang, Chemistry of Materials 14 (2002) 3808-3816.
[54] F. Kiriakidou, D.I. Kondarides, X.E. Verykios, Catalysis Today 54 (1999) 119-130.
[55] C. Burda, Y. Lou, X. Chen, A.C.S. Samia, J. Stout, J.L. Gole, Nano Letters 3 (2003) 1049-1051.
[56] A. Ghicov, J.M. Macak, H. Tsuchiya, J. Kunze, V. Haeublein, L. Frey, P. Schmuki, Nano Letters 6 (2006) 1080-1082.
[57] N. Serpone, The Journal of Physical Chemistry B 110 (2006) 24287-24293.
[58] S. Kim, S.-J. Hwang, W. Choi, The Journal of Physical Chemistry B 109 (2005) 24260-24267.
[59] K. Woan, G. Pyrgiotakis, W. Sigmund, Advanced Materials 21 (2009) 2233-2239.
[60] Z. Zhang, C.-C. Wang, R. Zakaria, J.Y. Ying, The Journal of Physical Chemistry B 102 (1998) 10871-10878.
[61] L. Lei, H.P. Chu, X. Hu, P.-L. Yue, Industrial & Engineering Chemistry Research 38 (1999) 3381-3385.
[62] E.P. Reddy, L. Davydov, P. Smirniotis, Applied Catalysis B: Environmental 42 (2003) 1-11.
[63] T. Cordero, J.-M. Chovelon, C. Duchamp, C. Ferronato, J. Matos, Applied Catalysis B: Environmental 73 (2007) 227-235.
[64] A.L.L. Linsebigler, G. Q.; Yates, J. T. , Chem. Rev. 95 (1995) 735-835.
[65] H. Valencia, A. Gil, G. Frapper, The Journal of Physical Chemistry C 114 (2010) 14141-14153.
[66] M.I. Rojas, E.P.M. Leiva, Physical Review B 76 (2007) 155415.
[67] F. Finocchi, Institut des NanoSciences de Paris (INSP) CNRS and University Pierre et Marie Curie (2011).
[68] K. Georg, Retrieved February 21, 2011 (March 31, 2010).
[69] J.A.S. David Sholl, Wiley Publication (2011).
[70] B. Das, B. Choudhury, A. Gomathi, A.K. Manna, S.K. Pati, C.N.R. Rao, ChemPhysChem 12 (2011) 937-943.

Chapter 2

Literature Review

2.1. Using carbon-based materials in Photocatalysis.

The performance of titania i.e. TiO_2 used in various end-use applications relies on its unique physico-chemical properties such as narrow band gap, and high crystallinity, specific surface area, thermal stability and quantum efficiency [1]. Heterogeneous catalysis is widely used as an effective method for water and air treatment. TiO_2 is the most widely examined photocatalyst for degradation of organic pollutants due to its chemical inertness, low cost, thermal and chemical stability and its strong oxidizing power. In each photocatalytic reaction, TiO_2 is normally suspended in a liquid or gas phase. Several parameters affect the kinetics of the reaction including the amount of catalyst, the intensity and wavelength of the light source, temperature of the reaction, oxygen pressure and the initial concentration of the reactant. However, effective adsorption of visible light is still a significant challenge. One of the approaches to enhance TiO_2□s performance for enhancing light adsorption is to immobilize it on a suitable, high surface area material such as zeolite, activated carbon or nanoclay. Porous materials can also act as coadsorbents; i.e. they adsorb pollutants at the surface, facilitating the ability of TiO_2 to degrade them to CO_2 and water. [2-4].

Among the porous materials, carbon-based materials are preferable due to their earth abundant and friendly nature, unique electronic properties, acidity, adsorption capacity, ability to recover precious metals and their unique pore structure. Researchers have found that the photocatalytic activity of TiO_2 increases on carbon-based materials due to enhanced TiO_2 dispersion and the ability of pollutants to adsorb onto the mesoporous structure. Different forms of carbon materials, with varying properties, play an important role in heterogeneous catalysis [5].

Carbon materials in a conventional form such as graphite, carbon black and activated carbon have been used extensively. More recently, new carbon materials such as carbon nanotubes (CNTs), carbon nanofibers, fullerenes and most recently graphene have emerged as attractive materials for photocatalysis [6].

2.1.1. Activated Carbon-TiO_2.

Activated carbon (AC) was one of the first carbonaceous materials used for modifying the properties of TiO_2. In one of the first studies, activated carbon was used as a support/adsorbent in the photocaltalytic decomposition of organic amide pollutants from air [7]. After that effort, many research groups have focused on studying the AC-TiO_2 system during the last decade. Comparisons between AC and other inert supports such as zeolites, silica, alumina in photocatalysis reactions were studied by Yoneyama et al [8]. Matos et al. also introduced synergy factors between TiO_2 and different kinds of AC from different sources on the photocatalytic activity of model pollutant molecules [9-12]. Ao et al found that the combined effect of AC and TiO_2 enhanced the photodegradation of air pollutants at typical indoor levels [13, 14]. More examples on the use of TiO_2 and AC system including preparation and photodegradation methods in both liquid and gas phases were presented in recent literature [15-17].

2.1.2. Carbon black and Carbon Fiber-TiO_2.

Carbon black and graphite/TiO_2 are used much less frequently than other forms of carbon in photocatalytic reactions due to their lower surface areas. Yoneyama and co-workers compared carbon black with other adsorbants as a support for TiO_2 for the photodecomposition of propyzamide and bromoform [18]. Yuan et al. immobilized TiO_2 on activated carbon fiber for the photocatalytic decomposition of methylene blue and phenol. Other studies on the carbon fiber-modified TiO_2 for photocatalysis have been performed in recent years [19, 20].

2.1.3. Carbon naotubes-TiO_2.

Carbon nanotube-titanium dioxide (CNT-TiO_2) composite systems have potential properties for solving a variety of environmental problems. Carbon nanotubes (CNTs) show high electrical conductivity behaving like metals, thus CNTs can accept TiO_2's excited electrons when they are in direct contact with one another, resulting in slowing down the recombination rate [21]. Carbon nanotubes have very high surface areas and can be used as porous mats such that TiO_2 and other metals and semiconductors can be mechanically or chemically dispersed on their surface. In the case of photocatalysis,

pollutant molecules can also absorb on the porous surface of the prepared composites allowing TiO_2 to degrade the pollutants more efficiently, as in the case of activated carbon [22].

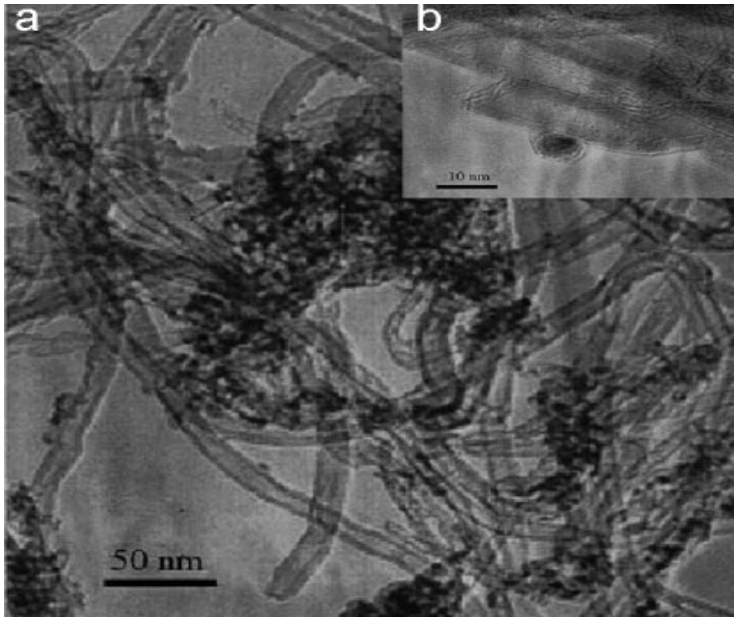

Figure 2.1. Typical TEM image of carbon nanotubes covered by TiO_2 [23].

TiO_2 in all of its crystalline forms is only active in the UV region of the solar spectrum, which represents only 5% of the available energy. Carbonaceous materials such as carbon nanotubes can act as a photosensitizer when in contact with TiO_2, absorbing more visible light, extending TiO_2's band gap into the visible region and thereby enhancing the efficiency of the photocatalytic reactions [23, 24]. With acid treatment some functional groups such as hydroxyl, carbonyl, epoxy and carboxyl can be introduced onto the carbon surface. These groups can be further modified with specific functionality to absorb specific pollutants and act as selective catalysts [22]. This is an advantage of CNTs compared to other kinds of carbon previously used as supports for TiO_2, as they typically absorb many types of pollutants and act as non-selective catalysts.

CNT-TiO_2 composites have been prepared by different methods, although most research has focused on using either the sol-gel chemistry method, hydrothermal treatment or

mechanical mixing [25, 26]. The final step in the synthesis procedure is normally a heat treatment step at 300-500° C to crystallize amorphous TiO_2, while avoiding burning of the carbon nanotubes.

Several different applications of CNT-TiO_2 materials have been reported such as photocatalysis, antibacterials, self-cleaning surfaces, photovoltaics, or in water splitting. However, most of the research has focused on photocatalysis with these new catalytic materials, which have attracted tremendous attention in recent years. The degradation typically follows Langmuir–Hinshelwood reaction kinetics, with several groups results summarized in Table 2.1. A wide variety of results have been reported with reactions depending on several factors including the target pollutants, UV intensity, amount of catalyst, surface area of catalyst, etc. Standard photocatalysts i.e. anatase TiO_2 or P_{25} are normally used as benchmarks for evaluation of other catalysts.

Table 2.1. Photocatalytic properties of CNT/TiO_2 in comparison to pure TiO_2 [27].

Reference	CNT Mass fraction	Reference material; reaction rate [min^{-1}]	TiO_2 [10^{-2} mg mL^{-1}]	UV intensity at (wavelength) [mW cm^{-2}] at [nm]	Degraded material; concentration [mg L^{-1}]	Enhancment factor over TiO_2
Yu et al.[28]	0.97	TiO_2; 2.693×10^{-3}	1.43	Not mentioned	Acetone; 400	1.5
	0.95					1.6
	0.91					0.85
	0.85					0.62
	0.75					0.51
Yu[29]	0.75 a	P_{25}; 0.0351	50.0	0.37 (365)	Procion Yellow	1.64
	0.75 a AC b					1.98
Wang et al.[30]	0.95	TiO_2; 1.8×10^{-3}	1.43	Not mentioned (366, 456, 546)	Phenol; 50	1.10

	0.92					**1.80**
	0.84					**4.10**
	0.73					**3.00**
	0.80					**1.80**
Pyrgiotakis et al.[27]	**0.50 a**	**TiO_2; 0.019**	**6.00**	**2.0 (305)**	**Procion Red MX-5B; 5**	**1.93**
	0.33 a					**0.98**
	0.25 a					**0.63**
	0.85	**TiO_2; 0.005**	**1.70**	**2.0 (350)**	**Procion Red MX-5B; 5**	**10.47**
	0.9997	**TiO_2; 7.3×10^{-3}**	**2.00**	**8.6 (350)**	**Procion Red MX-5B 5**	**0.91**
	0.9990					**2.50**
	0.9980					**1.67**
	0.9950					**0.99**

[a] CNT/particle mixture. [b] AC: activated carbon.

2.1.4. Graphene-TiO_2.

There are several recent reports examining graphene-TiO_2 for various applications, with most using the hydrothermal or sol-gel synthesis method. In all of these studies, TiO_2 on graphene sheets showed higher activities compared to solely using TiO_2. Williams et al. used UV irradiated TiO_2 to reduce graphene oxide to graphene sheets. They assumed that direct interaction between TiO_2 particles and graphene sheets prevented agglomeration of exfoliated graphene sheets. This method can also be used to reduce graphite oxide and obtain photoactive graphene-TiO_2 composites for different applications [31]. Wang et al. stabilized graphene in aqueous solution by using anionic sulphate surfactants. Rutile and anatase TiO_2 were grown on graphene sheets by using these surfactants, with the synthesized composites having 2X the Li-ion insertion properties compared to the pure TiO_2 phase [32].

Graphene Oxide/TiO_2 composites were prepared by Chen et al. with varying amounts of graphene oxide. They found that the concentration of graphene oxide in the starting solution played an important role in the photoelectronic and photocatalytic properties of the composites with either p or n-type semiconductors resulting in visible light active photocatalysts. This study showed a new useful way to synthesize graphene oxide/semiconductor composites with different properties and applications [33].

In TiO_2/graphene assemblies, when TiO_2 is in direct contact with graphene, excited electrons in the conduction band can easily transfer to graphene. Graphenes work function (4.2-4.5 eV) is higher than TiO_2, which results in enhanced charge separation, better stabilization, and a reduction in the electron-hole recombination rate [34]. TiO_2-graphene composites can absorb more visible light, with their band gap shifting to higher wavelengths according to formation of a Schottky barrier between them [35]. With these modifications, the photocatalytic or photovoltaic efficiency of the solar cells using TiO_2-graphene can potentially be improved significantly.

Another exciting potential application of TiO_2-graphene composites is surface decontamination or self cleaning coatings. TiO_2 nanoparticles have been used for this purpose but they are not suitable for general use as they are only active in the UV region [36]. Incorporating TiO_2 on the surface of graphene sheets can enhance its photocatalytic activity as well as extend the light absorption into the visible area. Harmful microbes and dirt can then be easily removed from the surface continuously.

2.1.4.1. Graphene-TiO_2 Composites in Photocatalysis.

Nanocomposites of TiO_2-graphene were prepared by Zhang et al. via the hydrothermal reaction of graphene oxide and TiO_2 in an ethanol-water mixture. The prepared catalysts were examined for the gas-phase degradation of benzene and showed higher photocatalytic activity versus bare TiO_2. Different ratios of graphene/TiO_2 were investigated for photocatalytic activity and it was found that by increasing the amount of graphene, the photocatalytic activity decreased. The higher addition ratio of graphene into the matrix increased the adsorption of pollutants and also lowered the contact surface of TiO_2 particles with light irradiation, leading to the observed reduction in photocatalytic

activity. They also tested the liquid-phase degradation of dyes over TiO_2-graphene, finding similar results [37].

Kamegawa et al. deposited graphene coated TiO_2 nanoparticles on mesoporous silica through the formation of surface complexes between TiO_2 nanoparticles and 2, 3-dihydroxynaphthalene following carbonization under N_2 flow. The prepared composites exhibited a high pore structure and surface area with a higher photocatalytic performance compared to the unmodified samples (without graphene) [38].

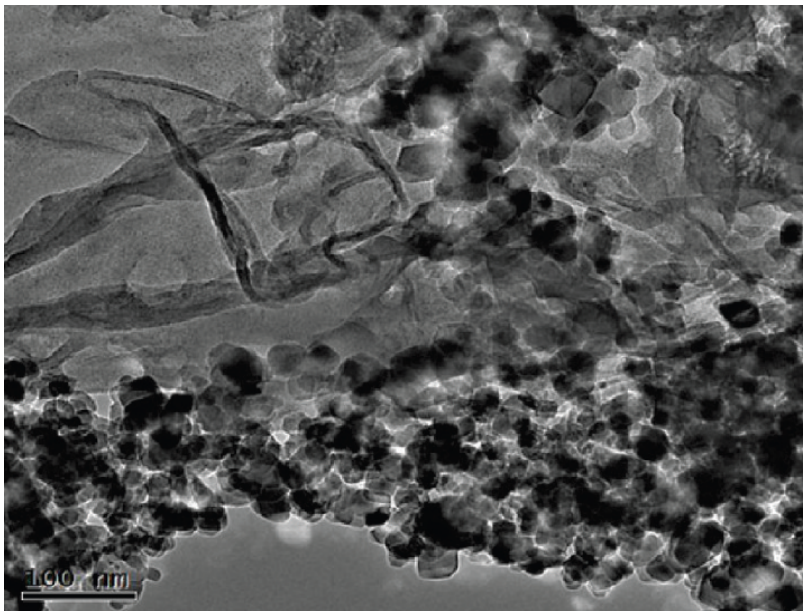

Figure 2.2. Typical TEM images of P25-0.5% Graphene nanocomposite [39].

Zhang et al. prepared chemically bonded TiO_2 (P25)-graphene nanocomposites using a hydrothermal method. The synthesized catalysts showed greater adsorption of dyes and extended the light absorption, along with enhancing the efficient charge separation properties. They observed significant enhancement in the degradation of methylene blue using these catalysts compared to bare P25 and CNT-P25 composites[39].

A series of TiO_2/graphene composites were prepared using the sol-gel chemistry method with different graphene contents. The synthesized materials were evaluated by hydrogen evolution from water photo-splitting under UV irradiation. They found that both the calcination temperature and the amount of graphene affected the photocatalytic activity of

the prepared materials. The highest photocatalytic activity was observed for the sample with 5% graphene sheets calcined under nitrogen[40].

Lui et al. used a water/toluene two-phase process for assembling TiO_2 nanorods on graphene oxide (GO) sheets. They demonstrated absorption of the contaminant methylene blue by the GO sheets with effective charge transfer from the TiO_2 nanorods to the GO sheets, which helped increase the photocatalytic activity of the prepared catalysts[41].

Liang et al. directly grew TiO_2 nanocrystals on graphene oxide (GO) using two steps: 1) TiO_2 was coated on the GO sheets by hydrolysis and then: 2) hydrothermal treatment led to the anatase TiO_2 being crystallized on the GO surface. The prepared graphene/TiO_2 nanocrystals were tested for photocatalytic activity in the degradation of rhodamine B, showing an impressive three-fold photocatalytic enhancement over P25 [42]. The gas-phase degradation of benzene liquid-phase degradation of dyes over TiO_2-graphene (prepared by hydrothermal reaction of graphene oxide and TiO_2 in ethanol and water) were studied by Ang et al [43]. These catalysts exhibited much higher photocatalytic activity and stability than bare TiO_2. They found that at higher weight ratios of TiO_2-graphene, the photocatalytic activity decreased [43]. The increase in photocatalytic activity of the TiO_2-graphene composites was explained by an enhancement of the adsorptivity of pollutants, light absorption intensity, electron hole pairs lifetime, and extended light absorption range of the prepared catalysts [43].

2.1.4.2. TiO_2-Graphene composites as an active layer in solar cells.

Dye-sensitized solar cells (DSSCs) were fabricated using graphene/TiO_2 composites as the photoanode by Sun et al. They used the composites to prepare thin films acting as electrodes of DSSCs. The small amount of graphene used for fabrication was found to extend the lifetime of excited electrons and also to increase dye adsorption, leading to enhanced performance [16].

Tang et al. used molecular grafting to attach TiO_2 to the graphene surface by chemisorption. The employed materials were used as the photoanodes for DSSCs. The presence of graphene in the composites significantly increased photocurrent through the DSSCs. The maximum energy conversion efficiency reported was 5 times higher than

bare TiO_2, showing that incorporation of graphene sheets significantly enhanced the photovoltaic performance [44].

Quantum dot-sensitized solar cells (QD-DSSCs) based on TiO_2 film photoanodes with different amounts of graphene have been fabricated, with PV results showing that incorporating 0.8 wt.% graphene in the TiO_2 photoanode resulted in a maximum power conversion efficiency of 56% higher than that without graphene. This increased efficiency was attributed to enhanced visible light absorption, a reduction of electron recombination and backtransport reaction, as well as enhanced electron transport with the introduction of graphene [45]. Zhu et al. synthesized graphene/TiO_2 composite nanosheets using graphite oxide and $TiCl_3$. $TiCl_3$ acts as both a reducing agent and a precursor. They also observed enhanced photocurrent response of the composites [46].

2.1.5. Mechanism of Photocatalytic Enhancement in carbon based materials-TiO_2 Composites.

The photocatalytic enhancement in carbon-TiO_2 composites has been explained using two different mechanisms. The first mechanism was proposed by Hoffmann et al [47], in which electrons in the valence band of TiO_2 are excited by high energy photons and transferred to the conduction band. Photogenerated electrons are then transferred into the carbon material and a hole remains in TiO_2, with redox reactions occurring on the surface of TiO_2. A schematic of this mechanism is shown in Figure 2.3a. Wang et al. proposed a second mechanism considering carbon materials as photosensitizers [48]. When absorbing visible light, electrons from the carbon material are excited and transfer to the conduction band of TiO_2, followed by formation of superoxide radicals from the adsorbed molecular oxygen. Meanwhile, the positively charged carbon takes an electron from the valence band of TiO_2, leaving a hole. The positively charged TiO_2 then reacts with adsorbed water to form hydroxyl radicals. This proposed mechanism is shown in Figure 2.3b.

However, the carbon–TiO_2 nanocomposite system is more complex than either of these proposed models. In some studies, functional groups such as –OH and –COOH are introduced onto the carbon materials by simple acid refluxing. Pyrgiotakis et al. proposed

that TiO_2 can make a chemical bond with functional groups on the carbon surface and carbon-oxygen-titanium bond. This helps to extend the light absorption to longer wavelengths, potentially improving the photocatalytic activity [49] This mechanism is shown in Figure 2.3c).

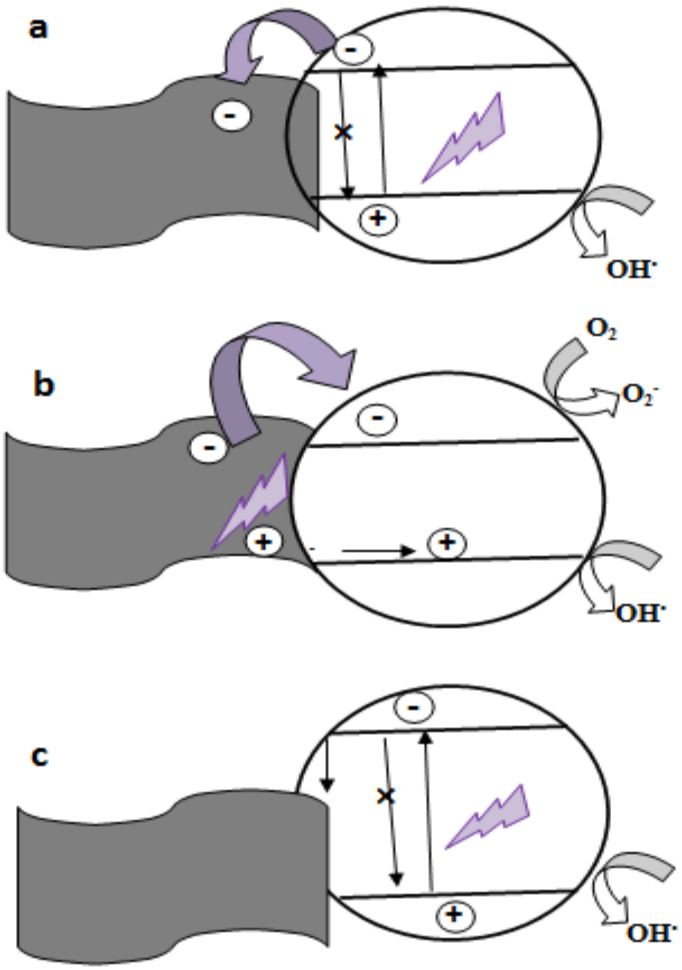

Figure 2.3. The proposed mechanisms for the carbon-based materials-TiO_2 composites enhancement of photocatalysis.

a) Carbon materials act as an electron trapper.
b) The photon generates an electron–hole pair in the Carbon substrate.
c) The carbon materials can act as impurity through the Ti–O–C bonds.

2.1.6. Carbon-TiO_2 composites used as a Heterogenous Photocatalysis in Liquid Phases.

Activated carbon-TiO_2 composites first attracted considerable attention due to possessing high adsorption capacity, while increasing the photocatalytic degradation rate [7]. In all previous work, the reaction rate of degradation was found to be a function of the amount of carbon phase, up to an optimal value beyond which the photocatalytic activity decreased. It is believed that after an optimal point, there is poor contact between carbon and TiO_2 [18].

Several model substrate molecules have been tested for photocatalytic degradation of aqueous solutions in the presence of TiO_2 and carbon phases. Most studies have focused on degradation of phenol and phenol derivatives. Additional model compounds such as different kinds of dyes, have also been studied [50-52].

Matos et al. defined a synergy factor (R) to compare the benefit of using TiO_2 in the presence of carbon phases [10]. Many authors use this factor as this is the ratio of first order constants for the reaction containing TiO_2 and carbon phases and just bare TiO_2:

$$R = \frac{k_{app}\ (TiO_2 + C)}{k_{app}\ (TiO_2)} \tag{2.1}$$

The R factor is difficult to use as an independent standard to compare the different results as the photodegradation reaction depends on many different variables, including the concentration of the organic compound, the reactor volume and the amount of catalyst used in the reaction [53]. The rate of reaction for photoconversion is defined as:

$$r = \frac{V}{W}\ \frac{dC}{dt} \tag{2.2}$$

where V is the reaction volume (liter), W is the weight of catalyst (gram), and C is the concentration (g/L) at a given time t (second).

2.2. Modifying TiO_2 by introducing foreigner atoms to its lattice.

Undoped TiO_2 has a large band gap and can absorb only a small fraction of the available solar energy (<5%). Therefore, it is highly desirable to improve the TiO_2 optical activity by shifting the onset of the response from UV to the visible region. Indeed, a great deal of research is focusing on modifying the properties of TiO_2 in order to achieve these desirable properties. Foreign-element-doping is one of the most common methods to enhance the performance of titania nanomaterials. There are two different approaches in the literature towards doping: 1) atoms which have a larger atomic radius than TiO_2 such as Zr, Al, or Si are added to increase the thermal stability, and surface area [54-56], and 2) atoms with a smaller atomic radius than TiO_2 such as Fe, Cr, V, Mn, Co C, N, S, are added to shift the absorption edge over a broader range [57, 58].

2.2.1. Doping TiO_2.

Shifting the bandgap of TiO_2 to the visible region would expand TiO_2's applications by allowing more solar energy to be absorbed [59, 60]. A suitable metal dopant can lead to improvement of the properties of TiO_2 such as an increase in the acidity of its surface, acceleration of phase transfer, and an increase in the degree of separation of any photogenerated charges. These factors are controlled by changes in the preparation method, loading of catalyst, and type of dopant element. The transition metal ions such as Fe, Ni, Ag, Cr, V, Mn, Co, etc. can be added as dopants [60-66]. This type of doping can also act as an electron-hole trap site and decrease the photoinduced electron/hole charge recombination. The other kinds of dopants which are usually used to shift the band gap of TiO_2 to higher wavelengths are anions such as C, N and S [67-73]. Asahi et al. showed that the substitutional doping of N was the most effective among all anions for band gap narrowing, because nitrogens p states mixed with oxygens 2p states [74].

2.2.2. Introducing ZrO_2 to TiO_2 lattice.

Enhanced specific surface area, crystallinty and thermal stability are important factors that strongly affect the performance of TiO_2. These can be modified by using different methods, catalysts, types and amounts of dopants and varying the temperatures of heat treatment [75, 76]. Zr has been reported as one of the most suitable dopants to enhance the thermal stability, surface area and activity of TiO_2 nanomaterials [77, 78]. Research has demonstrated that TiO_2–ZrO_2 binary metal oxides exhibit higher photocatalytic activity than either individual metal oxide [79]. The increase in surface area compared to pure TiO_2, the rise in surface acidity, or the creation of active sites on the surface are possible factors which may result in this improvement [80]. Mesoporous zirconium-containing TiO_2 was synthesized by Gnatuyak et al[81]. They observed that the zirconium content changed the acidity and specific surface area of films. The increase in photocatalytic activity of TiO_2/ZrO_2 compared to pure TiO_2 is connected with the increase in thermal stability of the porous structure, the increase in acidity of the surface, and with the generation of structural defects due to the incorporation of impurity ions in the TiO_2 lattice. Previously, the Charpentier research group has synthesized ZrO_2-TiO_2 nanotubes by using a sol-gel method in $scCO_2$. They observed that the morphology of the ZrO_2-TiO_2 nanotubes could be controlled by changing either the concentration of the starting materials or the acid-to-metal-alkoxide ratio. The synthesized materials showed higher surface areas, smaller crystallite size, and greater thermal stability compared to unmodified TiO_2 [82]. The kinetics of the reaction were also studied and revealed that temperature, concentration of the starting materials, and acid to metal (Zr and Ti) alkoxide ratio were the main factors altering the gelation kinetics, as well as the physical properties of the synthesized materials [83].

The Charpentier group has also studied the effect of different solvents on the morphology of the bimetallic ZrO_2-TiO_2 metal oxides. Solvents with low dielectric constant such as $scCO_2$, hexane, or xylenes showed lower gelation times. Gelation time was increased by using higher dielectric constants such as alcohols and theoretical calculations showed that the nanostructure was enhanced by lower dielectric constant solvents [84].

2.3. Supercritical Fluids (SCFs) and Supercritical CO_2 ($scCO_2$).

The use of volatile organic compounds (VOCs) is becoming strongly restricted due to increasing environmental concerns in recent years [85]. Consequently, considerable efforts have been devoted to finding environmentally friendly solvents and processes for industrial application [86]. In 1822, Baron Charles showed that there is a critical temperature (T_c) and pressure (P_c) above which a single substance can exist as a fluid and not as a vapour or liquid in equilibrium. These are called supercritical fluids (SCFs), which have the unique ability to diffuse through solids and provide greater mass and heat transfer than conventional solvents. In the last few decades, extensive research studies using SCFs in different industrial areas have shown its favourable properties as a solvent. In table 2.2, some useful materials typically used as supercritical fluids and their properties are listed.

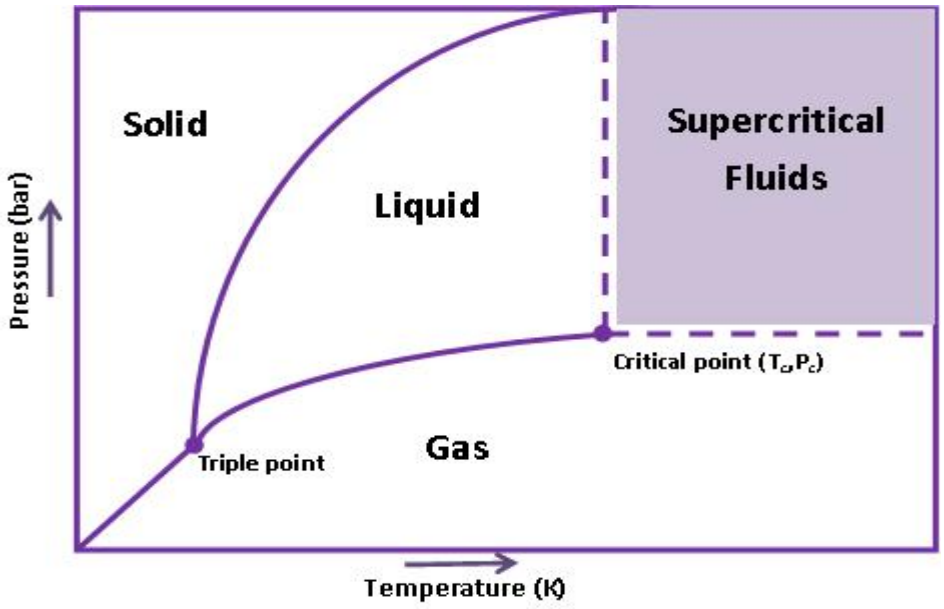

Figure 2.4. Schematic of the phase diagram of a single substance.

Table 2.2. Materials useful as supercritical fluids[87].

Materials	**T_c (K)**	**P_c (bar)**	**ρ_c (g/cm^3)**
Ethylene	282	50	0.22
Xenon	290	58	1.11
Fluoroform	299	49	0.53
Carbon dioxide	304	74	0.47
Ethane	305	49	0.20
Nitrous oxide	310	72	0.45
Propane	370	43	0.22
Ammonia	406	114	0.23
Water	647	221	0.32

Note: T_c P_c and ρ_c are critical temperature, critical pressure and critical density, respectively.

2.3.1. Properties of supercritical CO_2.

Supercritical carbon dioxide ($scCO_2$) has attracted considerable attention due to its physical properties for replacing organic solvents in a wide range of applications [88-90]. $ScCO_2$ is non-toxic, non-flammable, inexpensive, naturally abundant, chemically stable and has a convenient critical temperature (31.1°C) and pressure (1070 psig). In addition, it is environmentally friendly (i.e. is not a volatile organic compound (VOC)), is a by-product of fermentation, and it has lower operation costs due to lower energy consumption. $ScCO_2$ can be very beneficial for synthesizing nanomaterials as it has low viscosity, "zero" surface tension and high diffusivity. These properties can also help to increase the reaction rates [91]. The physical properties such as density and solvating strength can be "tuned" by adjusting the operating temperature and pressure which provide an easily tunable reaction medium [92]. Moreover, washing the synthesized materials is made easy when reactions are carried out in $scCO_2$, by simple venting. This allows reaction products with high porosity to be easily obtained without any additional drying process while also enabling recycling of the CO_2. All these properties make $scCO_2$ it an excellent candidate for using as a green solvent, especially in scale-up applications.

2.4. Sol-gel chemistry: (Synthesis Method)

The sol-gel method is a well-known method for synthesizing different oxide materials. Metal alkoxides such as titanium isopropoxide (TIP) are ideal precursors used in the sol-gel process because they react easily with water. This reaction is called hydrolysis, as a hydroxyl ion becomes attached to the metal atom as follows:

$$M(OR)_4 + H_2O \rightarrow HO\text{-}M(OR)_3 + R\text{-}OH \quad (2.3)$$

Depending on the amount of water and catalyst present, hydrolysis may proceed to completion, so that all the -OR groups are replaced by -OH groups as follows:

$$M(OR)_4 + 4\,H_2O \rightarrow M(OH)_4 + 4\,R\text{-}OH \quad (2.4)$$

Different intermediate species $[(OR)_2\text{–}M\text{-}(OH)_2]$, $[(OR)_3\text{–}M\text{-}(OH)]$ can be produced during the condensation process.

$$(OR)_3\text{–}M\text{-}OH + HO\text{–}M\text{-}(OR)_3 \rightarrow [(OR)_{3M}\text{–}O\text{–}M(OR)_3] + H\text{-}O\text{-}H \quad (2.5)$$

Or

$$(OR)_3\text{–}M\text{-}OR + HO\text{–}M\text{-}(OR)_3 \rightarrow [(OR)_{3M}\text{–}O\text{–}M(OR)_3] + R\text{-}OH \quad (2.6)$$

In addition, two partially hydrolyzed molecules can link together in a condensation reaction to form a [M–O–M] oxo bond. Complete polymerization and loss of solvent leads to the liquid sol transforming into a solid gel phase. For metal alkoxides, this method involves hydrolysis of the metal alkoxide with water and a catalyst, i.e. an acid or a base, condensation into macromolecules, forming a colloidal sol and subsequently three-dimensional network, solvent exchange to remove water by alcohol, and then drying the wet gel using a supercritical fluid to produce the aerogel.

The properties of the sol-gel products depend on the precursors, processing temperature, catalyst, solvents, and solvent removal process [93]. This method also has several advantages over other methods, such as allowing impregnation or co-precipitation which can be used to introduce dopants. The major advantages of the sol-gel technique includes molecular scale mixing, high purity of the precursors, and homogeneity of the sol-gel products with a high purity of physical, morphological, and chemical properties [94].

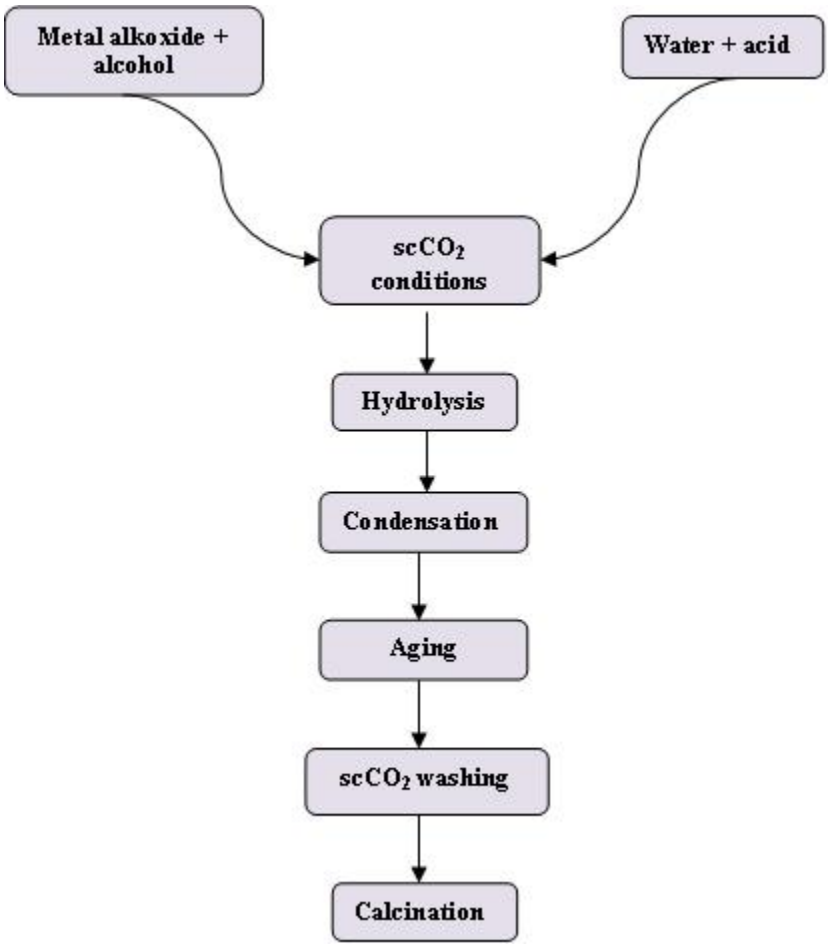

Figure 2.5. Aerogel synthesis scheme by the conventional sol-gel route.

2.5. The measurement of absorption edge and band gap of semiconductors. Using a UV spectrometer, diffuse reflectance spectra of different semiconductors can be acquired. A classical semiconductor exhibits minimal optical absorption for photons with energies smaller than the bandgap and high absorption for photons with energies greater than the bandgap. As a result, there is a sharp increase in absorption at energies close to the bandgap that manifests itself as an absorption edge (or "reflection threshold") in the UV-Vis absorbance spectrum [95]. Based upon these diffuse reflectance spectra, absorption edge and band gap energies can be calculated. For TiO_2 which has a bandgap between 3.0 and 3.2 eV, this absorption edge occurrs between 370 and 420 nm [96].

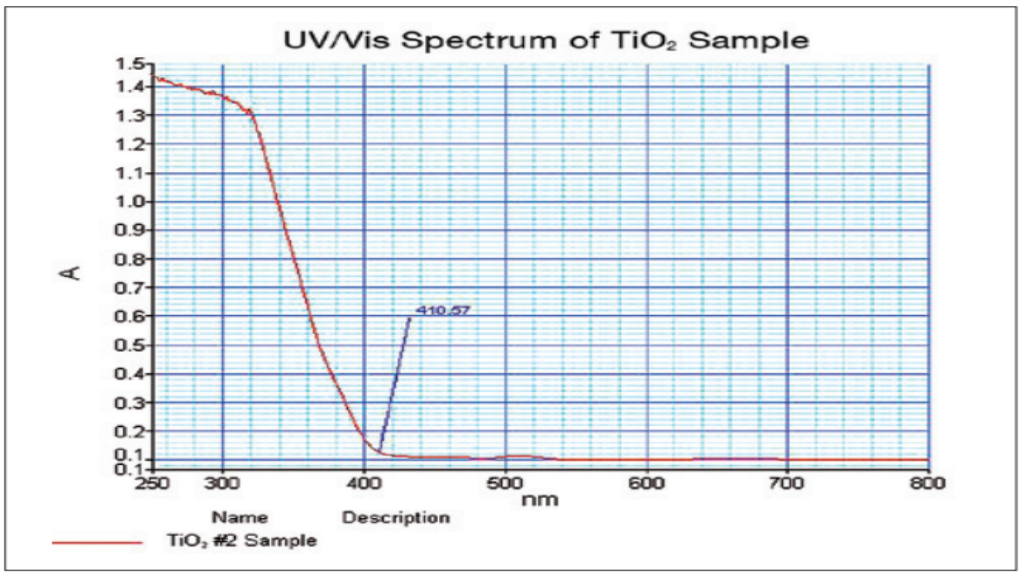

Figure 2.6. TiO_2's UV-vis spectra.

The resulting spectrum obtained on TiO_2 is shown in Figure 2.6. The spectral data recorded showed the strong cut off at 410.57 nm; where the absorbance value is minimum. While the absorption edge is indicative of the location of the bandgap, accurate estimation of the bandgap requires use of the following formula:

Band Gap Energy (E) = h*C/λ

h = Planks constant = 6.626 x 10^{-34} Joules sec

C = Speed of light = 3.0 x 10^{8} meter/sec

λ = Cut off wavelength = 410.57 x 10^{-9} meters

Calculated band gap energy is 4.84156E-19 Joules which is 3.025976eV.

2.6. References.

[1] B.O. Ohtani, Y.; Nishimoto, S. i, J. Phys. Chem. B 101 (1997) 3746-3752.
[2] J.F. Tanguay, Suib, S. L., and Coughlin, R. W., , J. Catal. 117 (1989) 335.
[3] C. Minero, Catozzo, F., and Pelizzetti, E., , Langmuir 8 (1992) 489.
[4] N. Takeda, Torimoto, T., Sampath, S., Kuwabata, S., and Yoneyama,, J. H., Phys. Chem. 99 (1995) 9986.
[5] P.a.F. Serp, J. L., John Wiley & Sons, Inc., Hoboken, New Jersey (2009).
[6] K. PV, Journal of Physical Chemistry Letters 1 (2010) 520-527.
[7] H.I. Uchida, S.; Yoneyama, H., Chem. Lett 22 (1993) 1995.
[8] T.O. Torimoto, Y.; Takeda, N.; Yoneyama, H., J. Phtochem. Photobiol. A 103 (1997) 153.
[9] J.L. Matos, J.; Herman, J. M., Appl. Catal. B 18 (1998) 281.
[10] J.L. Matos, J.; Herman, J. M., Carbon 37 (1999) 1870.
[11] J.L. Matos, J.; Herman, J. M., J.Catal. 200 (2001) 10.
[12] J.L. Matos, J.; Herman, J. M.; Uzcategui, D., Appl. Catal. B 73 (2007) 227.
[13] C.H.L. Ao, S. C., Appl. Catal. B 44 (2003) 191.
[14] C.H.L. Ao, S. C., J. Phtochem. Photobiol. A 161 (2004) 131.
[15] Y.J.L. Li, X. D.; Li, J. W.; Yin, J., Matter Lett 59 (2005) 2659.
[16] S.e. al., Applied Physics Letters 96 (2010) 083113.
[17] Y.J.L. Li, X. D.; Li, J. W.; Yin, J., Water Res. 40 (2006) 1119.
[18] N.I. Takeda, N.; Torimoto, T.; Yoneyama, H., J. Catal. 177 (1998) 240.
[19] J. Zhu, Y. Shi, X. Feng, H. Wang, X. Lu, Materials & Design 30 (2009) 1042-1049.
[20] X. Zou, N. Maesako, T. Nomiyama, Y. Horie, T. Miyazaki, Solar Energy Materials and Solar Cells 62 (2000) 133-142.
[21] A.K. Kongkanand, P. V. , ACS Nano 1 (2007) 13.
[22] K.P. Woan, G.; and Sigmund, W., Adv. Mater. 21 (2009) 2233-2239.
[23] Y.L. Ou, J. D.; Fang, S. M. ; Liao, D. W. , Chem. Phys. Lett. 429 (2006) 199.
[24] W.D.S. Wang, P.; Kalck, P.; Faria, J. L., J. Mol. Catal. A Chem. 235 (2005) 194.
[25] X.H.J. Xia, Z. H., Yu,Y. ; Liang, Y.; Wang, Z. ; Ma, L. L. , Carbon 45 (2007) 717.
[26] K.D. Byrappa, A. S. ; Sajan, C. P.; Basavalingu, B.; Shayan, M. B. ; , K.Y. Soga, M. , J. Mater. Sci. 43 (2008) 2348.
[27] K. Woan, G. Pyrgiotakis, W. Sigmund, Advanced Materials 21 (2009) 2233-2239.
[28] Y. Yu, J.C. Yu, J.-G. Yu, Y.-C. Kwok, Y.-K. Che, J.-C. Zhao, L. Ding, W.-K. Ge, P.-K. Wong, Applied Catalysis A: General 289 (2005) 186-196.
[29] Y. Yu, J.C. Yu, C.-Y. Chan, Y.-K. Che, J.-C. Zhao, L. Ding, W.-K. Ge, P.-K. Wong, Applied Catalysis B: Environmental 61 (2005) 1-11.
[30] W. Wang, P. Serp, P. Kalck, J.L. Faria, Journal of Molecular Catalysis A: Chemical 235 (2005) 194-199.
[31] G.e.a. Williams, ACS Nano 2 (2008) 1487-1491.
[32] D.C. Wang, D.; Li, J.;et al., ACS Nano 3 (2009) 907-914.
[33] C.C. Chen, W.; Long, M. et al., ACS Nano 4 (2010) 6425-6432.
[34] B. Czerw, D. Foley, et al., Phys. Rev. B 66 (2002) 033408.
[35] S. Heinze, J. Tersoff, R. Martel, V. Derycke, J. Appenzeller, P. Avouris, Physical Review Letters 89 (2002) 106801.

[36] H.I. K. Hashimoto, A. Fujishima, Jpn., J. Appl. Phys. Part 44 (2005) 8269-8273.
[37] T.Z. Zhang Y, Fu X, Xu YJ., ACS Nano 4 (2010) 7303-7314.
[38] Y.D. Kamegawa T, Yamashita H, JOURNAL OF PHYSICAL CHEMISTRY C 114 (2010) 15049-15053.
[39] L.X. Zhang H, Li YM, et al., ACS Nano 4 (2010) 380-386.
[40] X.Y.L.H.-P.C. Zhang, X-L; Linb, Y., Journal of Materials Chemistry 20 (2010) 2801-2806.
[41] J. Liu, Adv. Funct. Mater. 20 (2010) 4175-4181.
[42] Y.e.a. Liang, Nano Res. 3 (2010) 701-705.
[43] P.K. Ang, S. Wang, Q. Bao, J.T.L. Thong, K.P. Loh, ACS Nano 3 (2009) 3587-3594.
[44] Y.-B. Tang, ACS Nano 4 (2010) 3482-3488.
[45] Guang Zhu, Journal of Electroanalytical Chemistry 650 (2011) 248-251.
[46] Z.e. al., Chem. Commun. 46 (2010) 7148-7150.
[47] S.T.M. M. R. Hoffmann, W. Y. Choi, D. W. Bahnemann,, Chem. Rev. 95 (1995) 69-74.
[48] P.S. W. D. Wang, P. Kalck, J. L. Faria,, J. Mol. Catal. A Chem. 235 (2005) 194-200.
[49] S.H.L. G. Pyrgiotakis, W. M. Sigmund, presented at MRS Spring Meeting, San Francisco, CA (2005).
[50] C.H. Lettmann, K. et al., Appl. Catal. B 32 (2001) 215.
[51] B.M. Tryba, A. W. et al., Appl. Catal. B 41 (2003) 427.
[52] J.G. Sun, L., Carbon 41 (2003) 1063.
[53] H.S. Lasa, B.; Salaices, M., Photocatalytic Reaction Engineering Springer, New York (2005).
[54] M.R. Durr, S.; Yasuda, A.; Nelles, G., , J. Phys. Chem. B 110 (2006) 26507-26507.
[55] S.S. Sivakumar, C. P.; Mukundan, P.; Pillai, P. K.; Warrier, K. G. K., . Materials Letters 58 (2004) 2664-2669.
[56] U.B. Aust, S.; Dietze, M.; Rost, A.; Tomandl, G., , Journal of Membrane Science 281 (2006) 463-471.
[57] C.B. Adan, A.; Fernandez-Garcia, M.; Martinez-Arias, A., 2007, 72, (1-2), 11-17., Applied Catalysis B, Environmental 72 (2007) 11-17.
[58] J.P. Choi, H.;and Hoffmann, R., J. Phys. Chem. C 114 (2010) 783-792.
[59] A. Kumbhar, G. Chumanov, Journal of Nanoparticle Research 7 (2005) 489 - 498.
[60] C. Chen, X. Li, W. Ma, J. Zhao, H. Hidaka, N. Serpone, J. Phys. Chem. B 106 (2002) 318-324.
[61] C. Adan, A. Bahamonde, M. Fernandez-Garcia, A. Martinez-Arias, Applied Catalysis B, Environmental 72 (2007) 11-17.
[62] X. Chen, S.S. Mao, Chem. Rev. 107 (2007) 2891-2959.
[63] Y. Cong, J. Zhang, F. Chen, M. Anpo, D. He, J. Phys. Chem. C 111 (2007) 10618-10623.
[64] F. Gracia, J.P. Holgado, A. Caballero, A.R. Gonzalez-Elipe, J. Phys. Chem. B 108 (2004) 17466-17476.
[65] W.Q. Han, W. Wen, D. Yi, Z. Liu, M.M. Maye, L. Lewis, J. Hanson, O. Gang, J. Phys. Chem. C (2007).

[66] M. Kitano, M. Matsuoka, M. Ueshima, M. Anpo, Applied Catalysis A: General 325 (2007) 1–14.
[67] D.-G. Huang, S.-J. Liao, J.-M. Liu, Z. Danga, L. Petrik, Journal of Photochemistry and Photobiology A: Chemistry 184 (2006) 282-288.
[68] Q. Li, R. Xie, Y.W. Li, E.A. Mintz, J.K. Shang, Environ. Sci. Technol. (2007).
[69] D.-G. Huanga, S.-J. Liao, J.-M. Liu, Z. Danga, L. Petrik, Journal of Photochemistry and Photobiology A: Chemistry 184 (2006) 282-288.
[70] C.H. Rhee, J.S. Lee, J. Mater. Res 20 (2005) 3011-3020.
[71] Q. Zhang, L. Gao, Journal of the European Ceramic Society 26 (2006) 1535-1545.
[72] S. Yin, M. Komatsu, Q. Zhang, F. Saito, T. Sato, J Mater Sci 42 (2007) 2399–2404.
[73] J.M. Wu, B. Qi, J. Phys. Chem. C 111 (2007) 666-673.
[74] R. Asahi, T. Morikawa, T. Ohwaki, K. Aoki, Y. Taga, Science 293 (2001) 269.
[75] J.A.C. Navio, G.; Macias, M.; Real, C.; Litter, M. I., , Applied Catalysis A: General 177 (1999) 111-120.
[76] C.-y.B.t. Wang, C.; Bahnemannc, D. W.; Dohrmanna, J. r. K., , J. Mater. Chem. 13 (2003) 2322-2329.
[77] M.R. Durr, S.; Yasuda, A.; Nelles, G., , J. Phys. Chem. B 110 (2006) 26507.
[78] M.D.T.-T. HernA¡ndez-Alonso, I.; Coronado, J. M.; Soria, J.; Anderson, M. A., ,Thin Solid Films 502 (2006) 125-131.
[79] X.C. Fu, L. A.; Yang, Q.; Anderson, M. A., , Environ. Sci. Technol. 30 (1996) 647-653.
[80] B.W. Neppolian, Q.; Yamashita, H.; Choi, H., , Applied Catalysis A: General 333 (2007) 264-271.
[81] Y.I.Y. Gnatyuk, V. I.; Smirnova, N. P.; Granchak, V. M.; Eremenko, A. M., . Theoretical and Experimental Chemistry 41 (2005) 371-376.
[82] R.A.a.C. Lucky, P. A., Adv. Mater. 20 (2008) 1755–1759.
[83] R.A.l.M.-G. Lucky, Y. and Charpentier, P. A., Langmuir 26 (2010) 19014–19021.
[84] R.A.S. Lucky, R.;Lo, J. M. H and Charpentier P. A., Crystal Growth & Design 10 (2010) 1598-1604.
[85] C.M. Rayner, Organic Process Research & Development 11 (2007) 121-132.
[86] J.H.T. Clark, S. J.,, Org. Process Res. Dev. 11 (2007) 149-155.
[87] S. Stankovich, D.A. Dikin, R.D. Piner, K.A. Kohlhaas, A. Kleinhammes, Y. Jia, Y. Wu, S.T. Nguyen, R.S. Ruoff, Carbon 45 (2007) 1558-1565.
[88] H.M.S. Woods, M. M. C. G.; Nouvel, C.; Shakesheff, K. M.; Howdle, S. M.,, J Mater Chem. 14 (2004) 1663-1678.
[89] A.W. O'Neil, J. J., , Chem. Mater. 19 (2007) 5460-5466.
[90] P.A.D. Charpentier, J. M.; Roberts, G. W., , ACS Symposium Series 819 (2002).
[91] I.A. Smirnova, W., , Journal of Sol-Gel Science and Technology 28 (2003) 175-184.
[92] J.A.P. Darr, M., , Chem Rev 99 (1999) 495-541.
[93] C.J.S. Brinker, G. W., , The physics and Chemistry of Sol-Gel Processing Academic press, New York (1990).
[94] Y.V.K. Kolen'ko, K. A.; Gavrilov, A. I.; Garshev, A. V.; Meskin, P. E.; Churagulov, B. R.; Bouchard, M.; Colbeau-Justin, C.; Lebedev, O. I.; VanTendeloo, G.; Yoshimura, M., , J. Phys. Chem. B 109 (2005) 20303-20309.

[95] T. Nguyen, A.R. Hind, Varian Australia Rty Ltd, The measurment of absorption edge and band gap properties of novel nanocomposite materials.

[96] J. Dharma, A. Pisal; PerkinElmer, Inc. Application note, UV/Vis/NIR spectrometer, Simple method of measuring the band gap energy value of TiO_2 in the powder form.

Chapter 3

Growing TiO_2 Nanowires on the Surface of Graphene Sheets in Supercritical CO_2: Characterization and Photoefficiency

Abstract:

Tremendous interest exists towards synthesizing nanoassemblies for dye-sensitized solar cells (DSSCs) using earth abundant and friendly materials with green synthetic approaches. In this work, high surface area TiO_2 nanowire arrays were grown on the surface of functionalized graphene sheets (FGSs) containing –COOH functionalities acting as a template by using a sol-gel method in the green solvent, supercritical carbon dioxide ($scCO_2$). The effect of $scCO_2$ pressure (1500, 3000 and 5000 psi), temperature (40, 60 and 80°C), acetic acid/titanium isopropoxide monomer ratios (HAc/TIP= 2, 4 and 6), functionalized graphene sheets (FGSs)/TIP weight ratios (1:20, 1:40 and 1:60 w/w) and solvents (EtOH, hexane) were investigated. Increasing the HAc/TIP weight ratio from 4 to 6 in $scCO_2$ resulted in increasing the TiO_2 nanowire diameter from 10 to 40 nm. Raman and high resolution XPS showed the interaction of TiO_2 with the -COOH groups on the surface of the graphene sheets, indicating that graphene acted as a template for polycondensation growth. UV-Vis diffuse reflectance and photoluminescence spectroscopy showed a reduction in titania's band gap and also a significant reduction in electron-hole recombination compared to bare TiO_2 nanowires. Photocurrent measurements showed that the TiO_2 nanowire/graphene composites prepared in $scCO_2$ gave a 5X enhancement in photoefficiency compared to bare TiO_2 nanowires.

3.1. Introduction.

Titania, i.e. TiO_2 is one of the most promising candidate materials for fabrication of photoelectrodes for photovoltaic (PV) devices such as dye-sensitized solar cells (DSSCs) [1-3]. Modification of nanostructures with better morphological, optical, electrical properties and higher surface areas is required for researchers to produce higher efficiency solar cells [2]. There are several bottlenecks limiting the efficiency of these current DSSC's, including TiO_2's large band gap [4], agglomeration of nanoparticles [5] and the electron-hole recombination rate of excited electrons before reaching the collecting electrode [6]. Researchers attempt to solve these problems by band gap engineering through doping [7], synthesis of TiO_2 nanowires [8] and nanotubes [9] and also using extended charge-carrier pathways in the nanoparticle networks (TiO_2 in hybrid materials) [10]. The characteristic of the metal oxide in the form of nanoparticles, large surface-to-volume ratio and a Debye length comparable to the smallest dimensions, enhances titania's application in these emerging applications [11-13].

One-dimensional TiO_2 nanostructures are potentially more effective than TiO_2 nanoparticles as their precisely oriented nature makes them excellent percolation pathways for vectorial charge transfer [14-16]. However, most investigations have shown for DSSCs that nanowires or oriented nanotubes give lower efficiencies than nanoparticles, attributed to their lower surface areas. In order to increase these surface areas while also acting as an extended charge carrier, several recent studies on DSSCs have reported on using carbonaceous materials such as CNTs or graphene [17-19]. These materials have enhanced the photocatalytic properties of TiO_2 [19-21] while also improving the conductivity pathways of photogenerated carriers to the collecting electrode [22]. However, recently we showed that when using quantum dots attached to TiO_2 nanowires, that direct attachment without a linker provides higher photoefficiencies [23] .Hence, direct attachment of nanowires to graphene may enhance photoefficienes.

Fabrication of these nanostructured assemblies normally requires solution approaches, which are solvent dependent. However, ideally "green" synthetic approaches should be examined towards the new field of sustainable nanotechnology, where green solvents and one-pot synthesis approaches are preferable to conventional organic solvents containing many reaction steps. Supercritical carbon dioxide ($scCO_2$) has several advantages as the

green solvent for synthesizing advanced materials, as it is inexpensive, environmentally benign and nonflammable, with mild critical conditions (P_c = 73.8 bar; T_c = 31.1 °C) making it suitable for both laboratory and commercial scale applications [24]. Moreover, low viscosity, "zero" surface tension and high diffusivity of $scCO_2$ are highly favorable properties to synthesize superior high surface area ultrafine and uniform nanomaterials such as TiO_2 [25]. $ScCO_2$ has recently been shown to also enhance the exfoliation of graphene sheets, hence providing tremendous potential for producing new materials for DSSC's [26]. $ScCO_2$ can be easily and completely removed from the nanoassemblies simply by venting; hence, no additional drying process is required and the porous nanostructure can be maintained without collapsing the nanostructure [27]. In this report, we present a simple method for synthesizing high surface area TiO_2 nanowires directly on the surface of functionalized graphene sheets. A sol-gel method in $scCO_2$ is used for growing the nanowires on the graphene surface through formed carboxylate functionalities, while additionally providing better separation of the graphene sheets. The effect of temperature, pressure, HAc/TIP and FGSs/TIP ratio are reported and compared to those synthesized using ethanol and hexane as solvents. The efficient anchoring of TiO_2 onto FGSs surface was evidenced by AFM, TEM, Raman, XRD and XPS analysis. An increase in the I-V characteristics of the nanocomposites compared to bare TiO_2 nanowires further proves good attachment of TiO_2 to the graphene sheets and the feasibility of this approach for preparing DSSC's.

3.2. Experimental.

3.2.1. Materials.

Graphite flakes nominally sized at 7-10 microns were provided from Alfa Aesar, USA., fuming nitric acid (>90%), sulphuric acid (95-98%), potassium chlorate (98%), hydrochloric acid (37%), titanium isopropoxide (99.999%), ethanol anhydrous (>99.5%), hexane anhydrous (95%), glacial acetic acid (>99.7%), DMF (anhydrous, 99.8%), lithium iodide (99.9%), iodine (99.8%), acetonitrile (anhydrous, 99.8%) and Orange G dye ($C_{16}H_{10}N_2Na_2O_7S_2$) were purchased from Sigma-Aldrich Canada and used as received. 1,2-dimethyl-3-propylimidazolium iodide (DMPII) (98%) and 4-tert-butylpyridine (98%) were purchased from TCI America and used as received.

3.2.2. Synthesis.

3.2.2.1.Preparation of FGSs. Graphite oxide was prepared using the Staudenmaier method [28]. Graphite (5 g) was reacted with concentrated nitric (45 mL) and sulfuric acid (90 mL) with potassium chlorate (55 g). The potassium chlorate was added slowly over 15 min to avoid any sudden increase in temperature with the resulting mixture stirred at room temperature for 3 days. After completing the oxidation reaction, the mixture was added to excess water, washed with a 5% solution of HCl, and then repeatedly washed with water until the pH of the filtrate was neutral. The prepared graphite oxide was kept at 100º C in a vacuum oven until use to evaporate all the water. A quartz tube sealed at one end, the other side was closed with an inlet and outlet for continuously passing Nitrogen gas to provide an oxygen free environment. Then, the graphite oxide powder was placed in a quartz boat and inserted into a tubular furnace preheated to 1050 $^{\circ}$C and kept at this temperature for 30s. The graphite oxide was reduced and expanded to form functionalized graphene sheets[28].

3.2.2.2. Preparation of TiO_2/ FGSs composites via Sol- gel Chemistry. In a typical experiment, the FGSs were placed in a 10 ml high pressure view cell followed by quick addition of TIP alkoxide monomer, acetic acid and CO_2 to the desired pressure and temperature. A magnetic stirrer was used for mixing the reaction mixture in an experimental apparatus previously described by Sui et al. for producing TiO_2 nanofibers in $scCO_2$ [29]. It was found that the mixture of FGSs/TIP (three different concentrations; 1:20, 1:40 and 1:60 w/w) and acetic acid was miscible with CO_2 at the studied temperature range from 40 to 80 °C and pressure range from 1500 to 5000 psig. The stirrer was stopped after 24 h. Normally, several days of aging was required for complete reaction. After aging, the formed gel was washed continuously using 80 ml of CO_2 at a rate of approximately 0.5 mL/min, followed by controlled venting at 0.5 mL/min to prevent collapse of the solid network. For experiments using EtOH or hexane, the FGSs were dispersed in 100 ml pure solvent and stirred for 15 mins at 35 °C. Then TIP and acetic acid were added to the solution and mixed for 24 h. Aging was continued for 3 days with the resulting gel washed several times with solvent, which was subsequently removed by a rotary evaporator. For all samples the resulting powder was then calcined in

air (tubular furnace) using a heating rate of 10 °C/min to each examined calcination temperature for 2 h. The calcined powder was kept in a vacuum oven at 80° C.

3.2.3. Characterization. Atomic force microscopy (AFM, Veeco Multimode V) was used in tapping mode to characterize the morphology of the graphene sheets and TiO_2/FGSs composites. The samples for AFM study were prepared by adhering them in powder form on a metallic plate. 3D reconstructions were obtained from the AFM data by using Gwyddion software (Veeco). The morphologies of the samples were examined using Scanning Electron Microscopy (SEM) (Model LEO 1530) and Transmission Electron Microscopy (TEM) (Model JEOL 2010F). Samples for SEM imaging were prepared by applying the powder directly to carbon adhesive tape. For TEM analysis, the powdered samples were dispersed in methanol by sonication and then placed on a copper grid covered with holey carbon film and dried by evaporation. Structural analysis of the samples was performed using an X-ray powder diffractometer [Rigaku Miniflex XRD, Texas, U.S.A.], fitted with a rotating sample holder, a scintillation counter detector and a divergent beam utilizing a Cu Kα source of X-rays (λ= 1.5418 °*A*). FT-IR spectra were collected on samples as KBr pellets using a Bruker Tensor 27 spectrometer, with a resolution of 4 cm^{-1}. Raman analysis was performed using a Kaiser optical system (RXN1-785) with 5 times exposure and 20 times accumulation. The XPS analysis was carried out with a Kratos Axis Ultra spectrometer using a monochromatic AlK (alpha) source (15mA, 14kV). Photoluminescence spectra were carried out with PTI Quantamaster 50 spectrophotometer with a Xenon lamp (75 V). UV spectra were performed by (Shimadzu 3600) deuterium arc lamp and two different detectors (PMT, and PbS). An integrating sphere was utilized in order to measure diffuse reflectance of these materials.

3.2.4. Photocurrent measurements. Indium Tin Oxide (ITO) coated glass slides with a resistivity of 8-12 Ω/sq were purchased from Sigma-Aldrich Canada and thoroughly washed with a detergent solution, then with acetone under sonication and dried. TiO_2 and the synthesized TiO_2/FGSs nanocomposites were used as the photoactive layer in the dye sensitized solar cells (DSSCs). Deposition of the active layer on the conductive glass plate was achieved by the doctor blade technique: i.e. a solution of commercial TiO_2 or

TiO_2/FGS nanocomposites in DMF were sonicated for 30 mins and then spread on soda lime glass with an active cell area of 0.5 x 0.5 cm^2. The layer was dried at room temperature for several minutes, followed by calcining at 400°C for 20 min to improve crystallinity of TiO_2 or the TiO_2/FGS nanocomposites. The dye was then deposited on the active layer. A solution of DMPII (0.6M), lithium iodide (0.1M), iodine (0.05M) and 4-tert-butylpyridine (0.5M) in acetonitrile was used as the electrolyte [30]. The counter electrode was fabricated by sputtering gold with thickness of 40 nm. The photovoltaic device was tested under AM 1.5G simulated sunlight produced by xenon lamp solar simulator (Newport) with an intensity of 100 mW/cm^2 (equivalent to 1 SUN) and the PV response was measured using a Keithley 2400 General Purpose Sourcemeter.

3.3. Results and Discussion.

3.3.1 Effects of Synthesis Conditions on Nanostructure and Porosity.

Table 3.1. summarizes the experimental conditions used for this study, presenting the morphology of the titania/functionalized graphene sheets (TiO_2/FGSs) synthesized under various concentrations of titanium alkoxide monomer (TIP), acetic acid (HAc-used as the polycondensate agent), temperature, and pressure in supercritical carbon dioxide ($scCO_2$). The surface area (S_{BET}), adsorption average pore diameter (D_{pore}) and pore volume per gram (V_{pore}) were measured by BET and are also presented.

In Figure 3.1.a, an SEM image of the FGSs powder is shown in which the high porosity of the graphene sheets is clearly observable. A transmission electron microscopy (TEM) image of the FGSs is shown in Figure 3.1b; here a thin paper-like structure is observed with wrinkles on the edges. Most of the sheets are very thin; however some of them stack together due to van der Waals interactions [31]. The first set of experiments (Samples 1-6 in Table 3.1) examined the effect of synthesis temperature (40, 60, and 80°C) while growing TIP alkoxide on the graphene surface at a constant $scCO_2$ pressure of 5000 psig, with the weight ratio of FGSs/ TIP = 1/20 and the HAc/TIP weight ratio = 4. In this temperature range, curled nanowires with a diameter of 10 to 20 nm and length of 1 to 2 microns were obtained. As shown by the SEM in Figure 3.1c for the sample synthesized at 60°C, TiO_2 nanowires can be observed with a diameter between 10 to 20 nm and a length in the micron range. No obvious effect on the morphology of the nanowires was

observed with increased temperature, although the surface area decreased from 376 m^2/g at 40°C to 285 m^2/g at 80°C. The pore diameters increased with temperature from 48 A° at 40°C to 65 A° at 80°C with a corresponding increase of the pore volume of the resulting composites from 0.42 cm^3/g at 40°C to 0.46 cm^3/g at 80°C.

The reaction pressure's effect on the morphology of the composites was studied by varying the pressure from 1500 to 5000 psig, while keeping the temperature at 60 °C, the weight ratio of FGSs/TIP at 1/40 (w/w) and the HAc/TIP weight ratio at 4. Increasing pressure was observed to have little effect on the nanoassembly morphology, although the surface area significantly increased with increasing pressure, i.e. from 369 m^2/g at 1500 psig to 468 m^2/g at 5000 psig (Table 3.1). (Figure 3.2) The pore diameters increased with pressure from 44 A° at 1500 psig to 61 A° at 5000 psig with a corresponding increase of the pore volume of the resulting composites from 0.4 cm^3/g at 1500 psig to 0.71 cm^3/g at 5000 psig.

Table 3.1. Physiochemical properties of TiO_2/ FGSs nanostructures synthesized under various conditions.

	Experimental Parameters				T_{cal}	S_{BET}	average D_{pore}	V_{pore}	Nanostructure
Sample No.	FGSs/ TIP	HAc/ TIP	Temp. (°C)	Pres. (psi)	(°C)	(m^2/g)	(A°)	(cm^3/g)	
1	1:20	4	40	5000	AP	376	48.2	0.42	TiO_2nanowires on the surface of FGSs with diameter of 10 to 20 nm and length in micron range
2					400	186	88.2	0.35	
3			60	5000	AP	371	59.8	0.44	
4					400	176	98.1	0.37	
5			80	5000	AP	285	65.1	0.46	
6					400	176	97.3	0.43	
7	1:40	4	60	5000	AP	468	60.6	0.71	TiO_2 nanowires with the diameter of 10- 20 nm and length in micron range
8					400	191	95.2	0.46	
9				3000	AP	448	56.5	0.63	
10					400	174	96.6	0.49	
11				1500	AP	369	43.7	0.40	
12					400	166	86.2	0.31	
13	1:20	4	35	Ethanol	400	103	87.5	0.14	TiO_2nanoparticles less than 10 nm on the surface of FGSs
14	1:20	6	60	5000	AP	366	42.7	0.39	TiO_2 nanowires on the surface of FGSs with diameter of 40-50nm
15					400	165	55.7	0.37	
16					500	102	88.9	0.23	Some beads observed on the surface of TiO_2
17					600	58	99.9	0.15	

AP=As-prepared

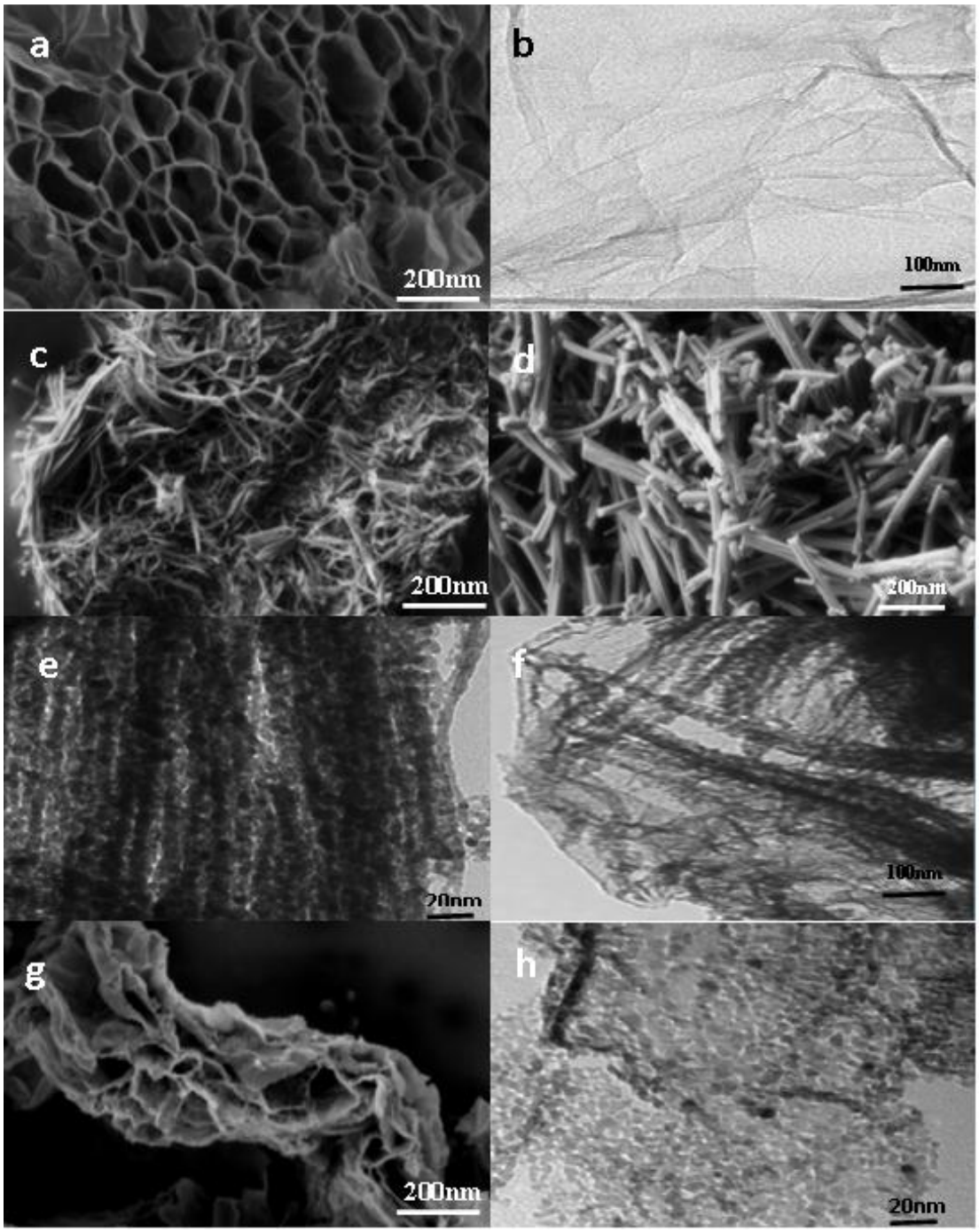

Figure 3.1. Effect of synthesis conditions on morphology of TiO_2/FGSs nanocomposites: a) SEM image of FGSs; b) TEM image of FGSs TiO_2/FGSscomposites prepared in $scCO_2$, FGSs/ TIP (1:20 w/w), 5000 psi, 60° C, c), SEM image of Sample 4 ;d) SEM image of sample 15 e) TEM images of sample 2 ; f) TEM images of sample 4; sample 13 g) SEM; h) TEM . All TiO_2 samples were calcined at 400°C for 2 hours.

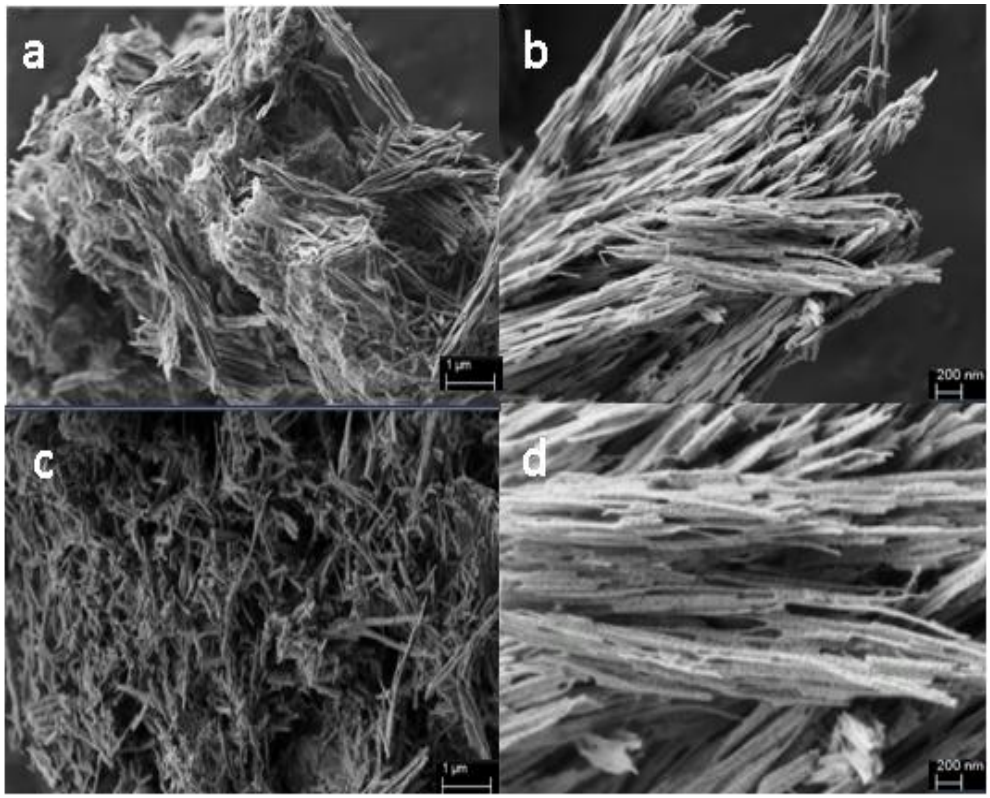

Figure 3.2. SEM images of TiO_2/ FGSs composites prepared in $scCO_2$:(FGSs/TIP (w/w): 1:40; HAc/TIP (w/w): 4, Temp 40°C; (a) and (b) Sample 12 (pressure 1500 psi); (c) and (d) Sample 8 (pressure 5000 psi).

Three different weight ratios of FGSs/TIP were examined by increasing the Ti alkoxide monomer ratio (at pressure 5000 psi, temperature 60° C, and HAc/TIP = 4). FGSs/TIP ratio 1/20 and 1/40 showed almost the same results with nanowires 10-20 nm in diameter grown on the surface of the graphene sheets. The surface area increased from 366 m^2/g at 1/20 weight ratio of FGSs/TIP (Sample 14) to 468 m^2/g at 1/40 (w/w) (Sample 7). A further increasing of the weight ratio of FGSs/TIP from 1/20 to 1/60 (w/w) resulted in TiO_2 nanoparticles becoming separated from the graphene sheets. The HAc/TIP weight ratio was found to have a significant effect on tuning the morphology of the resulting composites. Keeping the FGSs/TIP weight ratio at 1/20, and varying the HAc/TIP weight ratio from 2 to 6 resulted in TiO_2 nanowires with different morphologies on the surface of the graphene. At HAc/TIP equal 2, the materials in the view cell were not miscible, and TiO_2 nanoparticles were formed separately from the FGSs (Figure 3.3). When the amount

of HAc/TIP varied from 4 to 6, curled 10-20 nm fibers with S_{BET} 176 m^2/g (Figure 3.1c, sample 4) and straight 40-50 nm fibers with S_{BET} 165 m^2/g (Figure 3.1d, sample 15) were obtained. In Figure 3.1e (sample 2) and 3.1f (sample 4), the TEM image of the TiO_2/FGSs when $scCO_2$ was used as a solvent shows semi-aligned TiO_2 nanowires formed on the graphene surface with diameters between 10-15 nm and their lengths in the micron range. 3D AFM images of the nanoassemblies (sample 15) show a smooth graphene sheet surface (Figure 3.5a); the mean thickness of the sheets being 5 nm (Figure 3.5b), which is in agreement with previous studies [32]. FGSs covered with TiO_2 nanowires shows a surface in accord with SEM pictures (Figure 3.2c), where semi-aligned TiO_2 nanowires are apparent on the surface. The profile shown in Figure 3.2d is in good agreement with the morphology observed by the electron microscopy images (Figure 3.1d) in which the nanowires showed a diameter of 50 nm. These nanowires are directly attached to the graphene surface as also demonstrated by other physico-chemical measurements described in detail below.

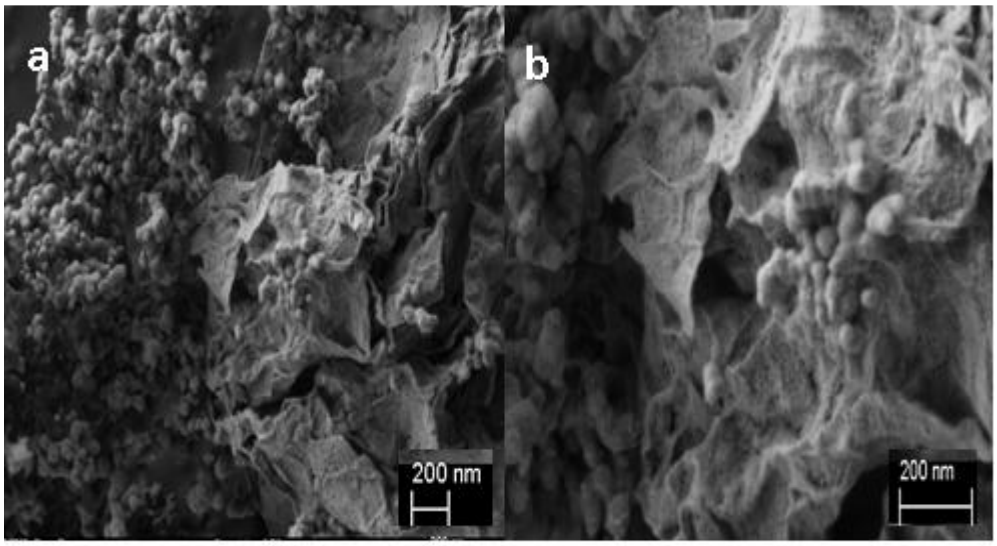

Figure 3.3. SEM images of TiO_2/ FGSs composites prepared a) in $scCO_2$, (5000 psi, 60° C, FGSs/TIP (w/w): 1/20, HAc/TIP (w/w): 2); b) in Hexane.

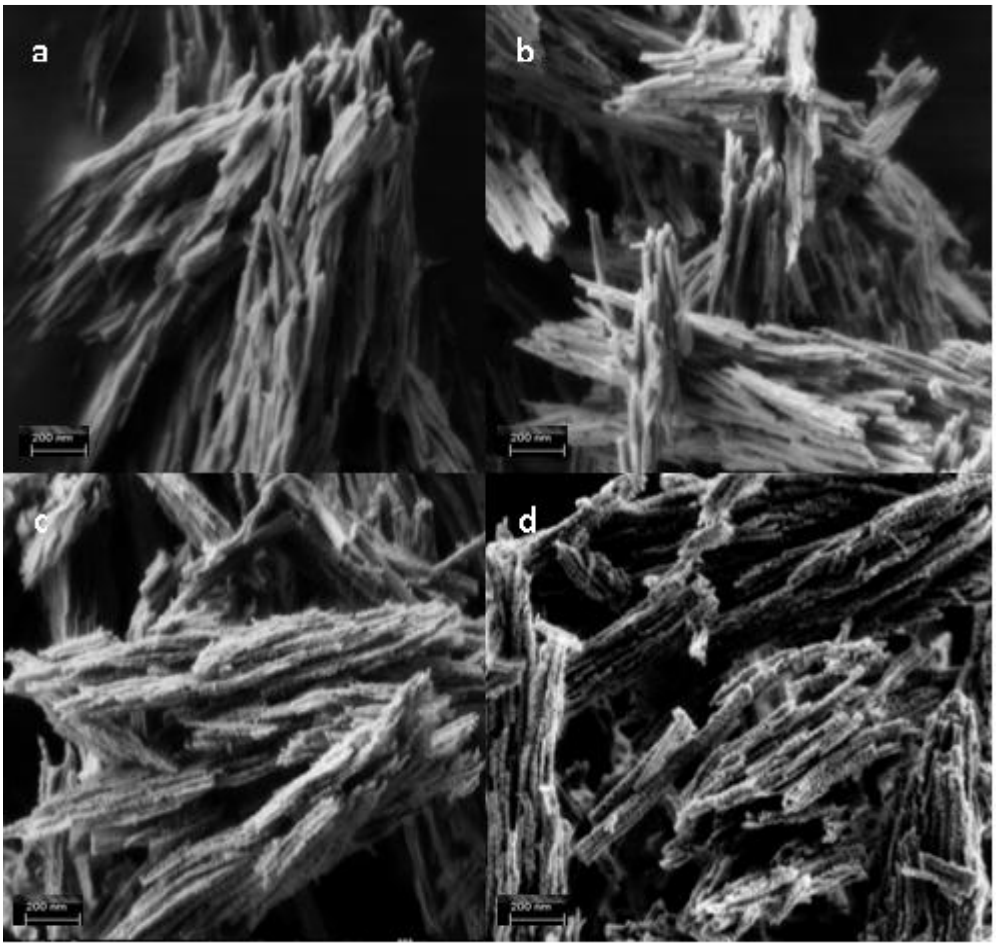

Figure 3.4. SEM images of TiO_2 nanowire on the graphene sheets in different calcination temperatures (FGSs/TIP): 1/20, 5000 psi, 40° C, HAc/TIP: 6, (a) before calcinations, calcined at (b) 400 (sample 15), (c) 500 (sample 16) and (d) 600° C (sample 17).

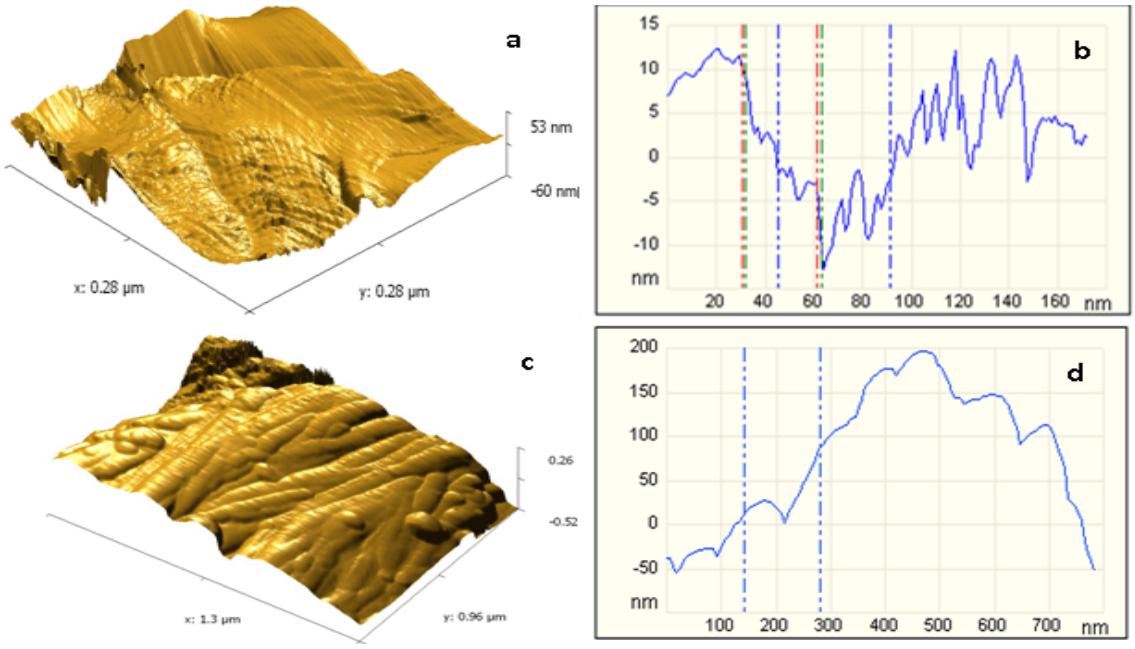

Figure 3.5. AFM images of FGSs (a) and TiO_2 /FGSs (sample 8) (c), obtained by using Gwyddion software; profile obtained with AFM in tapping mode for FGSs (b) and TiO_2/FGSs (d) respectively.

The SEM image of the TiO_2/FGSs sample prepared in ethanol is shown in Figure 3.1g (sample 13). The TiO_2 nanoparticles are well dispersed as a thin layer on the surface of the graphene sheets, with the sheets having noticeably poorer separation than those treated with $scCO_2$. Exfoliation of graphene sheets using $scCO_2$ has been previously shown by others [26]. Figure 3.1h shows the TEM image of TiO_2/ FGSs using EtOH as solvent in which TiO_2 nanoparticles are decorated on the surface of the Graphene sheets uniformly. There are some darker places presented in the images which are the decorated edge of the graphene sheets. When hexane was used as solvent, large size agglomerated TiO_2 was formed separated from the FGSs (Figure 3.3b).

Experiments 14-17 examined the effect of calcination temperature on the TiO_2/FGSs nanostructures from their as prepared (AP) state to 400, 500 and 600 °C. The surface area significantly decreased with increasing calcination temperature, i.e. from 366 m^2/g AP to 58 m^2/g at 600 °C (Table 3.1). The pore diameters increased from 43 A° AP psig to 100 A° at 600 °C with a corresponding increase of the pore volume of the resulting composites from 0.15 cm^3/g AP to 0.39 cm^3/g at 600 °C. Figure 3.6 compares the N_2 adsorption/desorption isotherms of these calcined samples as surface areas for the DSSC

applications of interest. After heat treatment in the temperature range from 400 to 600 °C, no obvious morphology change was observed by SEM, although the relatively smooth surface of the TiO_2 nanowires when calcined at low temperatures led to connected beads at 600 °C (Figure 3.4).

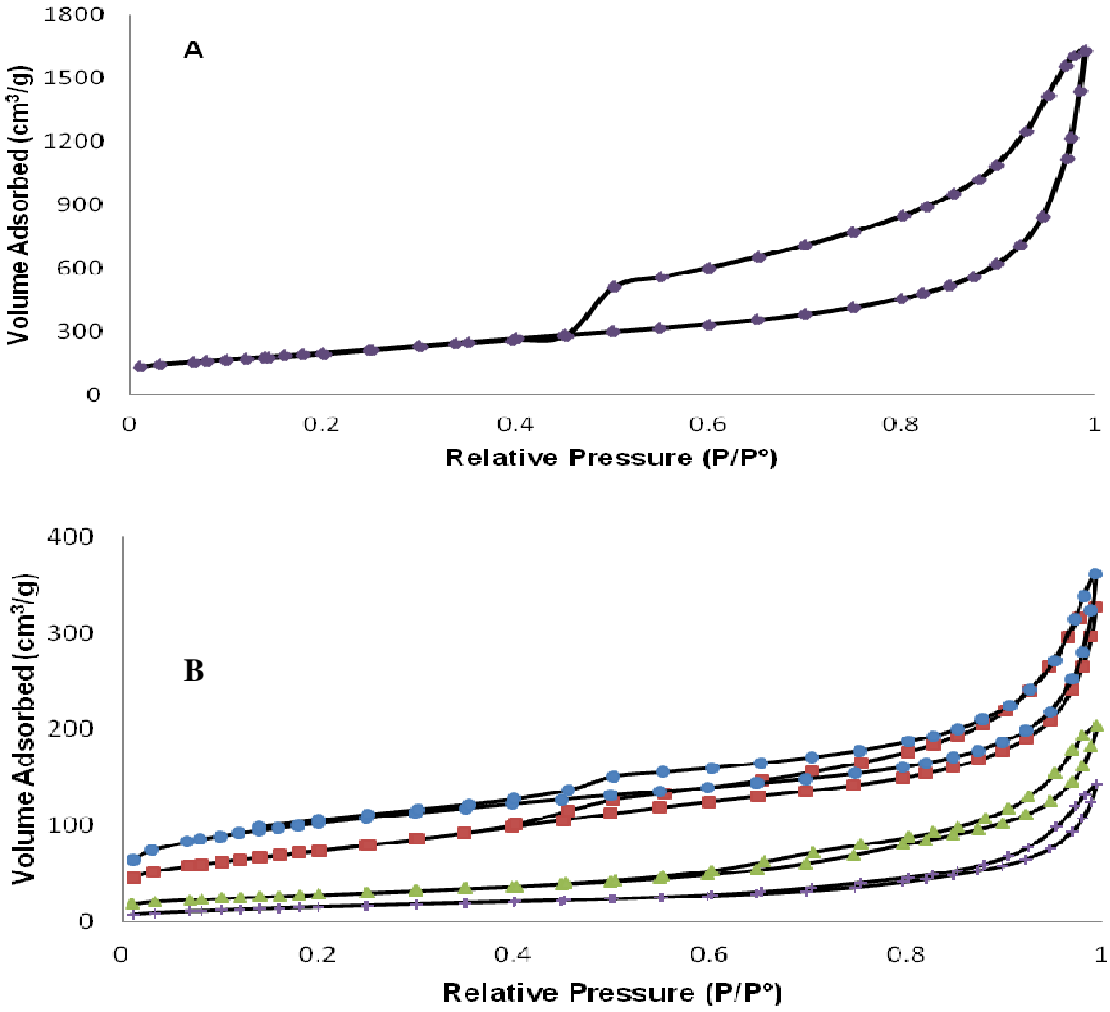

)$_2$ nanowire/ FGSs
) not calcined.

The FGSs synthesized in this work show no characteristic peak (Figure 3.7d), indicating that the graphene layers were disordered completely and any ordering was lost in the material [33]. The XRD pattern of the sample prepared with the FGSs/TIP weight ratio of 1:20, HAc/TIP weight ratio 6, calcined at 400 °C is displayed in Figure 3.7b. This figure demonstrates the highly crystalline nature of the TiO_2/graphene composites. The diffraction peaks in the range of 20< 2□ < 80 correspond to the 101, 004, 100, 200, 105, 211, 204, 116, 220 and 215 reflections of anatase crystal structure of TiO_2. By increasing the calcination temperature from 400° C to 500° C, the XRD pattern was not affected as shown in Figure 3.7c, although further increasing to 600 °C gave some rutile phase (Figure 3.7a). Hence, the XRD results show that TiO_2 nanowires formed on the surface of graphene sheets have excellent crystallinity characteristics suitable for investigation in DSSCs.

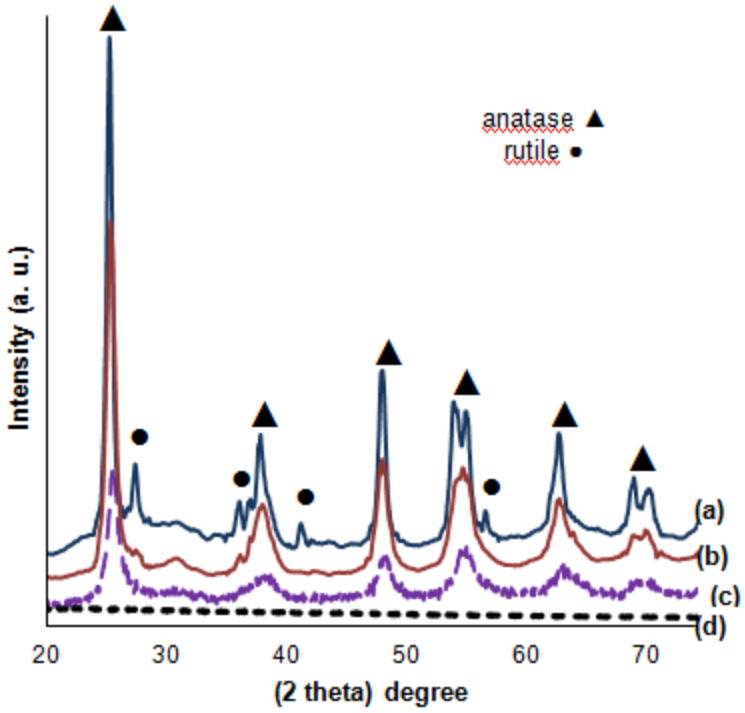

Figure 3.7. Powder XRD, Effect of calcinations temperature on FGSs/TiO_2; TiO_2/ FGSs composites calcined at (a) 600 °C ,(b) 500 °C, (c) 400 °C and (d) FGSs.

3.3.2. Nanoassembly Microstructure.

Raman spectroscopy is a valuable technique to identify the different forms of carbon in carbonaceous composites [34, 35] and crystal forms of TiO_2 [36]. Graphite has two active bands visible in the Raman spectra (Figure 3.8a), i.e. the strong in-phase vibration of the graphene lattice (G band) at 1575 cm^{-1} and the weak disorder band caused by the graphene edges (D band) at approximately 1355 cm^{-1}. After oxidation of graphite to Graphite oxide (Figure 3.8b) and then FGSs (Figure 3.8c), higher disorder leads to a broader G band, as well as to a broad D band of higher intensity increasing the D/G ratio [37]. After functionalization of FGSs with TiO_2, the D/G ratio increased indicating interaction of TiO_2 with functional groups on the graphene sheets. The D/G ratio is higher in the composite prepared in $scCO_2$ when the diameter of TiO_2 was between 10-20 nm (D/G~ 2.5) (Figure 3.9a) compared to the sample with a 50 nm TiO_2 diameter (D/G~ 2) (Figure 3.9b). The higher D/G ratio indicates enhanced attachment of the TiO_2 nanowires to the graphene surface. TiO_2/ FGSs composites prepared in ethanol show a lower D/G ratio(D/G~ 1.77) (Figure 3.9c) indicating that the TiO_2 nanowires prepared in $scCO_2$ have better attachment to the graphene sheets. In explanation, $scCO_2$ can potentially enhance the exfoliation of graphene, allowing better penetration of reactants to the graphene surface with better resulting coverage of nanowires. The main characteristic peak of anatase TiO_2 appears at 145 cm^{-1} in Figure 3.9 which is attributed to the main E_g anatase vibration mode [38]. Moreover, the presence of crystaline TiO_2 in the composites is confirmed by the vibration peaks at 400 cm^{-1} (B_{1g}), 519 cm^{-1} (A_{1g}) and 640 cm^{-1} (E_g) [36].

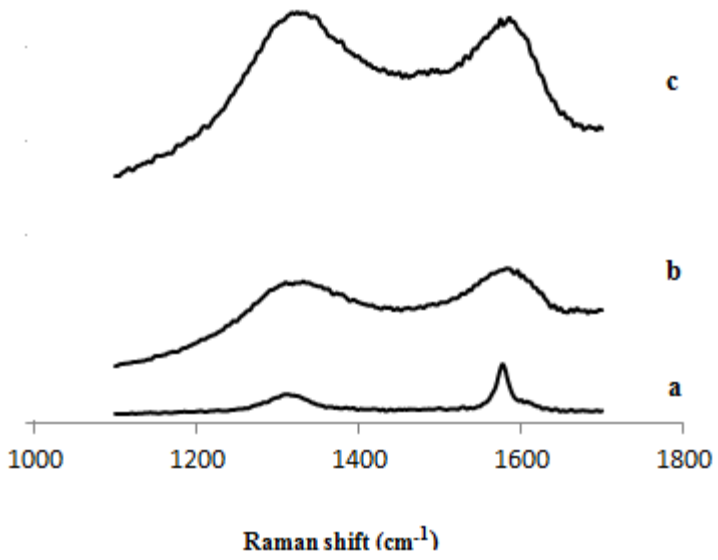

Figure 3.8. Raman spectra of graphite (a), graphite oxide (b), FGSs (c).

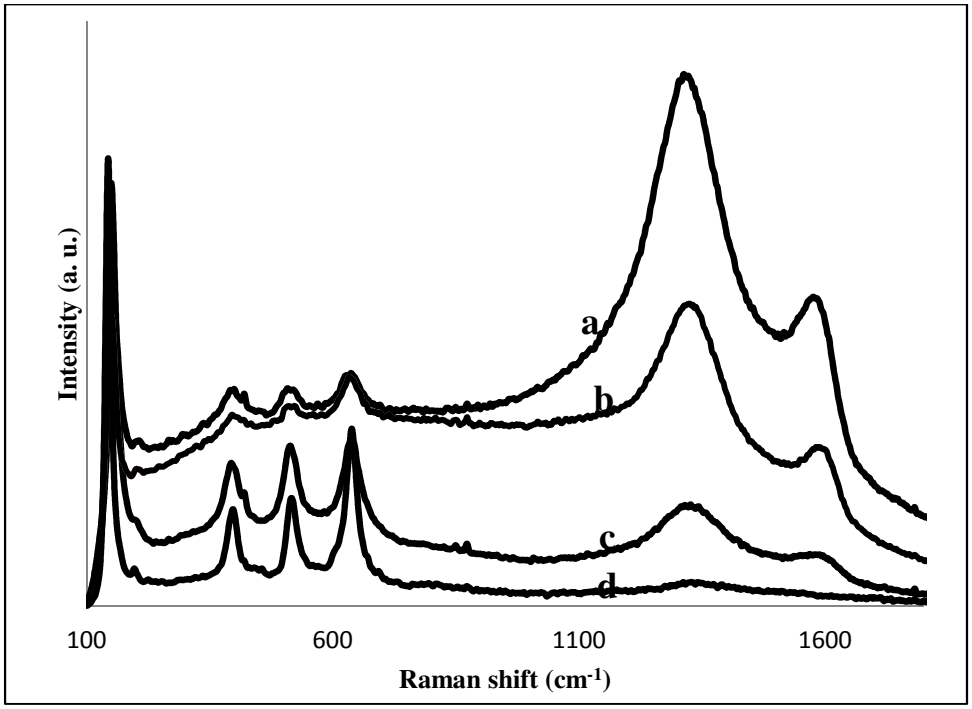

Figure 3.9. Raman spectra (comparison of D/G ratio) (a) sample 4 and (b) sample 15. (c) sample 13 and (d) TiO_2 (anatase).

In the XPS spectra of the FGSs, 90 % carbon and 10% oxygen were detected. In high resolution XPS record of C1s, four different peaks were observed at 284.7, 286.2, 287.7 and 289.25 eV which correspond to (C-C, C=C), (C-H), (C-OH, C-O-C) and C=O, respectively. (Figure 3.10b) Akhavan et al. studied the XPS spectra of graphite oxide and thermal expanded graphene sheets at different temperatures and reported similar results [39]. The XPS spectra of TiO_2 /FGSs prepared in $scCO_2$ (sample 4 of Table 3.1) showed 52.3% O1s, 22.2% Ti 2p and 25.2% C1s. In the high resolution XPS of the C1s peak (Figure 3.9d), the four different peaks of FGSs are still evident, although the peak intensities of C=O and C-OH decreased significantly. Also in the high resolution O1s (Figure 3.9c) the peak at 533.40 eV disappears corresponding to -OH while the peak at 531.38 eV corresponding to the carbonyl group is still evident. This indicates that all OH groups reacted with TiO_2, leaving no free -OH on the surface of the synthesized materials [39]. A new peak appeared at 529.96 eV which is assigned to the oxygen of TiO_2 [40].

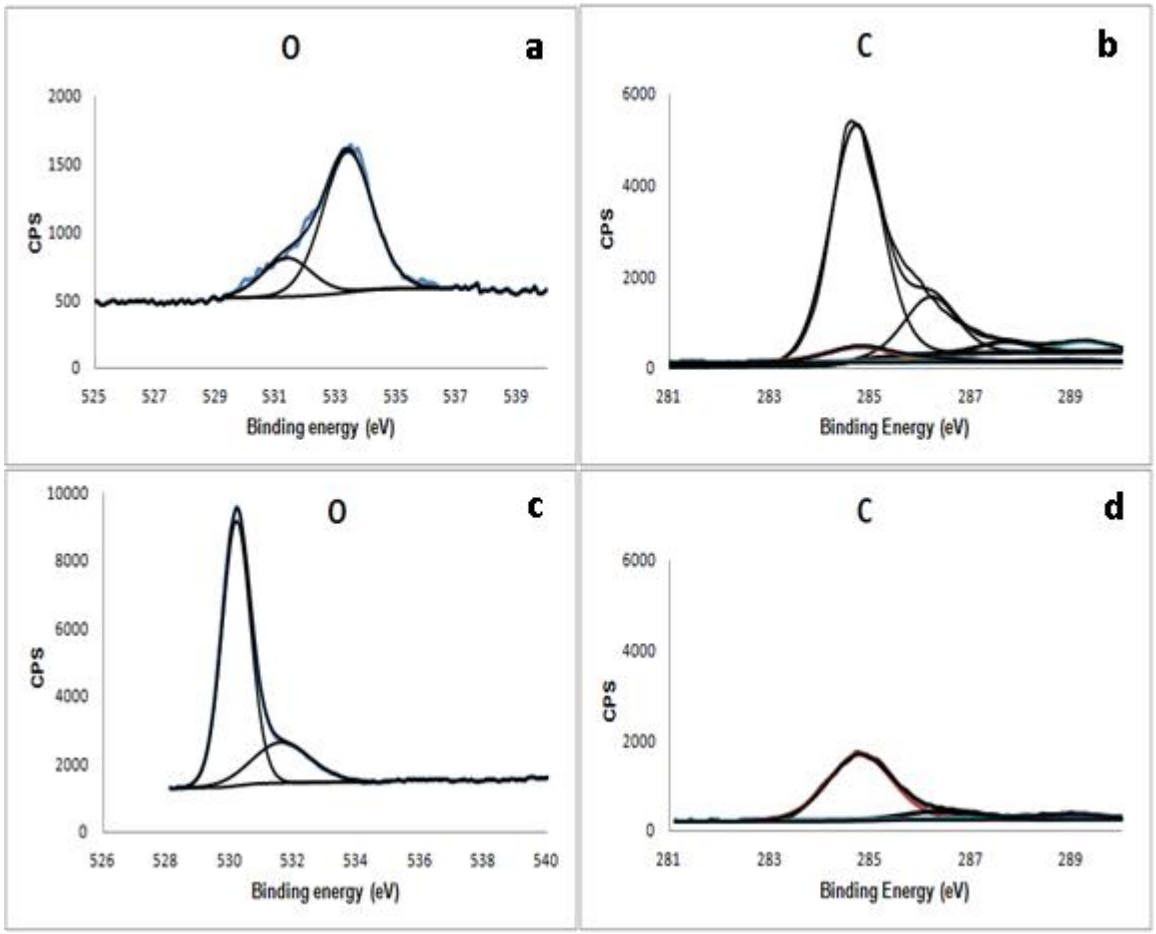

Figure 3.10. XPS spectra of FGSs, High resolution; (a) C (1s) and (b) O (1s); XPS spectra of TiO_2/ FGSs (S4); High resolution (c) C1s and (d) O1s.

The mechanism of TiO_2 nanowire formation using sol-gel chemistry in $scCO_2$ has been previously examined by our group [24, 41, 42]. Regarding the nanowire mechanism from graphene, TIP can similarly form coordination bonding to the –COOH group of graphene sheets, which acts a template for the formation of nanostructure growth, as illustrated schematically in Scheme 3.1. TiO_2 can be coordinated to carboxylate functionalities through different possible structures described by Gratzel et al [43]. Then, the complex can react through the polycondensation mechanism from both the graphene surface and with additionally provided acetic acid. Hydrolysis and oxidation are the next steps to stabilize TiO_2 nanowires on the graphene sheets as described through the following sequence of reaction steps.

$(Ti(OR)_4)_m$ + graphene $-(COOH)_n$ ⟶ graphene $-(COO^-)_n$ $(Ti\ (OR)_{4-x})_m$ + xROH

graphene $-(COO^-)_n$ $(Ti\ (OR)_{4-x})_m$ + yAcOH ⟶ graphene-$(COO^-)_n$ $(Ti\ (AcO)_y\ (OR)_{4-x-y})_m$ +yROH

AcOH+ (x+y) ROH ⟶ ROAc + H_2O

graphene-$(COO)_n$ $(Ti\ (AcO)_y\ (OR)_{4-x-y})_m$ —Hydrolysis, Oxidation→ graphene-$(COO)_n$ $(Ti- O- Ti)_m$

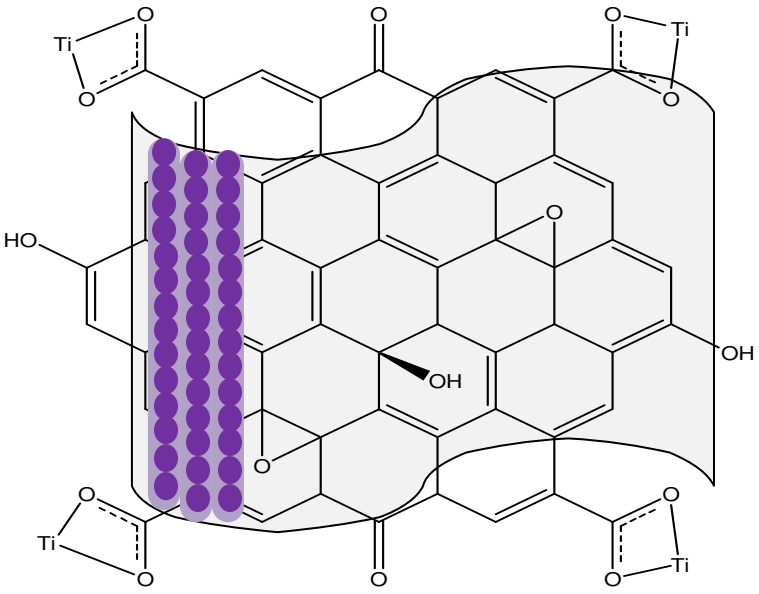

Scheme 3.1. Schematic of functionlaization of FGSs by TiO_2 (chelating bidentate mode).

Compared with spherical particles that are favored by reduced surface area, formation of 1-D oxide particulates is less common using sol-gel reactions. While the HAc/TIP weight ratio gave a significant effect on the morphology and size of the nanowires, the FGSs/TIP ratio, and the reaction temperature and pressure show a rather insignificant effect.

Similarly, in previous work using $scCO_2$ as solvent, TTIP and TTBO as Ti alkoxide precursors and HOAc as the polycondensation reagent gave randomly-oriented nanofibers or nanospheres of TiO_2 aerogels [24]. It was observed that a high acid ratio HOAc/TTIP (*R*) facilitated formation of the nanofibers (10-40 nm). Also, using aluminum isopropoxide reacting with acetic acid, Al_2O_3 nanofibers were synthesized in the forms of $[Al(OH)(CH_3CO_2)_2]_m$ (as-prepared) [44]. The mechanism of nanofiber formation was investigated by means of in situ ATR-FTIR[45], electrospray ionization mass spectrometry (ESI-MS)[46], single crystal X-ray diffraction[47], and powder FTIR and thermal analysis, e.g., DSC and TGA[45]. These works showed that hexanuclear titanium acetate complexes were formed which grew anisotropically leading to the formation of 1-D macromolecules (or sols), which eventually form nanofibers via a coacervate and tactoid pathway [45, 46].

3.3.3. Optical Properties.

Figure 3.11a compares the diffuse reflectance UV-Vis spectra of TiO_2 anatase and TiO_2/FGSs composites prepared in both ethanol and $scCO_2$. The TiO_2 nanoparticles show an absorption edge around 385 nm corresponding to the bandgap of anatase (~3.2 eV) (Figure 3.11a.a). With the incorporation of FGSs, the composites exhibit a strong absorbance in the entire visible light region. Carbon materials are known to provide enhanced absorption in the visible region which can extend TiO_2's band gap to higher wavelengths [48]. Compared to bare TiO_2, a red shift in the absorption spectra of TiO_2/ FGSs composites is noted for samples prepared in both ethanol and $scCO_2$. The red shift in the composites prepared in $scCO_2$ is greater than that prepared in ethanol attributed to a stronger bond formation between the carboxylate group and TiO_2 in $scCO_2$ (Band gap for composites prepared in ethanol ~ 3eV (Figure 3.11 a.b); $scCO_2$ ~2.9 eV (Figure 3.11 a.c,d)). By introducing graphene to the TiO_2, electrons of TiO_2 and graphene try to align their Fermi energy levels, slightly altering the TiO_2 band gap.

Photoluminecence (PL) spectroscopy is often used to study the surface structure and excited states of semiconductors following the efficiency of charge carrier trapping, migration, and transfer during irradiation to understand the fate of electron–hole pairs [49]. The PL spectra shown in Figure 3.11b compares the electron-hole recombination of

TiO_2/FGSs composites prepared in different conditions to anatase. TiO_2 anatase is characterized by a broad peak at around 540 nm (Figure 3.11b.a)[50]. The TiO_2 prepared on the graphene sheets shows a decrease in PL intensity. Introducing the graphene to TiO_2 improves its surface quality, reducing the density of trap states, resulting in an enhanced excitation lifetime. The reduction is greater in the nanocomposites prepared in $scCO_2$ (Figure 3.11.b.c) than that of composites prepared in ethanol (Figure 3.11 b.b). This result can be explained by better attachment between the TiO_2 nanowires with graphene sheets prepared in $scCO_2$ compared to those prepared in ethanol as shown earlier through TEM, Raman, and XRD results. Yao et al. prepared TiO_2/carbon nanotubes composites and reported a reduction in PL spectra as well [51].

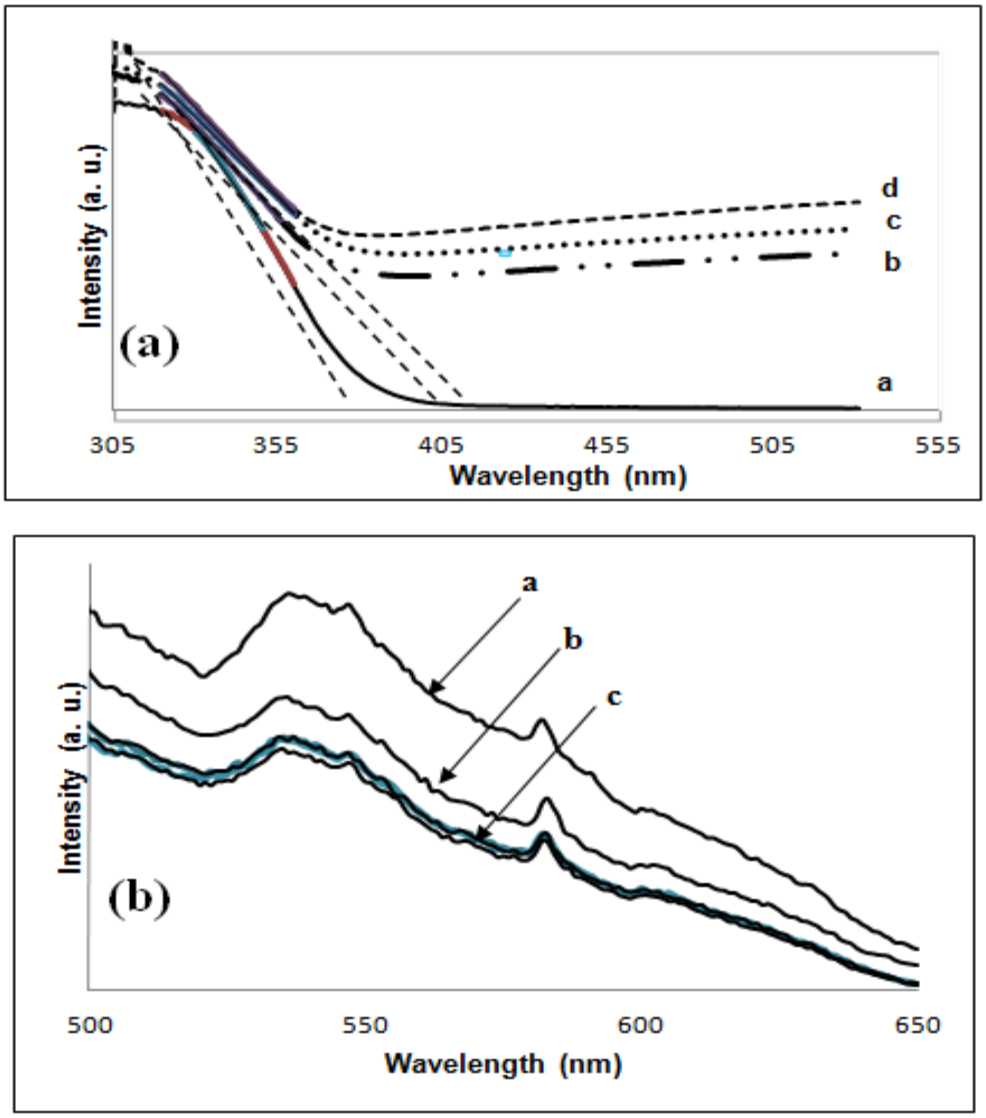

Figure 3.11. A) Diffuse reflectance UV-Vis spectra of (a) TiO_2 anatase, (b) TiO_2 /FGSs composites prepared in ethanol, (c) Prepared in $scCO_2$ (15 nm diameter) and (d) 45 nm diameter. B) Photoluminescence spectra of (a) TiO2, (b) TiO_2 /FGSs composites prepared prepared in ethanol (sample 13) and (c) in $scCO_2$ (15 and 45 nm diameters).

3.3.4. Photovoltaic Measurements. Table 3.2 summarizes the results of the photovoltaic performance of the prepared nanomaterials using fabricated DSSCs. Under simulated solar irradiation (AM 1.5), the optimum cell based on TiO_2/FGSs produced a short-circuit current density (J_{SC}) of 9.60 mA/cm^2, an open-circuit voltage (V_{OC}) of 618 mV, and a fill factor (FF) of 0.25, yielding a power conversion efficiency (η) of 1.48% for TiO_2-graphene nanofiber assemblies calcined at 400 °C (surface area 170 m^2/g). The corresponding values for the control cell fabricated by the same process without adding FGSs were J_{SC} = 2.83 mA/cm^2, V_{OC} = 543 mV, FF = 0.19, and η = 0.29%. This indicates a significant improvement, i.e. about a 5 fold increase in η. The higher η's for the TiO_2/FGSs cells are attributed to the higher experimental surface areas and decreased charge-transfer resistance in the composite film as a result of the FGSs. The higher surface areas and better surface coverage help create a continuous electron conducting network to the transparent electrode, facilitating the diffusion of photoinjected electrons, lowering the probability of recombination [21]. Narrower TiO_2 nanowires also showed higher photoefficiencies compared to the thicker ones, attributed to their better attachment to the graphene sheets which would help facilitate electron flow between TiO_2 and the graphene sheets. As well, the probability of electron-hole recombination is higher in defect sites containing thicker TiO_2 nanowires. Another factor to consider is that the higher surface areas and higher porosities of our novel nanoassemblies would allow more dye to be adsorbed, resulting in more visible light absorption, hence enhancing the efficiency.

A proposed mechanism for the charge transfer in TiO_2/FGSs composites is shown in scheme 3.2, in which TiO_2 (anatase) nanowires are in intimate contact with the FGSs. Under solar irradiation, electrons (e^-) are excited from the valence band (VB) to the conduction band (CB) of the TiO_2. Because of FGSs relative position (work function of FGSs is known to be around 4.2-4.5 eV) [52], electrons from the TiO_2 anatase conduction band transfer to its conduction band, allowing charge separation, stabilization, and hindering charge recombination.

Table 3.2. I-V Photovoltaic parameters of the solar cells fabricated by TiO_2 and TiO_2/FGSs composites under AM 1.5G irradiation.

Active layer	**TiO_2**	**S4**	**S15**	**S13**
V_{oc} (mV)	543	618	605	572
J_{sc} (mA/cm^2)	2.83	9.60	9.06	8.12
FF	0.19	0.25	0.23	0.24
η (%)	0.29	1.48	1.26	1.11
Increase of power conversion efficiency	-	5.1-fold	4.35-fold	3.82-fold

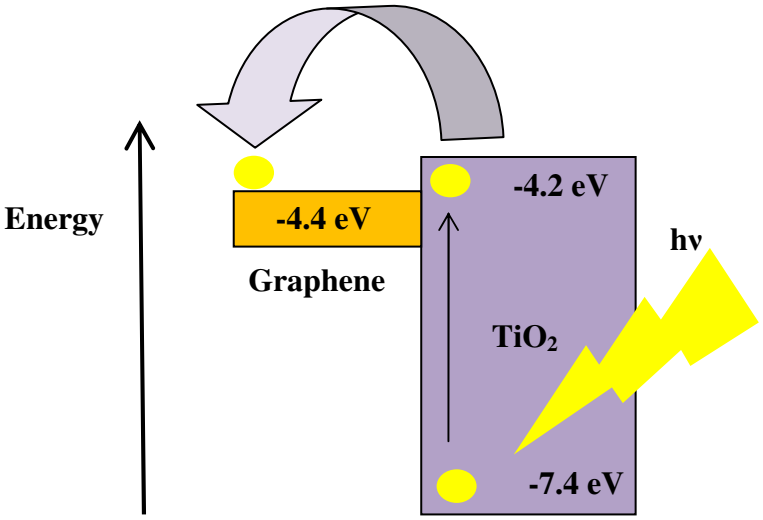

Scheme 3.2. Schematic diagram for energy band matching.

3.4. Conclusions.

A novel method for synthesizing TiO_2 nanowires on graphene sheets is reported for the first time using a one step sol-gel route in $scCO_2$ with acetic acid as the polycondensation agent. Different pressures, temperatures, HAc/TIP and FGSs/TIP weight ratios have been studied. HAC/TIP weight ratio and calcination temperature were found to play a key role in nanofiber formation with a limited effect of the other factors. A reduction in the band gap and also electron-hole recombination were observed for the TiO_2/FGSs composites

compared to the bare TiO_2 by using UV-vis and photoluminecense spectroscopies. TiO_2 bonded to the carboxylate groups on the graphene surfaces was confirmed by high resolution XPS. The surface area of TiO_2 nanowires was measured by BET and showed a high surface area. Ethanol and hexane were also examined as solvents for comparison, with TiO_2 nanospheres were formed on the graphene sheets when ethanol was used as the solvent and Hexane found unsuitable. The I-V characteristics of the nanocomposites have revealed that our method for anchoring TiO_2 on the FGSs makes charge transfer possible between TiO_2 and FGSs. Nevertheless, this enhancement was found maximum for a TiO_2 nanowires with 40 nm diameter prepared in $scCO_2$.

3.5. References.

[1] T.N. Obee, R.T. Brown, Environmental Science & Technology 29 (1995) 1223-1231.
[2] G.K. Mor, K. Shankar, M. Paulose, O.K. Varghese, C.A. Grimes, Nano Letters 6 (2005) 215-218.
[3] I. Ilisz, A. Dombi, K. Mogyorósi, A. Farkas, I. Dékány, Applied Catalysis B: Environmental 39 (2002) 247-256.
[4] K. Nagaveni, M.S. Hegde, N. Ravishankar, G.N. Subbanna, G. Madras, Langmuir 20 (2004) 2900-2907.
[5] N. Lakshminarasimhan, W. Kim, W. Choi, The Journal of Physical Chemistry C 112 (2008) 20451-20457.
[6] S. Nakade, Y. Saito, W. Kubo, T. Kitamura, Y. Wada, S. Yanagida, The Journal of Physical Chemistry B 107 (2003) 8607-8611.
[7] C. Burda, Y. Lou, X. Chen, A.C.S. Samia, J. Stout, J.L. Gole, Nano Letters 3 (2003) 1049-1051.
[8] M. Adachi, Y. Murata, J. Takao, J. Jiu, M. Sakamoto, F. Wang, Journal of the American Chemical Society 126 (2004) 14943-14949.
[9] S.M. Liu, L.M. Gan, L.H. Liu, W.D. Zhang, H.C. Zeng, Chemistry of Materials 14 (2002) 1391-1397.
[10] W. Choi, A. Termin, M.R. Hoffmann, The Journal of Physical Chemistry 98 (1994) 13669-13679.
[11] G. Shen, P.-C. Chen, K. Ryu, C. Zhou, J. Mater. Chem. 19 (2009) 828.
[12] A. Gurlo, N. Barsan, U. Wemar, in: J.L.G. Fierro (Ed.), Metal oxides: chemistry and applications, CRC Press, 2006, p. 683.
[13] Y. Furubayashi, T. Hitosugi, Y. Yamamoto, K. Inaba, G. Kinoda, Y. Hirose, T. Shimada, T. Hasegawa, Applied Physics Letters 86 (2005) 252101-252101-252103.
[14] A. Kongkanand, K. Tvrdy, K. Takechi, M. Kuno, P.V. Kamat, Journal of the American Chemical Society 130 (2008) 4007--4015.
[15] D.R. Baker, P.V. Kamat, Advanced Functional Materials 19 (2009) 805-811.

[16] M. Feng, H. Zhan, L. Miao, ACS Applied Materials \& Interfaces 2 (2010) 1129--1135.
[17] V.K. Prashant, |J. Phys. Chem. Lett. 1 (2010) 520-527.
[18] N. Yang, J. Zhai, D. Wang, Y. Chen, L. Jiang, ACS Nano 4 (2010) 887-894.
[19] P. Brown, K. Takechi, P.V. Kamat, The Journal of Physical Chemistry C 112 (2008) 4776-4782.
[20] K. Woan, G. Pyrgiotakis, W. Sigmund, Advanced Materials 21 (2009) 2233-2239.
[21] Y.-B. Tang, C.-S. Lee, J. Xu, Z.-T. Liu, Z.-H. Chen, Z. He, Y.-L. Cao, G. Yuan, H. Song, L. Chen, L. Luo, H.-M. Cheng, W.-J. Zhang, I. Bello, S.-T. Lee, ACS NANO 4 (2010) 3482-3488.
[22] A. Kongkanand, P.V. Kamat, ACS NANO 1 (2007) 13-21.
[23] Y. Medina-Gonzalez, W.Z. Xu, B. Chen, N. Farhanghi, P.A. Charpentier, Nanotechnology 22 (2011) 065603.
[24] R. Sui, A.S. Rizkalla, P.A. Charpentier, Langmuir 21 (2005) 6150-6153.
[25] P.A. Charpentier, W.Z. Xu, X. Li, Green Chem 9 (2007) 768-776. .
[26] N.W. Pu, C.A. Wang, Y. Sung, Y.M. Liu, M.D. Ger, Materials Letters 63 (2009) 1987-1989.
[27] M.J. Comstock (Ed.), Supercritical Fluid Science and Technology, American Chemical Society, 1989, pp. i-iv.
[28] L. Staudenmaier, Ber. Dtsch. Chem. Ges. 31 (1898) 1481.
[29] R. Sui, A.S. Rizkalla, P.A. Charpentier, J. Phys. Chem. B 108 (2004) 11886.
[30] B. O'Regan, M. Gratzel, Nature 353 (1991) 737-740.
[31] H.C. Schniepp, J.-L. Li, M.J. McAllister, H. Sai, M. Herrera-Alonso, D.H. Adamson, R.K. Prud'homme, R. Car, D.A. Saville, I.A. Aksay, The Journal of Physical Chemistry B 110 (2006) 8535-8539.
[32] M.J. McAllister, J.L. Li, D.H. Adamson, H.C. Schniepp, A.A. Abdala, J. Liu, M. Herrera-Alonso, D.L. Milius, R. Car, R.K. Prud'homme, I.A. Aksay, Chemistry of Materials 19 (2007) 4396-4404.
[33] S. Ansari, E.P. Giannelis, Journal of Polymer Science, Part B: Polymer Physics 47 (2009) 888-897.
[34] Y.y. Wang, Z.h. Ni, T. Yu, Z.X. Shen, H.m. Wang, Y.h. Wu, W. Chen, A.T. Shen Wee, The Journal of Physical Chemistry C 112 (2008) 10637-10640.
[35] M.S. Dresselhaus, G. Dresselhaus, R. Saito, A. Jorio, Physics Reports 409 (2005) 47-99.
[36] T. Ohsaka, F. Izumi, Y. Fujiki, Journal of Raman Spectroscopy 7 (1978) 321-324.
[37] K.N. Kudin, B. Ozbas, H.C. Schniepp, R.K. Prud'homme, I.A. Aksay, R. Car, Nano Letters 8 (2008) 36-41.
[38] Y. Lei, L.D. Zhang, J.C. Fan, Chemical Physics Letters 338 (2001) 231-236.
[39] O. Akhavan, Carbon 48 (2010) 509-519.
[40] X. Wu, D. Wang, S. Yang, Journal of Colloid and Interface Science 222 (2000) 37-40.
[41] R. Sui, A.S. Rizkalla, P.A. Charpentier, The Journal of Physical Chemistry B 110 (2006) 16212-16218.
[42] R. Sui, V. Thangadurai, C.P. Berlinguette, Chemistry of Materials 20 (2008) 7022-7030.
[43] F.P. Rotzinger, J.M. Kesselman-Truttmann, S.J. Hug, V. Shklover, M. Grätzel, The Journal of Physical Chemistry B 108 (2004) 5004-5017.

[44] M.B.I. Chowdhury, R. Sui, R.A. Lucky, P.A. Charpentier, Langmuir (2009).
[45] R. Sui, A.S. Rizkalla, P.A. Charpentier, J. Phys. Chem. B 110 (2006) 16212.
[46] R. Sui, V. Thangadurai, C.P. Berlinguette, Chem. Mater. 20 (2008) 7022.
[47] R. Sui, P.A. Charpentier, A.S. Rizkalla, M.C. Jennings, Acta Crystallogr., Sect. E: Struct. Rep. Online 62 (2006) m373.
[48] W. Wang, P. Serp, P. Kalck, J.L. Faria, Applied Catalysis B: Environmental 56 (2005) 305-312.
[49] Y. Ji, K.-C. Lin, H. Zheng, C.-C. Liu, L. Dudik, J. Zhu, C. Burda, ACS Applied Materials & Interfaces 2 (2010) 3075-3082.
[50] H. Tang, H. Berger, P.E. Schmid, F. Lévy, G. Burri, Solid State Communications 87 (1993) 847-850.
[51] Y. Yao, G. Li, S. Ciston, R.M. Lueptow, K.A. Gray, Environmental Science and Technology 42 (2008) 4952-4957.
[52] B. Czerw, F. D., T. A., R.P.M.e. al., Phys. Rev. B 66 66 (2002) 033408.

Chapter 4

Visible light active Fe doped TiO_2 nanowires grown on Graphene using Supercritical CO_2

Abstract:

Highly ordered, visible light driven TiO_2 nanowire arrays doped with Fe photocatalysts were grown on the surface of functionalized graphene sheets (FGSs) using a sol-gel method with titanium isopropoxide (TIP) monomer, acetic acid (HAc) as the polycondensation agent and iron chloride in the green solvent, supercritical carbon dioxide ($scCO_2$). The morphology of the synthesized catalysts was studied by SEM and TEM, which showed uniform formation of Fe doped TiO_2 nanowires on the surface of the graphene sheets, which acted as a template for nanowire growth through surface –COOH functionalities. Increasing Fe content in the nanowires did not change the morphology significantly, although higher BET surface areas were noted. Optical properties of the synthesized composites were examined by UV and Photoluminescence–spectroscopy which showed a significant reduction in band gap with increasing Fe content, i.e. 2.25 eV at 0.6% Fe. High resolution XPS and Raman analysis showed the interaction of Fe with the TiO_2 lattice and also bonding of TiO_2 with -COOH groups on the surface of the graphene sheets. The photocatalytic properties of the prepared catalysts were evaluated by photodegradation of 17β-estradiol (E2), an endocrine disrupting hormone which is commonly released into aquatic environments under visible light of solar irradiation. All prepared catalysts with different ratios of Fe were active in the visible region of solar spectrum and the photocatalytic activity increased with increasing Fe doping with possible plateau at 0.6-0.8%. Prepared catalysts showed higher activity than both Fe doped TiO_2 and TiO_2/ FGSs composites. In addition to reduction in electron–hole recombination of Fe doped TiO_2 in the composites, Graphene with its high surface area can absorb E2 molecules and then Fe doped TiO_2 which are anchored on its surface degrade pollutants more efficiently in the visible region. The enhancement of the optical properties of synthesized materials was also confirmed by photocurrent measurement. The optimum sample containing 0.6% Fe doped TiO_2 on the graphene sheets increased the power conversation efficiency by 6-fold in comparison to TiO_2 alone.

4.1. Introduction.

Heterogeneous photocatalysis has attracted considerable attention in recent years due to the potential for removal of emerging environmental contaminants such as endocrine disrupting hormones (EDHs) [1-3]. TiO_2-based photocatalysts have several advantages owing to titania's abundance, non-toxicity, low-cost, unique optical-electronic properties and long term thermodynamic stability[4]. Nanostructured TiO_2 has been used for various environmental applications including degrading organic pollutants [5], dye-sensitized solar cells [6], self cleaning surfaces[7], water splitting[8] and antimicrobial coatings [9, 10]. However, there are limitations for using commercial nano TiO_2 in these applications (e.g. Degussa P25) as TiO_2 nanoparticles easily agglomerate, have low surface areas, and give a low efficiency because of TiO_2's wide band gap (3.2 eV) which is only active in the UV region of the solar spectrum [11].Current research efforts are focussed on enhancing photocatalytic degradation using visible light (400 nm< λ<760nm) which is often unused in UV-photocatalysis, although a target for next-generation photocatalytic processes.

For extending the absorbance of TiO_2 into the visible region, doping with transition metals is a useful technique[12]. For doping of TiO_2, various metal ions have been used, but Fe^{3+} in particular is considered as a strong candidate as it has a similar radius to Ti^{4+} and can easily integrate into the crystal lattice of TiO_2[12-14]. Additionally, the redox potential (energy differential) of Fe^{2+}/ Fe^{3+} is close to that of Ti^{3+}/Ti^{4+}, resulting in a shift in optical absorption into the visible region[12, 14].

Another common method for increasing the photocatalytic efficiency of TiO_2 is immobilization of TiO_2 powder on a co-adsorbent surface such as zeolites[15], alumina [16], silica [17] or activated carbon [18]. Carbonaceous materials are of current interest due to possessing unique pore structure, electronic properties, adsorption capacity and acidity. These materials include activated carbon[19], carbon nanotubes, and more recently graphene sheets[20-23]. Graphene can be synthesized inexpensively from cheap, readily available graphite [24] provides a larger specific surface areas similar to activated carbon and carbon nanotubes. This facilitates pollutant adsorbtion enhancing the photocatalytic efficiency by TiO_2. In addition, functional groups such as alcohol and carboxylic acids can be introduced onto the graphene surface [25]. Groups such as

–COOH allows for both adsorption of specific pollutants and potentially can be exploited as a selective template for sol-gel nanowire growth on the graphene surface. Hence, graphene can potentially harness and stabilize different semiconductors on its surface to produce more stable and porous photocatalysts [26, 27].

There are currently few reports on the preparation of graphene-TiO_2 composites and also their corresponding applications. P25-graphene composites synthesized by a hydrothermal method were used as a photocatalyst for photodegradation of methylene blue. A large enhancement in reaction rate was observed compared to P25 and P25-CNTs[22]. Titanium oxide nanoparticle-graphene oxide (TiO_2-GO) and titanium oxide nanoparticle-reduced graphene oxide (TiO_2-RGO) composites were synthesized by Lambert et al. via the hydrolysis of TiF_4 at 60°C[28].

In this work, we show that Fe doped TiO_2 can be grown on the surface of functionalized graphene sheets (FGSs) containing –COOH functional groups use supercritical carbon dioxide ($scCO_2$), as the enabling solvent. TiO_2 nanowires were prepared previously in $scCO_2$ using Ti alkoxides and acetic acid as the polycondensation agent with the mechanism of wire formation examined[29]. $ScCO_2$ is an inexpensive, green alternative to conventional organic solvents [29, 30] which is inexpensive, environmentally benign and non-flammable with low viscosity, zero surface tension and high diffusivity which are favourable for synthesizing fine and uniform nanomaterials. $ScCO_2$ can facilitate doping in titania[31, 32] and has been used to enhance exfoliation of graphene sheets[33]. No additional drying process is required as complete removal of excess acetic reaction ingredients is easy by supercritical fluid extraction, maintaining the porous nanostructure[29, 30]. The resulting materials from this study are examined with visible light for the photocatalytic degradation of 17 β-estradiol (E2).

4.2. Experimental.

4.2.1. Materials.

Graphite flakes nominally sized at 7-10 microns were provided from Alfa aesar. Fuming nitric acid (>90%), sulphuric acid (95-98%), potassium chlorate (98%), titanium isopropoxide (99.999% trace metals basis), iron chloride $FeCl_3$, and hydrochloric acid (37%) were purchased from Sigma-Aldrich and used as received.

4.2.2. Methods.

4.2.2.1. 3.2.2.1.Preparation of FGSs. Graphite (5 g) was reacted with concentrated nitric (45 mL) and sulfuric acid (90 mL) with potassium chlorate (55 g). The potassium chlorate was added slowly over 15 min to avoid any sudden increase in temperature with the resulting mixture stirred at room temperature for 3 days. After completing the oxidation reaction, the mixture was added to excess water, washed with a 5% solution of HCl, and then repeatedly washed with water until the pH of the filtrate was neutral. The prepared graphite oxide was kept at 100º C in a vacuum oven until use to evaporate all the water. A quartz tube sealed at one end, the other side was closed with an inlet and outlet for continuously passing Nitrogen gas to provide an oxygen free environment. Then, the graphite oxide powder was placed in a quartz boat and inserted into a tubular furnace preheated to 1050 $^{\circ}$C and kept at this temperature for 30s. The graphite oxide was reduced and expanded to form functionalized graphene sheets [33].

4.2.2.2. Preparation of Fe doped TiO2/Graphene sheets composites. TiO_2 nanowires were synthesized on the surface of graphene sheets in $scCO_2$ using HAc/TIP: 4, 60 °C and 5000 psi as previously determined as the optimal experimental conditions.(Chapter 3) In a typical experiment, FGSs (0.05 g) were first placed in a 10 ml, high pressure view cell followed by quick addition of titanium isopropoxide (1ml), $FeCl_3$ dissolved in isopropanol (at varius volumes) , acetic acid (4 ml) and CO_2 to the desired pressure and temperature. Magnetic stirring with TFE stir bar was used for mixing the reaction mixture. It was found that the mixture of iron chloride/isopropanol, functionalized graphene sheets, titanium isopropoxide and acetic acid was miscible with CO_2 at 60°C and 5000 psig pressure. Stirring was stopped after 24 h while normally several days of aging were required for complete reaction. After aging, the formed gel was washed continuously using 80 ml of CO_2 at a rate of approximately 0.5 mL/min, followed by

controlled venting at 0.5 mL/min to prevent collapse of the solid network. The resulting powder was calcined at 450°C in air for 2hrs (tubular furnace) using a heating rate of 10 °C/min. The calcined powder was kept in a vacuum oven at 80° C to remove moisture.

4.2.3. Characterization.

Atomic force microscopy (AFM, Veeco Multimode V) was used in tapping mode to characterize the morphology of the graphene sheets and TiO_2/FGSs composites. The samples for AFM study were prepared by adhering them in powder form on a metallic plate. 3D reconstructions were obtained from the AFM data by using Gwyddion software (Veeco). The morphologies of the samples were examined using Scanning Electron Microscopy (SEM) (Model LEO 1530) and Transmission Electron Microscopy (TEM) (Model JEOL 2010F). Samples for SEM imaging were prepared by applying the powder directly to carbon adhesive tape. For TEM analysis, the powdered samples were dispersed in methanol by sonication and then placed on a copper grid covered with holey carbon film and dried by evaporation. Structural analysis of the samples was performed using an X-ray powder diffractometer [Rigaku Miniflex XRD, Texas, U.S.A.], fitted with a rotating sample holder, a scintillation counter detector and a divergent beam utilizing a Cu Kα source of X-rays (λ= 1.5418 °*A*). FT-IR spectra were collected on samples as KBr pellets using a Bruker Tensor 27 spectrometer, with a resolution of 4 cm^{-1}. Raman analysis was performed using a Kaiser optical system (RXN1-785) with 5 times exposure and 20 times accumulation. The XPS analysis was carried out with a Kratos Axis Ultra spectrometer using a monochromatic AlK (alpha) source (15mA, 14kV). Photoluminescence spectra were carried out with PTI Quantamaster 50 spectrophotometer with a Xenon lamp (75 V). UV spectra were performed by (Shimadzu 3600) deuterium arc lamp and two different detectors (PMT, and PbS). An integrating sphere was utilized in order to measure diffuse reflectance of these materials.

4.2.4. Photocatalytic Activity Measurements.

Photodegradation of 17β-Estradiol (Sigma-Aldrich) as a model endocrine disrupting compound (EDC) was investigated under visible solar irradiation ($\lambda \geq 420$ nm). A solar simulator (Model: SS1KW, Sciencetech) with a 1000 watt xenon arc lamp equipped with an air mass filter (AM filter) AM 1.5G ($\lambda > 290$ nm) and a special UV cut-off filter

(290≤λ≤ 420 nm) were used as the visible light source. Typically, a mixture of aqueous E2 solution (5µg/L) and 0.5 g/L of catalyst was vigorously stirred for 30 min to establish an adsorption/desorption equilibrium in the dark. Then the reaction solution was irradiated under visible light in an open water-jacketed vertical photo-reactor which was placed on a magnetic stirrer during all experiments, under aerated conditions [1]. The temperature of the reactions was controlled at 22+1°C by circulating cooling water. At given time intervals, 5 mL aliquots were sampled and centrifuged to remove the particles. Supernatant were analyzed by HPLC using a (ICS 300, Dionex), which included a DP pump, an AS auto sampler, a DC column oven and PDA UV detector, connected to Chromeleon software. Separations were carried out with an Acclaim 120 C18 reversed-phase column (150 mm × 4.6 mm i.d., 5 µm particle size, Dionex, USA). The injection volume was 40 µL from a 2 mL HPLC vial, capped and sealed with PTFE lid. The mobile phase was the mixture of acetonitrile (AcN) and deionized water (Milli-Q) (50:50 v/v), delivered at a flow rate of 1 mL/min. The column temperature was maintained at 30°C and detection wavelength was set at 280 nm which shows maximum absorbance of E2. The retention time of E2 in HPLC column was 5.33 min.

4.3. Results and discussion.

4.3.1. Characterization of synthesized materials.

Different percentages of Fe doped TiO_2 and Fe doped TiO_2/Functionalized Graphene Sheets (FGSs) were synthesized in $scCO_2$. The experimental conditions and properties of the synthesized materials are summarized in Table 4.1. The morphology and particle size of Fe doped TiO_2/FGSs materials synthesized via an acid-modified sol-gel progress in $scCO_2$ were assessed by SEM and TEM analysis.

Table 4.1. Synthesis conditions, morphology**,** BET surface area, pore volume,and pore size distribution of TiO_2, Fe doped TiO_2/ FGSs composites (0.1%, 0.2%, 0.4%, 0.6% and 0.8%).

Materials	BET surface area (m^2/g)	Total pore volume (cm^3/g)	Average pore size (nm)	Band Gap (eV)	Morphology
TiO_2	**50**	**-------**	**-------**	**3.2**	**Nanoparticles**
Fe / TiO_2 (0.4%)	**156**	**0.11**	**38.7**	**2.5**	**Nanoflower**
Fe/ TiO_2/ FGSs (0.1%)	**128**	**0.10**	**41.6**	**2.82**	**Nanowires on the sheet**
Fe/ TiO_2/FGSs (0.2%)	**174**	**0.13**	**39.3**	**2.53**	**Nanowires on the sheet**
Fe/TiO_2/FGSs (0.4%)	**214**	**0.20**	**37.48**	**2.42**	**Nanowires on the sheet**
Fe/TiO_2 /FGSs (0.6%)	**256**	**0.23**	**31.5**	**2.25**	**Nanowires on the sheet**
Fe/TiO_2 /FGSs (0.8%)	**297**	**0.29**	**29.2**	**2.25**	**Nanowires on the sheet**

*All materials prepared in $scCO_2$ (60° C, 5000 psi), FGSs/TIP: 1:20, AcOH/ TIP: 4 and calcined at 450° C
*All percentages represent volume % of Fe in the composites.

In Figure 4.1a typical SEM image of Fe doped TiO_2/FGSs (0.2%-Figure 4.1a) and (0.6%-Figure 4.1b) are shown. Increasing the amount of Fe was not found to change the

morphology of nanowires on the surface of the graphene sheets significantly; however the nanowires with higher amounts of Fe appear to be more porous. In Figures 4.1c and d, TEM images show that the diameter of TiO_2 nanowires is less than 20 nm. Good dispersion of TiO_2 nanowires on the graphene sheets can be observed, along with excellent contact between the graphene sheet and wires. SEM images of 0.2% Fe doped TiO_2 and TiO_2/FGSs have been shown in Figure 4.2 for comparison. When Graphene sheets were not used as the support, the morphology of synthesized materials showed a flower-like structure. TiO_2/FGSs composites also showed similar structure as Fe doped TiO_2/FGSs with less porosity.

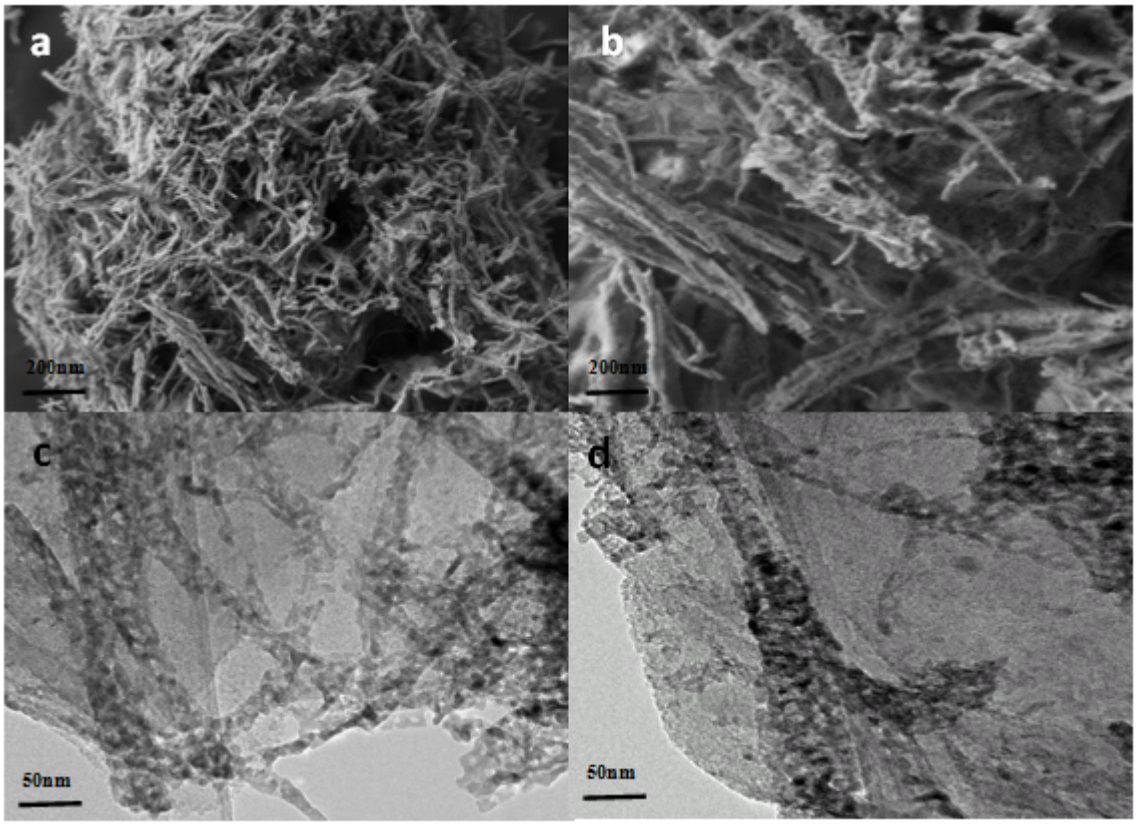

Figure 4.1. SEM images of (a) Fe doped TiO_2/FGSs 0.2% (200 nm scale), (b) 0.6% (200 nm scale); TEM images of Fe doped TiO_2/FGSs (c) 0.2% (50 nm) and (d) 0.6% (50 nm).

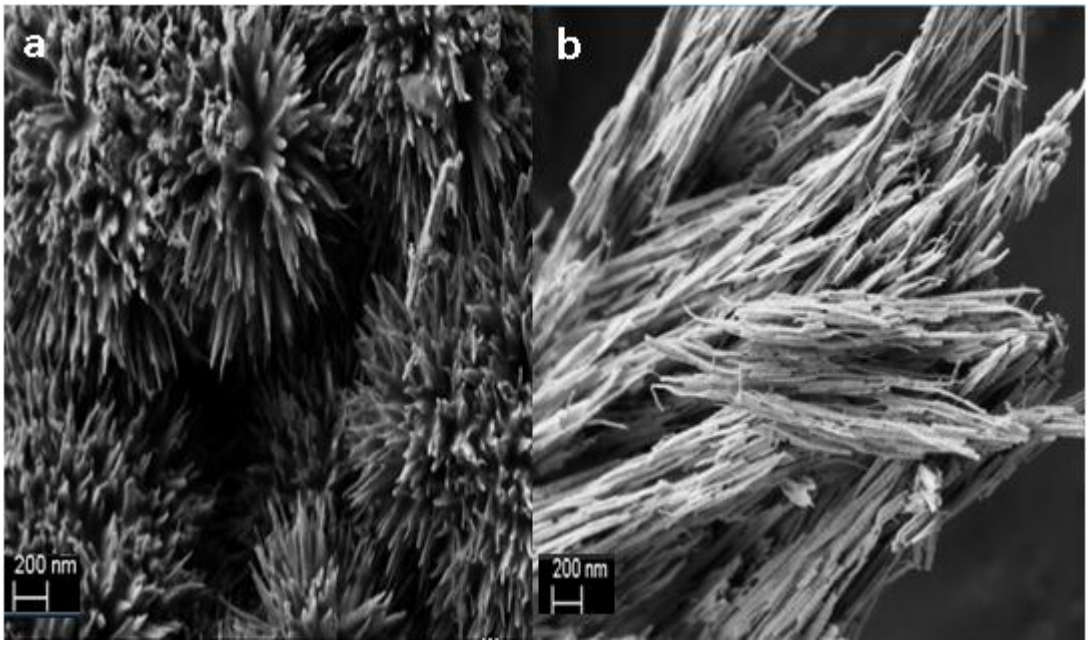

Figure 4.2. SEM images of (a) Fe doped TiO_2 (0.4%) and (b) TiO_2/FGSs.

The HRTEM micrographs of the lattice image of 0.2% Fe doped titania/graphene calcined at 450 ^oC are given in Figure 4.3a, showing uniform dispersion of anatase with d-spacing 0.39 nm (101) as well as some rutile with d-spacing 0.21 nm (111) [34]. No iron was detected in HRTEM, which implies that all the Fe is contained within the TiO_2 lattice. However d-spacing increased which is in good agreement with XRD data as explained later confirming expansion of TiO_2 lattice due to Fe incorporation. In Figure 4.3b EDX spectra with elemental analysis of this sample shows 25.56% of C, 59.06 % of O, 14.08% of Ti and 1.17% of Fe on the surface of this sample. Elemental mapping was measured in several selected areas confirming uniform dispersion of Ti, C, O and Fe in the synthesized material.

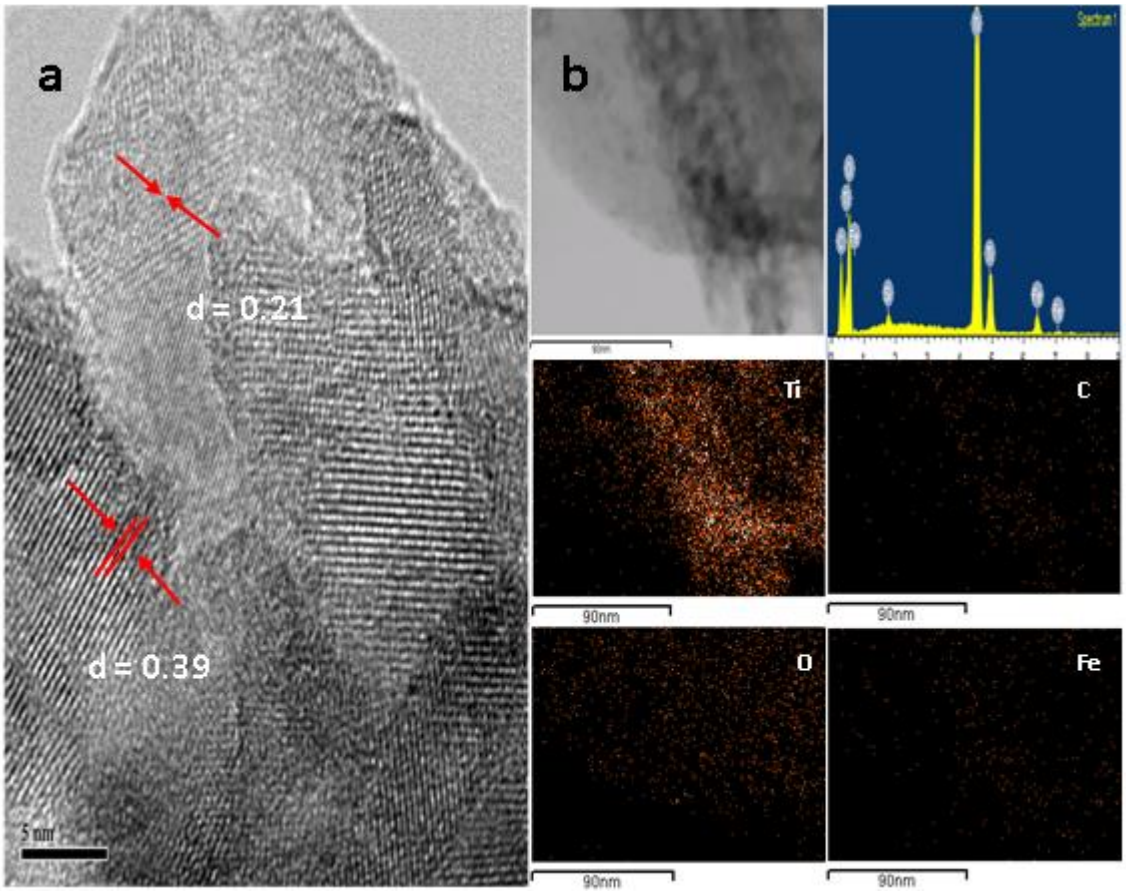

Figure 4.3. (a) HRTEM image of Fe doped TiO_2/FGSs (0.2%), (b) HRTEM-EDS elemental mapping of Fe doped TiO_2/FGSs assembly.

BET surface areas (Table 4.1) were determined using nitrogen adsorption and desorption isotherms (Figure 4.4). The BET surface areas of the Fe doped TiO_2 /FGSs samples were found to be larger compared to that of undoped TiO_2. Introducing Fe to the TiO_2 during synthesis on the graphene sheets increases the surface area by producing more pores within the composites. By increasing the amount of Fe doping, the pore size increased whereas the pore volume decreased meaning an enhancement in the mesoporous structure. Lucky and Charpentier previously synthesized Fe-doped TiO_2 nanofibers in $scCO_2$ and reported similar results [29].

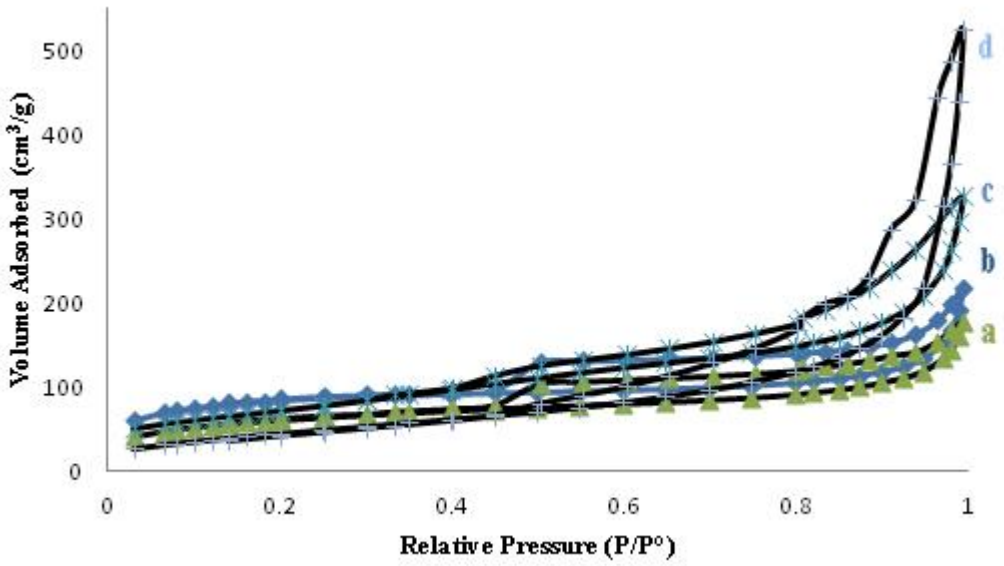

Figure 4.4. N_2 adsorption/desorption isotherm of the Fe doped TiO_2 /FGSs prepared in $scCO_2$, (a) 0.2%, (b) 0.4%, (c) 0.6% and (d) 0.8%.

The optical absorption spectra obtained by the diffuse reflection method for TiO_2 nanowires and different percentages of Fe doped TiO_2 on the surface of graphene sheets prepared in $scCO_2$ are shown in Figure. 4.5a. By adding Fe to the TiO_2/FGSs composites, a noticeable shift in the absorption edge into the visible light region was observed (up to to 550nm). The band gap energy of doped TiO_2 samples calculated using basic energy equation ($E=hC/\lambda$) where E is band gap energy, h is Planks constant, C is Speed of light, λ is Cut off wavelength. (It can be obtained by drawing a tangent line on the edge of the UV spectra and find the cut off wave length at y=0) [34]. Pure TiO_2 has a sharp decrease of reflection around 420 nm, which corresponds to the anatase band gap of 3.2 eV. The band gap energy of doped TiO_2 samples was calculated using the basic energy equation ($E=hc/\lambda$) was found to decrease with increasing amount of Fe in the composites. The smallest band gap was found 2.25 eV for 0.6% Fe doping. Further increasing of the Fe concentration to 0.8% did not result in a further decrease the band gap. In Fig 4.5b, the diffuse reflectance UV-Vis spectra of TiO_2 nanowires (1), 0.4% Fe doped TiO_2 (2) and 0.4% Fe doped TiO_2/FGSs (3) prepared in $scCO_2$ are compared. By adding graphene to the system, the band gap of Fe doped TiO_2 decreased from 2.5 to 2.4 eV attributed to enhanced electron hole recombination of TiO_2 and graphene. In Figure 4.5c, the UV

spectra of TiO_2 with band gap of 3.2 eV compared to TiO_2/FGSs which has a band gap of 2.9 eV.

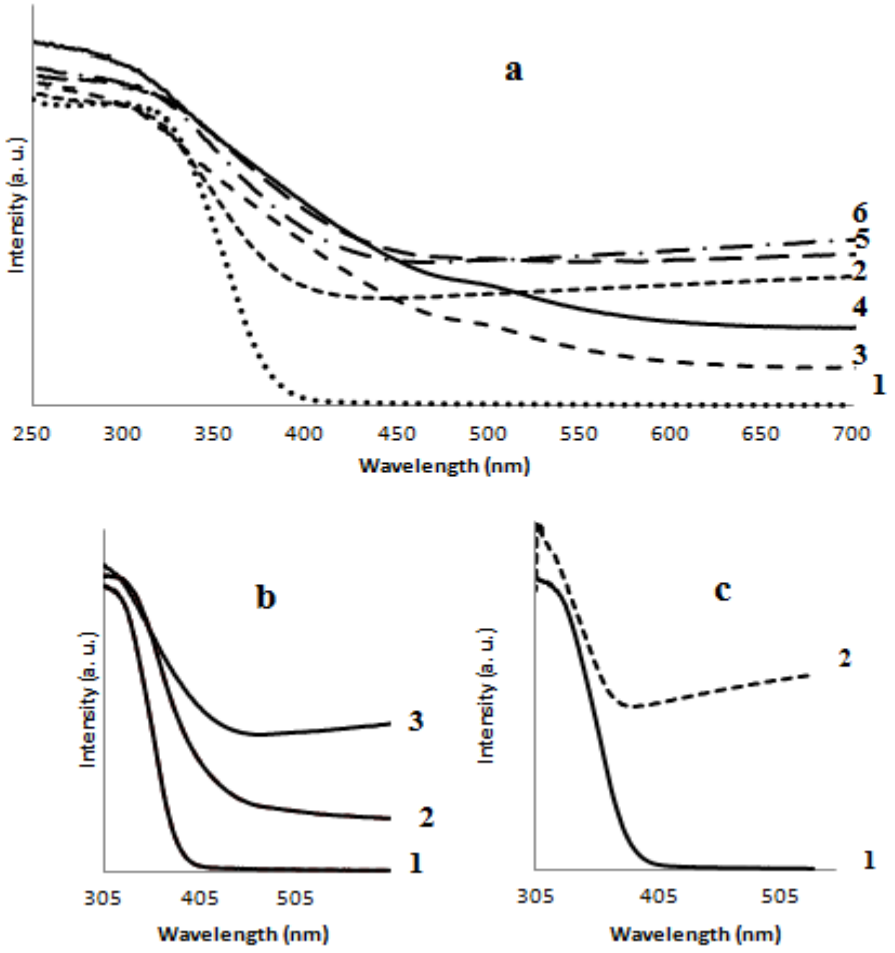

Figure 4.5. Diffuse reflectance UV-Vis spectra of: a (1) TiO_2 anatase; Fe doped TiO_2/FGSs (2) 0.1 %,(3) 0.2%, (4) 0.4%, (5) 0.6% (5) and (6) 0.8%; b (1) TiO_2, (2) 0.4% Fe doped TiO_2 and (3) 0.4% Fe doped TiO_2/FGSs; c (1) TiO_2 and (2) TiO_2/FGSs prepared.

Photocatalytic activity is a function of trapping of electrons and holes. TiO_2 surface phenomena such as excited states and electron-hole recombination are usually studied by using photoluminecense (PL) spectroscopy [35]. Electrons in semiconductors are excited to higher energy levels, when they spontaneously de-excite they emit luminescence. The luminescence is analyzed with a spectrometer and the peaks in the spectra represent a direct measure of the energy levels in the semiconductors [36]. For increasing the

photocatalytic activity of TiO_2, the lifetime of excited electrons should be decreased by trapping with another material which is attached to the TiO_2.With electron-hole pair recombination after a photocatalyst is irradiated (i.e., laser), photons are emitted from conduction band to valence band resulting in photoluminescence. Reduction in PL spectra intensity represents decreasing in energy levels or band gap of TiO_2. The PL spectra of TiO_2 and the $scCO_2$ synthesized composites are shown in Figure 4.6. TiO_2 (anatase) has a characteristic broad peak at around 540 nm as shown in spectra a [37]. Although the PL intensity decreased in both the Fe doped TiO_2 nanowires and the TiO_2 nanowires/FGSs composites compared to anatase alone, the reduction is significantly greater in the Fe doped TiO_2/ FGSs composites. When Fe doped TiO_2 nanowires are in contact with graphene sheets, excited electrons have less chance for recombination resulting in a decreased band gap and enhanced visible light activity. These results help confirm the UV-Vis results.

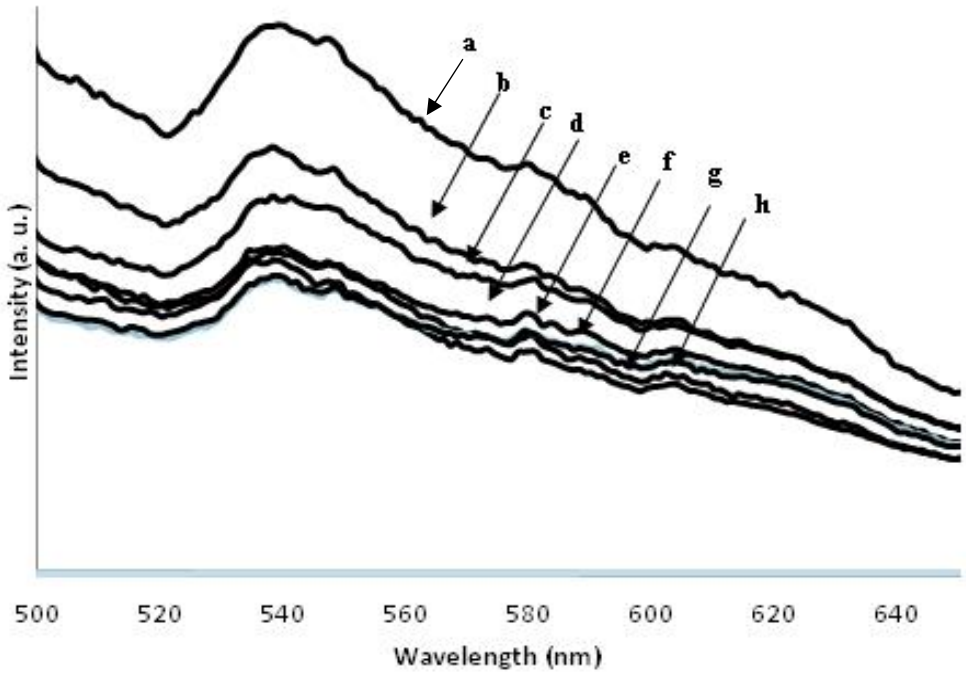

Figure 4.6. Photoluminesence Spectra of (a) TiO_2(anatase), (b) TiO_2 /FGSs composites, (c)Fe doped TiO_2 , (d) 0.1, (e) 0.2, (f) 0.4, (g) 0.6 and (h) 0.8 % Fe doped TiO_2/ FGSs Composites.

The structure of Fe-doped TiO_2/FGSs composites that were synthesized using the sol-gel method in $scCO_2$ appear to be amorphous; however, by thermal annealing at 450 °C, depending on dopant loading, anatase or a mixture of anatase and rutile TiO_2 was obtained. In Figure 4.7, XRD spectra of different percentages of Fe doped TiO_2/ FGSs are shown. No obvious peaks for Fe could be detected indicating that the Fe ions were fully integrated in the TiO_2 crystal lattice. In the 0.2% Fe doped TiO_2/FGSs (Fig 4.7a), a mixture of anatase and rutile TiO_2 is observed. By increasing the concentration of Fe to 0.4% (Fig 4.7b), the amount of rutile phase decreased. Further increasing the concentration of Fe to 0.6 and 0.8% (Fig 4.7c and 4.7d), only anatase phase was obtained. These results indicate that the specific concentration of Fe ions can affect the rate of anatase-rutile phase transformation. By increasing the amount of dopant in TiO_2, the oxygen vacancies increased and more anatase phase can result from A-R phase transformations involving a contraction of the oxygen structure [36]. Choi et al. studied the effect of different dopants on A-R phase transformation and suggested that addition of dopants with small radii could be directly integrated into the TiO_2 crystal lattice and by introducing more oxygen sites in the lattice, more anatase TiO_2 would be formed [37]. On the other hand, an increase in the Fe content leads to a shift of the (101) and (200) reflections to lower angles corresponding to the unit cell expansion due to the replacement of Ti^{4+} ions by slightly larger Fe^{3+} ions. The same changes in *d* spacing with increasing Fe content were observed in the HRTEM images of doped materials.

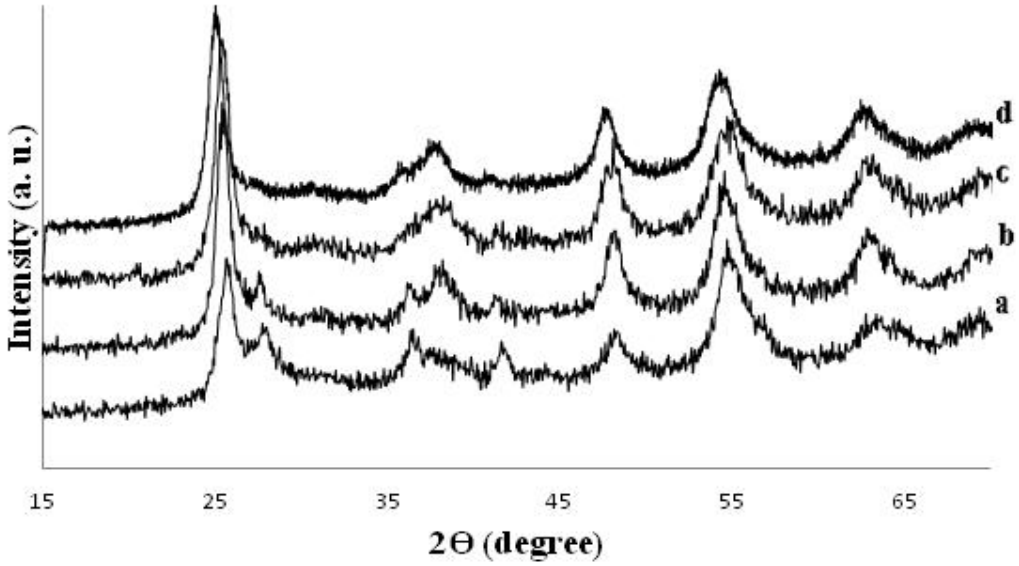

Figure 4.7. XRD pattern of (a) 0.2%, (b) 0.4%, (c) 0.6% (c) and (d) 0.8% of Fe doped TiO2 /FGSs composites prepared at 60° C and 5000 psi and calcined at 450° C.

Graphite has two well known characteristic bands in the Raman spectra; the strong G band at 1575 cm^{-1} and the weak D band at approximately 1355 cm^{-1}(Figure 4.8a)[38]. After oxidation of graphite to graphite oxide and then thermal expansion to FGSs, both the G and D bands change noticeably. A higher disorder in graphite resulted in a broader G band, as well as a higher intensity, broader D band compared to that of the G band (Figure 3.8b and c)[38]. After functionalization of FGSs with TiO_2, the D/G ratio, which represents the degree of functionalization increased dramatically indicating good attachment of the TiO_2 nanowires to the surface of the graphene sheets. The main characteristic peak of anatase TiO_2 appears at 145 cm^{-1} which is attributed to the main E_g anatase vibration mode[39]. Moreover, the presence of crystaline TiO_2 in the composites is confirmed by the vibration peaks at 400 cm^{-1} (B_{1g}), 519 cm^{-1} (A_{1g}) and 640 cm^{-1} (E_g) (Figure 4.8a) [40]. After Fe doping, the raman spectra did not change significantly (D/G ratio did not changed~ 2.6) attributed to all the Fe being integrated into the TiO_2 lattice. (Figure 4.8b,c) The only change is a shift of the TiO_2 peak to the higher wavenumbers in the Fe doping composites, indicating an increase in the surface oxygen vaccancies[40].

Zhu et al. (2007) prepared Fe-doped nanocrystalline via a nonhydrolytic sol-gel method and observed the same shift in the Raman study [41].

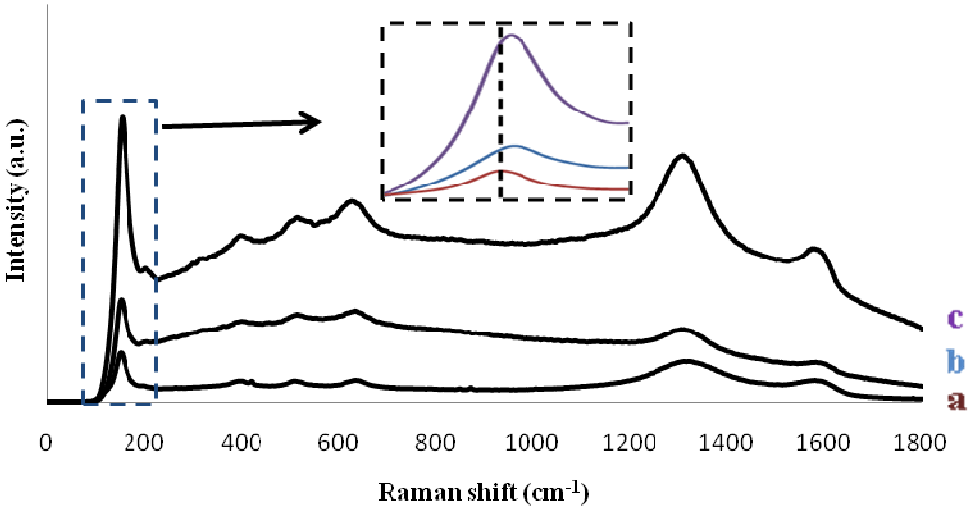

Figure 4.8. Raman Spectra of (a) TiO_2/FGSs composites, (b) Fe doped TiO_2/FGSs (0.2%) and (c) (0.6%).

In the XPS spectra of FGSs, 90 % Carbon and 10% Oxygen were detected. In high resolution XPS of C1s, four different peaks were observed at 284.7, 286.2, 287.7 and 289.3 eV which correspond to the (C-C, C=C), (C-H), (C-OH, C-O-C) and C=O, respectively (Chapter 3). Akhavan (2010) studied the XPS spectra of Graphite oxide and thermal expanded Graphene sheets at different temperatures and reported similar results. [42]. The XPS spectra of 0.6% Fe doped TiO_2/ FGSs (appendix 2) shows 6.1% Fe 2p, 54.7% O1s, 18.7% Ti 2p and 20.5% C1s. In high resolution of C1s, four different peaks of FGSs are still available but the intensity of peaks which represented C=O and C-OH decreased. The peak at 289.25eV corresponds to C=O also shifted to lower energy (288.80eV) implying coordination bonding between Ti and carboxylic acids on the surface of the graphene sheets. The O 1s main peak at 530.3 eV is assigned to the metallic oxides (Ti-O), which is consistent with the binding energy of O^{2-} in the TiO_2 lattices. The peak at 533.40 eV corresponds to -OH disappearance, but the peak at 531.38 eV corresponding to the carbonyl group is still available [42]. The Ti 2p3/2 and Ti 2p1/2 for

Fe doped TiO_2 on the graphene surface are located at binding energies of 458.36 eV and 464.1 eV respectively, which is consistent with the values for Ti^{4+} in the TiO_2 lattices.[43] The peaks at 711.9 eV and 724.6 eV are assigned to 2p3/2 and 2p1/2 of Fe^{3+}, respectively. These data exhibit a slightly positive shift compared to those in Fe_2O_3 (710.7 eV for 2p3/2 and 724.3 eV for 2p1/2). The positive shift of the Fe2p level binding energy may be due to transferring the electrons from Fe^{3+} into TiO_2 lattice and the formation of Fe–O–Ti bond in the composite [43]. A proposed mechanism for the charge transfer in Fe doped TiO_2 /FGSs composite is shown in Scheme 4.1. Fe doped TiO_2 nanowires are in intimate contact with FGSs. Fe can help TiO_2 to absorb more visible light. On the other hand, FGSs also has a work function around 4.2-4.5 eV, [44] which electrons from the TiO_2 anatase conduction band can transfer to its (FGSs) conduction band, allowing charge separation, stabilization, and hindering charge recombination.

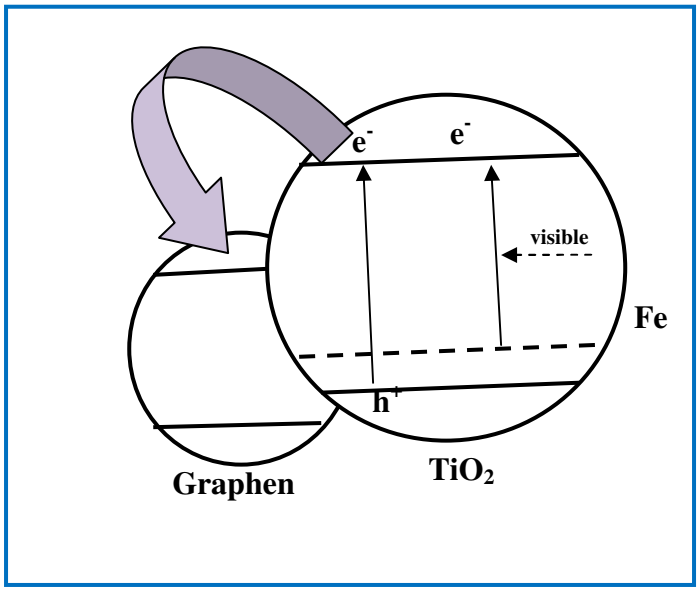

Scheme 4.1. Schematic of a proposed model for Fe doped TiO_2/FGSs with enhanced Visible light photocatalytic reactivity.

4.3.2. Visible-light photocatalytic activity.

The photocatalytic activities of the different iron doped (0%, 0.2%, 0.4%, 0.6% and 0.8%) TiO_2 nanowire/ graphene sheets and also Fe doped TiO_2 were evaluated through the photodegradation effects of E2 (Figure. 4.9) in aqueous solution under visible irradiation (λ>420 nm) using a solar simulator. We found no photodegradation of E2 in presence of pure TiO_2 under visible irradiation as expected, as TiO_2 does not produce $OH^{\bullet}$ in the presence of visible light. The results for different Fe doped TiO_2 nanowires/ graphene sheets and also Fe doped TiO_2 are shown in Figure 4.10.

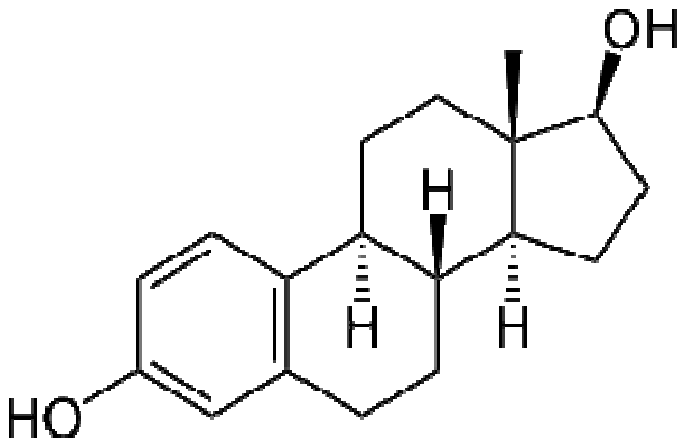

Figure 4.9. Structure of 17β-estradiol (E2).

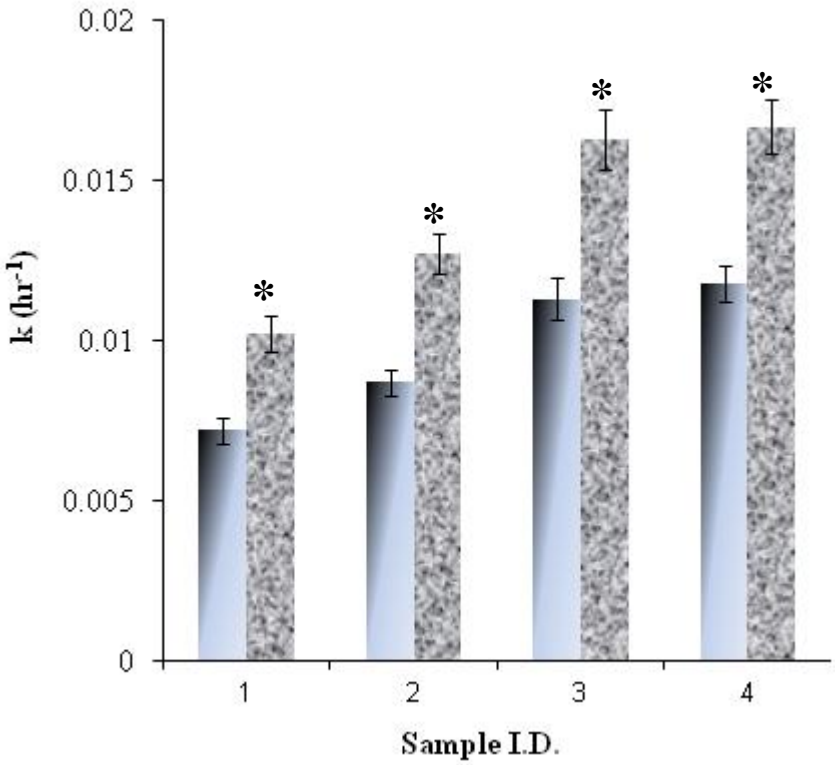

Figure 4.10. The photodegradation rate constant of E2 using various TiO_2 nano wires/ graphene sheets (*) and Fe doped TiO_2 calcined at 500°C (S1-0.2%, S2-0.4%, S3-0.6%, and S4-0.8% Fe).

The degradation rate increased with increasing Fe dopant level inside the TiO_2 lattice on the graphene sheets, but a marginal increase in rate occurred by increasing the Fe loading from 0.6% to 0.8% indicating the presence of an optimal loading. Although, the band gap energy of both 0.6% and 0.8% Fe doped TiO_2 nano wires/ grapheme is 2.25 eV, the surface area of 0.8% Fe was 297 m^2/g compared to 256 m^2/g of 0.6% Fe catalyst. This increase in surface area provides slightly higher rate for 0.8% Fe doped catalyst as shown in Figure 4.3. Whereas, only Fe doped TiO_2 composites show lower photocatalytic activity than that of Fe doped TiO_2 nanowire/graphene, because it seems that pollutants can be adsorbed more on the pores of graphene in addition to shifting in band gap to visible area, resulting in the enhancement in photocatalytic efficiency. As mentioned before, in TiO_2/graphene composites band gap shifted to visible area but this material tested and still is not totally active in just visible area.

The degradation kinetics is further studied in Figure 4.11 at 0.6% Fe loading. There was no photo-degradation of E2 in the presence of visible light ($\lambda \geq 420$ nm) due to direct photolysis, because E2 does not have any absorbance in the visible wavelength region[1]. The experiments in the presence of catalyst illustrate that 30 min was sufficient to reach the adsorption equilibrium. The degradation of E2 could occur because of photocatalytic reactions in the presence of catalyst under visible light ($\lambda \geq 420$ nm), with E2 almost completely degraded in less than 180 min. The photocatalytic degradation followed pseudo-first-order reaction kinetics in the studied concentration range. Reaction kinetics is often described in terms of the Langmuir–Hinshelwood model, which can be expressed as:

$$-\frac{dC}{dt} = k_r \frac{K_a C}{1+K_a C} \tag{4.1}$$

where *(−dC/dt)* is the degradation rate of E2, *C* is the concentration of E2 in the solution, t is reaction time, k_r is the reaction rate constant, and K_a is the adsorption coefficient of the reactant. K_aC is negligible when the value of *C* is very small. As a result, Eq. (4.2) can be described as a pseudo-first order kinetics. Setting Eq. (2) at the initial conditions of the photocatalytic experiment, when t = 0, C = C_0, it can be described as:

$$\ln\left(\frac{C_0}{C}\right) = K_{app} \times t \tag{4.2}$$

The half-life of E2 can be calculated as per Eq. 4.3:

$$t_{1/2} = \frac{\ln 2}{K_{app}} \tag{4.3}$$

The calculated half-life of E2 at 1 sun intensity for 0.6% Fe doped TiO_2 nano wires/ graphene sheet was only 43 min, whereas it was about 10 hrs in absence of catalyst due to direct photolysis under 1 Sun solar irradiation (AM 1.5G) at similar experimental conditions [1, 44].

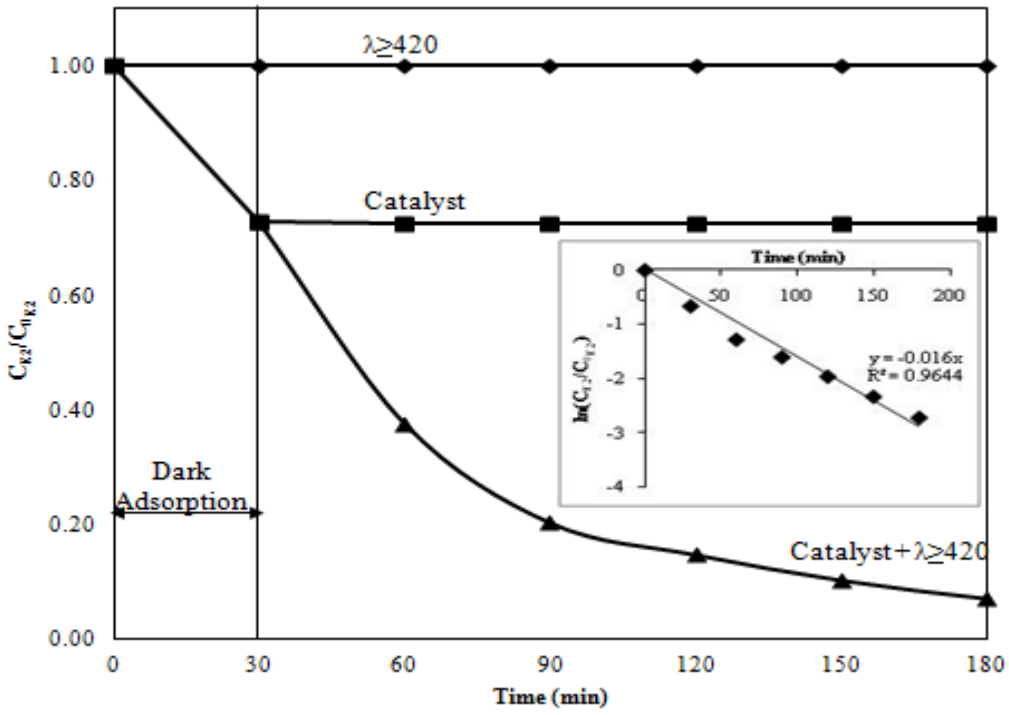

Figure 4.11. Photocatalytic degradation of E2 with the illumination time under visible solar irradiation ((λ>420 nm). = 5 µg/L, pH = 6.5, solar intensity= 1 SUN and irradiation time = 2.5 hours.

4.4. Photoefficiency Test.

Under simulated solar irradiation, different synthesized Fe doped TiO_2 on the garaphene sheets were examined for photoefficency. The optimum cell based on 0.6% Fe doped TiO_2/FGSs yielding power conversion efficiency (η) almost 6 times higher than that of TiO_2 (Figure 4.12). This significant improvement efficiency (η) for the Fe doped TiO_2/ FGSs based cell is due to the decreased charge-transfer resistance in the composite films as a result of the implanted FGSs, which creates a continuous electron conducting network to the transparent electrode, thus facilitating the diffusion of photoinjected electron between them. This sample for this DSSC study gave an efficiency of 1.8% which is 6.2 times higher than that of TiO_2 itself. Doping with Fe resulted in samples with higher surface area (256 m^2/g) which can absorb in the visible region (band gap reduced to 2.25 eV) resulting in cells with higher efficiency[38].

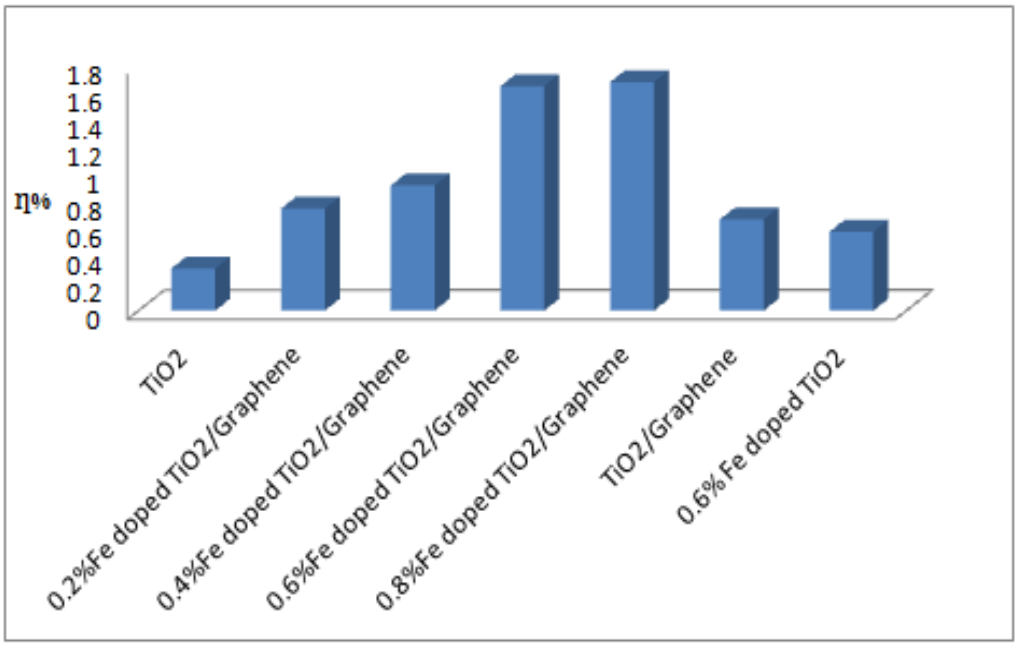

Figure 4.12. Efficiency of the solar cells fabricated by TiO_2 and different Fe doped TiO_2 on the graphene under AM 1.5G irradiation.

4.5. Conclusions.

Fe doped TiO_2 nanomaterials on the surface of graphene sheets were successfully synthesized by a simple sol-gel process using the green solvent $scCO_2$. Fe doped TiO_2 nanowires were uniformly formed on the surface of graphene sheets, with increasing surface area confirmed by BET analysis. UV-Vis analysis was used to show a reduction in the band gap of Fe doped TiO_2/graphene sheets compared to commercial TiO_2. By increasing the amount of Fe, the band gap decreased to the visible region with 0.6% Fe/TiO_2 being the optimum condition found in this work, confirmed by PL spectra. Photocatalytic activity of synthesized catalysts was successfully examined by the photodegradation of model environmental endocrine disruptors (E2) under solar visible irradiation. This work suggests that the high porous, visible-light Fe-doped TiO_2/ FGSs photocatalysts have potential for the development of an environmentally sustainable treatment process using sunlight in place of an artificial light source, since visible light comprises a much larger portion of the solar spectrum than UV light.

4.6. References.

[1] R.R. Chowdhury, P. Charpentier, M.B. Ray, Industrial & Engineering Chemistry Research (2010).
[2] R.R. Chowdhury, P.A. Charpentier, M.B. Ray, Journal of Photochemistry and Photobiology A: Chemistry (2011).
[3] Y. Zhang, J. Zhou, B. Ning, Water Research 41 (2007) 19-26.
[4] X. Wang, J.C. Yu, C. Ho, Y. Hou, X. Fu, Langmuir 21 (2005) 2552-2559.
[5] I.K. Konstantinou, T.A. Albanis, Applied Catalysis B: Environmental 49 (2004) 1-14.
[6] J.R. Jennings, A. Ghicov, L.M. Peter, P. Schmuki, A.B. Walker, Journal of the American Chemical Society 130 (2008) 13364-13372.
[7] K.T. Meilert, D. Laub, J. Kiwi, Journal of Molecular Catalysis A: Chemical 237 (2005) 101-108.
[8] J. Tang, J.R. Durrant, D.R. Klug, Journal of the American Chemical Society 130 (2008) 13885-13891.
[9] G. Fu, P.S. Vary, C.-T. Lin, The Journal of Physical Chemistry B 109 (2005) 8889-8898.
[10] Y.D. Wang, GJ; Liu, H, et al., Advanced Functional Materials 18 (2008).
[11] Y. Furubayashi, T. Hitosugi, Y. Yamamoto, K. Inaba, G. Kinoda, Y. Hirose, T. Shimada, T. Hasegawa, Applied Physics Letters 86 (2005) 252101-252101-252103.
[12] J. Wang, R. Limas-Ballesteros, T. Lopez, A. Moreno, R. Gomez, O. Novaro, X. Bokhimi, The Journal of Physical Chemistry B 105 (2001) 9692-9698.
[13] Z. Ambrus, N. Balazs, T. Alapi, G. Wittmann, P. Sipos, A. Dombi, K. Mogyorósi, Applied Catalysis B: Environmental 81 (2008) 27-37.
[14] K. Nagaveni, M. Hegde, G. Madras, The Journal of Physical Chemistry B 108 (2004) 20204-20212.
[15] S. Fukahori, H. Ichiura, T. Kitaoka, H. Tanaka, Environmental science & technology 37 (2003) 1048-1051.
[16] A.M. Turek, I.E. Wachs, E. DeCanio, The Journal of Physical Chemistry 96 (1992) 5000-5007.
[17] J. Aguado, R. van Grieken, M.J. Lopez-Munoz, J. Marugán, Applied Catalysis A: General 312 (2006) 202-212.
[18] J. Matos, A. García, P.S. Poon, Journal of Materials Science (2010) 1-11.
[19] J. Matos, A. Garcia, T. Cordero, J.M. Chovelon, C. Ferronato, Catalysis Letters 130 (2009) 568-574.
[20] K. Woan, G. Pyrgiotakis, W. Sigmund, Advanced Materials 21 (2009) 2233-2239.
[21] D. Wang, D. Choi, J. Li, Z. Yang, Z. Nie, R. Kou, D. Hu, C. Wang, L.V. Saraf, J. Zhang, ACS Nano 3 (2009) 907-914.
[22] H. Zhang, X. Lv, Y. Li, Y. Wang, J. Li, ACS Nano 4 (2009) 380-386.
[23] Y.-B. Tang, C.-S. Lee, J. Xu, Z.-T. Liu, Z.-H. Chen, Z. He, Y.-L. Cao, G. Yuan, H. Song, L. Chen, L. Luo, H.-M. Cheng, W.-J. Zhang, I. Bello, S.-T. Lee, ACS Nano 4 (2010) 3482-3488.
[24] M.J. McAllister, J.L. Li, D.H. Adamson, H.C. Schniepp, A.A. Abdala, J. Liu, M. Herrera-Alonso, D.L. Milius, R. Car, R.K. Prud'homme, Chemistry of Materials 19 (2007) 4396-4404.

[25] H.C. Schniepp, J.L. Li, M.J. McAllister, H. Sai, M. Herrera-Alonso, D.H. Adamson, R.K. Prud'homme, R. Car, D.A. Saville, I.A. Aksay, The Journal of Physical Chemistry B 110 (2006) 8535-8539.
[26] I.V. Lightcap, T.H. Kosel, P.V. Kamat, Nano Letters 10 (2010) 577-583.
[27] P.V. Kamat, The Journal of Physical Chemistry Letters 1 (2009) 520-527.
[28] T.N. Lambert, C.A. Chavez, B. Hernandez-Sanchez, P. Lu, N.S. Bell, A. Ambrosini, T. Friedman, T.J. Boyle, D.R. Wheeler, D.L. Huber, The Journal of Physical Chemistry C 113 (2009) 19812-19823.
[29] R. Sui, A.S. Rizkalla, P.A. Charpentier, Crystal Growth & Design 8 (2008) 3024-3031.
[30] R.A. Lucky, P.A. Charpentier, Advanced Materials 20 (2008) 1755-1759.
[31] R.A. Lucky, P.A. Charpentier, Science of Advanced Materials 1 (2009) 167-174.
[32] R.A. Lucky, P.A. Charpentier, Applied Catalysis B: Environmental 96 (2010) 516-523.
[33] N.W. Pu, C.A. Wang, Y. Sung, Y.M. Liu, M.D. Ger, Materials Letters 63 (2009) 1987-1989.
[34] C.N. Banwell, E.M. McCash, Fundamentals of molecular spectroscopy, McGraw-Hill London, 1983.
[35] Y. Yao, G. Li, S. Ciston, R.M. Lueptow, K.A. Gray, Environmental science & technology 42 (2008) 4952-4957.
[36] G.D. Gilliland, Materials Science and Engineering: R: Reports 18 (1997) 99-399.
[37] K. Fujihara, S. Izumi, T. Ohno, M. Matsumura, Journal of Photochemistry and Photobiology A: Chemistry 132 (2000) 99-104.
[38] Y.M.-G. Nasrin Farhangi, and Paul A. Charpentier, Proc. SPIE 8007, 800721 (2011).

Chapter 5

Synthesis and photocatalytic activity of ZrO_2/TiO_2 nanomaterials on the surface of graphene sheets prepared in Supercritical CO_2

Abstract:

Functionalized Graphene Sheets (FGSs) are of tremendous current interest as supports for surface dispersion of catalyst nanoparticles to develop multifunctional mats. Semiconductors can be uniformly dispersed on these highly porous FGSs, which can help prevent sheet aggregation while extending visible light absorption and decreasing the electron-hole recombination rate resulting in enhanced photocatalytic activity. In this work, high-activity ZrO_2-TiO_2 nanostructures were grown from the surface of FGSs possessing templating carboxyl functionalities using a sol-gel method in supercritical carbon dioxide ($scCO_2$). Synthesized nanotubes with diameters less than 50 nm, nanofibers and also nanosheets were found to be dispersed on the surface of the graphene sheets. The resulting morphology depends on initial concentrations as confirmed by SEM and TEM analysis. Optical properties and surface areas of the prepared catalysts were evaluated by UV-Vis, PL spectroscopy and BET surface area and showed significant improvements compared to similarly synthesized metal oxide nanostructures without graphene. Chemical interactions between the ZrO_2-TiO_2 nanomaterials and graphene sheets were confirmed by XPS analysis. The activities of the prepared photocatalysts were characterized by UV-light induced photodegradation of 17β-estradiol (E2) in water. The experimental results revealed that the strong interphase linkage between the graphene sheets and the ZrO_2-TiO_2 nanomaterials played a significant role in improving the composite surface area from 89 up to 300 m^2/g, optical properties (band gap decreased from 3.2 to 2.9 eV) and photocatalytic activity (degradation rate increased from 0.095 to 0.23 min^{-1}). The resulting composites showed excellent activity and enhanced efficiency compared to bare TiO_2, ZrO_2-TiO_2 and TiO_2/ graphene nanostructures.

5.1. Introduction.

Titania (TiO_2) is one of the most commonly used semiconductors for pollution control in waste water systems [1]. Several attempts have been made to improve the photocatalytic efficiency of titania by various approaches including synthesizing TiO_2 nanotubes to increase surface area[2], using a metal or conductive material support to decrease its electron – hole recombination rate [3], using mesoporous supports to absorb more pollutants and prevent semiconductor agglomeration [4], doping different materials for enhancing visible light absorption [5, 6] and mixing with other metal oxides [7-9]. Among the various binary metal oxide catalysts, the combination of titania and zirconia has attracted much attention, as both catalysts and catalyst supports for a wide variety of reactions [10-13]. TiO_2 and ZrO_2 are both n-type semiconductors and exhibit excellent properties; TiO_2 acts as an active catalyst and support and ZrO_2 as an acid-base site. In all reported literature, by introducing ZrO_2 to TiO_2, the resulting nanomaterials have enhanced thermal stability, reduced crystallite size, and enhanced surface areas. These properties result in improved photocatalytic activity as efficiency strongly relies on these properties [7, 14-16] .

Previously, our group developed a direct sol-gel process using supercritical carbon dioxide ($scCO_2$) as the solvent/drying agent to synthesize TiO_2 nanofibers [17, 18], ZrO_2 nanofibers [19], and ZrO_2-modified TiO_2 nanorods and tubular structures. Ti-Zr nanostructures could be tailored by changing the operating variables with a nanotubular structure formed at metal alkoxide concentrations of 1.2 mol/L, R = 5-6, and Zr ratios between 4% and 20%. [20-22]. Lucky et al. also prepared ZrO_2 modified N-doped TiO_2 nanomaterials in $scCO_2$. The synthesized materials showed higher surface areas, smaller crystallite sizes, greater thermal stabilities and better catalytic performance compared to pure TiO_2 and N-doped TiO_2 for degradation of Methylene Blue [23].

Graphene, a monolayer of packed benzene rings has attracted tremendous interest in areas including electronics, photovoltaics, fuel cells, catalysis and medicine [24-34]. One of the most interesting applications of graphene is when used to anchor different metals and semiconductors to its surface for applications including photocatalysis and photovoltaics [35-38]. Graphene sheets with high surface areas (2600 m^2/g) are highly desirable for use as 2-D catalyst supports [30, 39-41]. Different materials can be

uniformly dispersed onto individual graphene sheets and between the pores, preventing agglomeration and enhancing the optical and surface area properties[42]. Furthermore, after reduction processes (graphite oxide to graphene), some functional groups are still available on the graphene surface which can be used for attaching different metal oxides [43]. In addition, the electrical conductivity of graphene is high and its work function is lower than most of the semiconductors, such as TiO_2 [25, 44, 45]. When graphene is in contact with semiconductors, a Schlocky barrier is formed. This allows excited electrons from the semiconductor to be easily transferred to graphene, with the resulting reduction in electron-hole recombination rate resulting in improvement of the photocatalytic activity of the assembly [46]. Several recent reports have described preparation of graphene-TiO_2 composites for applications mainly in photocatalysis and photovoltaics [47-52].

Supercritical CO_2 is an attractive solvent for the synthesis of these emerging materials as it is inexpensive, environmentally benign and non-flammable, with mild critical conditions. It is favoured for the synthesis of uniform, highly porous, ultrafine nanomaterials since it possesses “zero” surface tension, low viscosity and high diffusivity[53]. Furthermore, by $scCO_2$ washing, dry, porous structure can be obtained directly without collapsing the pores of the nonmaterials [18, 54].

In this study we have modified the properties of TiO_2 nanomaterials in two different ways; by introducing ZrO_2 into its lattice and by the synthesis of ZrO_2-TiO_2 binary oxides on the surface of graphene sheets via the sol–gel process in $scCO_2$. The morphology, crystal structure, surface area, chemical bonding and optical properties of the synthesized nanomaterials were examined, along with characterizing the photocatalytic activity using the model compound 17β-estradiol (E2), with the aim of achieving materials possessing superior photocatalytic ability compared to the corresponding materials without graphene.

5.2. Experimental.

5.2.1. Materials.

Graphite flakes nominally sized at 7-10 microns were provided from Alfa aesar, US. Fuming nitric acid (>90%), sulphuric acid (95-98%), potassium chlorate (98%), hydrochloric acid (37%), titanium (IV) isopropoxide (TIP, 97%, Aldrich), zirconium (IV) propoxide (ZPO, 70%, Aldrich), and glacial acetic acid (>99.7%), were purchased from Sigma-Aldrich Canada and used as received.

5.2.2. Synthesis.

5.2.2.1. Preparation of FGSs.

Graphite oxide was prepared using the Staudenmaier method [55] with graphite (5 g) reacted with concentrated nitric (45 mL) and sulfuric acid (90 mL) with potassium chlorate (55 g). The potassium chlorate was added slowly over 15 min to avoid sudden increases in temperature. The mixture was stirred at room temperature for more than 3 days. After reaction completion, the viscous dark green mixture was added to excess water, washed with a 5% solution of HCl, and then repeatedly washed with water until the pH of the filtrate was neutral. The prepared graphite oxide was kept in a vacuum oven at 80º C until use. Then, the graphite oxide powder was placed in a quartz tube with an inlet and outlet for continuously passing Nitrogen gas. The tube was then inserted into a tubular furnace at 1050 $^{\circ}$C for 30s, forming functionalized graphene sheets (FGSs).

5.2.2.2 Preparation of ZrO_2-TiO_2/FGSs composites via Sol-gel Chemistry. In a typical experiment, the FGSs were placed in a 10 ml high pressure view cell followed by quick addition of TIP, ZPO and acetic acid and CO_2 to the desired pressure and temperature. A magnetic stirrer was used for mixing the reaction mixture in an experimental apparatus previously described by Sui et al. for producing TiO_2 nanofibers in $scCO_2$ [17]. In our previous work, TiO_2 nanofibers were synthesized on the surface of Graphene sheets in $scCO_2$ [56]. Different TIP/ FGSs weight ratios were investigated and 1/20 was found optimized. It was also found that the mixture of FGSs/TIP, ZPO and acetic acid was miscible with CO_2 at the temperature range from 40 to the 80 °C and pressure range from 3000 to 7000 psig. The stirrer was stopped after 24 h with several days of aging required for complete reaction. After aging, the formed gel was washed continuously using 80 ml

of CO_2 at a rate of approximately 0.5 mL/min, followed by controlled venting at 0.5 mL/min to prevent collapse of the solid network. The resulting powder was then calcined in air (tubular furnace) using a heating rate of 10 °C/min at 450° C for 2 h with the calcined powder kept in a vacuum oven at 80° C.

5.2.3 Characterization.

The nanostructure morphologies of the samples were obtained from Scanning Electron Microscopy (SEM) micrographs (Model LEO 1530) and Transmission Electron Microscopy (TEM) images (Model JEOL 2010F). Samples for SEM imaging were prepared by applying the powder directly to a carbon adhesive tape. For TEM analysis, the powdered samples were dispersed in methanol by sonication and then placed on a copper grid covered with holey carbon film and dried by normal evaporation. The BET (Brunauer-Emmett-Teller) surface area was determined from nitrogen adsorption and desorption isotherm data obtained at 77 K with a constant-volume adsorption apparatus (Micromeritic Tristar II) using N_2 gas (99.995% pure; obtained from Praxair, Canada). The prepared samples were degassed at 150°C overnight before measurements. Structural analysis of the samples was performed using an X-ray powder diffractometer (Rigaku Miniflex XRD, Texas, U.S.A.), fitted with a rotating sample holder, a scintillation counter detector and a divergent beam utilizing a Cu Kα source of X-rays (λ= 1.5418 °*A*). The XPS analysis was carried out with a Kratos Axis Ultra spectrometer using a monochromatic Al K(alpha) source (15mA, 14kV). Photoluminescence spectra were carried out with a PTI Quantamaster 50 spectrophotometer with the Xenon lamp (75 V). UV spectra were performed by (Shimadzu 3600) deuterium arc lamp and two different detectors (PMT, and PbS). An integrating sphere was utilized in order to measure the diffuse reflectance of the material. Thermo-gravimetric analysis (TGA) was performed under nitrogen atmosphere on a TA Instrument TA-Q500 at a heating rate of 10 °C/min from room temperature to 1200 °C.

5.2.4. Photocatalytic Activity Measurements.

The photocataltic activity of the catalysts was determined by the photodegradation of 17β-Estradiol (E2) as a model endocrine disrupting compound under UV light irradiation using a 100W high-pressure mercury lamp (B 100 AP, UVP) with a wavelength of 365 nm. Typically, a mixture of aqueous E2 solution (5μg/L) and 0.25 g/L of catalyst was vigorously stirred for 20 min to establish an adsorption/desorption equilibrium in the dark. Then the reaction solution was irradiated under UV irradiation in an open water-jacketed vertical photo-reactor which was placed on a magnetic stirrer during all experiments, under aerated conditions. The temperature of the reactions was controlled at 22±1°C by circulating cooling water. At given time intervals, 5 mL aliquots were sampled and centrifuged to remove the particles. The filtrates were analyzed by a HPLC (ICS 300, Dionex) using an Acclaim 120 C18 reversed-phase column (150 mm × 4.6 mm i.d., 5 μm particle size, Dionex, USA). The injection volume was 40 μL from 2 mL HPLC vial, capped and sealed with PTFE lid. The mobile phase was the mixture of AcN and Milli-Q water (50:50 v/v) at a flow rate of 1 mL/min by the HPLC pump. The column temperature was maintained at 30°C and detection wavelength was set at 280 nm, the maximum absorbance of E2. The retention time of E2 in HPLC column was 5.33 min.

5.3. Results and Discussion.

Functionalized graphene sheets (FGSs) prepared in this work have several functional groups present such as carboxylate on its surface, as confirmed by XPS analysis in Chapter 3. TiO_2 and ZrO_2 can be chemically bonded to its surface during the sol-gel process. Table 5.1 summarizes the experimental conditions used for this study, presenting the resulting morphology of the ZrO_2-TiO_2/FGSs samples synthesized under various concentrations of titanium and zirconium alkoxide monomer, acetic acid (used as the polycondensate agent), temperature, and pressure in supercritical carbon dioxide ($scCO_2$) and the corresponding BET surface areas.

In Figure 5.1a, an SEM image of the FGSs powder is shown in which the high porosity of the graphene sheets is clearly observable. A paper-like structure is observed which are not completely flat, showing wrinkles on the edges. Some of the graphene sheets stack together due to van der Waals interactions [39].

The first set of experiments examined the effect of synthesis pressure on the morphology of the composites by varying the pressure from 3000 to 7000 psig, while keeping the temperature at 60 °C, the weight ratio of TIP/ FGSs at 20 (w/w), ZOP/ TIP at 0.2 (w/w) and AcOH/TIP weight ratio at 6. Increasing pressure was observed to have little effect on the resulting morphology although the surface area increased with increasing pressure, from 526 m^2/g at 3000 psig to 589 at 5000 psig. By further increasing the pressure to 7000 psig, the surface area slightly decreased to 574 m^2/g. However, the morphology of the synthesized materials was similar; with ZrO_2-TiO_2 nanotubes being formed of ~50 nm diameters uniformly spread on the surface of the graphene sheets. (Figure 5.1b, 5.1c)

Table 5.1. Physiochemical properties of ZrO_2-TiO_2/FGSs nanostructures synthesized under various conditions.

Materials	TIP/FGSs	AcOH/TIP	ZPO/TIP	P (psi)	T (° C)	Calcination T (°C)	Morphology	BET [m^2 g]
Zr-TiO_2	-----	6	0.2	5000	60	AP	nanotube	385
						450		89
$ZrTiO_2$/FGS1	20	6	0.1	5000	60	AP	nanotube on FGSs	502
						450		297
$ZrTiO_2$/FGSs2	20	6	0.2	3000	60	AP	nanotube on FGSs	526
						450		285
$ZrTiO_2$/FGSs3	20	6	0.2	5000	60	AP	nanotube on FGSs	589
						450		310
Zr-TiO_2/FGSs4	20	6	0.2	7000	60	AP	nanotube on FGSs	574
						450		294
Zr-TiO_2/FGSs5	20	6	0.2	5000	40	AP	nanotube on FGSs	532
						450		229
Zr-TiO_2/FGSs6	20	6	0.2	5000	80	AP	nanotube on FGSs	548
						450		256
Zr-TiO_2/FGSs7	40	6	0.2	5000	60	AP	nanotube on FGSs	558
						450		281
Zr-TiO_2/FGS8	20	6	0.4	5000	60	AP	nanofiber on FGSs	488
						450		204
Zr-TiO_2/FGSs9	20	3	0.4	5000	60	AP	sheets on FGSs	364
						450		74
$ZrTiO_2$/FGSs10	20	3	0.2	5000	60	AP	mix of Sheets and FGSs	420
						450		91
Zr-TiO_2/FGSs11	20	3	0.1	5000	60	AP	mix of Sheets and FGSs	349
						450		69

AP: As Prepared

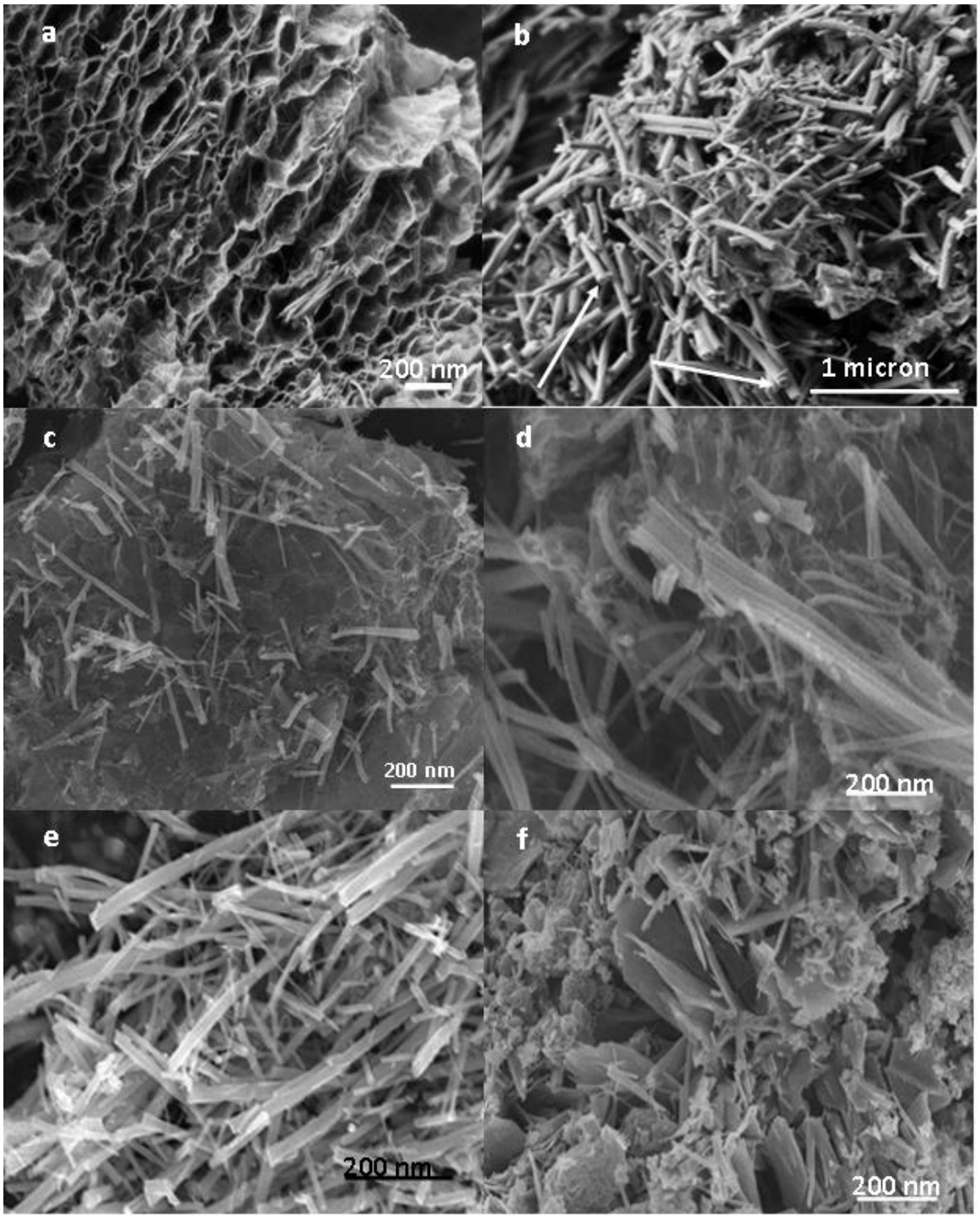

Figure 5.1. SEM: (a) FGSs, (b) Zr-TiO_2/FGSs3, (c) Zr-TiO_2/FGSs4, (d) Zr-TiO_2/FGSs5, (e) Zr-TiO_2/FGSs8, (f) Zr-TiO_2/FGSs10.

Three different temperatures (40, 60, and 80°C) were used to investigate the effect of temperature on the composites morphology at a constant pressure of 5000 psig, with the weight ratio of TIP to FGSs at 20, ZPO/ TIP at 0.2 and AcOH/ TIP weigh ratio 6, as shown in Table 5.1 (Zr-TiO_2/FGSs6, Figure 5.2d). Temperature also had a limited impact on the morphology and surface area of the prepared composites, however, 60 °C showed slightly higher surface areas.

By increasing the ZPO/ TIP weight ratio from 0.1 to 0.2 (Zr-TiO_2/FGSs 1 and 2) to 0.4, while the other parameters were kept constant, ZrO_2-TiO_2 nanofibers on the graphene sheets formed (Zr-TiO_2/FGS8, Figure 5.1.e). The surface area also decreased from 589 to 488 m^2/ g. Previously, we showed that by increasing the Zr concentration, more than 20% nanofibers formed[22]. The major parameter controlling the morphology of Zr-TiO_2/ FGSs prepared in this study was the AcOH/ TIP weight ratio. By decreasing the AcOH/ TIP weight ratio from 6 to 3 in three different ZPO/ TIP concentrations (0.1, 0.2 and 0.4), the ZrO_2-TiO_2 nanosheets (ZPO/ TIP= 0.2) randomly formed between the graphene sheets (Figure 5.1f). The surface area of these materials also decreased to 364, 420, 349 m^2/ g respectively. Figure 5.2 shows the N_2 adsorption isotherms for TiO_2 (Figure. 5.2a), ZrO_2-TiO_2 nanotubes on graphene (Figure 5.3c) and without graphene sheets, which exhibit type IV isotherms. By introducing ZrO_2 to the TiO_2 lattice, the N_2 adsorption increased resulting in higher surface areas as shown in Table 5.1. By further modifying the ZrO_2-TiO_2 nanotubes and preparing them on the surface of graphene sheets, N_2 adsorption significantly increased.

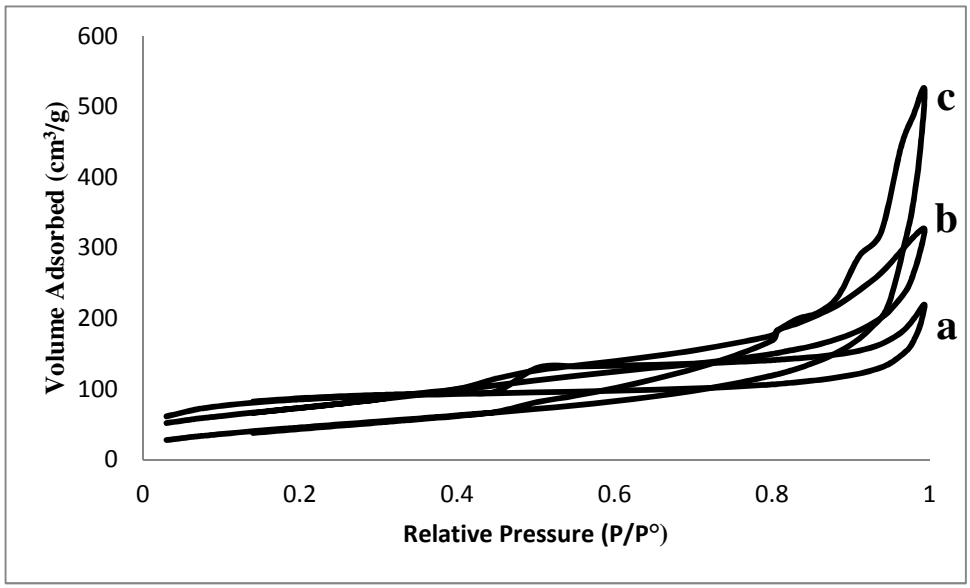

Figure 5.2. N_2 adsorption/desorption isotherm of the TiO_2 (a), Zr-Ti oxides (b) and Zr-Ti oxides on the surface of graphene sheets (Zr-TiO_2/FGS3) (c) prepared in $scCO_2$.

In the TEM images of the ZrO_2-TiO_2 nanotube/graphene assemblies, nanotube diameters less than 50 nm are randomly spread on the graphene sheets. (Figure 5.3a) The presence of graphene is not obvious in the low resolution TEM images resulting from the thin layer of FGSs which are dissolved in methanol during sample preparation. However, in the HRTEM micrographs shown in Figure 5.3, the lattice image of ZrO_2-TiO_2/FGSs calcined at 450 ^oC shows uniform dispersion of two different nanomaterials ; TiO_2 and ZrO_2; The 'd' value of 0.35 nm matches with anatase TiO_2 (101) while the 'd' value of 0.295 nm matches very well with that of the (111) lattice spacing of tetragonal zirconia [57]. These results are in good agreement with the XRD results, as described below. Significant amorphous area is detected in the HRTEM spectra which correspond to the presence of graphene sheets in the composites.

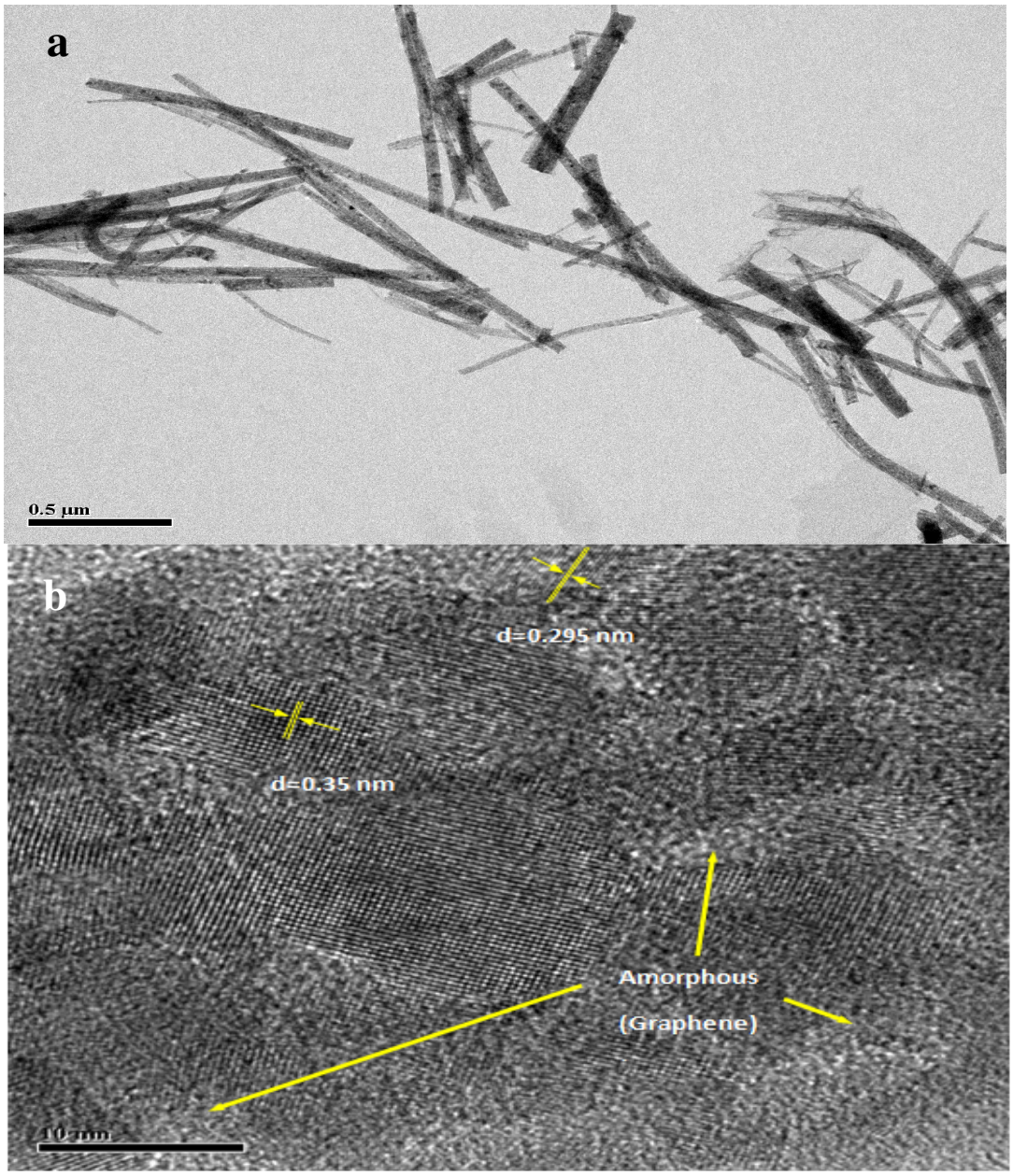

Figure 5.3. TEM ZrO_2-TiO_2/FGSs2 calcined at 450 ° C (a) 500 nm scales, (b) 50 nm scales, (c) HRTEM images of ZrO_2-TiO_2/FGS3 calcined at 450° C.

Figure 5.4 shows the XRD patterns of different concentrations of ZrO_2-TiO_2/FGSs calcined at 450° C. These results show that when the weight ratio of ZPO/ TIP is 0.1 (Zr-TiO_2/FGS1), only TiO_2 anatase can be detected. This means that the addition of a small amount of ZrO_2 did not change the structure of TiO_2 (anatase). By increasing the amount

of ZPO/TIP to 0.2 (Zr-TiO_2/FGS3), TiO_2 is still in the anatase phase with the main tetragonal peak appearing at 2θ equal 30.0, corresponding to the diffraction patterns of (101). By further increasing the ZPO/ TIP ratio to 0.4 (Zr-TiO_2/FGS8) in addition to the previous peak in which nanofibers formed on the graphene sheets, new small peaks appeared at 2θ equal 50.4 and 60.0. These correspond to the diffraction patterns of (1 1 2) and (2 1 1), respectively, of the pure tetragonal phase of ZrO_2 [57]. Lucky et al. prepared ZrO_2-TiO_2 nanotubes in $scCO_2$ with anatase crystallity at all initial concentrations [58]. These results indicate that in the presence of graphene, both TiO_2 and ZrO_2 anchor to the functional groups on the surface of the graphene sheets while producing a sheet of mixed oxides which then rolls-up, similarly forming a tube during the $scCO_2$ drying process. These XRD results confirm the presence of ZrO_2 in the nanotubes, with this result in agreement with the HRTEM results.

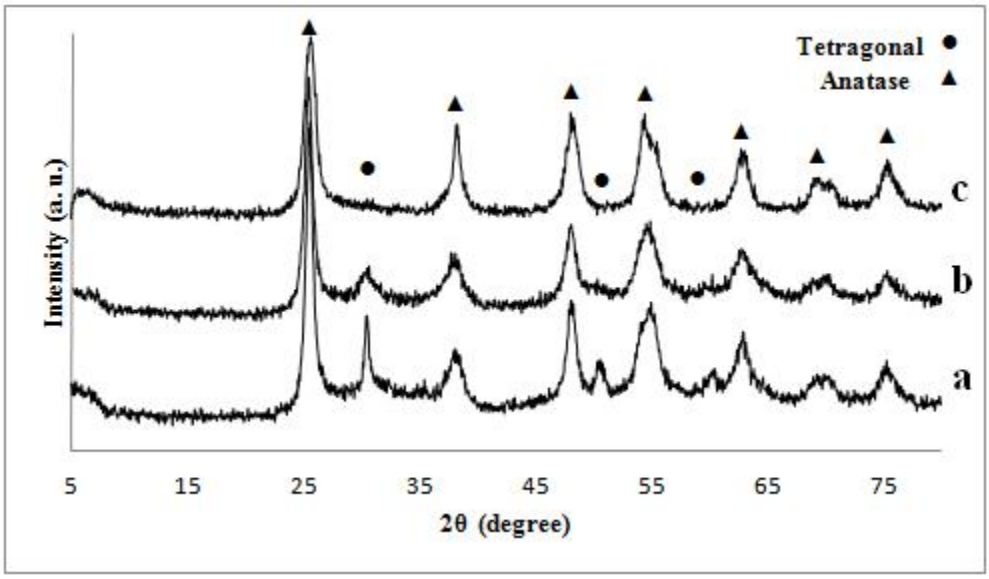

Figure 5.4. XRD pattern of (a) Zr-TiO_2/FGSs8, (b) Zr-TiO_2/FGSs3, (c) Zr-TiO_2/FGSs1 naomaterials, all prepared in $scCO_2$ and calcined at 450° C.

Figure 5.5 shows the UV-visible diffuse reflectance spectra of pure TiO_2, ZrO_2-TiO_2 binary oxide and different ZrO_2-TiO_2/FGSs catalysts prepared in $scCO_2$ and calcined at 450° C. By addition of ZrO_2 to TiO_2, a smooth blue shift of the absorption edge of the catalysts towards lower wavelength regions of light is observed, as shown in Figure. 5.5e.

By adding graphene to the system, more visible light absorption and an obvious red shift in the absorption edge of ZrO_2-TiO_2/FGSs can be observed (Figure 5.5 b,c,d), in comparison to bare TiO_2 (Figure 5.5a) and ZrO_2-TiO_2 (Figure 5.5e). This reduction in band gap is attributed to enhanced electron hole recombination between ZrO_2-TiO_2 and the graphene sheets. Different concentrations of FGSs and also ZPO/ TIP ratios slightly change the visible light absorption; however, the red shift in the UV spectra is almost the same for all prepared catalysts as shown in Figure 5.5. This narrowing can also be related to the chemical bonding between TiO_2 and ZrO_2 with graphene sheets and the formation of Ti-O-C bond Zr-O-C, similar to the case of carbon doped TiO_2 composites [59, 60]. Zhang et al. prepared P25 on the surface of graphene sheets by using a hydrothermal method and observed an absorption edge of P25-graphene, compared to bare P25 according to physical and chemical interactions between them [49]. Gold nanoparticles were also decorated on the surface of graphene by Goncalves [35] and Jasuia et al [61] which resulted in a significant improvement in the UV-Vis spectra of the nanoparticles. They also showed that the oxygen functionalities on the graphene surface act as reactive sites for the nucleation and growth of gold nanoparticles.

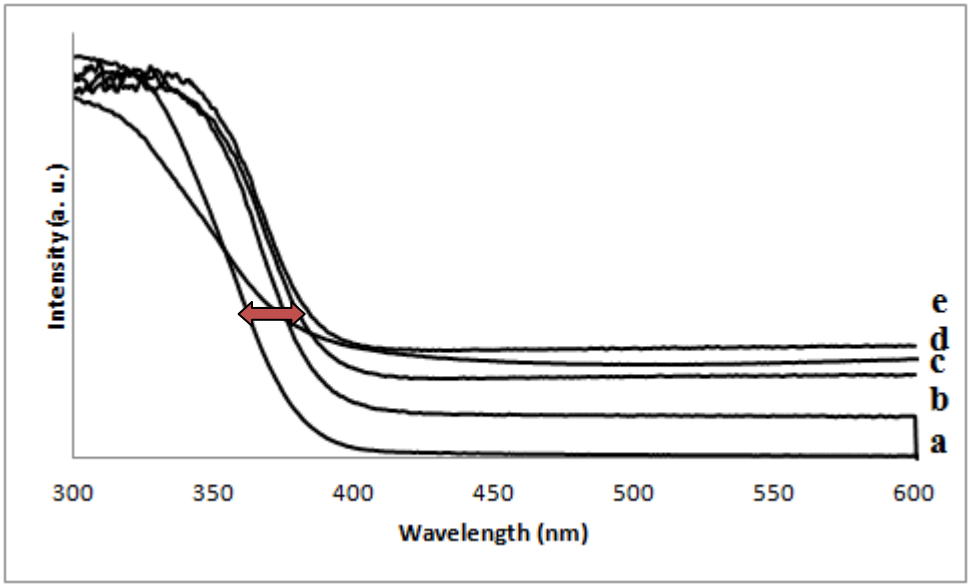

Figure 5.5. UV-vis spectra of (a) TiO_2, (b) Zr-TiO_2/FGSs3, (c) Zr-TiO_2/FGSs7, (d) Zr-TiO_2/FGSs8, (e) TiO_2-ZrO_2 nanomaterials, all prepared in $scCO_2$, calcined at 450° C.

Figure 5.6 compares the PL spectra of the TiO_2 nanowires, TiO_2/FGSs and ZrO_2-TiO_2/ FGSs nanomaterials prepared in $scCO_2$. The excitation wavelength used for analysis was 473 nm. The main peak of TiO_2 is located at about 540 nm under this excitation [62]. These results indicate that the PL intensity of TiO_2 nanowires is higher than all other composites. By synthesising TiO_2 nanowires on the surface of the graphene sheets, the intensity of the PL spectra decreased. The introduction of graphene improves the surface quality of TiO_2, reducing the density of trap states, which is generally considered to enhance the exciton lifetimes. When ZrO_2-TiO_2 metal oxides were prepared on the surface of graphene sheets, the PL intensity further decreased due to a reduction in the density of trap states. Excited electrons in both TiO_2 and ZrO_2 can be transferred to the graphene sheets, giving more stable holes in the mixture of semiconductors which causes the observed reduction in PL intensity.

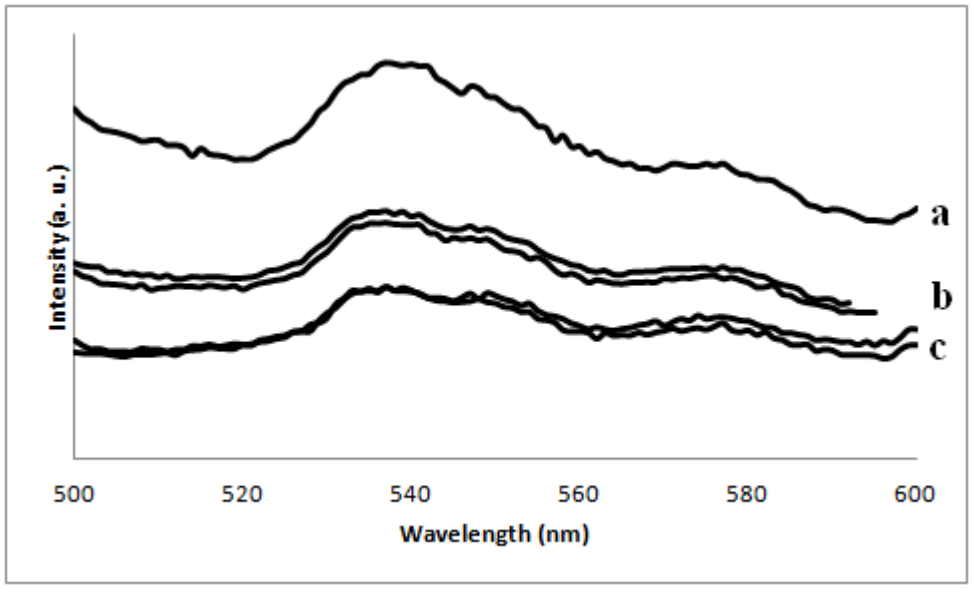

Figure 5.6. Photoluminescence spectra of (a) TiO_2, (b) TiO_2/ FGSs, (c) ZrO_2- TiO_2/ FGSs, all prepared in $scCO_2$ and calcined at 450° C.

TGA analysis was also carried out to study the thermal decomposition behaviour of the synthesized ZrO_2-TiO_2/graphene nanostructures. The results of TGA for calcined TiO_2, FGSs, TiO_2/ FGSs, ZrO_2- TiO_2 on graphene and without graphene are shown in Figure 5.7. There are three decomposition stages for TiO_2 which are in the ranges: (i) 25–125^oC, (ii) 125–500^oC and more than (iii) 500^oC. In the TGA curve of TiO_2 (Figure 5.7a), the weight loss below 120°C is about 5 %, which is attributed to the loss of absorbed water. Besides, there is a mass loss for TiO_2 in the temperature range of 120–1200°C, suggesting the presence of unreacted Ti precursor in the sample [63]. After reacting TiO_2 with FGSs (Figure 5.7c), the weight loss of the sample is greatly restricted. TiO_2 nanowires immobilized on the surface of FGSs can act as a template with carboxylate groups, resulting in homogeneous weight loss in the TGA spectrum. This indicates that there is a strong interaction between FGSs and TiO_2 and the amount of unreacted Ti precursor and acetic acid in the reaction were significantly decreased. By introducing ZrO_2 to the TiO_2 lattice, the samples became more condensed compared to TiO_2 as previously observed and its thermal stability increased with only 9% weight loss achieved (Figure 5.7d). By further modification and immobilizing ZrO_2-TiO_2 on the surface of the graphene sheets, the weight loss decreased to just 5% (Figure 5.7e). Based on the XPS results (described below), it is apparent that graphene acts as a template for ZrO_2- TiO_2 growth, in which the bimetallic metal oxide is chemically bonded to the surface of graphene, which provides enhanced thermal stability to 1200° C.

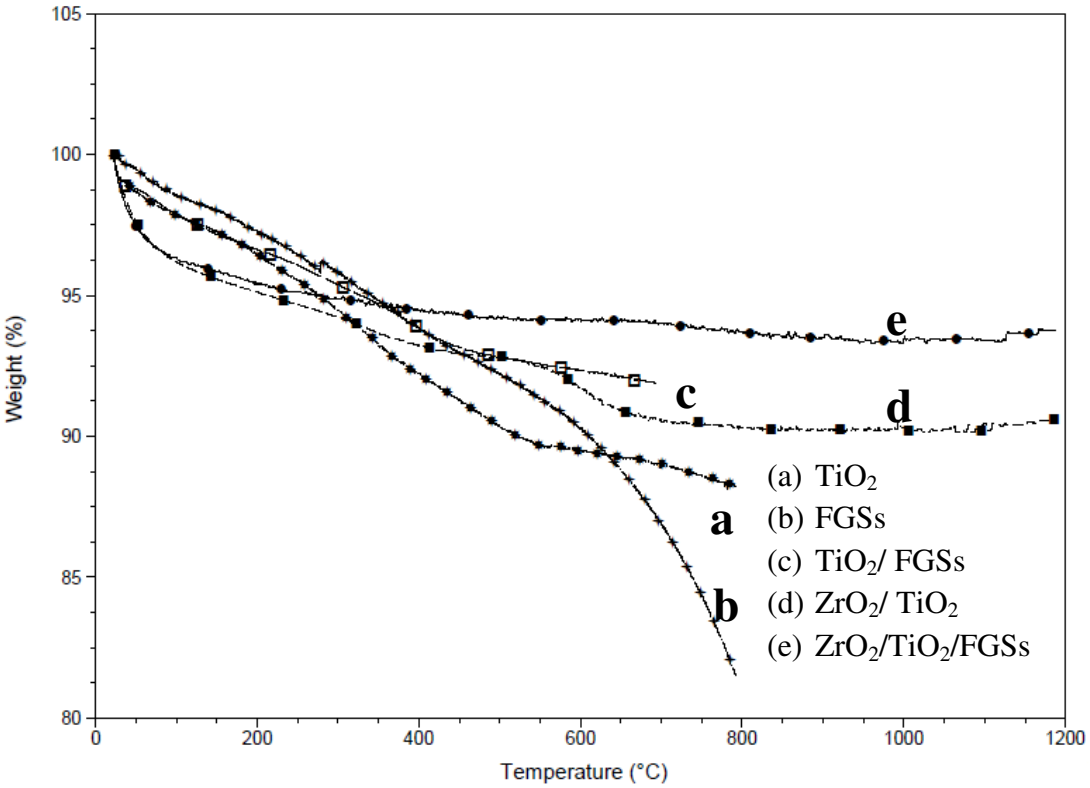

Figure 5.7. TGA spectra of (a) TiO_2, (b) FGSs, (c) TiO_2/ FGSs, (d) ZrO_2- TiO_2 and (d) ZrO_2-TiO_2/ FGSs calcined at 450 °C.

The chemistry of titanium alkoxides reacting with acetic acid in conventional solvents is reasonably well understood. Doeuff et al. explained the formation of the Ti hexamer complex through modification, esterification, hydrolysis and condensation.[64] Sui et al., [15] proposed a mechanism for the formation of titania nanofibers in $scCO_2$ using acetic acid where the titania formed a $Ti_6O_6(OPri)_6(OAc)_6$ hexamer (Figure 5.8a), which was the proposed building block for formation of the titania nanofibers. ZrO_2–TiO_2 nanotubes were also prepared in this work by using the mixed sol-gel chemistry of zirconium propoxide and titanium isopropoxide with acetic acid in $scCO_2$. To investigate the nanotube formation, different amounts of AcOH were reacted with the Ti(IV) and Zr(IV) precursors in $scCO_2$. From the XPS results, we found that the Zr/Ti molar ratio is about 1/5 in the nanotubes. Given the fact that as Ti(IV) has a dominant concentration compared to Zr(IV), it can be rationalized that as Zr(IV) is incorporated into the Ti(IV) hexanuclear structure, the building block of the nanotubes is $Ti_5ZrO_6(OAc)_6(OPr^i)_6$ (Figure 5.8b).

During the $scCO_2$ washing process that is intended to remove the organic species (e.g., excess AcOH, and by–products: alcohol and esters), the solvation effect for stabilization of the nanostructures decreases. Thus, the interfacial tension of the nanosheets increases and helps drive the sheets to roll into nanotubes.

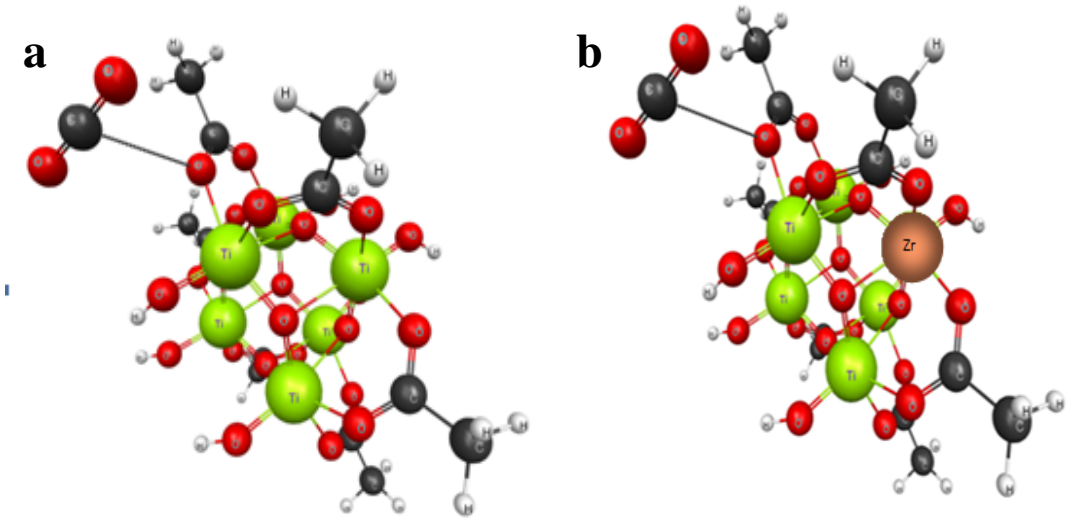

Figure 5.8. $Ti_6O_6(OPri)_6(OAc)_6$, building block of TiO_2 nanofiber, (b) $Ti_5ZrO_6(OAc)_6(OPri)_6$,building block of ZrO_2-TiO_2 nanotubes. (Ti = green, O = red, C = black, H = grey, Zr = orange).Reprint with permission from ref [65]. Copyright 2009 American Chemistry Society.

The reaction of ZrO_2-TiO_2 nanomaterials on the surface of graphene can be written as the following sol gel process;

$$(Zr\ (OR)_4)_p + (Ti(OR)_4)_m + \text{graphene} -(COOH)_n \longrightarrow \text{graphene} -(COO^-)_n\ (Ti\ (OR)_{4-x})_m\ (Zr\ (OR)_{4-y})_p + (x+y)\ ROH$$

$$\text{graphene} -(COO^-)_n\ (Ti\ (OR)_{4-x})_m (Zr\ (OR)_{4-y})_p + q\ AcOH$$

$$\downarrow$$

$$\text{graphene-}(COO^-)_n (Ti\ (AcO)_q (OR)_{4-x-q})_m\ (Zr\ (AcO)_q\ (OR)_{4-y-q})_p + qROH$$

$$ROH + AcOH \rightleftharpoons ROAc + H_2O$$

$$\text{graphene-}(COO^-)_n (Ti\ (AcO)_q (OR)_{4-x-q})_m\ (Zr\ (AcO)_q\ (OR)_{4-y-q})_p$$

$$\downarrow \quad \textbf{Hydrolysis}$$

$$\downarrow \quad \textbf{Oxiation}$$

$$\text{graphene-}(COO^-)_n\ (TiO_2\text{-}ZrO_2)_{m+p}$$

First, both the Zr and Ti precursors react with carboxylate groups on the graphene sheets. Next, an excess amount of acetic acid reacts with the precursors attached to the graphene sheets. After hydrolysis and oxidation, ZrO_2-TiO_2 nanomaterials are formed on the surface of the graphene sheets.

For further analysis of the chemical structure of the investigated samples, five areas of the deconvoluted XPS spectrum for the ZrO_2–TiO_2 on the graphene sheets were examined i.e. for sample Zr-TiO_2/FGS3, the following peaks were identified: Ti2p around 455.85 eV, Zr 3d around 179.35 eV, O 1s around 527.25 eV and the C 1s around 282.25 eV region (Figure 5.9). The weight ratio of Zr/Ti in this complex is about 1/5 (confirmed by XPS) indicating $Ti_5ZrO_4(OAc)_{10}(OPr^i)_6$ as the major building block for nanotube formation. The reported binding energies are 458.8 and 183 eV for pure Ti 2p3/2 and pure Zr 3d5/2 respectively [66]. Introducing Zr to the TiO_2 matrix causes shifting of the binding energy of Ti 2p3/2 and Zr 3d5/2 to lower energies. For example, in sample ZrO_2-TiO_2/FGSs3, the binding energy of Ti $2p_{3/2}$ and Zr $3d_{5/2}$ were 458.72 and 182.30 eV, respectively. This binding energy shift might be attributed to the presence of Zr in the

matrix and the formation of Zr-O-Ti bonding by changing the electronic environment as well as the binding energy. This analysis indicates that Zr atoms were substituted for some Ti atoms in the TiO_2 lattice. Similar results were observed by Lucky and Reddy et al [67, 68]. On the other hand, by comparison between the XPS spectra of FGSs and ZrO_2-TiO_2 on the surface of the graphene sheets, high resolution XPS of C1s showed four different peaks at 284.7, 286.2, 287.7 and 289.25 eV. These correspond to (C-C, C=C), (C-H), (C-OH, C-O-C) and C=O functionalities, respectively. Akhavan et al. studied the XPS spectra of graphite oxide and thermal expanded graphene sheets at different temperatures and reported similar results [69]. In high resolution of the C1s peak of TiO_2-ZrO_2 on the graphene sheets (Figure 5.10), four different peaks of FGSs were identified with small shifts to 284.8, 286.3, 287.8 and 288.9 eV, indicating interaction of TiO_2 and ZrO_2 with the graphene sheets. However, the intensity of peaks which represent C=O and C-OH decreased and the O1s peak at 533.40 eV corresponding to O-H disappeared. The peak at 531.38 eV corresponding to the carbonyl group is still evident. Interestingly, it seems that all OH groups reacted with TiO_2-ZrO_2, leaving no free OH on the surface of the synthesized materials. A new peak appeared at 530.25 eV which is assigned to the oxygen of TiO_2-ZrO_2. All these data correspond to the bridging structure of TiO_2-ZrO_2 with carboxyl groups on the surface of the FGSs.

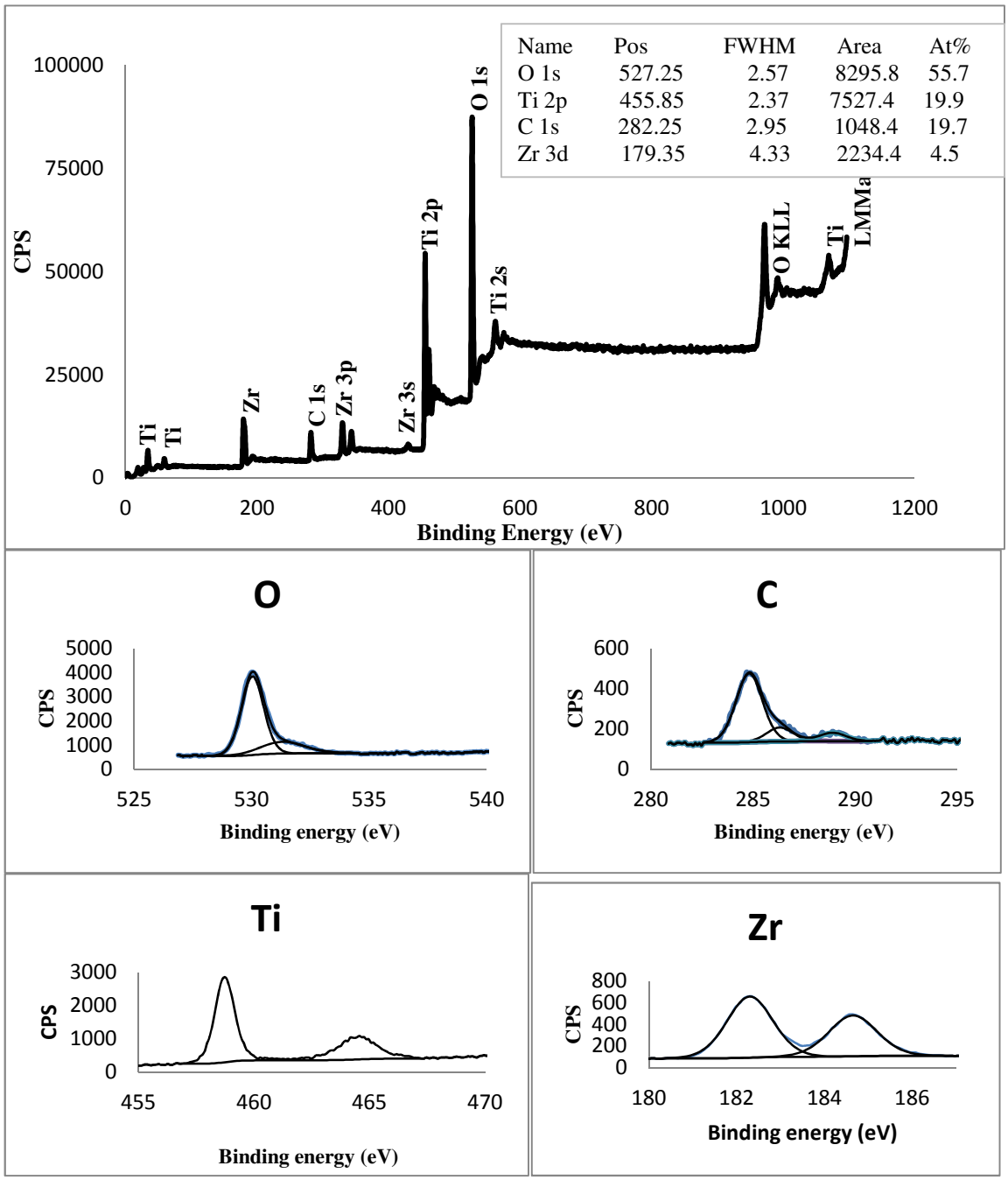

Figure 5.9. Typical XPS spectrum for Zr modified TiO_2 nanotubes calcined at 450 °C. Deconvoluted XPS spectrum for C, O, Ti and Zr in Zr modified TiO_2 nanotubes calcined at 450°C.

5.4. Photocatalytic performance.

The photocatalytic activity of TiO_2, ZrO_2-TiO_2 nanotubes and different ZrO_2-TiO_2/ FGSs nanostructures was evaluated under UV irradiation (λ= 365 nm) by photodegradation of E2 (17β-estradiol), as a model endocrine disrupting compound. The photodegradation kinetics of Zr-TiO_2/FGSs3 are shown in Figure 5.10. The experiments in the presence of photocatalyst illustrate that 20 min was sufficient to reach the adsorption equilibrium. The degradation of E2 could occur because of photocatalytic reactions in the presence of catalyst under UV irradiation with a wavelength 365 nm, with E2 almost completely degraded in less than 120 min. The photocatalytic degradation followed pseudo-first-order reaction kinetics in the studied concentration range, as developed in Chapter 4. Similarly, these results are consistent in following the Langmuir–Hinshelwood model.

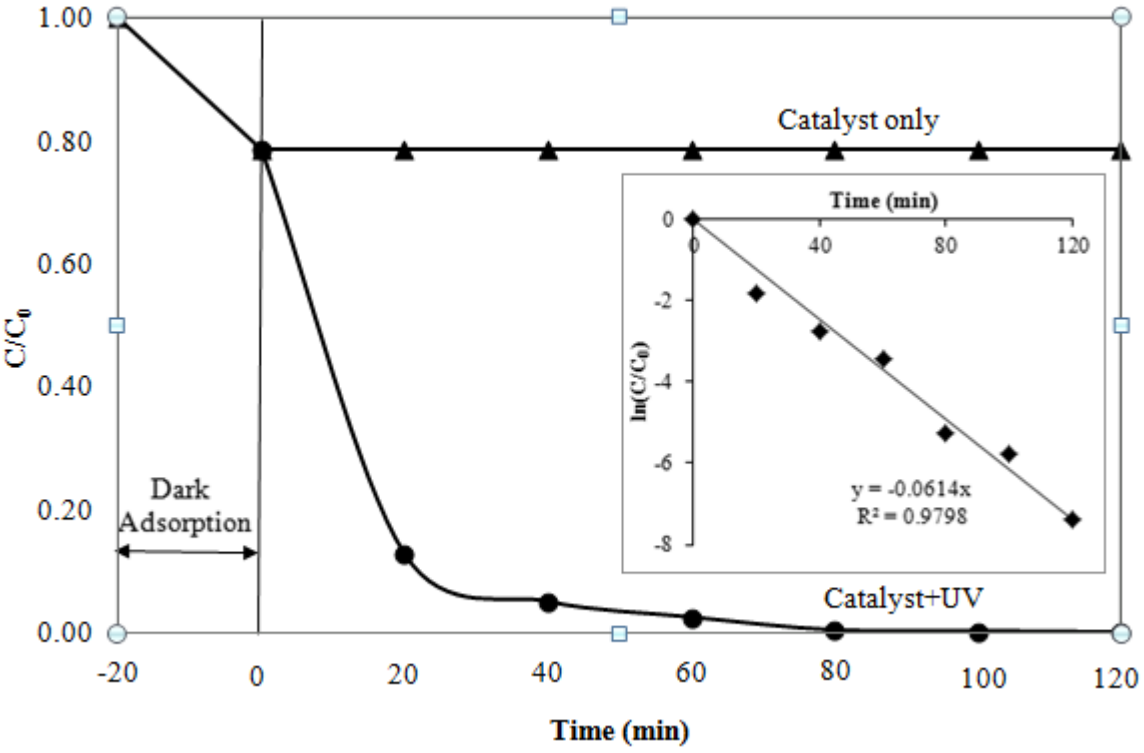

Figure 5.10. Photocatalytic degradation of E2 with the Zr-TiO_2/FGSs3 under UV irradiation ((λ=365 nm). = 5 µg/L and irradiation time = 2 hours.

The determined degradation rates are compared in Figure 5.11. The degradation rate for pure TiO_2 was 0.027 min^{-1} and this value increased by 33% to (k= 0.036 min^{-1}) by introducing ZrO_2 into the TiO_2 lattice. Usually, when two different kinds of

semiconductors are in direct contact with one another, the interface between them may act as a rapid separation site for photogenerated electrons and holes due to difference in their energy levels (conduction bands and valence bands). This results in reducing the recombination of electrons and holes and enhancing their photocatalytic activity [16]. However, the TiO_2 prepared on the graphene sheets showed significantly higher photocatalytic activity compared to bare TiO_2, with k= 0.047 min^{-1} i.e. double that of without graphene. In explanation, the highly porous graphene nanostructure provides the capability to adsorb pollutants. As well, TiO_2 photogenerated electrons can be easily transported to the conductive graphene nanosheets, strongly reducing the recombination of electrons and holes, resulting in an enhancement in the photcatalytic activity[70]. By preparing ZrO_2-TiO_2 on the graphene surface, e.g. for sample Zr-TiO_2/FGSs8 which contains nanofibers on graphene sheets with a surface area of 204 m^2/g, the rate constant for photodegradation increased to 0.051 min^{-1}, i.e. 2.4 times higher than that of TiO_2. It seems that both ZrO_2 and graphene help to increase the lifetime of photogenerated electrons in these composites, further increasing the rate constant. When ZrO_2-TiO_2 nanotubes (sample Zr-TiO_2/FGSs3) were prepared on the graphene sheets, the surface area increased to 310 m^2/g, followed by increasing the rate constant to 0.0614 min^{-1} which is 2.8 time higher than that of bare TiO_2. The observed enhancement in photocatalytic performance of the bimetallic nanotubes can be explained by the higher surface area of the prepared catalysts. Higher surface areas with mesoporous structure favors the adsorption of reactant molecules, as well as light absorbance. Graphene sheets are aromatic molecules with some defective sites including –COOH, -OH, -C=O as shown by the XPS results. As E2 is an aromatic pollutant, these chemical similarities will result in various chemical and physical interactions with graphene □s surface functionalities. On the other hand, ZrO_2- TiO_2 oxides also have chemical interactions with graphene as shown in the XPS and UV sections. This would allow the E2 molecules to be stabilized on the graphene surface, enhancing degradation by the ZrO_2-TiO_2 photocatalyst. On the other hand, there is a space-charge region between TiO_2, ZrO_2 and graphene. After UV irradiation, excited electrons in both TiO_2 and ZrO_2 can be transferred to graphene, with any holes remaining on the metal oxide surface taking part in the photocatalysis reaction. This mechanism is consistent with that described by

Hoffmann and co-workers to describe the observed enhancement in the photocatalytic activity of CNT-TiO_2 composites [71].

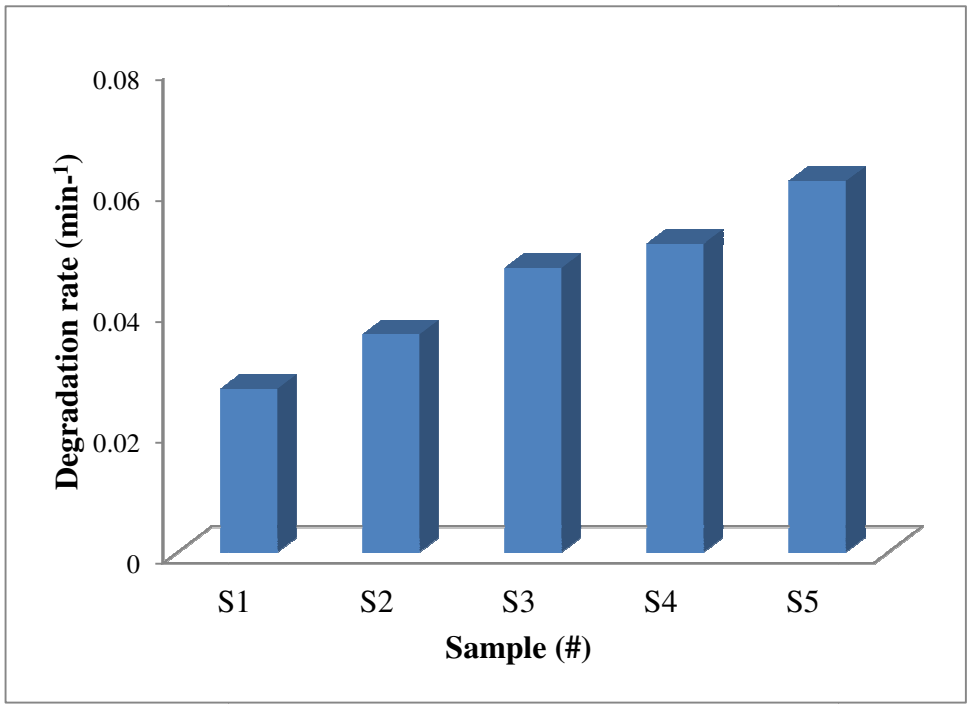

Figure 5.11. The photodegradation rate constant of (E2) using TiO_2 S1, ZrO_2- TiO_2 nanotubes S2, TiO_2 /FGSs composites S3, Zr-TiO_2/FGSs8 S4 and Zr-TiO_2/FGSs3 S5.

5.5. Conclusion.

High performance ZrO_2-TiO_2 nanostructured materials having both fiber and tubular morphology on the surface of graphene sheets were successfully synthesized via a one-step sol-gel method in $scCO_2$. The bimetallic morphology could be tailored by changing the operating variables, with nanotubes only formed in a narrow experimental window with Zr precursor concentrations less than 20% (of Ti alkoxide precursors) and the AcOH/TIP concentration between 5-6 [22]. The synthesized catalysts showed higher photocatalytic activity compared to bare TiO_2 and TiO_2/graphene sheets. Nanoassemblies having ZrO_2-TiO_2 nanotubes on graphene sheets showed the highest photocatalytic activity, which was 2.8 times higher than that of TiO_2 alone. When the metal oxides and graphene are in direct contact with one another, excited electrons from the semiconductors are transfered to the conduction band of graphene, reducing the electron-

hole recombination rate. As well, by decreasing agglomeration of the nanomaterials, the photocatalytic activities were enhanced. Moreover, graphene with its aromatic structure can absorb aromatic pollutants on its surface through both physical and chemical interactions, helping the synthesized assemblies degrade them more efficiently. The UV-VIS and PL results showed that the graphene assemblies can absorb more visible light and slightly shift the absorption spectra to the visible area. This work suggests that highly porous and active graphene based catalysts are suitable candidates for further investigation.

5.6. References.

[1] K. Vinodgopal, D.E. Wynkoop, P.V. Kamat, Environmental Science & Technology 30 (1996) 1660-1666.
[2] T. Kasuga, M. Hiramatsu, A. Hoson, T. Sekino, K. Niihara, Langmuir 14 (1998) 3160-3163.
[3] W. Choi, A. Termin, M.R. Hoffmann, The Journal of Physical Chemistry 98 (1994) 13669-13679.
[4] B. Tryba, A.W. Morawski, M. Inagaki, Applied Catalysis B: Environmental 41 (2003) 427-433.
[5] C. Burda, Y. Lou, X. Chen, A.C.S. Samia, J. Stout, J.L. Gole, Nano Letters 3 (2003) 1049-1051.
[6] N. Serpone, The Journal of Physical Chemistry B 110 (2006) 24287-24293.
[7] X. Fu, L.A. Clark, Q. Yang, M.A. Anderson, Environmental Science & Technology 30 (1996) 647-653.
[8] P.A. Connor, K.D. Dobson, A.J. McQuillan, Langmuir 11 (1995) 4193-4195.
[9] B. Olthof, A. Khodakov, A.T. Bell, E. Iglesia, The Journal of Physical Chemistry B 104 (2000) 1516-1528.
[10] B.M. Reddy, B. Chowdhury, P.G. Smirniotis, Applied Catalysis A: General 211 (2001) 19-30.
[11] M.E. Zorn, D.T. Tompkins, W.A. Zeltner, M.A. Anderson, Applied Catalysis B: Environmental 23 (1999) 1-8.
[12] J. Fling, I. Wang, Journal of Catalysis 130 (1991) 577-587.
[13] H. Zou, Y.S. Lin, Applied Catalysis A: General 265 (2004) 35-42.
[14] B. Reddy, A. Khan, ChemInform 36 (2005) no-no.
[15] B. Neppolian, Q. Wang, H. Yamashita, H. Choi, Applied Catalysis A: General 333 (2007) 264-271.
[16] X. Wang, J.C. Yu, Y. Chen, L. Wu, X. Fu, Environmental Science & Technology 40 (2006) 2369-2374.
[17] R.R. Sui, A. S. and Charpentier, P. A. , Langmuir 21 (2005) 6150- 6153.
[18] R. Sui, A.S. Rizkalla, P.A. Charpentier, Langmuir 21 (2005) 6150-6153.
[19] R. Sui, A.S. Rizkalla, P.A. Charpentier, Langmuir 22 (2006) 4390-4396.
[20] R.A.a.C.P.A. Lucky, Advanced materials 20 (2008) 1755-1759

[21] R.A. Lucky, R. Sui, J.M.H. Lo, P.A. Charpentier, Crystal Growth & Design 10 (2010) 1598-1604.
[22] R.A. Lucky, Y. Medina-Gonzalez, P.A. Charpentier, Langmuir 26 (2010) 19014-19021.
[23] R.A.a.C. Lucky, P. A., Applied Catalysis B: Environmental 96 (2010) 516–523.
[24] A.K. Geim, K.S. Novoselov, Nat Mater 6 (2007) 183-191.
[25] A.A. Balandin, S. Ghosh, W. Bao, I. Calizo, D. Teweldebrhan, F. Miao, C.N. Lau, Nano Letters 8 (2008) 902-907.
[26] C. Xu, X. Wang, J. Zhu, The Journal of Physical Chemistry C 112 (2008) 19841-19845.
[27] P. Avouris, Nano Letters 10 (2010) 4285-4294.
[28] X. Yan, X. Cui, B. Li, L.-s. Li, Nano Letters 10 (2010) 1869-1873.
[29] P.W. Sutter, J.-I. Flege, E.A. Sutter, Nat Mater 7 (2008) 406-411.
[30] B. Seger, P.V. Kamat, The Journal of Physical Chemistry C 113 (2009) 7990-7995.
[31] A.K. Geim, Science 324 (2009) 1530-1534.
[32] S. Gilje, S. Han, M. Wang, K.L. Wang, R.B. Kaner, Nano Letters 7 (2007) 3394-3398.
[33] K.V. Emtsev, A. Bostwick, K. Horn, J. Jobst, G.L. Kellogg, L. Ley, J.L. McChesney, T. Ohta, S.A. Reshanov, J. Rohrl, E. Rotenberg, A.K. Schmid, D. Waldmann, H.B. Weber, T. Seyller, Nat Mater 8 (2009) 203-207.
[34] K.S. Kim, Y. Zhao, H. Jang, S.Y. Lee, J.M. Kim, K.S. Kim, J.-H. Ahn, P. Kim, J.-Y. Choi, B.H. Hong, Nature 457 (2009) 706-710.
[35] G. Goncalves, P.A.A.P. Marques, C.M. Granadeiro, H.I.S. Nogueira, M.K. Singh, J. Grácio, Chemistry of Materials 21 (2009) 4796-4802.
[36] R. Muszynski, B. Seger, P.V. Kamat, The Journal of Physical Chemistry C 112 (2008) 5263-5266.
[37] G. Williams, B. Seger, P.V. Kamat, ACS Nano 2 (2008) 1487-1491.
[38] C. Zhu, S. Guo, Y. Zhai, S. Dong, Langmuir 26 (2010) 7614-7618.
[39] M.J. McAllister, J.L. Li, D.H. Adamson, H.C. Schniepp, A.A. Abdala, J. Liu, M. Herrera-Alonso, D.L. Milius, R. Car, R.K. Prud'homme, Chemistry of Materials 19 (2007) 4396-4404.
[40] P.V. Kamat, The Journal of Physical Chemistry Letters 1 (2009) 520-527.
[41] E. Yoo, T. Okata, T. Akita, M. Kohyama, J. Nakamura, I. Honma, Nano Letters 9 (2009) 2255-2259.
[42] I.V. Lightcap, T.H. Kosel, P.V. Kamat, Nano Letters 10 (2010) 577-583.
[43] H.C. Schniepp, J.-L. Li, M.J. McAllister, H. Sai, M. Herrera-Alonso, D.H. Adamson, R.K. Prud'homme, R. Car, D.A. Saville, I.A. Aksay, The Journal of Physical Chemistry B 110 (2006) 8535-8539.
[44] R. Ramprasad, P.v. Allmen, L.R.C. Fonseca, Physical Review B 60 (1999) 6023.
[45] Y.-J. Yu, Y. Zhao, S. Ryu, L.E. Brus, K.S. Kim, P. Kim, Nano Letters 9 (2009) 3430-3434.
[46] E. Bekyarova, M.E. Itkis, P. Ramesh, C. Berger, M. Sprinkle, W.A. de Heer, R.C. Haddon, Journal of the American Chemical Society 131 (2009) 1336-1337.
[47] Y. Zhang, Z.-R. Tang, X. Fu, Y.-J. Xu, ACS Nano 4 (2010) 7303-7314.
[48] Y. Qiu, K. Yan, S. Yang, L. Jin, H. Deng, W. Li, ACS Nano 4 (2010) 6515-6526.
[49] H. Zhang, X. Lv, Y. Li, Y. Wang, J. Li, ACS NANO 4 (2009) 380-386.

[50] C. Chen, W. Cai, M. Long, B. Zhou, Y. Wu, D. Wu, Y. Feng, ACS Nano 4 (2010) 6425-6432.
[51] O. Akhavan, M. Abdolahad, A. Esfandiar, M. Mohatashamifar, The Journal of Physical Chemistry C 114 (2010) 12955-12959.
[52] J. Liu, H. Bai, Y. Wang, Z. Liu, X. Zhang, D.D. Sun, Advanced Functional Materials 20 (2010) 4175-4181.
[53] K.P. Johnston, P.S. Shah, Science 303 (2004) 482-483.
[54] H. Wakayama, Y. Fukushima, Industrial & Engineering Chemistry Research 39 (2000) 4641-4645.
[55] L. Staudenmaier, Ber. Dtsch. Chem. Ges. 31 (1898) 1481.
[56] Nasrin Farhangi, Yaocihuatl Medina-Gonzalez, Rajib Roy Chowdhury, P.A. Charpentier, Nanotechnology Submitted (2011).
[57] S.K. Maity, M.S. Rana, S.K. Bej, J. Ancheyta-Juárez, G. Murali Dhar, T.S.R. Prasada Rao, Catalysis Letters 72 (2001) 115-119.
[58] R.A.l.M.-G. Lucky, Y. and Charpentier, P. A., Langmuir 26 (2010) 19014–19021.
[59] S. Sakthivel, H. Kisch, Angewandte Chemie International Edition 42 (2003) 4908-4911.
[60] W. Ren, Z. Ai, F. Jia, L. Zhang, X. Fan, Z. Zou, Applied Catalysis B: Environmental 69 (2007) 138-144.
[61] K. Jasuja, V. Berry, ACS Nano 3 (2009) 2358-2366.
[62] Y.X. Zhang, G.H. Li, Y.X. Jin, Y. Zhang, J. Zhang, L.D. Zhang, Chemical Physics Letters 365 (2002) 300-304.
[63] G.I. Spijksma, C. Huiskes, N.E. Benes, H. Kruidhof, D.H.A. Blank, V.G. Kessler, H.J.M. Bouwmeester, Advanced materials 18 (2006) 2165-2168.
[64] S. Doeuff, Y. Dromzee, F. Taulelle, C. Sanchez, Inorg Chem 28 (1989) 4439-4445.
[65] R. Sui, J.M.H. Lo, P.A. Charpentier, The Journal of Physical Chemistry C 113 (2009) 21022-21028.
[66] I.R. Galindo, T. Viveros, D. Chadwick, Industrial & Engineering Chemistry Research 46 (2007) 1138-1147.
[67] R.A. Lucky, P.A. Charpentier, Advanced materials 20 (2008) 1755-1759.
[68] B.M. Reddy, E.P. Reddy, S.T. Srinivas, V.M. Mastikhin, A.V. Nosov, O.B. Lapina, The Journal of Physical Chemistry 96 (1992) 7076-7078.
[69] O. Akhavan, Carbon 48 (2010) 509-519.
[70] V. Štengl, D. Popelková, P. Vláčil, The Journal of Physical Chemistry C 115 (2011) 25209-25218.
[71] M.R. Hoffmann, S.T. Martin, W. Choi, D.W. Bahnemann, Chemical Reviews 95 (1995) 69-96.

Chapter 6

TiO_2 and Graphene Sheet Interactions:

Theoretical Studies

Abstract

In this work, potential interactions of molecular, rutile and anatase TiO_2 with graphene and Functionalized graphene sheets were studied using Density Functional Theory (DFT) calculations. Molecular, rutile and anatase TiO_2 were decorated on the graphene sheets in 3 different positions corresponding to physical adsorption phenomena (physisorption): the top, the bridge and the hollow sites. An additional position corresponding to a chemical adsorption phenomenon (chemisorption) was created by the organic functionalization process of graphene at the carboxylate site. In all cases, rutile (Ti_2O_4) and anatase (Ti_4O_8) showed higher stability than molecular TiO_2 when adsorbed on graphene. In the specific case of functionalized graphene, the carboxylate site showed a much higher adsorption energy value (~5 eV) compared to calculated adsorption energies in physisorption (~2 eV) confirming the presence of strong chemisorption between TiO_2 and the Functionalized graphene sheets.

6.1. Introduction.

Graphene, a 2-D form of carbon made up of a single layer of atoms arranged in a honeycomb lattice, has attracted significant recent attention. This interest is due to graphene's excellent thermal, mechanical and electrical properties which are desirable for improving the properties of composites [1-6]. Nowadays, high quality graphene sheets can be synthesized in laboratories through various physical and chemical methods. Nanostructures on graphene provide new ways to design graphene-based composites for a wide range of applications in medicine, energy, environment and electronics [7]. The next step is learning how to harness the power of graphene for controlling these diverse applications, which will require a detailed theoretical understanding of the bonding interactions. Density functional theory (DFT) calculations can be used for this molecular understanding by calculating the adsoption energies of these nanostructures; providing an understanding on whether they are thermodynamically stable, in addition to explaining their electronic, mechanical and optical properties.

As previously described, several experimental reports have investigated synthesizing graphene-TiO_2 composites by sol gel and hydrothermal techniques, which have shown higher efficiency for both photovoltaic and photocatalysis compared to TiO_2 itself. [9-15] During preparation of graphene, various functional groups such as C-O-C (epoxide), C-OH groups and -COOH groups are available on the graphene surfaces [8].However, most theoretical research examining graphene is still based on idealized models which neglect both the functional groups and defect sites on its surface. As a consequence, many of these models for ideal graphene lack a realistic understanding as they do not account for the various surface functionalities and defects. In addition, only a few recent theoretical studies have investigated the interaction of different nanoparticles and graphene sheets. A systematic DFT study was performed by Valencia et al. on 3d materials interactions with planar and curved graphitic surfaces. This study showed that both graphene and SWCNT surfaces provided hollow adsorption sites that gave stable configurations with metals bound either by covalent or ionic forces, depending on their electronegativity[16]. Das et al. deposited different semiconductor nanoparticles including TiO_2 and ZnO and some magnetic nanoparticles such as Fe_3O_4 and Ni on graphene. By using first principle calculations, they showed that charge transfer occurs between graphene and the deposited

nanoparticles [17]. Rojas et al. used DFT calculations for a titanium modified graphene system for the adsorption of different molecules. They concluded that this system can considerably improve hydrogen storage capacity. They also showed that nitrogen and water molecules can be adsorbed but their selectivity was less than that of hydrogen[18]. However, the detailed interactions through DFT modeling between TiO_2 and graphene and functionalized graphene sheets have not yet been investigated.

In this work, DFT calculations were carried out showing the possible physisorption and chemisorption interactions between TiO_2 and graphene. Interactions of Functionalized Graphene sheets and different structural TiO_2 unit cells were calculated and compared to that of ideal graphene.

6.2. Model and Computations Methods.

Theoretical adsorption energy values were studied using the Vienna ab-initio Simulation Package (VASP) [19, 20] based on density functional theory (DFT). Electronic structure calculations were carried out using the GGA PW91[21] functional implemented with the VASP code for all graphene and titania systems. The electron-ion interactions were described by the projector-augmented wave scheme (PAW) [20]. A constant energy cutoff of 240 eV was used for all the calculations for consistency in the bond length and angles. A 1-dimensional and periodic single sheet of 60 carbon atoms supercell passivated with hydrogens and organic groups was used for the chemical adsorption (chemisorption) purposes. A 2-dimensional and periodic single sheet of 100 carbon atoms supercell was used for the description of physical adsorption (physisorption) phenomena.

6.3. Theoretical Approach.

Since the discovery of graphene, much research interest has shifted to potential applications of metal and semiconductor deposition (decorations) on the surface of graphene sheets [22, 23]. Many experimental and theoretical studies have focused on the adsorption of different materials onto graphene sheets with various preferential coordination sites and the adsorption energies that are important for predicting the

possibility of the interaction of metals and semiconductors with graphene and also the behavior of adsorbed materials on the graphene surfaces for various applications [16].

In the present study, we analyzed trends in adsorption energies of different structural TiO_2 unit cells on graphene by means of density functional theory (DFT) calculations with periodic boundary conditions.

The graphene sheet used for physisorption and chemisorption was represented by a basis of 100 and 60 carbon atoms distributed in a honeycomb arrangement. Recall that graphene is a single sheet of carbon atoms arranged in the well known honeycomb structure, as shown in Figure 6.1. Carbon has four valence electrons, of which three are used for the sp^2 bonds. Thinking in terms of atomic orbitals, this fourth electron is in a p_z orbital. Referring to Figure 6.1, the lattice vectors can be written as:

$$\overrightarrow{a_1} = {}^{\vec{a}_0}/_2\ (3,\sqrt{3},\ 0),\ \ \overrightarrow{a_2} = {}^{\vec{a}_0}/_2\ (3,\ -\sqrt{3},\ 0) \tag{6.1}$$

where $\vec{a}_0$= 1.43A° is used as the C-C bond length. In a Graphene primitive cell there are two atoms. With these vectors and the primitive cell, $\overrightarrow{a_2}$*5$\overrightarrow{a_1}$*5$\overrightarrow{a_2}$ = 50 atoms supercell can be constructed. A four atoms unit cell and two perpendicular lattice vectors are chosen to construct a square lattice. The 2 new vectors are:

$$\overrightarrow{a3} = \vec{a}_0\ (3,\ 0,\ 0),\ \overrightarrow{a4} = \vec{a}_0\ (0,\sqrt{3},\ 0) \tag{6.2}$$

With these new vectors and the four atoms unit cell, $\overrightarrow{a4}$ *5$\overrightarrow{a3}$*5$\overrightarrow{a4}$ = 100 atoms super cell is constructed (Figure 6.2a).

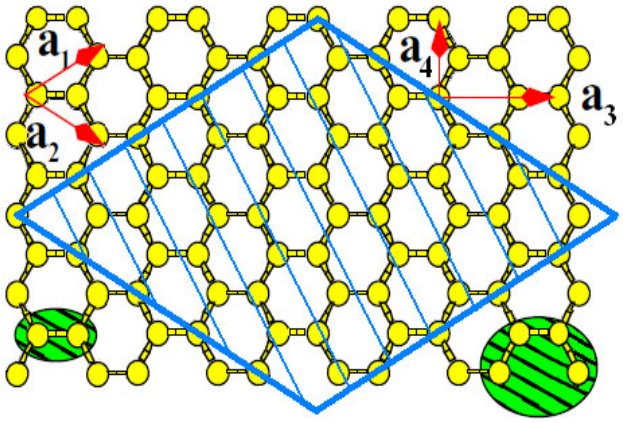

Figure 6.1. Graphene supercell. The dashed supercell is a $\overrightarrow{a_2}$*5$\overrightarrow{a_1}$*5$\overrightarrow{a_2}$ = 50 atoms lattice with a 2 atoms primitive cell. The full supercell (yellow carbon atoms) is a $\overrightarrow{a4}$ *5$\overrightarrow{a3}$*5$\overrightarrow{a4}$ = 100 atoms lattice with a 4 atoms unit cell.

The graphene sheet used for chemisorption has functional groups such as –OH (alcohol) and –COO (carboxylate), as shown previously (Ch. 3) by the XPS results. This graphene sheet is infinite in the Y direction and is terminated by hydrogen atoms and functional groups in the X direction (Figure 6.2b). The simulation boxes for chemisorption and physisorption were tetragonal respectively 21.9*12.94*20 A3 and 30*12.94*20A3 with periodic boundary conditions in x, y and z in order to have an infinite graphene sheet on x and y in the case of physisorption and an infinite sheet on y in the case of chemisorption.

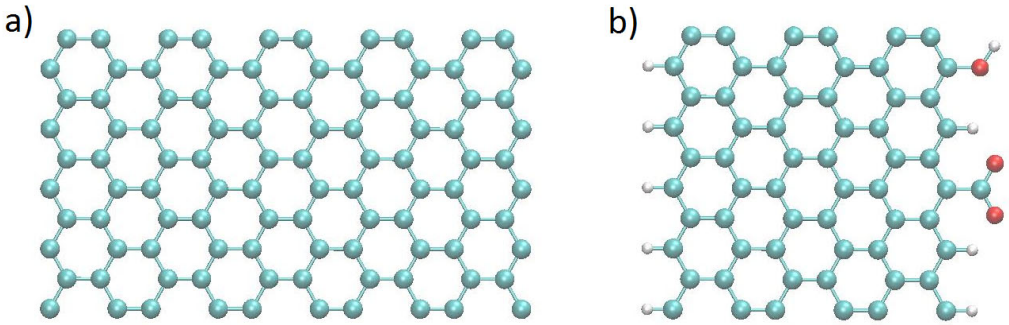

Figure 6.2. Graphene supercells used for all calculations (a) for physisorption study a 100 carbon atoms supercell (b) for chemisorption study a 60 carbon atoms supercell terminated by hydrogens, carboxylate and alcohol groups.

The utilized energy cutoff for all calculations was 240 eV. To investigate the interactions between TiO_2 and graphene sheets, we studied molecular TiO_2 (Figure 6.3a), Ti_2O_4 as the unit cell for rutile (Figure 6.3b) and Ti_4O_8 as the unit cell for anatase TiO_2 (Figure 6.3c).

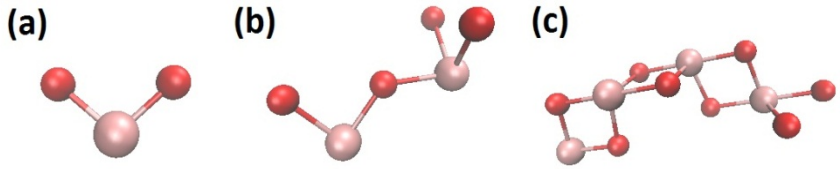

Figure 6.3. Molecular TiO_2 (a), one unit cell of Rutile TiO_2 (b), and one unit cell of anatase TiO_2(c).

It is known from theory that in vacuum the ground state geometry of the TiO_2 molecule presents a bent structure with Ti-O bond distance of 1.67 Å and O-Ti-O bond angle =110.57° (Figure 6.3 a). Rutile (Figure 6.6 b) has a Ti-O Bond length of 1.96 Å while the Ti-Ti Bond length =3.61 Å , the O-O bond length = 2.56 Å (smallest distance), 2.81 Å and 4.01 Å for the 2nd and 3rd nearest and the O-Ti-O bondangle = 81.58°. Anatase (Figure 6.3 c) has a Ti-O Bond length of 1.93 Å, Ti-Ti Bond length of 3.03 Å, O-O bond length of 2.46 Å (smallest distance) 2.79 Å and 3.03 Å for 2nd and 3rd nearest and O-Ti-O bond angle of 78.07.

Figure 6.4 shows the different possible adsorption configurations of TiO_2 on graphene sheets. The titanium decoration was represented by one titanium atom adsorbed on different positions of the benzene ring, either directly attached to the conjugated systems (on top of the carbon atom (top), on top of the C-C bond (bridge) and on the hollow side of a benzene ring (hollow)). TiO_2 molecules can be 90° rotated on each of the configurations while they can also be directly adsorbed to the caroxylate group on the functionalized graphene surface.

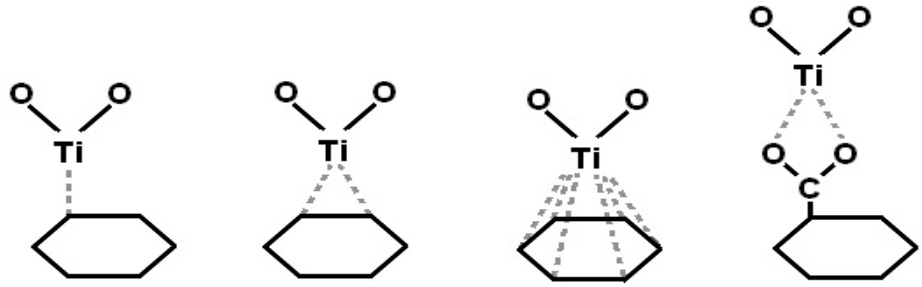

Figure 6.4. Possible adsorption sites of TiO_2 nanocrystals on a clean graphene sheet, a top site, a bridge site and a hollow site (first 3 left), and an additional adsorption site on functionalized graphene sheet, a carboxylate site (right).

The adsorption energy (E_{ads}) can be calculated using the following relation:

$$E_{ads}(>0) = E(\text{graphene}) + E(TiO_2) - E(TiO_2/\text{graphene})$$

where $E_{ads}(>0)$ represents the positive amount of the adsorption energy E_{ads}[16]. E(graphene) represents the total energy of the graphene sheet while $E(TiO_2)$ represents the total energy of the anatase TiO_2 nanostructure. $E(TiO_2/\text{graphene})$ represents the total energy of a system in which both graphene and TiO_2 are interacting. The adsorption energy was assumed to be thermodynamically favored when the binding energy was negative. For convenience, the binding energy $E_{ads}(>0)$ will be used in place of E_{ads} in the remaining sections[16].

Table 6.1 presents all the calculated binding energies and distances of different configurations of the TiO_2/graphene system. Although graphene is considered pristine in most of the theoretical calculations, all the experimental results (e.g. XPS) showed that the graphene samples contain a trace amount of oxygen functionalities, for example, carboxylic acid and alcoholic groups. To study the effect of functional groups on interactions of TiO_2 and graphene, we introduce a –COOH and -OH group on one of the edges of the graphene sheets. The adsorption energy was then calculated for molecular TiO_2 in the different positions with the bridging orientation resulting in the most stable orientation with adsorption energy of 1.212 eV and C-Ti 2.60 A°. By rotating molecular TiO_2, the hollow site was found the most stable configuration with adsorption energy of 1.224 eV and C-Ti 2.78 A°.

Table 6.1. Binding energies and distances of different configurations of TiO_2 and graphene.

Adsorption Sites	Molecular TiO_2		Rutile TiO_2		Anatase TiO_2	
	Eads (eV)	Ti-C (Å)	Eads (eV)	Ti-C (Å)	Eads (eV)	Ti-C (Å)
Top	**1.110**	**2.56**	**1.926**	**2.28**	**1.419**	**2.19**
Bridge	**1.212**	**2.60**	**2.022**	**2.33**	**1.433**	**2.30**
Hollow	**1.180**	**2.78**	**2.250**	**2.50**	**1.946**	**2.45**
Rotated top	**1.172**	**2.56**	**1.939**	**2.27**	**1.359**	**2.22**
Rotated bridge	**1.113**	**2.64**	**1.826**	**2.39**	**1.135**	**2.35**
Rotated hollow	**1.224**	**2.78**	**2.210**	**2.54**	**1.868**	**2.42**
Carboxylate	**3.379**	**2.11 (Ti-O)**	**5.482**	**2.01 (Ti-O)**	**5.394**	**1.92 (Ti-O)**

Figure 6.5a presents the physisorption of anatase TiO_2 on a graphene sheet. The adsorption energies for all three configurations and the corresponding rotated ones were calculated. The hollow orientation was found to be the most stable with E_{ads}= 1.946 eV. After introducing carboxylate groups on the graphene sheets and adsorption of TiO_2 on its surface, the adsorption energy increased significantly to 5.394 eV. In the case of adsorption of structural rutile TiO_2 on the graphene sheets, the hollow orientation was found the most stable configuration with (E_{ads}>0) of 2.250 eV and the adsorption energy for chemisoption was calculated as 5.482 eV.

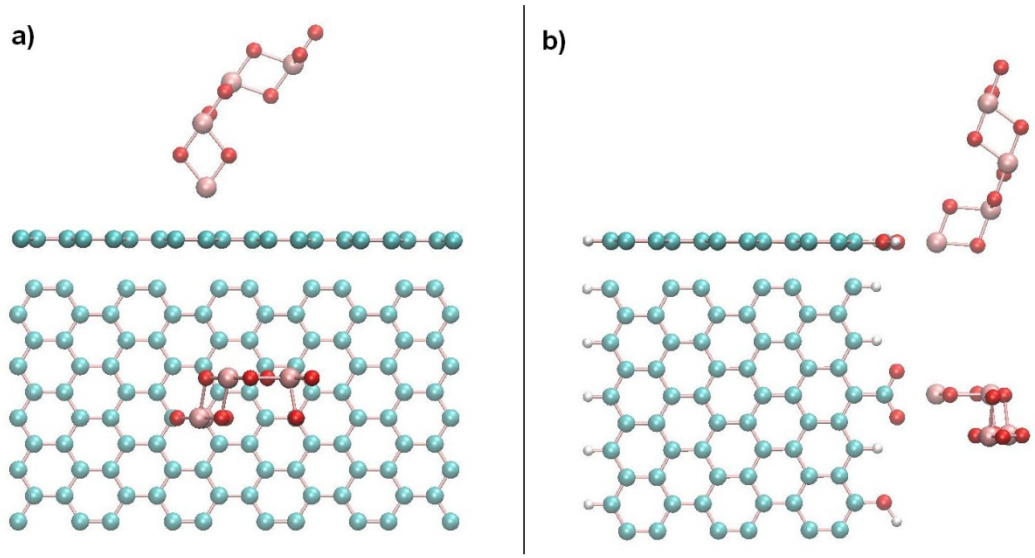

Figure 6.5. Side and top view of an anatase TiO_2 unit cell physisorbed on a clean graphene sheet (a). Side and top view of an anatase TiO_2 unit cell chemisorbed on a functionalized graphene sheet at its carboxylate group

Of the investigated physisorption configurations, the hollow one resulted in the highest and most stable configuration. Apparently TiO_2 at the hollow side of the benzene ring can be affected by all the aromatic bonds equally, resulting in the most stable configuration. As shown before, when TiO_2 interacts with graphene sheets at a carboxylic acid site (Figure 6.5b), the adsorption energy dramatically increased confirming strong chemical interactions between TiO_2 and the carboxylate group. When replaced by anatase TiO_2, it was calculated that E_{ads} increased from 3.379 eV to 5.394 eV with a corresponding increase in the Ti-O distance to 2.11 A°. These results are in good agreement with the XPS data as well which described in chapter 3 confirming strong interactions between carboxylic groups on the graphene sheets and TiO_2.

Figure 6.6 compares the adsorption energies of different structural TiO_2 units when in direct contact with graphene sheets. In the case of physisorption, the rutile configuration shows the highest energy. However, the energy of anatase in the TiO_2/graphene system is lower than that of rutile and higher than that of molecular TiO_2. It seems that the rutile structure is more desirable, providing effective adsorption with graphene. In the case of rotated TiO_2, similar results were obtained, indicating that the direction of TiO_2 and graphene is not an important parameter in physisorption.

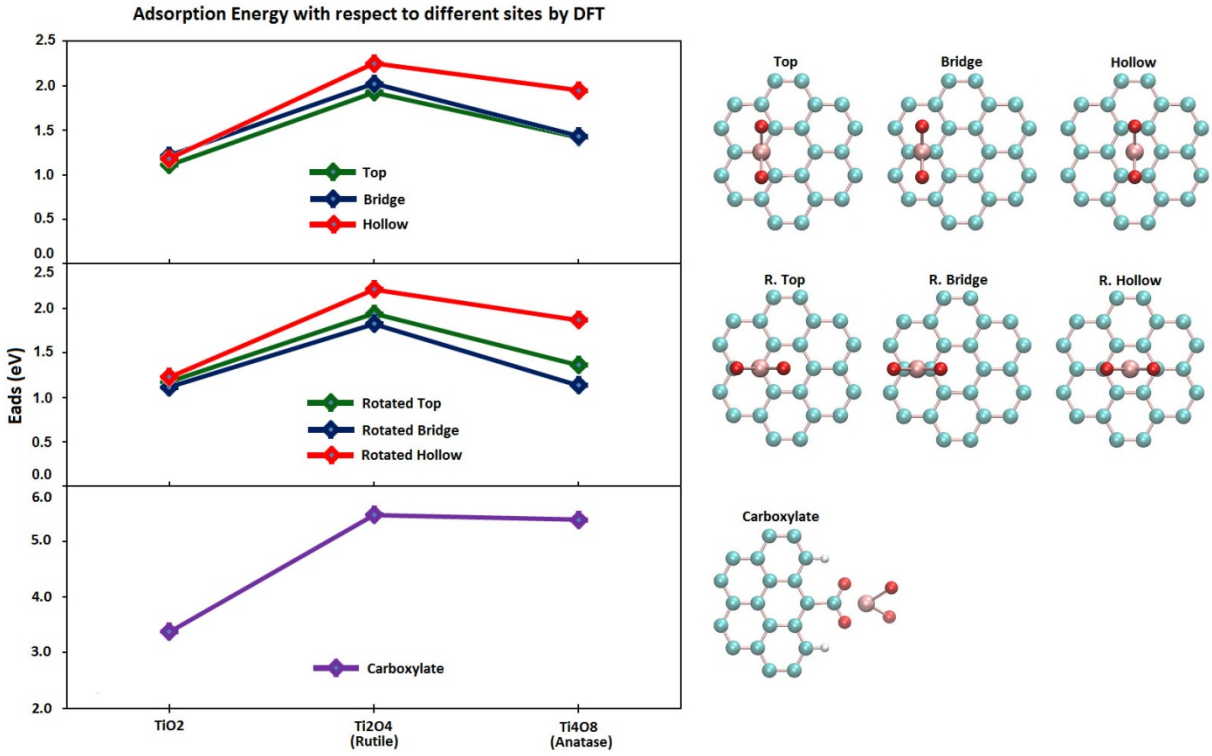

Figure 6.6. Comparison between different structural TiO_2 adsorbed on graphene sheets, (a) top, bridge and hollow positions, (b) rotated top, bridge and hollow positions and (c) Functionalized graphene sheets.

6.4. Conclusion.

A systematic DFT study of different structures of TiO_2 interactions with graphene and carboxylated graphene surfaces was performed. It is clear that molecular, rutile and anatase TiO_2 were physisorbed on different positions of the graphene sheets. The two crystalline structures show similar adsorption energies in physisorption (hollow configuration was found the most stable geometry (E_{ads}>0= 1.80, 2.25 eV)). The adsorption distances are also similar in both the anatase and rutile crystal structures and shorter than the adsorption distance of a molecular TiO_2 unit on graphene. An additional position corresponding to a chemical adsorption phenomenon (chemisorption) was created by introducing a carboxylate group on the surface of graphene. When TiO_2 interacts directly with this carboxylic group, the binding energy value increased to ~5 eV,

confirming strong chemical interactions between TiO_2 and the functionalized graphene sheets.

6.5. References.

[1] M.J. Allen, V.C. Tung, R.B. Kaner, Chemical Reviews 110 (2009) 132-145.
[2] A.K. Geim, K.S. Novoselov, Nat Mater 6 (2007) 183-191.
[3] A.A. Balandin, S. Ghosh, W. Bao, I. Calizo, D. Teweldebrhan, F. Miao, C.N. Lau, Nano Letters 8 (2008) 902-907.
[4] J.B. Oostinga, H.B. Heersche, X. Liu, A.F. Morpurgo, L.M.K. Vandersypen, Nat Mater 7 (2008) 151-157.
[5] H.C. Schniepp, J.-L. Li, M.J. McAllister, H. Sai, M. Herrera-Alonso, D.H. Adamson, R.K. Prud'homme, R. Car, D.A. Saville, I.A. Aksay, The Journal of Physical Chemistry B 110 (2006) 8535-8539.
[6] M.J. McAllister, J.L. Li, D.H. Adamson, H.C. Schniepp, A.A. Abdala, J. Liu, M. Herrera-Alonso, D.L. Milius, R. Car, R.K. Prud'homme, I.A. Aksay, Chemistry of Materials 19 (2007) 4396-4404.
[7] K. PV, Journal of Physical Chemistry Letters 1 (2010) 520-527.
[8] V.K. Prashant, |J. Phys. Chem. Lett. 1 (2010) 520-527.
[9] H. Zhang, X. Lv, Y. Li, Y. Wang, J. Li, ACS Nano 4 (2009) 380-386.
[10] Y.-B. Tang, C.-S. Lee, J. Xu, Z.-T. Liu, Z.-H. Chen, Z. He, Y.-L. Cao, G. Yuan, H. Song, L. Chen, L. Luo, H.-M. Cheng, W.-J. Zhang, I. Bello, S.-T. Lee, ACS Nano 4 (2010) 3482-3488.
[11] D. Wang, D. Choi, J. Li, Z. Yang, Z. Nie, R. Kou, D. Hu, C. Wang, L.V. Saraf, J. Zhang, I.A. Aksay, J. Liu, ACS Nano 3 (2009) 907-914.
[12] C. Zhu, S. Guo, P. Wang, L. Xing, Y. Fang, Y. Zhai, S. Dong, Chemical Communications 46 (2010) 7148-7150.
[13] X.-Y. Zhang, H.-P. Li, X.-L. Cui, Y. Lin, Journal of Materials Chemistry 20 (2010) 2801-2806.
[14] Y. Zhang, Z.-R. Tang, X. Fu, Y.-J. Xu, ACS Nano 4 (2010) 7303-7314.
[15] S. Sun, L. Gao, Y. Liu, Appl. Phys. Lett. 96 (2010) 083113.
[16] H. Valencia, A. Gil, G. Frapper, The Journal of Physical Chemistry C 114 (2010) 14141-14153.
[17] B. Das, B. Choudhury, A. Gomathi, A.K. Manna, S.K. Pati, C.N.R. Rao, ChemPhysChem 12 (2011) 937-943.
[18] M.I. Rojas, E.P.M. Leiva, Physical Review B 76 (2007) 155415.
[19] G. Kresse, J. Furthmüller, Computational Materials Science 6 (1996) 15-50.
[20] G. Kresse, D. Joubert, Physical Review B 59 (1999) 1758-1775.
[21] J.P. Perdew, J.A. Chevary, S.H. Vosko, K.A. Jackson, M.R. Pederson, D.J. Singh, C. Fiolhais, Physical Review B 46 (1992) 6671-6687.
[22] I.V. Lightcap, T.H. Kosel, P.V. Kamat, Nano Letters 10 (2010) 577-583.
[23] P.V. Kamat, The Journal of Physical Chemistry Letters 1 (2009) 520-527.

Chapter 7

Fe doped TiO_2–Graphene Nanostructures as Advanced Photocatalytic Materials- Experimental and Theoretical Studies

Abstract:

In this work, Fe-doped TiO_2 nanoparticles ranging from 0.2 to 1 weight % were grown on the surface of graphene sheets to compare their morphology and properties with composites prepared in supercritical carbon dioxide ($scCO_2$). SEM and TEM images show excellent dispersion of the Fe-doped TiO_2 nanoparticles less than 5 nm in diameter on the surface of the graphene sheets. The surface area and optical properties of the Fe-doped photocatalysts were measured by BET, UV and PL spectrometry and compared to non-graphene and pure TiO_2 analogs, showing a plateau at 0.6% Fe. Fe doped TiO_2/graphene composites also showed 0.2 eV reduction in its band gap compared to the non-graphene configuration. To study the effect of radius, various other transition metals (M) were prepared on the graphene sheets including: Nickel (Ni^{2+}), Platinum (Pt^{4+}) and Lanthanum (La^{3+}). These dopants showed either anatase TiO_2 structure or a mixture of anatase and rutile by XRD depending on their ionic radius and calcination temperature. The activities of the photocatalysts were examined for the photodegradation of 17β-estradiol (E2), an endocrine disrupting hormone which is commonly released into aquatic environments. All of the investigated catalysts showed significant enhancements in photocatalytic activity compared to bare TiO_2, TiO_2/graphene and M-TiO_2 assemblies. Through various Strong absorption of aromatic pollutants on the pores of graphene, enhancement of the excitation lifetime of M-TiO_2 when are in direct contact with graphene and high visible light absorption and electron mobility of graphene are important factors which increase the photocatalytic activity of synthesized composites. Interactions between graphene and Fe doped TiO_2 were studied using the Vienna ab-initio Simulation Package (VASP) based on Density Functional Theory (DFT). Our first-principles theoretical investigations validated the experimental findings, clearly showing physical interactions between the graphene and adsorbed Fe doped TiO_2 as well as strong chemical interactions between carboxylated graphene sheets and Fe doped TiO_2.

7.1. Introduction.

Control of environmental pollution is a current critical challenge. Heterogeneous photocatalysis has been widely utilized as an efficient method in purifying wastewater [1-4]. TiO_2, in particular has been investigated for photocatalysis for several years as it has a number of useful properties including being non-toxic, biocompatible, inexpensive, and thermodynamically stable. It has been shown to be efficient for the degradation of hazardous aromatic molecules in polluted water and air [5]. However, TiO_2 needs to be modified to obtain its maximum efficiency in different applications as it has a large band gap and its photocatalytic efficiency is rather low[6]. Doping is a common method to extend the band gap of TiO_2 into the visible region [7-10]. Numerous ions of transition metals have been investigated as potential dopants [11-13]. However, results have proven inconsistent in different research studies due to a large variation of experimental conditions investigated. Transition metals shift the TiO_2 band gap in different ways depending on their individual ionic radii, synthesis method, etc [14, 15].

Fast recombination of photogenerated electrons in TiO_2 leads to a reduction in the photocatalytic efficiency. Using an extended charge carrier with higher work function (typically metals) helps to decrease the electron-hole recombination rate, allowing an enhancement in the photocatalytic activity[16]. Carbon nanotubes and graphene possess high electrical conductivity [17] and large electron-storage capacity and therefore can be considered good electron acceptors [18]. They serve as charge trapping sites, helping to reduce the electron-hole recombination rate and thereby enhancing the photocatalytic activity of TiO_2.

Another problem with TiO_2, particularly when investigating nanoparticles, is that the nanoparticles agglomerate easily and have low selectivity in aqueous phases [19]. Researchers have shown that when TiO_2 is used on the surface of different porous materials such as zeolites [20], silica [21], activated carbon [22-27] and carbon naotubes [16, 28-33], the aggregation effects are minimized giving higher photocatalytic efficiencies. Carbonaceous materials have attracted large attention versus other supports due to their high chemical stability and conductivity, in addition to their high porosity. Pollutant molecules can be adsorbed and stabilized on the pores of the carbon materials

due to various chemical interactions, providing sufficient time for TiO_2 to degrade them to CO_2 and water more efficiently.

As a next generation carbon support, functionalized graphene sheets (FGSs) can be prepared inexpensively from earth abundant graphite without using a high pressure reaction [34]. Functional groups can be introduced on its surface during a redox process. [35]. These functional groups such as carbonyl, carboxylate, hydroxyl and epoxy can help to absorb pollutants and can also be used as a template to grow semiconductors on their surface [36]. Dispersing different metals or semiconductors on the individual graphene sheets can provide more selective catalysts or sensors for solving pollutions issues and also energy harnessing [37, 38]. When graphene is in contact with semiconductors, such as titania, it serves as charge trapping sites and helps reduce the electron-hole recombination [39].

Several recent studies have examined the synthesis and application of TiO_2/graphene composites for photocatalysis and photovoltaic applications [40-44]. In all studies, the photocatalytic performance of catalysts improved compared to bare TiO_2 (correlating to higher surface area materials). Pollutants can be stabilized on graphene □s pores, shifting the absorption towards the visible spectrum of light. However, further absorption in the visible region is required for practical catalysts. The unique properties of graphene have made it interesting to examine for numerous applications in recent years. However, use of graphene in catalysis has not studied comprehensively. High porous graphene sheets have the capacity to absorb larger quantities of pollutants on their surface, and to provide selective adsorption for desired pollutants.

There are very few reports investigating the interaction of different nanoparticles and graphene sheets. Das et al. deposited different semiconductors nanoparticles such as TiO_2 and ZnO and some magnetic nanoparticles such as Fe_3O_4 and Ni on graphene. By using first principle calculations, they showed that charge transfer occurs between graphene and deposited nanoparticles [45] . Rojas et al. used DFT calculation for Titanium modified Graphene system for the adsorption of different molecules. They concluded this system can considerably improve hydrogen storage capacity. They also showed that Nitrogen and water molecules can also be adsorbed but their selectivity is less than hydrogen[46]. Herein, we synthesize different weight ratio of Fe-doped TiO_2 ranging from 0.2 to 1%

and 0.6%Pt-TiO_2, 0.6%Ni-TiO_2 and 0.6%La-TiO_2 on the surface of graphene sheets using a sol-gel method and evaluate the resulting materials for degradation of estrodine (E2) with the results compared to catalysts prepared in identical conditions without graphene. DFT calculations are provided to further investigate the Fe doped TiO_2/graphene system.

7.2. Experimental.

7.2.1. Materials.

Graphite flakes nominally sized at 7-10 microns were provided from Alfa aesar. Fuming nitric acid (>90%), sulphuric acid (95-98%), potassium chlorate (98%), hydrochloric acid (37%), acetic acid, titanium isopropoxide (99.999%) trace metals basis, Iron chloride $FeCl_3$, Nickel nitrate $Ni(NO_3)_2 \cdot 6H_2O$, Platinium chloride $PtCl_4 \cdot 5H_2O$ and Lanthanum chloride $LaCl_3 \cdot 7H_2O$ were purchased from Sigma-Aldrich (Canada Ltd, Oakville, ON) and used as received.

7.2.2. Methods.

7.2.2.1. Preparation of Functionalized Graphene Sheets (FGSs). Graphite oxide was prepared using the Staudenmaier method [47]. Graphite (5 g) was reacted with concentrated nitric (45 mL) and sulfuric acid (90 mL) with potassium chlorate (55 g). The potassium chlorate was added slowly over 15 min to avoid any sudden increase in temperature. The mixture was stirred at room temperature for more than 3 days. After completing the oxidation reaction, the mixture was added to excess water, washed with a 5% solution of HCl, and then repeatedly washed with water until the pH of the filtrate was neutral. The prepared graphite oxide was kept at 100º C in a vacuum oven until use to evaporate all the water. A quartz tube sealed at one end, the other side was closed with an inlet and outlet for continuously passing Nitrogen gas to provide an oxygen free environment. Then, graphite oxide powder was placed in a quartz boat and inserted into a tubular furnace preheated to 1050 $^{\circ}$C and kept at this temperature for 30s. The graphite oxide was reduced and expanded to form functionalized graphene sheets.

7.2.2.2. Preparation of Metal doped TiO_2/ Graphene sheet Composites.

A simple sol-gel method used in this study as reported by Hoffman et al[48]. Acetic acid was added to 50 ml of distilled water to adjust it pH to 2.6. Previously, we studied different FGSs: TIP ratios and 1:20 was found as an optimum value ratio. In this study, we used the same FGSs: TIP weight ratio. Graphene sheets (FGSs/ TIP: 1:20) were added to this solution gradually over 10 mins to avoid agglomeration. In the next step, the appropriate amount of dopants (dopants percentage is the weight ratio of metal to the TIP), were dissolved in 2 ml ethanol and added to the graphene solution. In another beaker, TiO_2 sols were prepared by dropwise addition of 5 mL of an ethanolic TIP solution, which had been dissolved in 50 mL of absolute ethanol, into the first beaker. After continuously stirring for 24 h, the resulting transparent solution was evaporated using a rotary evaporator at 50 °C and washed with distilled water and dried in the oven (80 °C) overnight. The obtained powder was calcined at either 450 °C or 700° C for 2 h under air.

7.2.3. Characterization.

The morphologies of the samples were examined using Scanning Electron Microscopy (SEM) (Model LEO 1530) and Transmission Electron Microscopy (TEM) (Model JEOL 2010F). Samples for SEM imaging were prepared by applying the powder directly to a carbon adhesive tape. For TEM analysis, the powdered samples were dispersed in methanol by sonication and then placed on a copper grid covered with holey carbon film and dried by evaporation. Structural analysis of the samples was performed using an X-ray powder diffractometer [Rigaku Miniflex XRD, Texas, U.S.A.], fitted with a rotating sample holder, a scintillation counter detector and a divergent beam utilizing a Cu Kα source of X-rays (λ= 1.5418 °*A*). FT-IR spectra were collected on samples as KBr pellets using a Bruker Tensor 27 spectrometer, with a resolution of 4 cm^{-1}. Raman analysis was performed using a Kaiser optical system (RXN1-785) with 5 times exposure and 20 times accumulation. The XPS analysis was carried out with a Kratos Axis Ultra spectrometer using a monochromatic AlK (alpha) source (15mA, 14kV). Photoluminescence spectra were carried out with PTI Quantamaster 50 spectrophotometer with a Xenon lamp (75 V). UV spectra were performed by (Shimadzu 3600) deuterium arc lamp and two different

detectors (PMT, and PbS). An integrating sphere was utilized in order to measure diffuse reflectance of these materials. Thermo-gravimetric analysis (TGA) was performed under nitrogen atmosphere on a TA Instrument TA-Q500 at a heating rate of 10 °C/min from room temperature to 1200 °C.

7.2.4. Photocatalytic Activity Measurements.

Photodegradation of 17β-Estradiol (Sigma-Aldrich) as a model endocrine disrupting compound (EDC) was investigated under visible solar irradiation ($\lambda \geq 420$ nm). A solar simulator (Model: SS1KW, Sciencetech) with a 1000 watt xenon arc lamp equipped with an air mass filter (AM filter) AM 1.5G ($\lambda > 290$ nm) and a special UV cut-off filter ($290 \leq \lambda \leq 420$ nm) were used as the visible light source. Typically, a mixture of aqueous E2 solution (5µg/L) and 0.5 g/L of catalyst was vigorously stirred for 30 min to establish an adsorption/desorption equilibrium in the dark. Then the reaction solution was irradiated under visible light in an open water-jacketed vertical photo-reactor which was placed on a magnetic stirrer during all experiments, under aerated conditions [1]. The temperature of the reactions was controlled at 22+1°C by circulating cooling water. At given time intervals, 5 mL aliquots were sampled and centrifuged to remove the particles. Supernatant were analyzed by HPLC using a (ICS 300, Dionex), which included a DP pump, an AS auto sampler, a DC column oven and PDA UV detector, connected to Chromeleon software. Separations were carried out with an Acclaim 120 C18 reversed-phase column (150 mm × 4.6 mm i.d., 5 µm particle size, Dionex, USA). The injection volume was 40 µL from a 2 mL HPLC vial, capped and sealed with PTFE lid. The mobile phase was the mixture of acetonitrile (AcN) and deionized water (Milli-Q) (50:50 v/v), delivered at a flow rate of 1 mL/min. The column temperature was maintained at 30°C and detection wavelength was set at 280 nm which shows maximum absorbance of E2. The retention time of E2 in HPLC column was 5.33 min. The measurements were repeated for each catalytic system, and the experimental error was found to be within (±1%).

7.3. Computational methods.

Theoretical band structures and adsorption energy values were studied using the Vienna ab-initio Simulation Package (VASP)[49, 50] based on density functional theory (DFT). Electronic structure calculations were carried out using the GGA PW91[51] functional implemented with VASP code for all graphene and titania systems. The electron-ion interactions are described by the projector-augmented wave scheme (PAW)[50]. A constant energy cutoff of 240 eV was used for all the calculations for consistency in the bond length and angles. Band gaps have been calculated for structural TiO_2 in the bulk and by adsorption on graphene. One unit cell of clean and one unit cell of 25% Fe-doped Anatase TiO_2 respectively Ti_4O_8 and Ti_3FeO_8 have been used for all band gap and adsorption properties. A 1-dimensional and periodic single sheet of 60 carbon atoms supercell passivated with hydrogens and organic groups have been used for the chemical adsorption (chemisorption) purposes. A 2-dimensional and periodic single sheet of 100 carbon atoms supercell has been used for the description of physical adsorption (physisorption) phenomena.

7.4. Results and discussion.

Different percentages of Fe doped TiO_2/Functionalized Graphene Sheets (FGSs) were synthesized by a sol gel method in a green solvent mixture of water and ethanol to give decorated graphene sheets (Scheme 7.1). To study the effect of ionic radius, M (Ni, Pt and La) were also prepared on the graphene sheets under similar conditions. The experimental conditions and resulting properties of the synthesized materials are summarized in Table 7.1.

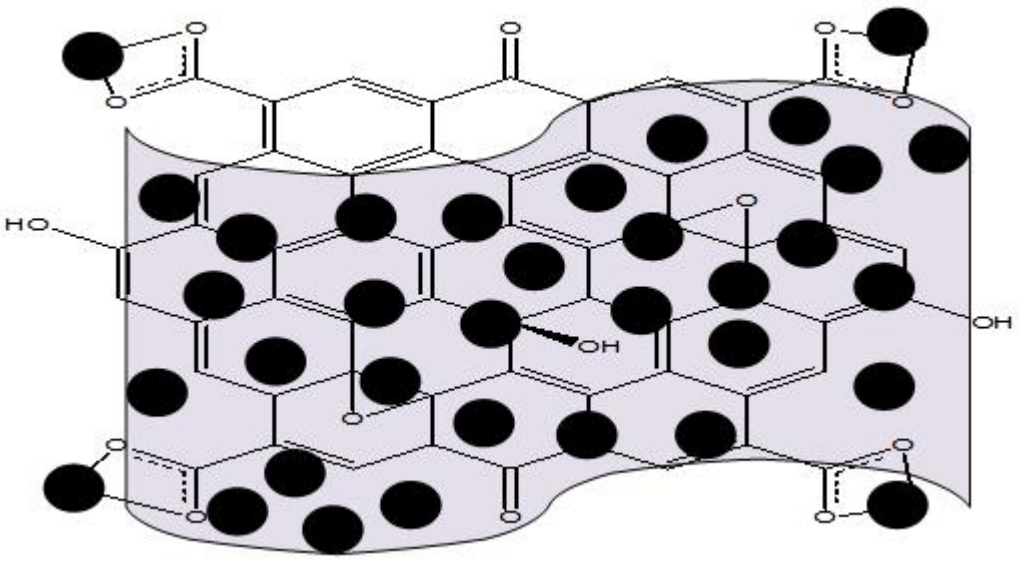

Scheme 7.1: Schematic of Fe-doped TiO_2 nanoparticles on the surface of graphene sheets.

Table 7.1. Synthesis conditions, morphology**,** BET surface area, pore volume, and pore size distribution of TiO_2, Fe, Ni, pt and La doped TiO_2/ FGSs composites.

Dopant	**Calcination T (°C)**	**rutile (%)**	**Bandgap (eV)**	**Surface area (m^2g^{-1})**	**Color**
TiO_2	450	0	3.2	50	White
TiO_2/ FGSs	450	0	2.9	124	Grey
0.6 % Fe doped TiO_2	450	0	2.6	68	Yellow
0.2% Fe doped TiO_2/ FGSs	450	0	2.9	130	light yellow
0.4% Fe doped TiO_2/ FGSs	450	0	2.7	158	light yellow
0.6% Fe doped TiO_2/ FGSs	450	0	2.5	188	Yellow

0.6% Fe doped TiO_2/ FGSs	700	53	2.5	98	Yellow
0.8% Fe doped TiO_2/ FGSs	450	0	2.5	190	Orange
1% Fe doped TiO_2/ FGSs	450	0	2.5	193	Orange
0.6% Pt/ TiO_2/ FGSs	450	51	2.6	175	light brown
0.6% Pt/ TiO_2/ FGSs	700	94	2.6	87	light brown
0.6% Ni/ TiO_2/ FGSs	450	0	2.5	184	Green
0.6 % Ni/ TiO_2/ FGSs	700	73	2.5	81	Green
0.6% La/TiO_2/ FGSs	450	0	3.2	169	White
0.6% La/TiO_2/ FGSs	700	0	3.2	72	White

Typical morphology of the as-prepared FGSs is shown in Figure 7.1a and 7.1b using SEM and TEM imaging. The SEM image of the FGSs shows the exfoliation of the reduced graphite oxides and high porosity of graphene sheets. A transmission electron microscopy (TEM) image of the FGSs is shown in Figure 7.1b; here a thin paper-like structure is observed which is not completely flat showing wrinkles on the edges [35].

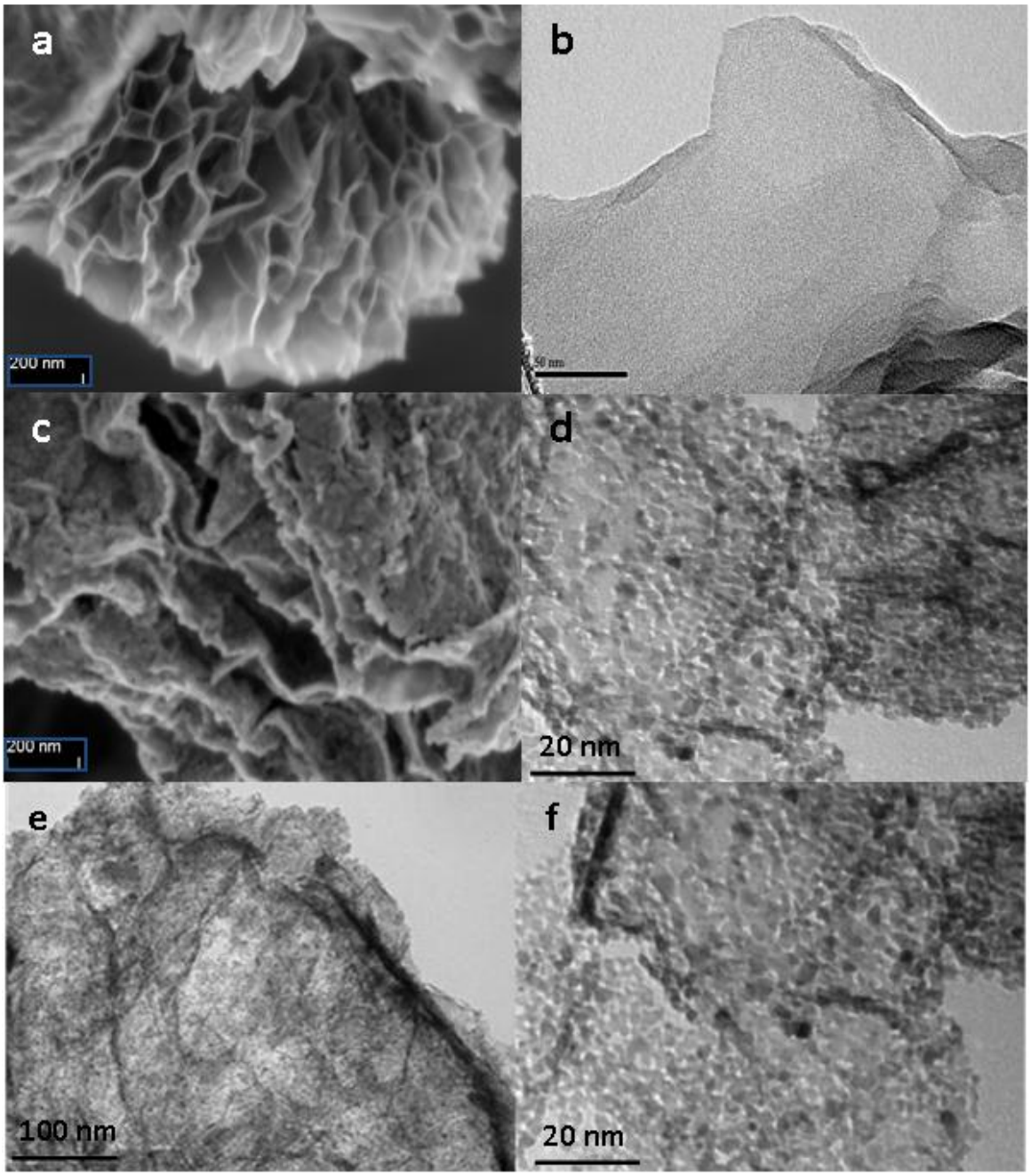

Figure 7.1. Functionalized Graphene Sheets (FGSs) (a) SEM, (b) TEM; 0.6% Fe doped TiO_2/FGSs (c) SEM and (d) TEM. TEM images of Pt- TiO_2/ FGSs; (e) 100nm scale and (f) 20 nm scale.

Most of the graphene sheets are very thin as has been previously observed; however some of them stack together due to van der Waals interactions. In Figure 7.1c and 7.1d typical SEM and TEM images of the metal (Fe) doped TiO_2 grown on the surface of graphene sheets is shown in which the uniform dispersion of small nanoparticles on the sheets is observable. Different metal doped TiO_2/graphene sheets nanostructures show similar morphologies. In the TEM images, doped TiO_2 nanoparticles less than 5 nm covered the entire surface of the graphene sheets with no significant agglomeration of nanoparticles detected. However, more nanoparticles are observed on the edges of the graphene sheets due to a higher amount of functional groups on that area as darker spots are obvious on the graphene edges. The morphology of other doped TiO_2/FGSs composites were also investigated by TEM which gave similar morphologies to the Fe doped TiO_2/FGSs composites. TEM images of Pt-doped TiO_2/FGSs composites are shown in Figure 7.1 e and f.

Typical SEM and TEM images of Fe doped TiO_2 are presented in Figure 7.2a and 7.2b. When graphene sheets were not used as a support, the size of TiO_2 particles significantly increased up to 50 nm and some of the particles agglomerated. Hence, it is apparent that the graphene sheets can facilitate uniform dispersion of the particles on its surface while controlling size. As described in detail below, doped TiO_2 particles grow from carboxyl groups on the surface of the graphene sheets, significantly decreasing the degree of agglomeration. A HRTEM micrograph of the lattice image of 0.6% Fe doped titania/ graphene calcined at 450 ^oC is given in Figure 7.2c, showing uniform dispersion of anatase with d-spacing 0.35 nm (101) [52]. There was no Fe detected in the HRTEM micrographs, indicating that all the Fe is impregnated within the TiO_2 lattice. Some amorphous regions are also observable, corresponding to the presence of graphene sheets in the composites.

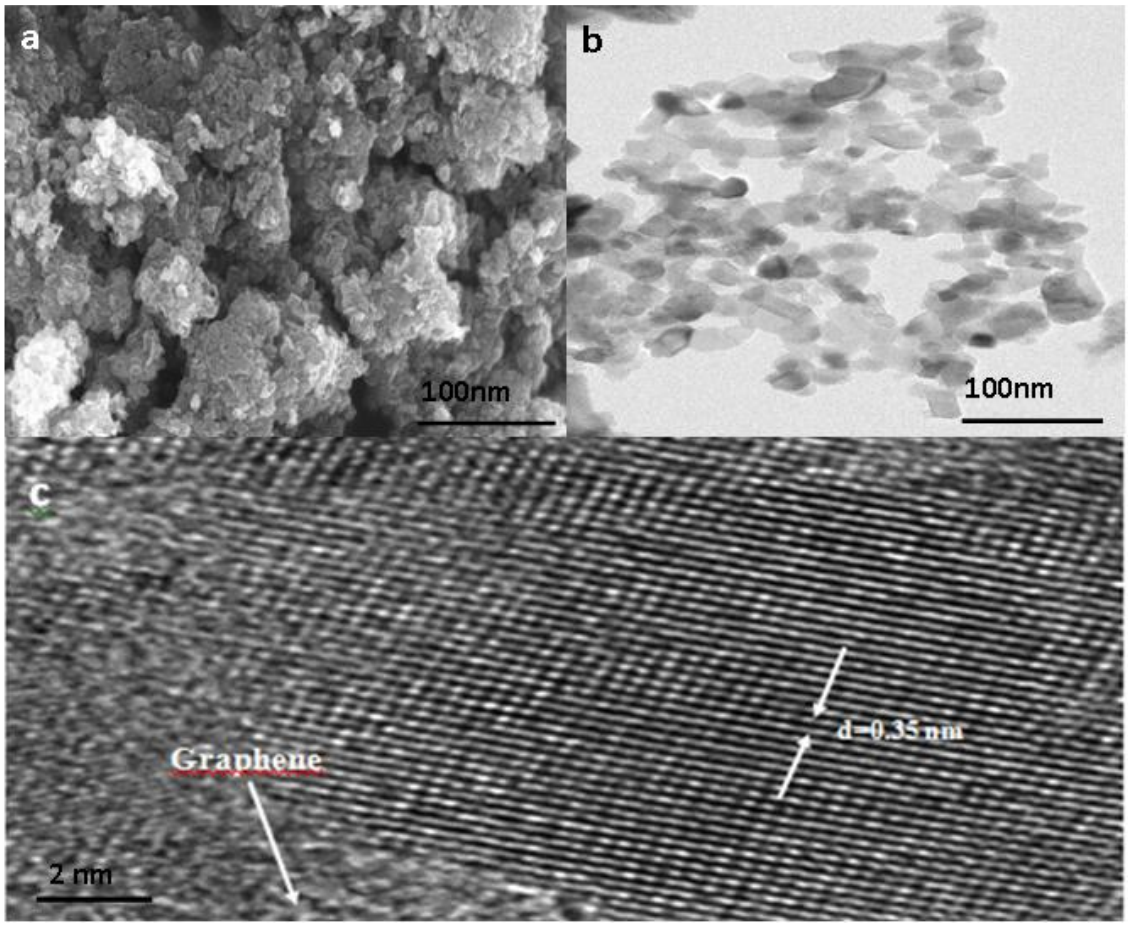

Figure 7.2. 0.6% Fe doped TiO_2 (a) SEM and (b) TEM, (c) HRTEM image of Fe doped TiO_2/ FGSs (0.6%) calcined at 450° C.

The FGSs did not show any peak in XRD which means that either all stacking is lost or the remaining stacking is disordered [53]. Figure 7.3.1 shows the XRD patterns of different amounts of Fe-doped TiO_2/ FGSs composites calcined at 450° C. All spectra show anatase phase, however the crystallinity varies. By increasing the amount of Fe from 0.2 to 0.6 %, the crystallity increases, whereas further increasing to 1% decreases the crystallity. In Figure 7.3.2, the XRD patterns of Fe doped TiO_2 (0.6%) with and without graphene are compared. The crystallinity is significantly higher when grown on the FGSs. In explanation, when Fe doped TiO_2 nanostructures were grown on the surface of the graphene sheets, the functional groups on the graphene sheets acted as templates, enhancing crystallization and resulting in smaller sized TiO_2 nanocrystals being obtained.

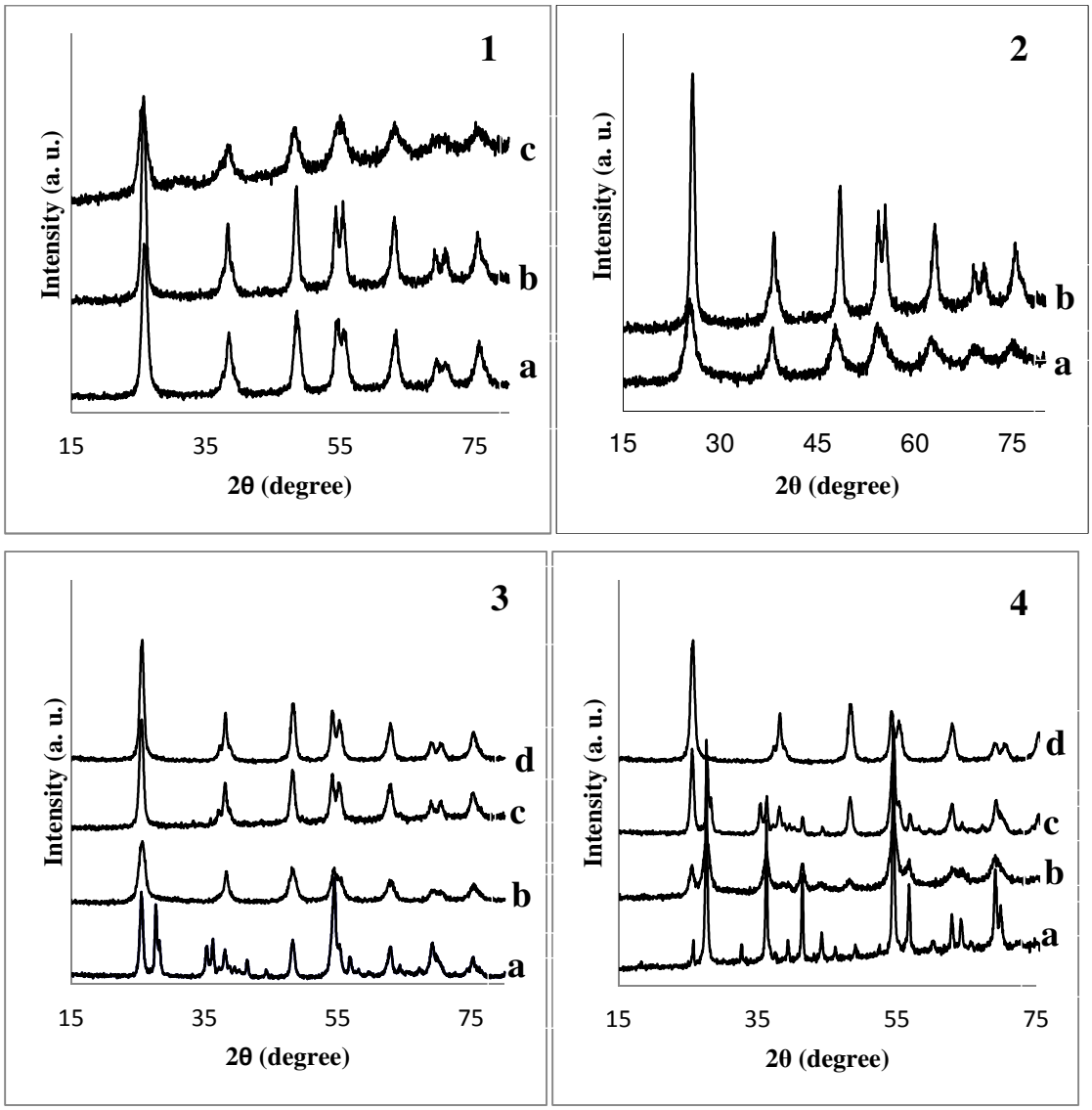

Figure 7.3. (1) Fe doped 0.2% (a), 0.6% (b) and 1% (c), (2) 0.6 Fe doped TiO_2 (a), 0.6 Fe doped TiO2/ Graphene (b) Pt 0.6% (a), Fe 0.6% (b), Ni 0.6%(c), and Fe 0.6% (d) doped TiO_2 on the surface of graphene sheets. Calcined at 450° C (3), Calcined at 700° C.

Different metal doped TiO_2 particles were also prepared on the graphene sheets. The fraction of rutile (X_R) can be calculated using the following equation [48]:

$$X_R(\%) = \{1-(1+ 1.26\, I_R/I_A)-1\} \times 100 \quad (7.1)$$

where *I*R and *I*A are the X-ray intensities of the rutile (101) and anatase (110) peaks, respectively. Anatase to rutile phase transformation has been explored by a few research groups. Choi et al. studied the effect of different dopants on A-R phase transformations and suggested that addition of dopants with small radii resulted in direct integration with the TiO_2 crystal lattice, introducing more oxygen sites in the lattice leading to increased anatase formation [48]. In this work, Fe and Ni-doped TiO_2/FGSs present well-crystallized anatase phase when calcined at 450°C. This means that all the dopants were integrated inside the TiO_2 lattice as no characteristic peaks were observable in the XRD pattern (Figure 7.3.3 b,c). By increasing the calcination temperature to 700° C, both Fe and Ni (74% rutile) doped TiO_2/FGSs had a mixture of anatase and rutile (Figure 7.3.4 b,c). The Pt-TiO_2/ FGSs exhibited high rutile fractions (X_R) at both 450 and 700° C calcination temperatures (Figure 7.3.3.a, 7.3.4.a). The amount of rutile phase at 450 °C is 50%, which increased to 94% at 700 °C. In explanation, Pt has a larger ionic radius than Fe and Ni resulting in decreasing the oxygen vacancies inside the TiO_2, which is more preferable for the rutile phase. La-TiO_2/FGSs helps prevent A-R phase transformation at both 450 and 700°C calcination temperature, with only anatase phase TiO_2 resulting (Figure 7.3.3d, 7.3.4d). As no rutile phase was detected, doping with La appeared to inhibit the anatase to rutile phase transformation. This inhibition has been explained by the relatively large differences in ionic radius of TiO_2 and La, as the La ion cannot fit within the TiO_2 lattice and with the Ti-O-La formed at the interface, resulting in inhibition of crystal transformation [48, 54].

Diffuse reflectance UV-Vis spectroscopy was applied to further study the interactions between the metal doped TiO_2 and graphene in the composites. The UV-Vis spectra (Figure 7.4.1) indicates that Fe, Ni and Pt-doped TiO_2/graphene gave strong absorbance in the visible region (300-700 nm) with the band gap decreasing to 2.5 eV, as calculated using the basic energy equation ($E= hc/\lambda$) (Table 7.1). Different studies on TiO_2/graphene composites have shown that graphene can narrow the band gap of TiO_2, as we also observed in Chapter 4[40, 44, 55]. Formation of Ti-O-C bonding between TiO_2 and graphene sheets, similar to that observed with carbon-doped TiO_2 composites, is a potential reason for the red shift in the UV spectra [56].

Metal-doping enhances visible light absorption owing to the formation of intermediate energy levels, leading to a decrease in the energy band gap[57]. La doped TiO_2 does not show any shift in absorption peaks of TiO_2. (Figure 7.4.1b) As explained from the XRD results, La has a large radius and cannot enter the TiO_2 lattice. Figure 7.4.2 compares the UV spectra of Fe-doped TiO_2 with and without graphene sheets. By adding graphene to the system, the band gap of Fe doped TiO_2 decreased from 2.6 to 2.5 eV, which helps confirm that graphene acts as a photosensitizer. In Figure 7.4.3, the UV spectra of TiO_2 with band gap of 3.2 eV is compared to TiO_2/FGSs with a band gap of 2.9 eV.

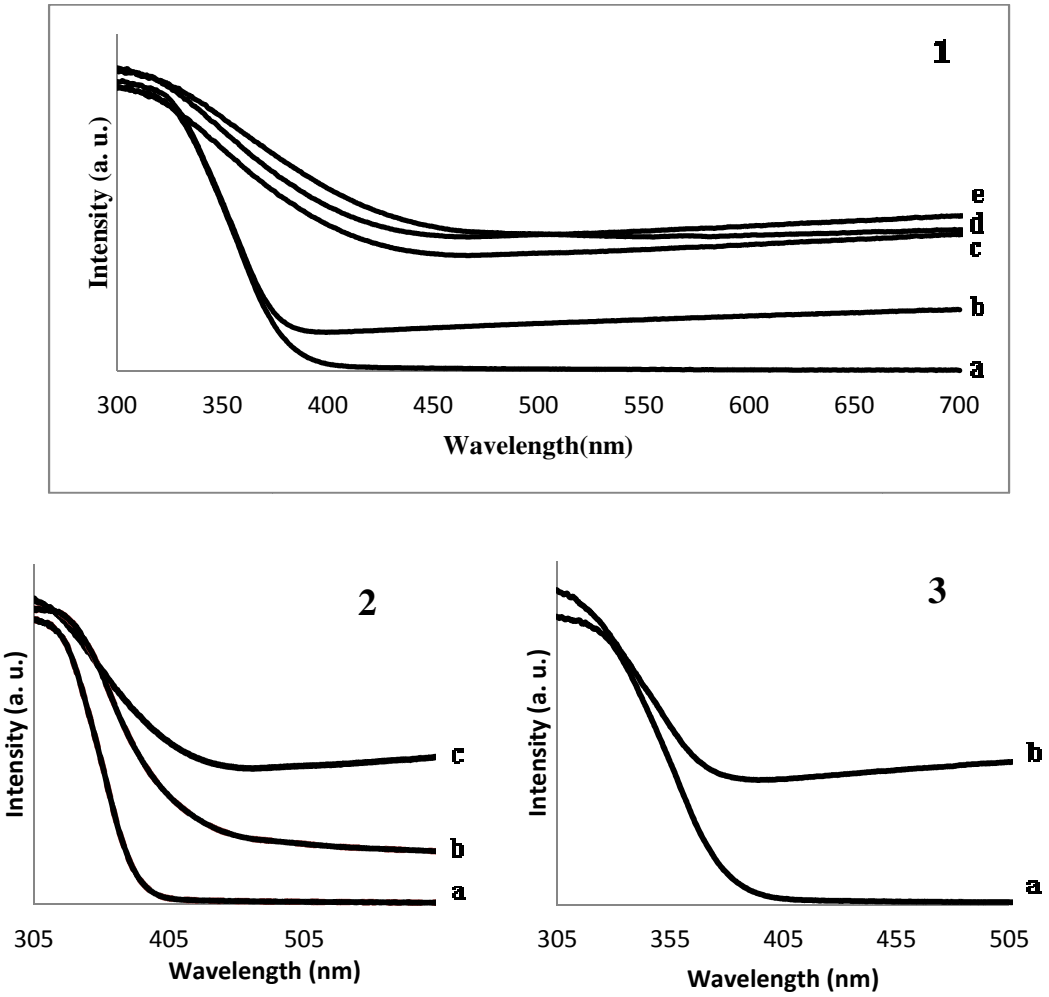

Figure 7.4. Diffuse reflectance UV-Vis spectra of: (1) (a) TiO_2 anatase; (b) 0.6% La doped TiO_2/FGSs , (c) 0.6 %, Pt doped TiO_2/ FGSs, (d) 0.6%Ni doped TiO2/ FGSs and (d) 0.6% Fe doped TiO_2/FGSs(2) (a) TiO_2, (b) 0.4% Fe doped TiO_2 and (c) 0.4% Fe doped.

Photoluminescence spectroscopy usually is used to analyze TiO_2 surface phenomena, such as excited states and electron-hole recombinations [58]. The PL spectra of TiO_2 and the synthesized doped TiO_2 on the surface of graphene are shown in Figure 7.5. TiO_2 (anatase) has a characteristic broad peak at around 540 nm which is assigned to the light absorption coefficient, known as a dual-frequency peak as shown in Figure 7.5.a. [59]. The decrease in the peak intensity from TiO_2 when doping with the investigated metals represents an enhanced ability for light absorbance with the doped TiO_2/FGSs composites. Although the PL intensity decreased in all the investigated doped TiO_2/FGSs composites compared to anatase TiO_2 alone, the reduction was obviously greater in the Fe, Ni and Pt doped TiO_2/FGSs composites. La doped TiO_2/FGSs showed the minimum reduction, while Fe doped TiO_2 without graphene and TiO_2/graphene composites both showed a reduction in the PL peak intensity. However, the reduction is less than the similar composites prepared on the surface of graphene (Figure 7.5c). As a possible mechanism, when metal-doped TiO_2 nanoparticles are in contact with graphene sheets, their excited electrons have less chance for recombination and transfer to graphene resulting in an improvement in its surface quality, reducing the density of trap states while providing an enhanced excitation lifetime.

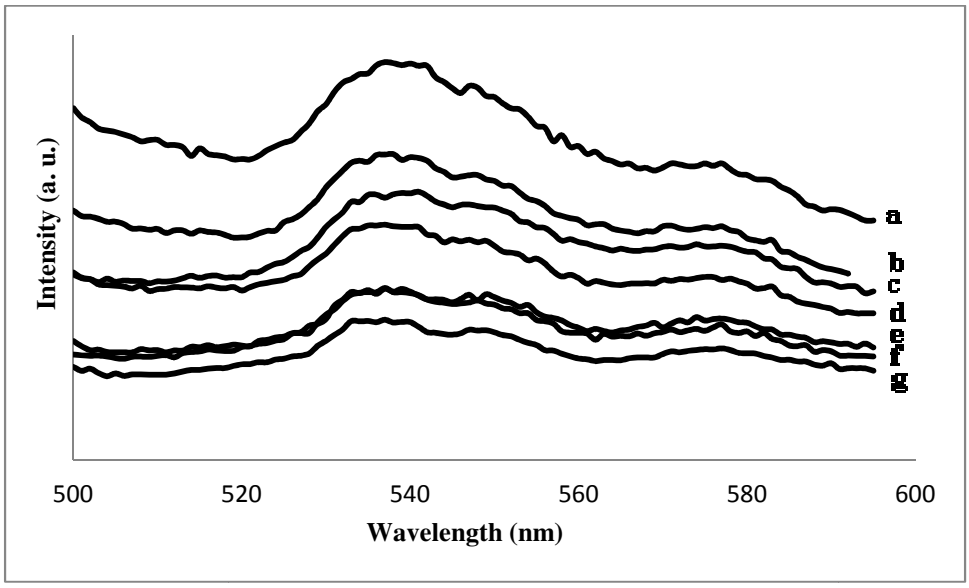

Figure 7.5. Photoluminesence Spectra of TiO_2 (anatase) (a), La doped TiO_2 /FGSs composites (b), Fe doped TiO_2 (0.6) (c) Fe doped TiO_2/ FGSs (0.6) (d), Ni doped TiO_2/ FGSs (0.6) (e) and Pt doped TiO_2/FGSs (0.6) composites.

BET surface areas (Table 7.1) were determined using nitrogen adsorption and desorption isotherms. Synthesized FGSs showed high surface area (1100 m^2g^{-1}) while the BET surface area of the undoped sol-gel synthesized TiO_2, which was calcined at 450 °C was found to be 85 m^2 g^{-1}. The BET surface areas of the Fe-doped TiO_2 samples were found to be slightly larger than the undoped TiO_2 (105 m^2 g^{-1}). When Fe-doped TiO_2 was grown on the surface of the graphene sheets, the surface area increased to 180 m^2g^{-1}. By increasing the amount of Fe in the composites, the surface area was enhanced (230m^2g^{-1} for 0.6% Fe doped/ TiO_2/FGSs), which is attributed to producing more pores inside the composites. Ni, Pt and La doped TiO_2/FGSs also showed similar results. By increasing the calcination temperature to 700° C, the surface area decreased to 70-112 m^2g^{-1} for all cation dopants investigated. Both the agglomeration of TiO_2 nanoparticles and the collapse of the porous structure are attributed to the decreasing surface areas at high calcination temperatures.

Graphene has two characteristic peaks in the raman spectra; (Figure 7.6.d) i.e. a broad D and G band, which are assigned to the C sp^2 atoms and one to C sp^3 atoms, respectively [60]. After functionalization of graphene with TiO_2, the intensity ratio of the D band to G band, which is proposed as an indication of disorder in the prepared catalysts, increased dramatically indicating good attachment of the TiO_2 nanoparticles to the graphene surface. All doped TiO_2/FGSs samples calcined at 450 °C are present in the anatase phase corresponding to characteristic peaks around 143 cm^{-1}, which are attributed to the main E_g anatase vibration mode. The presence of crystalline TiO_2 in the composites is confirmed by the vibration peaks at 400 cm^{-1} (B_{1g}), 519 cm^{-1} (A_{1g}) and 640 cm^{-1} (E_g) [61]. The Raman spectra of the prepared Fe-doped TiO_2/FGSs are shown in Figure 5.6b, c which is in good accordance with the XRD patterns as no Fe peak is detected. The peak position shifts toward a higher wavenumber in the order of 0.2 and 0.8% Fe doped TiO_2/FGSs, indicating an increase in the number of surface oxygen vacancies. The more oxygen vacancies induced by Fe-doping could be attributed to the incorporation of Fe-dopants into the TiO_2 lattice. Zhu et al. prepared Fe-doped nanocrystalline via a nonhydrolytic sol-gel method and observed the same shift in the Raman study [62].

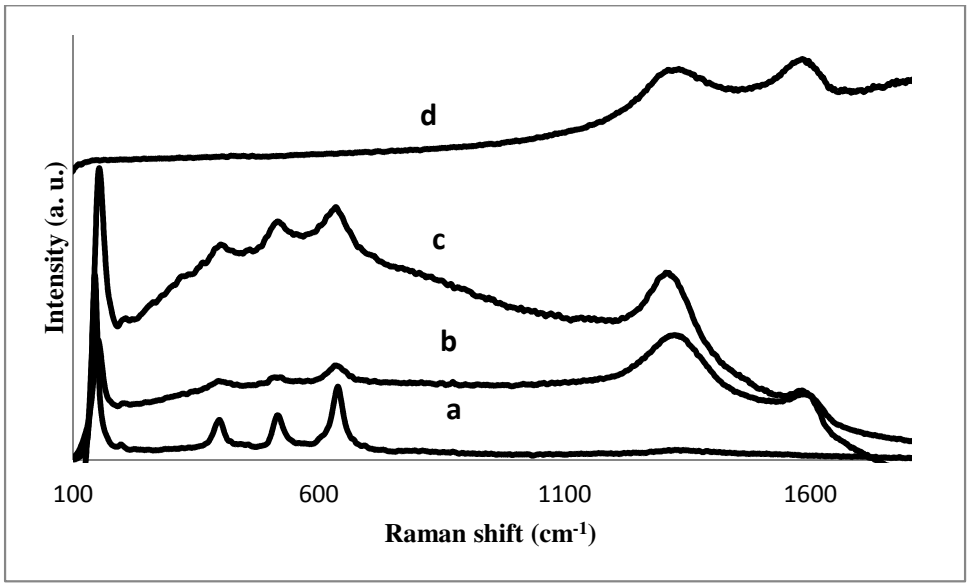

Figure 7.6. Raman spectrum of TiO_2 (a) Fe doped TiO_2/ FGSs (0.2%) (b), Fe doped TiO_2 (0.8%) (c), and Functionalized Graphene Sheets (FGSs) (d).

The XPS spectrum of FGSs was explained in previous chapters (Figure 7.7). [63]. The XPS spectra of 0.6% Fe doped TiO_2/ FGSs shows 6.1% Fe 2p, 54.7% O1s, 18.7% Ti 2p and 20.5% C1s. (Figure 7.8)

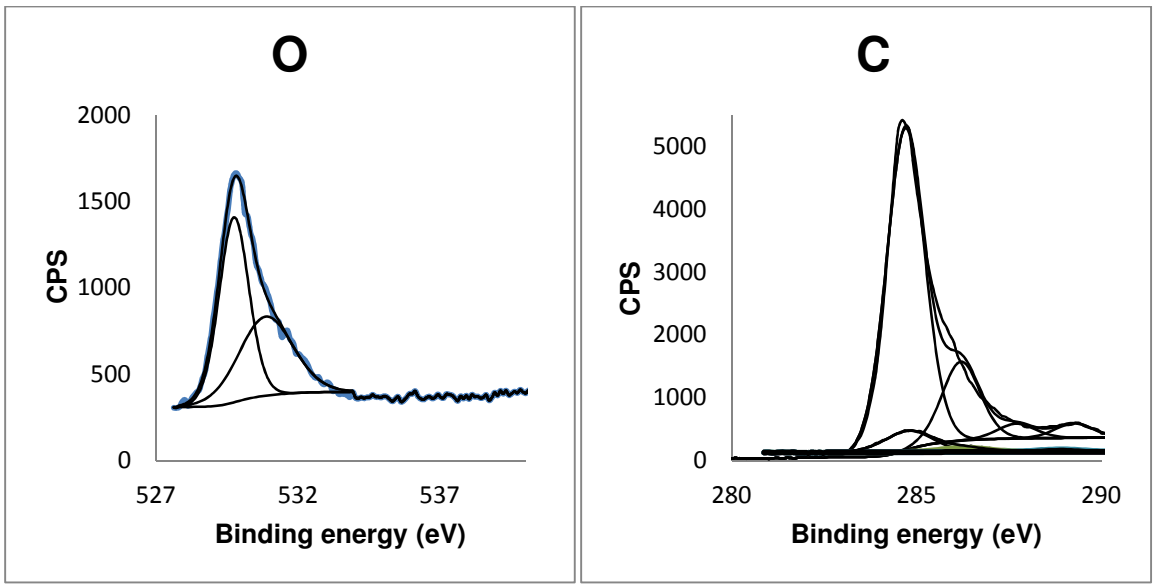

Figure 7.7. XPS spectra of FGSs, High resolution (a) C (1s) and (b) O (1s).

In high resolution of C1s, four different peaks of FGSs are still available but the intensity of peaks representing the C=O and C-OH functionalities decreased. The peak at 289.25eV corresponds to C=O also shifted to lower energy (288.8eV) implying coordination bonding between Ti and carboxylic acids on the surface of the graphene sheets. The O 1s main peak at 530.3 eV is assigned to the metallic oxides (Ti-O), which is consistent with the binding energy of O^{2-} in the TiO_2 lattices. The peak at 533.4 eV, corresponding to O-H disappeared, but the peak at 531.4 eV corresponding to the carbonyl group is still available [63]. The Ti 2p3/2 and Ti 2p1/2 for Fe doped TiO_2 on the graphene surface are located at binding energies of 458.4 eV and 464.1 eV, respectively, which is consistent with the values of Ti^{4+} in the TiO_2 lattices [64]. The peaks at 711.9 eV and 724.6 eV are assigned to 2p3/2 and 2p1/2 of Fe^{3+}, respectively. These data exhibit a slightly positive shift compared to those in Fe_2O_3 (710.7 eV for 2p3/2 and 724.3 eV for 2p1/2). The positive shift of the Fe2p level binding energy may be due to transferring the electrons from Fe^{3+} into TiO_2 lattice and the formation of Fe–O–Ti bonding in the composite. [64]. We observed similar results comparing Fe-Doped TiO_2/FGSs nanowires in $scCO_2$ in Chapter 5.

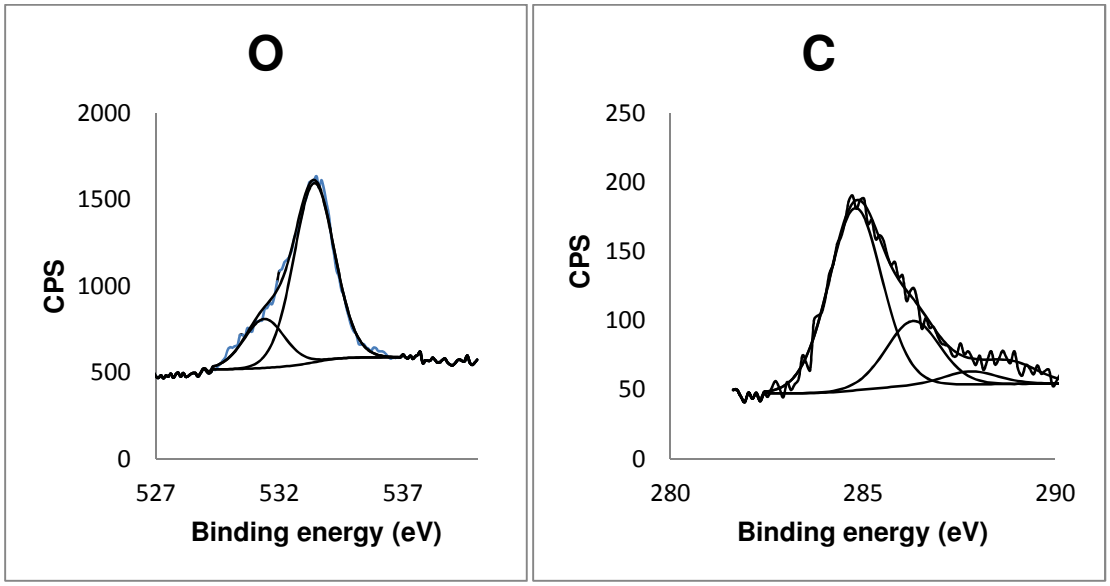

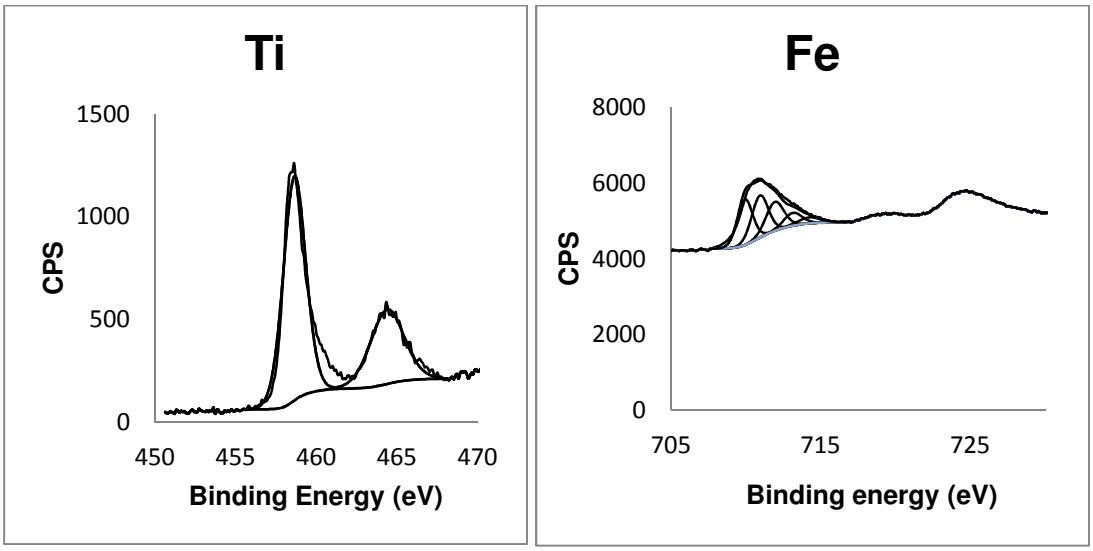

Figure 7.8. XPS spectra of 0.6% Fe doped TiO_2/ FGSs, High resolution (a) O, (b) C, (c) Ti and (d) Fe.

Pristine graphite displayed a simple linear weight loss after 500°C (Figure 7.9a), indicating uniform weight loss of the carbon skeleton. In contrast, the TGA curve of graphite oxide (Figure 7.9b) showed three regions: the weight loss up to 120 °C results from physically adsorbed water or organic residues, the weight loss from 120 to 320 °C is attributed to the burn off of chemically bound organic residues (carboxyl, anhydride), and the weight loss above 320°C is attributed to the removal of more stable oxygen groups (e.g. phenol, carbonyl). Compared to the curve of graphite oxide, the weight loss of FGSs (Figure 7.9c) below 200°C is much lower, indicating that the main oxygen-containing functional groups of graphite oxide have been converted after rapid thermal reduction, resulting in increasing FGSs thermal stability. Moreover, high temperature pyrolysis of FGSs is similar to graphite after 500°C, which is attributed to pyrolysis of the carbon skeleton, which is in agreement with a previous report [65](Figure 7.9c).

The successful functionalization of FGSs with TiO_2 nanoparticles was also shown by the TGA curves. In the TGA curve of TiO_2 (Figure 7.9d), the weight loss below 120°C is about 20% up to 800° C, which is due to the loss of absorbed water. Besides, there is a mass loss for TiO_2 in the temperature after 120°C, suggesting that there may be some unreacted Ti precursor in the sample. For TiO_2-FGSs (Fig. 7.9e), the weight loss of the sample is greatly reduced to (90%). In explanation, FGSs can act as a template,

immobilizing the TiO_2 nanoparticles and thereby resulting in homogeneous heating and the avoidance of heat concentration. This indicates that there is a strong interaction between the FGSs and TiO_2, and there is only limited unreacted Ti precursor and acetic acid remaining from the reaction. By further modification and immobilizing the Fe-doped TiO_2 on the surface of FGSs, the weight loss decreased to just 1%, indicating that the Fe-doped TiO_2 nanomaterials contain lower amounts of chemically bound organic residue.

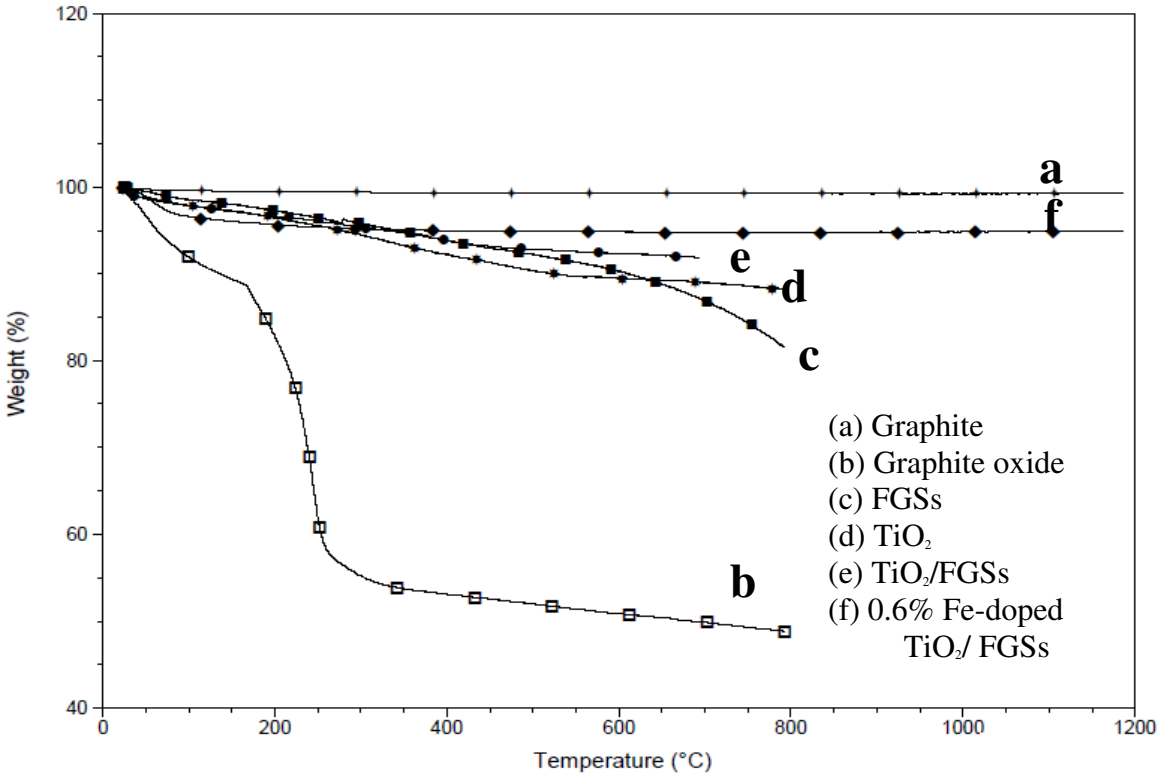

Figure 7.9. TGA spectra of (a) Graphite, (b) graphite oxide, (c) FGSs, (d) TiO_2, (e) TiO_2/ FGSs and (f) 0.6% Fe doped TiO_2 calcined at 450 °C.

Typically, nanostructure evolution in the modified sol-gel process goes through the following steps: (i) modification, (ii) hydrolysis, (iii) condensation, (iv) nucleation, and (v) growth [66]. First, TiO_2 precursors (TIP) react with carboxylate groups on the surface of graphene sheets. After modification, titanium isopropoxide (TIP) undergoes hydrolysis in acidic solution by the following reaction:

$$(Ti(OR)_4)_m + \text{graphene} -(COOH)_n \longrightarrow \text{graphene} -(COO^-)_n (Ti(OR)_{4-x})_m + xROH$$

In the next step, excess amount of acetic acid react with graphene/TIP composites following by hydrolysis which releases some –Ti-OH in the medium of the reaction.

graphene $-(COO^-)_n$ $(Ti\ (OR)_{4-x})_m$+ yAcOH ⟶ graphene-$(COO^-)_n$ $(Ti\ (AcO)_y\ (OR)_{4-x-y})_m$ +yROH

AcOH+ (x+y) ROH ⟶ ROAc + H_2O

graphene-$(COO)_n(Ti\ (AcO)_y\ (OR)_{4-x-y})_m$ $\xrightarrow{\textbf{Hydrolysis}}$ graphene-$(COO)_n(Ti\ (AcO)_y\ (OH)(OR)_{4-x-y-1})_m$

In addition, usually Fe $(NO_3)_3$ dissociates to produce $Fe(OH)_3$ in the presence of water [67].

$$Fe\ (NO_3)_3+3H_2O\rightarrow Fe\ (OH)_3+3HX$$

According to the sol-gel principle, the hydrolysis products (Ti-OH and M-OH) condense producing metal-oxygen bonds, resulting in the evolution of nanostructure.

Graphene-$(COO)_n$ $(Ti\ (AcO)_y\ (OR)_{4-x-y})_m$ $\xrightarrow{\textbf{Oxidation}}$ graphene-$(COO)_n$ $(Ti- O - Fe- -O-Ti)_m$

7.5. Visible-Light Photocatalytic Activities of M-TiO_2/FGSs.

17β-estradiol (E2) was chosen as the model organic compound to evaluate the photoactivity of the prepared doped TiO_2 on Graphene sheets under visible light irradiation (λ > 400 nm). As we saw in Chapter 4, normally photocatalytic degradation follows first-order kinetics:

$$\frac{dC}{dt} = -k_r \frac{K_a C}{1+K_a C} \qquad (7.2)$$

where *(dC/dt)* is the degradation rate of E2, *C* is the concentration of E2 in the solution, t is reaction time, k_r is the reaction rate constant, and K_a is the adsorption coefficient of the

reactant. K_aC is negligible when the value of C is very small. As a result, Eq. (7.2) can be described by pseudo-first order kinetics. Setting Eq. (7.3) at the initial conditions of the photocatalytic experiment, when t = 0, C = C_0, it can be described as:

$$\ln\left(\frac{C_0}{C}\right) = K_{app} \times t \quad (7.3)$$

The photocatalytic activities are shown in Table 7.2, in which the observed rate constant was increased slightly to 0.003 h^{-1} in the presence of undoped TiO_2. However, Fe, Ni and Pt-TiO_2 showed significantly enhanced photocatalytic activities under the visible-light irradiation. By increasing the amount of Fe in the composites from 0.4% to 0.6%, the rate constant increased from 0.0091 to 0.0123 h^{-1}. Further increasing the amount of Fe to 0.8% did not affect the rate constant significantly (k= 0.0123 h^{-1}). Among all the tested M-TiO_2 samples, Pt-TiO_2 showed the highest visible-light photoactivity for E2 degradation. The Fe and Ni TiO_2 samples showed slightly increased rate constants, while La-TiO_2 had a negligible effect when compared to undoped TiO_2. The difference in photocatalytic activity of the different dopants can be explained by their ionic radius. La has a relatively larger radius than TiO_2, which limits penetration inside the TiO_2 and changes its electrical and optical properties. Fe, Ni and Pt have a smaller radius than TiO_2, which can affect its properties and photocatalytic activity. Pt has a larger ionic radius and can introduce less oxygen inside the TiO_2 lattice. All these data are in good agreement with results reported previously by Hoffman et al [48]. By preparing all M-TiO_2 on the surface of graphene, the rate constant of E2 photodegradation increased significantly (Table 7.2).

To examine recycling, all catalysts were filtered, then tested for the second cycle. Although the rate constants decreased, the catalysts were still active. Catalysts calcined at 700°C were also tested for E2 photodegradation. The rate constant decreased significantly compared to catalysts calcined at 450° C. This reduction should be because of catalyst sintering, i.e. collapsing the pores at high temperature and a subsequent decreasing of surface area as described above.

Table 7.2. Visible-Light Photocatalytic Activities of Various M-TiO_2 and M-TiO_2/ FGSs Samples for the Degradation of E2.

Materials	k (h^{-1}) (Calcined at 450° C) First cycle	k (h^{-1}) (Calcined at 450 °C) Second cycle	k (h^{-1}) (Calcined at 700° C)
TiO_2	0.002	0.0015	0.0012
TiO_2/ FGSs	0.003	0.0018	0.00176
0.2% Fe doped TiO_2	0.004	0.0032	0.0018
0.2% Fe doped TiO_2/ FGSs	00.007	0.0054	0.0037
0.4% Fe doped TiO_2	0.0071	0.0052	0.00501
0.4% Fe doped TiO_2/ FGSs	0.0091	0.0076	0.00721
0.6% Fe dopedTiO_2	0.0083	0.0059	0.00521
0.6%Fe doped TiO_2/ FGSs	0.0123	0.0096	0.00892
0.8% Fe doped TiO_2	0.0087	0.0062	0.00592
0.8% Fe doped TiO_2/ FGSs	0.0122	0.0093	0.00891
0.6% Ni doped TiO_2	0.0085	0.0054	0.00419
0.6% Ni doped TiO_2/ FGSs	0.0119	0.0971	0.0891
0.6% Pt doped TiO_2	0.0121	0.0101	0.0091
0.6% Pt doped TiO_2/ FGSs	0.0250	0.0212	0.0223
0.6% La doped TiO_2	0.0023	0.0014	0.0011
0.6% La doped TiO_2/ FGSs	0.0025	0.0016	0.0011

The enhancement in photocatalytic properties of the Fe-doped TiO_2/FGSs composites can be described by two different mechanisms. First, visible light can be absorbed by the Fe doped TiO_2, with electrons transferred from the valence band to the conduction band of TiO_2. In various space-charge regions between TiO_2 and graphene, excited electrons can then be transferred to graphene with holes remaining on the surface of TiO_2 taking part in the photocatalysis reactions. This mechanism was first described by Hoffmann and co-workers to describe the observed photocatalytic enhancement of carbon nanotube (CNT)-TiO_2 composites [68] (Scheme 7.2.a). Another explanation for the observed photocatalysis enhancement in the CNT-TiO_2 system was described by Wang et al, which can be extended to the graphene-TiO_2 system. In this mechanism, graphene can absorb visible light and its excited electrons are then transferred to the conduction band of doped TiO_2. Then, the positively charged graphene makes a hole in the TiO_2 valence band by

removing an electron from it. Positively charged doped TiO_2 can then react with water, producing hydroxyl radicals which would then degrade the E2 molecules [69]. These mechanisms are shown in Scheme 7.2. It seems that graphene can act as both photosenitizer and also charge trapper resulting in enhancement in photocatalytic activity of synthesized catalysts. In this study, the slight red shift in the UV spectra of TiO_2/graphene composites confirms that graphene can act as a photosenitizer. However, this shift wasn't strong enough to make the photocatalyst visibly active as when synthesized using supercritical carbon dioxide ($scCO_2$) as previously shown in chapter 3.

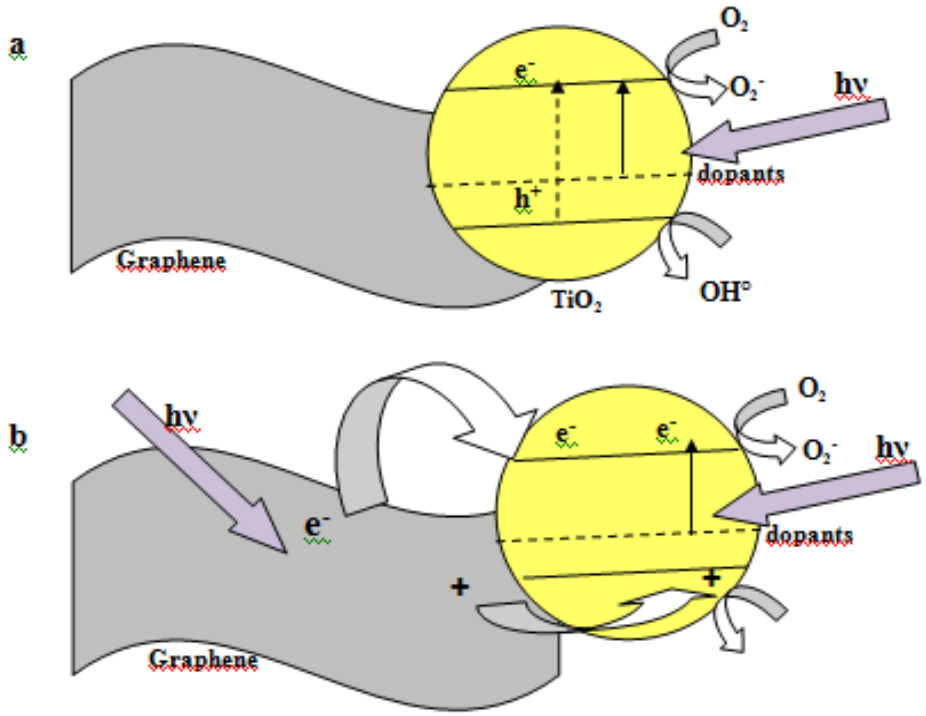

Scheme 7.2. The proposed mechanisms for enhancement of photocatalysis in the M-doped TiO_2/ Graphene composites; a) Graphene acts as an electron trapper (Hoffman et al.) ; b) Graphene acts as sensitizers and transfer electrons to the TiO_2 (Wang et al.).

7.6. Theoretical Approach.

Presently, only a few theoritcal studies exist on the interactions of TiO_2 and graphene sheets[45]{Valencia, 2010 #691}. However, most of these studies have only focused on ideal graphene sheets, without any functional groups or defective sites interacting with TiO_2. Hence, here we investigate the interactions of Fe doped TiO_2 when in direct contact with both ideal graphene and also functionalized graphene sheets, comparing the results

with undoped TiO_2. The unit cell of anatase TiO_2 (Ti_4O_8) was used which was doped with an Fe cation, which can be can be placed in 4 different positions of the unit cell. The general formula for a Fe-doped anatase TiO_2 unit cell can be defined as follows:

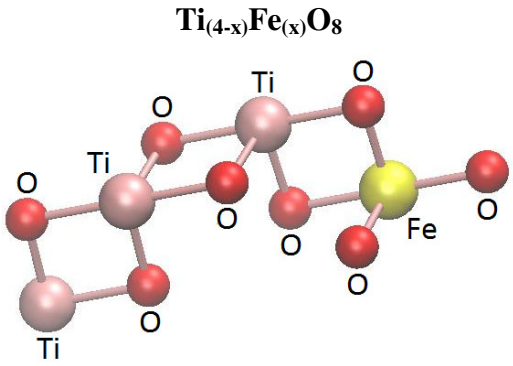

Figure 7.10. Single unit cell of Fe-doped Anatase TiO_2 (Ti_4O_8). Chemical formula: Ti_3FeO_8. Fe replaces Ti in a cation doping process.

where x represents the number of Fe atoms in the doped Anatase TiO_2. Ti represents the titanium atoms, Fe the iron atom and O the oxygen atoms. From the XPS results, we chose (x=1) as the unit cell, which corresponds to the formula Ti_3FeO_8 and to a 25% (w %) cation doping of anatase. Figure 7.10 shows one unit cell of Ti_3FeO_8 and specifically where the Fe atom was doped within the anatase TiO_2 structure. Note that the Fe atom is not involved in binding to the graphene sheet, as the Fe-doping only plays a role in the electronic structure of anatase. As shown previously in Chapter 6, Titanium binds to the clean and functionalized graphene sheet in all cases of physisorption and chemisorption. These adsorption sites are the top, the bridge, the hollow, and the carboxylate site. Figure 7.11 (a), (b) and (c) show these 3 types of physical adsorptions (physisorption) while Figure 7.11 (d) shows the unique chemical adsorption (chemisorption) site. If Anatase TiO_2 is rotatated by 90 degrees on graphene, it results in a rotated adsorption site that may lead to slightly different results, as previously discussed.

All adsorption energy values of anatase TiO_2 adsorbed on graphene are presented in Table 7.3. Similar graphene supercells as in chapter 6 have been used for this study.

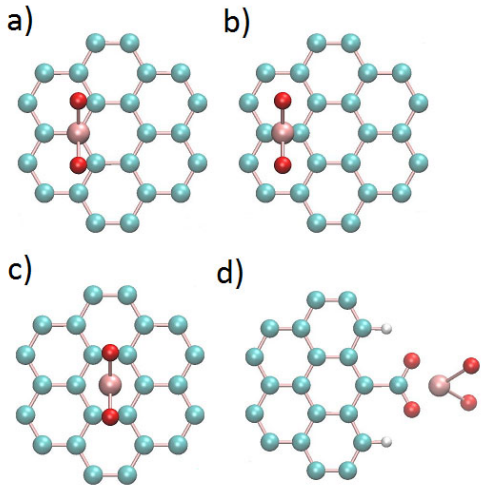

Figure 7.11. Possible adsorption sites of TiO_2 on functionalized graphene sheets. Three physisorption sites: (a) the top site, (b) the bridge site and, (c) the hollow site and one chemisorption site (d) the carboxylate site.

A 100 carbon atom supercell was used for the physisorption study (Figure 6.2a), while a 60 carbon atom supercell terminated by hydrogens, alcohol and carboxylates groups was used for the chemisorption study (Figure 6.2b). The adsorption energy can be calculated using the following equation:

$$E_{ads}(>0) = E(\text{graphene}) + E(TiO_2) - E(TiO_2/\text{graphene}) \quad (7.4)$$

where $E_{ads}(>0)$ represents the positive amount of binding energy [5]. E(graphene) represents the total energy of the graphene sheet while $E(TiO_2)$ represents the total energy of the anatase (clean or doped) nanostructure. $E(TiO_2/\text{graphene})$ represents the total energy of a system in which both graphene and Titania are interacting. The adsorption energy was assumed to be favored when the binding energy was positive. For convenience, the binding energy $E_{ads}(>0)$ will be used in place of E_{ads} in the remaining sections [70].

A summary of the results for the optimized structures for all TiO_2/graphene and also Fe doped TiO_2/graphene complexes is provided in Table 7.3. For both Ti_4O_8 and Ti_3FeO_8, the carboxylate adsorption site of functionalized graphene is more favorable and as a result shows a higher binding energy than all the other adsorption sites. The carboxylate site stands preferably on the edges of graphene sheets so the chemisorption is less likely to occur than the physisorption phenomenon. In terms of physisorption of Titania on graphene, the hollow site shows a higher binding energy followed by the bridge site and

the top site in both doped and clean anatase compounds. As a result, anatase TiO_2 nanostructures are more likely to start their growth on the hollow sites of gaphene.

As can be seen, the shortest separation between an atom of TiO_2 and the closest carbon atom of the graphene layer is between 2.19 and 2.45 A° in the case of physisorption and 1.92 A° for chemisorption. After doping TiO_2 with Fe, all distances increased by just 0.02 A°. Das et al. deposited different nanoparticles such as TiO_2, ZnO, Fe_3O_4, and Ni on graphene surfaces and reports that the closest distances of graphene's carbon and nanoparticles range from 2.4 to 3.0 A° [45].

Interestingly, in physisoprtion, the relative bonding energies are higher in Fe doped TiO_2 embedded in graphene than the corresponding undoped composites, almost by 0.4eV. It seems that when we replace one Ti atom with Fe, some magnetization in the composites occurs altering the charge transfer between the deposited nanoparticles and graphene. Das et al. studied the interaction of graphene decorated by semiconducting and magnetic nanoparticles and found significant electronic and magnetic interactions facilitating charge transfer between the nanoparticles and graphene.

Higher bonding energies with almost the same Ti-C bond distances helps confirm strong physisorption occurred between the Fe doped TiO_2 and the graphene sheets. Moreover, the binding energy in the presence of carboxylate groups on graphene results in slightly decreased chemisorption. However, the chemisorption value between the Fe doped TiO_2 and graphene surface was relatively strong, i.e. having a calculated bonding energy of 5.394 eV.

Table 7.3. Calculated binding energy values for clean and Fe-doped anatase TiO_2 adsorbed on graphene substrates.

Adsorption Sites	Anatase TiO_2		Fe-doped Anatase TiO_2	
	E_{ads}(>0) (eV)	Ti-C (Å)	E_{ads}(>0) (eV)	Ti-C (Å)
Top	1.419	2.19	1.774	2.20
Bridge	1.433	2.30	1.742	2.32
Hollow	1.946	2.45	2.201	2.47
Carboxylate	5.785	2.19 (Ti-O)	5.394	1.94 (Ti-O)

Figure 7.12 shows the band energy structure plots of pure anatase TiO_2 (a) and Fe-doped anatase TiO_2 (b) both in the bulk. (Each line represents energy of individual orbitals) The

clean graphene band structure has already been reported in both theoretical and experimental cases [71], with our calculated results in agreement. Graphene is a zero band gap semiconductor (i.e. is a conductor). The valence band of graphene overlaps with the conduction band at the Fermi level region. However, graphene has an active role in nanostructural devices as it influences the semi-conductivity of adsorbed compounds. Graphene also has a direct role in the growth mechanism of metal oxides nanostructures such as anatase TiO_2. Table 7.4 summarizes the band gap values of Ti_4O_8 and Ti_3FeO_8 compounds. Based on our DFT calculations, the band gap of un-doped TiO_2 at Γ point is about 1.89 eV (Figure 7.12a) which is smaller than the experimental value (3.2eV) due to shortcomings in describing the excited states. After doping TiO_2 with Fe, the calculated band gap was 1.66eV (Figure 7.12b) which shows a reduction in the band gap of TiO_2. This indicates that the excitation requires less energy and the light absorbance has a significant shift to the visible area compared to pure TiO_2, being in good agreement with the experimental UV-vis absorption results. When adsorbed on graphene, both band gap values decrease to 1.21 eV and to 1.66 eV for Ti_3FeO_8 and Ti_4O_8, respectively. This is in qualitative agreement with the experimental values of 2.50 eV and 2.90 eV for Ti_3FeO_8 and Ti_4O_8 on the graphene sheets respectively. There is a significant decrease in the band gap for pure anatase TiO_2 of 0.23 eV when is in direct contact with graphene, which confirms that graphene can be act as a photosanitizer in the composites as explained by other groups [40, 70]. Similar changes in band structure have been observed for anatase TiO_2 of lower concentration of Fe-dopants (1/8, 1/16). For these cases, the band gap reduces significantly in the bulk with the Iron cation deforming locally the structure of the TiO_2 anatase unit cell [72]. More information can be provided on the effect of graphene on metal oxides growth properties as the graphene defects show another important role in band structures[73, 74]. The organic functionalization of graphene may also affect graphene band properties and also the growth properties of the metal oxide adsorbates such as Rutile, anatase or brookite TiO_2[75].

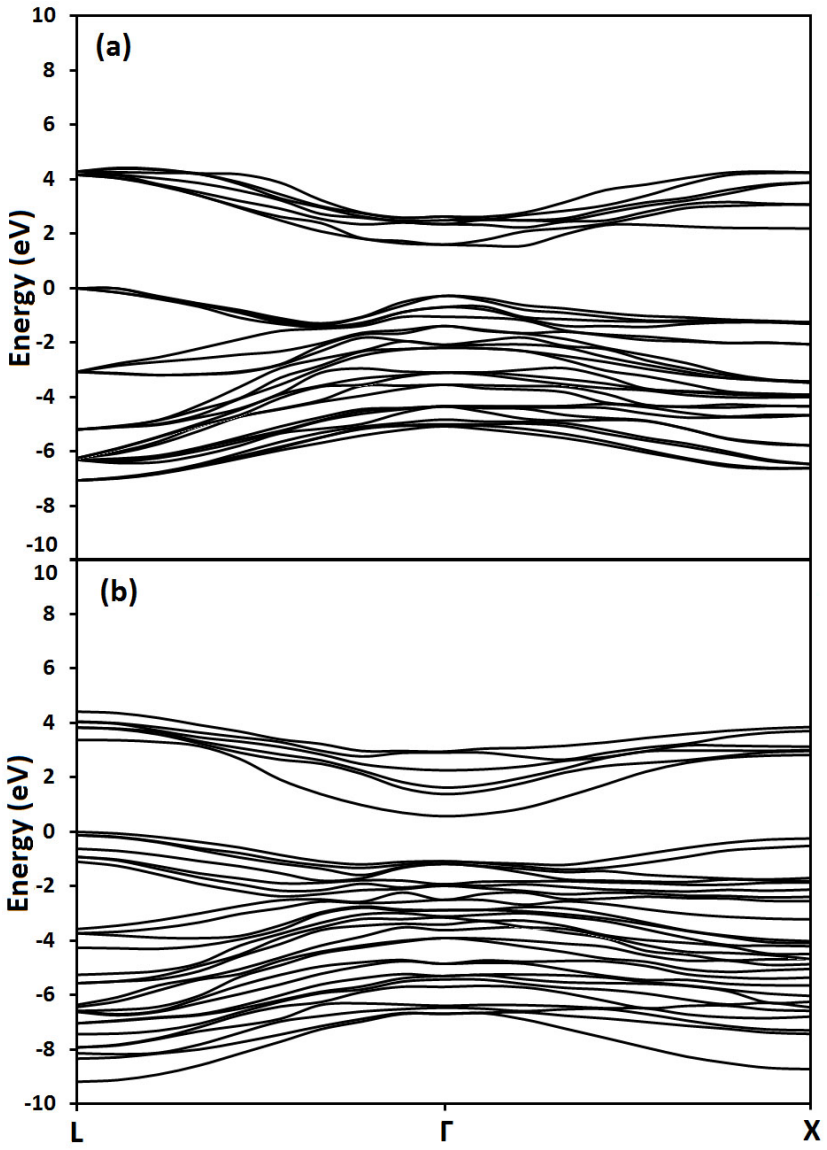

Figure 7.12. Band structure plots for (a) pure anatase TiO_2 in the bulk and (b) Fe-doped anatase TiO_2 in the bulk. The Fermi level is located at zero eV on the energy axis.

Table 7.4. Calculated and experimental band gap values of clean and Fe-doped anatase TiO_2 in the bulk and adsorbed on graphene substrate.

Materials	Band Gap (eV)	
	Ti_4O_8	Ti_3FeO_8
Bulk	1.89	1.66
Adsorbed on graphene (Theoretical)	1.66	1.21
Adsorbed on graphene (Experimental)	2.90	2.50

7.6. Conclusions

High performance Fe doped TiO_2 on the surface of graphene sheets were successfully synthesized via a simple sol-gel process in the green solvent mixture of water/ethanol. Fe-TiO_2/FGSs showed higher visible light absorption, higher surface areas than corresponding samples prepared without graphene. The prepared materials were examined for visible light degradation of E2-an endocrine disrupting hormone, which showed higher photocatalytic activity compared to TiO_2/graphene and metal doped TiO_2 composites. The observed photocatalytic enhancement can be explained by enhanced adsorptivity of dyes, extending the photoresponse range, and enhancing the charge separation and transportation properties simultaneously. Density Functional Theory (DFT) calculations were also performed, indicating possible physical interactions between Fe doped TiO_2 and graphene sheets on 3 different positions i.e. the top, the bridging and the hollow sites. The hollow sites were shown as the most stable configuration. Fe doped TiO_2/graphene composites showed higher stability than TiO_2/graphene composites because of higher charge transfer from the doped semiconductor to the graphene sheets. Fe doped TiO_2 decorated on carboxylated graphene sheets were also investigated which show strong chemical interactions between the Fe doped TiO_2 and graphene. These materials provide new possibilities in the investigation of TiO_2–graphene composites and promote their practical application in addressing various environmental issues.

We have demonstrated the existence of charge-transfer as well as physical interactions between graphene and adsorbed Fe doped TiO_2 on its surface. Our first-principles theoretical investigations validate the experimental findings and clearly show the importance of weak charge-transfer between the graphene and adsorbed Fe doped TiO_2.

7.6. References.

[1] J. Matos, A. Garcia, T. Cordero, J.-M. Chovelon, C. Ferronato, Catalysis Letters 130 (2009) 568-574.

[2] J. Matos, J. Laine, J.-M. Herrmann, Applied Catalysis B: Environmental 18 (1998) 281-291.

[3] J.-M. Herrmann, J. Matos, J. Disdier, C. Guillard, J. Laine, S. Malato, J. Blanco, Catalysis Today 54 (1999) 255-265.

[4] S. Sato, Chemical Physics Letters 123 (1986) 126-128.
[5] J.A.C. Navio, G.; Macias, M.; Real, C.; Litter, M. I., , Applied Catalysis A: General 177 (1999) 111-120.
[6] T. Rajh, A.E. Ostafin, O.I. Micic, D.M. Tiede, M.C. Thurnauer, The Journal of Physical Chemistry 100 (1996) 4538-4545.
[7] J. Choi, H. Park, M.R. Hoffmann, The Journal of Physical Chemistry C 114 (2009) 783-792.
[8] W. Choi, A. Termin, M.R. Hoffmann, The Journal of Physical Chemistry 98 (1994) 13669-13679.
[9] Y. Wang, Y. Wang, Y. Meng, H. Ding, Y. Shan, X. Zhao, X. Tang, The Journal of Physical Chemistry C 112 (2008) 6620-6626.
[10] J.J. Sene, W.A. Zeltner, M.A. Anderson, The Journal of Physical Chemistry B 107 (2003) 1597-1603.
[11] A. Di Paola, E. GarcIa-López, S. Ikeda, MarcI, G., B. Ohtani, L. Palmisano, Catalysis Today 75 (2002) 87-93.
[12] S. Sakthivel, M.V. Shankar, M. Palanichamy, B. Arabindoo, D.W. Bahnemann, V. Murugesan, Water Research 38 (2004) 3001-3008.
[13] M.S. Park, S.K. Kwon, B.I. Min, Physical Review B 65 (2002) 161201.
[14] N.H. Hong, J. Sakai, W. Prellier, A. Hassini, A. Ruyter, F. Gervais, ccedil, ois, Physical Review B 70 (2004) 195204.
[15] Y. Wang, Y. Hao, H. Cheng, J. Ma, B. Xu, W. Li, S. Cai, Journal of Materials Science 34 (1999) 2773-2779.
[16] Y. Yao, G. Li, S. Ciston, R.M. Lueptow, K.A. Gray, Environmental science & technology 42 (2008) 4952-4957.
[17] C.N.R. Rao, B.C. Satishkumar, A. Govindaraj, M. Nath, ChemPhysChem 2 (2001) 78-105.
[18] K. Woan, G. Pyrgiotakis, W. Sigmund, Advanced Materials 21 (2009) 2233-2239.
[19] J.L. Gole, J.D. Stout, C. Burda, Y. Lou, X. Chen, The Journal of Physical Chemistry B 108 (2003) 1230-1240.
[20] E.P. Reddy, L. Davydov, P. Smirniotis, Applied Catalysis B: Environmental 42 (2003) 1-11.
[21] M. Hirano, K. Ota, H. Iwata, Chemistry of Materials 16 (2004) 3725-3732.
[22] W. Wang, C.G. Silva, J.L. Faria, Applied Catalysis B: Environmental 70 (2007) 470-478.
[23] T. Torimoto, Y. Okawa, N. Takeda, H. Yoneyama, Journal of Photochemistry and Photobiology A: Chemistry 103 (1997) 153-157.
[24] C.H. Ao, S.C. Lee, Applied Catalysis B: Environmental 44 (2003) 191-205.
[25] J. Araña, J.M. Doña-Rodríguez, E. Tello Rendón, C. Garriga I Cabo, O. González-Díaz, J.A. Herrera-Melián, J. Pérez-Peña, G. Colón, J.A. Navío, Applied Catalysis B: Environmental 44 (2003) 161-172.
[26] P. Fu, Y. Luan, X. Dai, Journal of Molecular Catalysis A: Chemical 221 (2004) 81-88.
[27] X. Zhang, M. Zhou, L. Lei, Carbon 43 (2005) 1700-1708.
[28] A. Jitianu, T. Cacciaguerra, R. Benoit, S. Delpeux, F. Béguin, S. Bonnamy, Carbon 42 (2004) 1147-1151.
[29] H. Huang, W.K. Zhang, X.P. Gan, C. Wang, L. Zhang, Materials Letters 61 (2007) 296-299.

[30] I. Moriguchi, R. Hidaka, H. Yamada, T. Kudo, H. Murakami, N. Nakashima, Advanced Materials 18 (2006) 69-73.
[31] S.-R. Jang, R. Vittal, K.-J. Kim, Langmuir 20 (2004) 9807-9810.
[32] B. Liu, H.C. Zeng, Chemistry of Materials 20 (2008) 2711-2718.
[33] B. Gao, G.Z. Chen, G. Li Puma, Applied Catalysis B: Environmental 89 (2009) 503-509.
[34] M.J. McAllister, J.-L. Li, D.H. Adamson, H.C. Schniepp, A.A. Abdala, J. Liu, M. Herrera-Alonso, D.L. Milius, R. Car, R.K. Prud'homme, I.A. Aksay, Chemistry of Materials 19 (2007) 4396-4404.
[35] H.C. Schniepp, J.-L. Li, M.J. McAllister, H. Sai, M. Herrera-Alonso, D.H. Adamson, R.K. Prud'homme, R. Car, D.A. Saville, I.A. Aksay, The Journal of Physical Chemistry B 110 (2006) 8535-8539.
[36] P.V. Kamat, The Journal of Physical Chemistry Letters 1 (2009) 520-527.
[37] I.V. Lightcap, T.H. Kosel, P.V. Kamat, Nano Letters 10 (2010) 577-583.
[38] R. Muszynski, B. Seger, P.V. Kamat, The Journal of Physical Chemistry C 112 (2008) 5263-5266.
[39] G. Williams, B. Seger, P.V. Kamat, ACS Nano 2 (2008) 1487-1491.
[40] Y. Zhang, Z.-R. Tang, X. Fu, Y.-J. Xu, ACS Nano 4 (2010) 7303-7314.
[41] Y. Liang, H. Wang, H. Sanchez Casalongue, Z. Chen, H. Dai, Nano Research 3 (2010) 701-705.
[42] D. Wang, D. Choi, J. Li, Z. Yang, Z. Nie, R. Kou, D. Hu, C. Wang, L.V. Saraf, J. Zhang, I.A. Aksay, J. Liu, ACS Nano 3 (2009) 907-914.
[43] H. Zhang, X. Lv, Y. Li, Y. Wang, J. Li, ACS Nano 4 (2009) 380-386.
[44] Y.-B. Tang, C.-S. Lee, J. Xu, Z.-T. Liu, Z.-H. Chen, Z. He, Y.-L. Cao, G. Yuan, H. Song, L. Chen, L. Luo, H.-M. Cheng, W.-J. Zhang, I. Bello, S.-T. Lee, ACS Nano 4 (2010) 3482-3488.
[45] B. Das, B. Choudhury, A. Gomathi, A.K. Manna, S.K. Pati, C.N.R. Rao, ChemPhysChem 12 (2011) 937-943.
[46] M.I. Rojas, E.P.M. Leiva, Physical Review B 76 (2007) 155415.
[47] L. Staudenmaier, Ber. Dtsch. Chem. Ges. 31 (1898) 1481.
[48] J.P. Choi, H.;, and Hoffmann, M. R., J. Phys. Chem. C 114 (2010) 783–792.
[49] G. Kresse, J. Furthmüller, Computational Materials Science 6 (1996) 15-50.
[50] G. Kresse, D. Joubert, Physical Review B 59 (1999) 1758-1775.
[51] J.P. Perdew, J.A. Chevary, S.H. Vosko, K.A. Jackson, M.R. Pederson, D.J. Singh, C. Fiolhais, Physical Review B 46 (1992) 6671-6687.
[52] L. Miao, P. Jin, K. Kaneko, A. Terai, N. Nabatova-Gabain, S. Tanemura, Applied Surface Science 212-213 (2003) 255-263.
[53] G. Wang, J. Yang, J. Park, X. Gou, B. Wang, H. Liu, J. Yao, The Journal of Physical Chemistry C 112 (2008) 8192-8195.
[54] B.M. Peng, X.; Tang, F., Ren, X.; Chen, D.; and Ren, J. , J. Phys. Chem. C 113 (2009) 20240–20245.
[55] L.X. Zhang H, Li YM, et al., ACS Nano 4 (2010) 380-386.
[56] J.H. Park, S. Kim, A.J. Bard, Nano Letters 6 (2005) 24-28.
[57] D. Eder, M. Motta, A.H. Windle, Nanotechnology 20 (2009).
[58] K. Fujihara, S. Izumi, T. Ohno, M. Matsumura, Journal of Photochemistry and Photobiology A: Chemistry 132 (2000) 99-104.

[59] S.I. K. Fujihara, T. Ohno, Matsumura, M. Time-resolved J. Photochem. Photobiol. 132 (2000) 99–104.
[60] K.N. Kudin, B. Ozbas, H.C. Schniepp, R.K. Prud'homme, I.A. Aksay, R. Car, Nano Letters 8 (2008) 36-41.
[61] Y.L.H.M.S.Z.Z.Y. W F Zhang, Q. Chen, J. Phys. D: Appl. Phys. 33 (2000) 912-9121-9916.
[62] J.R. J. Zhu, Y. Huo, Z. Bian, H. and Li, , J. Phys. Chem. C 111 (2007) 18965-18969.
[63] O. Akhavan, Carbon 48 (2010) 509-519.
[64] K. Nagaveni, M.S. Hegde, G. Madras, The Journal of Physical Chemistry B 108 (2004) 20204-20212.
[65] S. Stankovich, D.A. Dikin, R.D. Piner, K.A. Kohlhaas, A. Kleinhammes, Y. Jia, Y. Wu, S.T. Nguyen, R.S. Ruoff, Carbon 45 (2007) 1558-1565.
[66] G. Cao, Imperial College Press: London (2004) p xiv, 433 p.
[67] S.W. Wenting Dong, Danping Chen, Xiongwei Jiang and Congshan Zhu, Chemistry Letters (2000) 496-497.
[68] M.R. Hoffmann, S.T. Martin, W. Choi, D.W. Bahnemann, Chemical Reviews 95 (1995) 69-96.
[69] W. Wang, P. Serp, P. Kalck, J.L. Faria, Journal of Molecular Catalysis A: Chemical 235 (2005) 194-199.
[70] H. Valencia, A. Gil, G. Frapper, The Journal of Physical Chemistry C 114 (2010) 14141-14153.
[71] L. Liu, Z. Shen, Applied Physics Letters 95 (2009) 252104-252103.
[72] J. Yu, Q. Xiang, M. Zhou, Applied Catalysis B: Environmental 90 (2009) 595-602.
[73] E. Cockayne, Physical Review B 85 (2012) 125409.
[74] W. Oswald, Z. Wu, Physical Review B 85 (2012) 115431.
[75] S.D. Mo, W.Y. Ching, Physical Review B 51 (1995) 13023-13032.

Chapter 8

Conclusions and Recommendations

8.1. Conclusions.

Recently, two-dimensional graphene has initiated a rapid exploration of its potential in a broad range of fields including energy conversion, catalysis, sensing and nanocomposites[1]. Graphene shows excellent properties such as high chemical stability, high surface area and high electrical and thermal conductivity [2].

Various catalyst particles can be incorporated onto individual graphene sheets providing higher properties for various applications of current interest [3]. There is great interest in using titanium dioxide for controlling air and water pollution using photocatalysts as well as energy production technology using cheaper higher efficiency materials for photovoltaic devices [4]. TiO_2 has excellent photocatalytic properties and chemical stability, and it is an environmentally friendly and abundant substance[5].

There are some recent studies on modifying TiO_2 on the graphene sheets [6-8]. Graphene is a good electron acceptor and can serve as charge trapping sites and reduce the electron-hole recombination rate to enhance the photocatalytic activity of titania[9]. Graphene□s high surface area makes it an excellent candidate for use in photocatalysis. Both TiO_2 and pollutants can be adsorbed on the pores of graphene, producing active sites that enhance activity for degrading pollutants to carbon dioxide and water efficiently[10]. Some literature also emphasizes that graphene can act as a photosensitizer to promote optical responses in the visible light region, however, the shift to the visible region is not significant[11].

In this research, TiO_2 and modified TiO_2 were prepared on the surface of graphene sheets in different solvents. Different weight ratios of TiO_2-graphene nanocomposites were synthesized and characterized using sonication following by supercritical carbon dioxide ($scCO_2$) washing. The synthesized materials were applied as an electrode in a photovoltaic device, showing 4.7 times higher efficiency compared to bare commercial anatase TiO_2. One-dimensional TiO_2 nanostructures are potentially more effective than commercial TiO_2 nanoparticles as they are oriented, enhancing vectorial charge transfer. To improve the property of prepared TiO_2, we synthesized TiO_2 nanowires on the surface of graphene sheets using a sol-gel method in $scCO_2$ to prevent agglomeration and control the particle size. Different temperatures, pressures, acetic acid to TIP ratios, and TIP to FGSs weight ratios were examined for this reaction. We found the optimum conditions

for preparing uniform decoration of TiO_2 on the graphene sheets. The synthesized materials were then used as an active layer for the electrode in photovoltaic devices (dye sensitized solar cells), showing 5.1 times higher efficiency compared to bare commercial anatase TiO_2. These one-dimentional nanostructures on the graphene sheets showed higher efficiency compared to TiO_2 nanoparticles on the graphene sheets prepared in ethanol as well.

To further improve the properties of TiO_2/FGSs composites, we doped TiO_2 using a sol-gel method in $scCO_2$. The band gap of the prepared materials was significantly shifted to lower wavelengths, which were subsequently examined for the degradation of E2, showing higher activity than both TiO_2/graphene composites and Fe doped TiO_2 nanostructures. These materials were also applied as an active layer in the photovoltaic cells, showing an enhancement in efficiency compared to TiO_2 by 6.2.

To further study the effect of solvent, Fe-doped TiO_2 nanoparticles were prepared in a mixture of ethanol and water. The band gap change was similar, although the surface area and rate constant for the photodegradation of E2 decreased compared to using $scCO_2$ as solvent. Ni, Pt and La also were doped on the TiO_2/graphene sheets, showing enhanced photocatalytic activities under the visible-light irradiation by an order of magnitude while La-TiO_2 had a negligible effect when compared to undoped TiO_2. The difference in photocatalytic activity of the different dopants can be explained by their ionic radius. Dopants with larger radius than TiO_2, i.e. La, cannot integrate inside the TiO_2 lattice, minimizing any impact on the optical and photoactive properties.

ZrO_2-TiO_2 nanomaterials were also synthesized on the graphene sheets using a sol-gel method in $scCO_2$. The materials showed enhancement in surface area and thermal stability resulting in higher activity of the catalysts in the photodegradation of E2.

Furthermore, possible interactions between TiO_2 and graphene sheets were studied using VASP based DFT. According to calculated energies, there are both physisoption and chemisorptions between TiO_2 and graphene sheets with hollow sites resulting in the most stable configuration. Introducing carboxylate groups onto the graphene sheet surface also resulted in further decreasing in E_{ads} to ~ -5 eV, indicating active chemisorption between TiO_2 and the functionalized graphene sheets. By replacing one Ti atom with Fe in the anatase structure and calculating the bonding energies, all the energies slightly increased.

The Fe doped TiO_2/graphene system was found more stable than the corresponding undoped system, attributed to higher charge transfer between Fe doped TiO_2 and graphene sheets.

8.2. Recommendations.

Recommendations for future work include:

1. Controlling the exfoliation of graphite oxide in $scCO_2$ by varying temperature and pressure and studying their effect on the degree of functionalities on the graphene sheets.
2. The successful synthesis of the TiO_2-based nanostructure materials on the graphene sheets via sol-gel process in $scCO_2$ is encouraging to extend this method for synthesizing other oxide nanostructures, such as ZnO and corresponding doped ZnO.
3. Evaluate these materials as an electrode in solar cells and optimize the synthesis parameters for this application.
4. Detailed kinetics study including the effects of temperature, acid to metal alkoxide ratio, and concentration on the sol-gel process for TiO_2 and modified TiO_2 in $scCO_2$ using *in situ* ATR-FTIR and Raman techniques.
5. Study the effect of TiO_2 and modified TiO_2 on the graphene sheets for other pollutants of interest.
6. Control Functionalized surface of graphene sheets by selective functional groups to adsorb only the desired pollutants.
7. Apply different prepared metal-doped TiO_2 nanoparticles and also ZrO_2-TiO_2 nanomaterials prepared on the surface of graphene sheets as an electrode in photovoltaic solar cells and compare the efficiencies with TiO_2 nanowires and Fe doped TiO_2 on the graphene sheets.
8. Modify the surface of TiO_2/graphene prepared in $scCO_2$ by Quantom dots such ZnO, CdS, CdSe and evaluate as an electrode for solar cell application.
9. Theoretical Study of the band gap of TiO_2 and modified TiO_2 when in contact with graphene using VASP.

10. Comprehensive theoretical study on different possible interactions between TiO_2 doped TiO_2 and ZrO_2-TiO_2 and graphene sheets and calculates E_{ads} for each configuration.
11. DFT calculation on TiO_2 and graphene with some defect sites on its surface and compare the results with ideal graphene.
12. Consideration of the $scCO_2$ conditions in DFT calculation and explain the mechanism of TiO_2 nanoassembly growth formation.
13. Decorating graphene sheets with other metals and semiconductors and calculate the corresponding adsorption energies and charge transfer.

8.3. References.

[1] I.V. Lightcap, T.H. Kosel, P.V. Kamat, Nano Letters 10 (2010) 577-583.
[2] Anone, Nature Materials 10 (2011) 1.
[3] H. Zhang, X. Lv, Y. Li, Y. Wang, J. Li, ACS Nano 4 (2009) 380-386.
[4] I.K. Konstantinou, T.A. Albanis, Applied Catalysis B: Environmental 49 (2004) 1-14.
[5] A.H. Fujishima, K.; Watanabe, T., BKC, Inc. (1999).
[6] T.N. Lambert, C.A. Chavez, B. Hernandez-Sanchez, P. Lu, N.S. Bell, A. Ambrosini, T. Friedman, T.J. Boyle, D.R. Wheeler, D.L. Huber, The Journal of Physical Chemistry C 113 (2009) 19812-19823.
[7] D. Wang, D. Choi, J. Li, Z. Yang, Z. Nie, R. Kou, D. Hu, C. Wang, L.V. Saraf, J. Zhang, I.A. Aksay, J. Liu, ACS Nano 3 (2009) 907-914.
[8] H. Zhang, X. Lv, Y. Li, Y. Wang, J. Li, ACS Nano 4 (2010) 380-386.
[9]
[10] X.Y.L.H.-P.C. Zhang, X-L; Linb, Y., Journal of Materials Chemistry 20 (2010) 2801-2806.
[11] Y.-B. Tang, C.-S. Lee, J. Xu, Z.-T. Liu, Z.-H. Chen, Z. He, Y.-L. Cao, G. Yuan, H. Song, L. Chen, L. Luo, H.-M. Cheng, W.-J. Zhang, I. Bello, S.-T. Lee, ACS Nano 4 (2010) 3482-3488.

Appendix 1: XPS spectra of (a) FGSs, High resolution (b) C (1s) (b) and (c) O (1s).

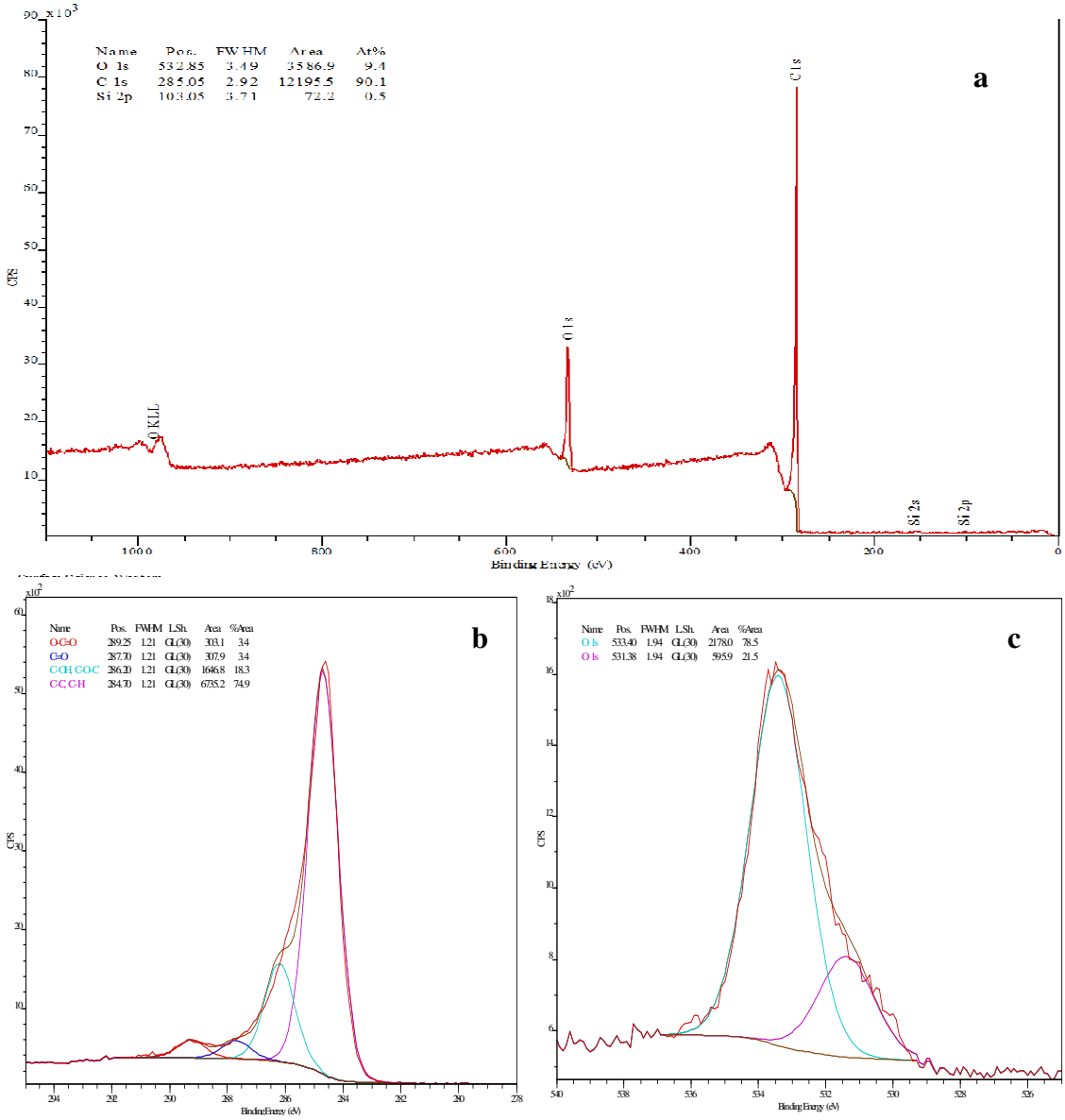

Appendix 2: XPS spectra of Fe doped TiO_2/ FGSs (0.6%) prepared in $scCO_2$.

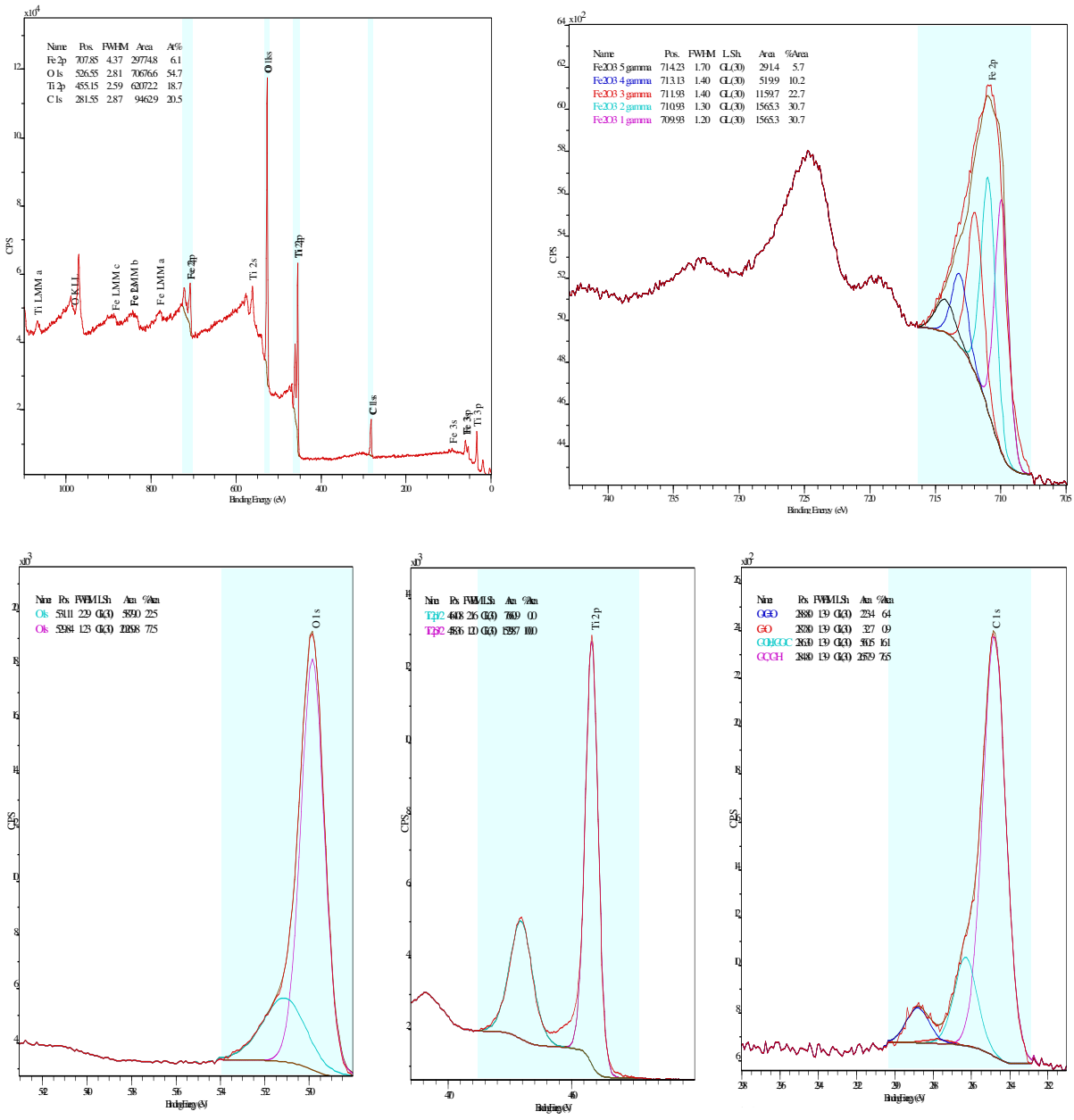

Appendix 3. Assignment of copyright form - IOP Publishin Limited

1. **1. IOP Publishing Limited ("IOP") agrees to publish:**

Manuscript Title: "Growing TiO_2 Nanowires on the Surface of Graphene Sheets in Supercritical CO_2: Characterization and Photoefficiency" written by "Nasrin Farhangi, Yaocihuatl Medina-Gonzalez, Rajib Roy Chowdhury, and Paul A. Charpentier" in the following journal " Nanotechnology"

2. Transfer of Copyright Agreement

2.1 On acceptance for publication the undersigned author(s) ("Author") of the Article assigns exclusively to IOP worldwide copyright in the Article for the full term and for all media and formats in all material published as part of the Article, which expression includes but is not limited to the text, abstract, tables, figures, graphs, video abstracts and other multimedia content but excludes any other item referred to as supplementary material.

2.2 If any of the Named Authors are Government employees, on acceptance for publication the Author shall grant IOP a royalty free exclusive licence for the full term of copyright for all media and formats to do in relation to the Article all acts restricted by copyright worldwide.

2.3 On acceptance for publication the Author shall grant IOP a royalty free non-exclusive licence for the full term of copyright for all media and formats to do in relation to any supplementary material deemed to be part of the Article all acts restricted by copyright worldwide.

3. Author Rights

3.1 IOP grants the Named Authors the rights specified in 3.2 and 3.3. All such rights must be exercised for non-commercial purposes, if possible should display citation information and IOP's copyright notice, and for electronic use best efforts must be made to include a link to the on-line abstract in the Journal. Exercise of the rights in 3.3 additionally must not use the final published IOP format but the Named Author's own format (which may include amendments made following peer review).

3.2 The rights are:
3.2.1 To make copies of the Article (all or part) for teaching purposes;
3.2.2 To include the Article (all or part) in a research thesis or dissertation;
3.2.3 To make oral presentation of the Article (all or part) and to include a summary and/or highlights of it in papers distributed at such presentations or in conference proceedings; and
3.2.4 All proprietary rights other than copyright.

3.3 The additional rights are to:
3.3.1 Use the Article (all or part) without modification in personal compilations or publications of a Named Author's own works (provided not created by third party publisher);

3.3.2 Include the Article (all or part) on a Named Author's own personal web site;
3.3.3 Include the Article (all or part) on web sites of the Institution (including its repository) where a Named Author worked when research for the Article was carried out; and
3.3.4 No sooner than 12 months after publication to include the Article (all or part) on third party web sites including e-print servers, but not on other publisher's web sites.

4. Signature

In signing this Agreement the Author represents and warrants that the Article is the original work of the Named Authors, it has not been published previously in any form (other than as permitted under clause 3.2.2 which fact has been notified to IOP Publishing Ltd in writing), all Named Authors have participated sufficiently in the conception and writing of the Article, have received the final version of the Article, agree to its submission and take responsibility for it, and submission has been approved as necessary by the authorities at the establishment where the research was carried out.

The Author warrants that he/she signs this Agreement as authorised agent for all Named Authors and has the full power to enter into this Agreement and to make the grants it contains, that the Article has not been and will not be submitted to another publisher prior to withdrawal or rejection, it does not infringe any third party rights, it contains nothing libellous or unlawful, all factual statements are to the best of the Author's knowledge true or based on valid research conducted according to accepted norms, and all required permissions have been obtained in writing.

All Named Authors assert their moral rights.

Author's signature . . . . . Date . . . . . .

Signature on behalf of Institution . . . . . Date . . . . . .

Note that if the Article was prepared as part of a Named Author's duties for their institution this Agreement must be signed by their institution as Author. Further, if there are several Named Authors it should be signed by one author in a representative capacity. If all Named Authors are employees of the US Government and the Article was prepared as part of their duties the Article is not eligible for copyright and one of the Named Authors should sign below to confirm this fact. If at least one of the Named Authors is not a US Government employee the above should be signed.

I . . . . . (print name . . . . .) confirm that all Named Authors are employees of the US Government and the Article was prepared as part of their duties and consequently the Article is not eligible for copyright.

Please return ALL of this form as soon as possible to IOP Publishing Ltd, Temple Circus, Temple Way, BRISTOL BS1 6BE, UK.

Appendix 4: License Agreement with Elsevier Limited.

ELSEVIER LICENSE
TERMS AND CONDITIONS

This is a License Agreement between Nasrin Farhangi ("You") and Elsevier ("Elsevier") provided by Copyright Clearance Center ("CCC"). The license consists of your order details, the terms and conditions provided by Elsevier, and the payment terms and conditions.

All payments must be made in full to CCC. For payment instruction, please see information listed at the bottom of this form.

Supplier Elsevier Limited
The Boulevard, Langford Lane
Kidlington, Oxford, OX5 1GB, UK
Registered Company Number 1982084
Customer Name Nasrin Farhangi
Customer Address London, Ontario, N6G 5A6
License Number 2860921065264
License date March 02, 2012-06-25
Licensed Content Publisher:Elsevier
Licensed Content Publication Applied Catalysis B: Environmental
Licensed Content Title Visible light active Fe doped TiO2 nanowires grown on Graphene using Supercritical CO2
Licensed Content Author Nasrin Farhangi, Rajib Roy Chowdhury, Yaocihuatl Medina-Gonzalez, Madhumita B. Ray and Paul A. Charpentier
Licensed Content date 2 November 2011
Licensed Content Volume Number 110
Number of Pages 8
Start Page 25
End page 32
Type of use reuse in a thesis/ dissertation
Portion full article
Format both print and electronic
Are you the author of this Elsevier article? Yes
Will you be translating? No
Title of your thesis / dissertataion? TiO2 on graphene sheets
Expected Completion date Aug 2012
Estimated size (Number of pages) 220
Elsevier VAT number GB 494 627212
Permission price 0.00 USD

ELSEVIER LICENSE
TERMS AND CONDITIONS
Mar 15, 2012
This is a License Agreement between Nasrin Farhangi ("You") and Elsevier ("Elsevier") provided by Copyright Clearance Center ("CCC"). The license consists of your order details, the terms and conditions provided by Elsevier, and the payment terms and conditions.
Supplier Elsevier Limited
The Boulevard,Langford Lane
Kidlington,Oxford,OX5 1GB,UK
Registered CompanyNumber 1982084
Customer name Nasrin Farhangi
Customer address 50 Reid ct.
London, ON N6G 5A6
License number 2870221492382
License date Mar 15, 2012
Licensed content publisher Elsevier
Licensed contentpublication Applied Catalysis B: Environmental
Licensed content title Photocatalytic degradation of phenol on MWNT and titania composite catalysts prepared by a modified solgel method
Licensed content author Wendong Wang,Philippe Serp,Philippe Kalck,Joaquim Luís Faria
Licensed content date 8 April 2005
Licensed content volume number 56
Licensed content issue number 4
Number of pages 8
Start Page 305
End Page 312
Type of Use reuse in a thesis/dissertation
Portion figures/tables/illustrations
Number of figures/tables/illustrations 1
Format both print and electronic
Are you the author of this Elsevier article? No
Will you be translating? No
3/15/12 Rightslink Printable License
https://s100.copyright.com/AppDispatchServlet 2/5
Order reference number
Title of your thesis/dissertation
TiO2-based nanomaterials on the graphene sheets
Expected completion date Jul 2012
Estimated size (number of pages) 220
Elsevier VAT number GB 494 6272 12
Permissions price 0.00 USD
VAT/Local Sales Tax 0.0 USD / 0.0 GBP
Total 0.00 USD

Appendix 5. License Agreement with John Willey and Sons.

JOHN WILEY AND SONS LICENSE
TERMS AND CONDITIONS
Mar 02, 2012
License Number 2860930497914
License date Mar 02, 2012
Licensed content publisher John Wiley and Sons
Licensed content publication
Journal of Polymer Science Part B: Polymer Physics
Licensed content title Functionalized graphene sheet—Poly(vinylidene fluoride) conductive nanocomposites
Licensed content author Seema Ansari,Emmanuel P. Giannelis
Licensed content date May 1, 2009
Start page 888
End page 897
Type of use Dissertation/Thesis
Requestor type University/Academic
Format Print and electronic
Portion Figure/table
Number of figures/tables 1
Number of extracts
Original Wiley figure/table number(s) Figure 1
Will you be translating? No
Order reference number
Total 0.00

NASRIN FARHANGI

EDUCATION:

PhD in Chemical Engineering (Aug 2012)
Department of Chemical and Biochemical Engineering, University of Western Ontario, Canada.
Master in Organic Chemistry (March 2001)
Azzahra University,Tehran, Iran.
Bachlor in Chemistry (July 1997)
Azzahra University, Tehran, Iran.

RESEARCH EXPERIENCE

Research Assistant (January 2007 – present)
Department of Chemical and Biochemical Engineering, University of Western Ontario, Canada.
Research Assistant (1998-2005)
Azzahra University, Tehran, Iran.

TECHNICHAL SKILLS:

Synthesis and characterization of Advanced Nanomaterials.
Operating TEM, SEM, UV-vis spectrometer, Photoluminescence Raman spectrometer, BET surface area, Extruder, TGA, XRD.
Analyzing high resolution XPS data.

PUBLICATIONS:

1. **Nasrin Farhangi**, Rajib Roy Chowdhury, Yaocihuatl Medina-Gonzalez, Madhumita B. Ray and Paul A. Charpentier: Visible light active Fe doped TiO_2 nanowires grown on Graphene using Supercritical CO_2. Applied Catalysis B, 2011, 110, 25-32.
2. **Nasrin Farhangi**, Yaocihuatl Medina-Gonzalez, Rajib Roy Chowdhury and Paul Charpentier: Growing TiO_2 Nanowires on the Surface of Graphene Sheets in
3. Supercritical CO_2: Characterization and Photoefficiency. Nanotechnology 2012, 23 294005 doi:10.1088/0957-4484/23/29/294005.
4. Yaocihuatl Medina-Gonzalez, William Z Xu, Bo Chen, **Nasrin Farhangi** and Paul A Charpentier: CdS and CdTeS quantum dot decorated TiO_2 nanowires. Synthesis and photoefficiency, Nanotechnology, 22 (2011) 065603 (8pp).
5. Serge Ayissi, **Nasrin Farhangi** and Paul A. Charpentier; Simulation of Graphene and TiO_2 Interactions by Density Functional Theory (In preparation).
6. **Nasrin Farhangi** and Paul Charpentier: Synthesis and photocatalytic activity of ZrO_2/TiO_2 nanotubes on the surface of graphene sheets prepared in Supercritical CO_2, (In preparation).